Nanomanufacturing for Biological Sensing Applications

by

Robert J. Barsotti, Jr.

B.S.E. Materials Science Engineering
University of Pennsylvania, 2002

SUBMITTED TO THE DEPARTMENT OF MATERIALS SCIENCE AND ENGINEERING IN PARTIAL FULFILLMENT OF THE REQUIREMENTS FOR THE DEGREE OF

DOCTOR OF PHILOSOPHY IN MATERIALS SCIENCE AND ENGINEERING
AT THE
MASSACHUSETTS INSTITUTE OF TEHCNOLOGY

FEBRUARY 2007

Signature of Author: _____
Department of Materials Science and Engineering
October 23, 2006

Certified by: _____
Dr. Francesco Stellacci
Finmeccanica Career Development Assistant Professor of Materials Science and Engineering
Thesis Supervisor

Accepted by: _____
Samuel M. Allen
POSCO Professor of Materials Science and Engineering
Chair, Departmental Committee on Graduate Students

NANOMANUFACTURING FOR BIOLOGICAL SENSING APPLICATIONS

by

ROBERT J. BARSOTTI JR.

Submitted to the Department of Materials Science and Engineering on October 23, 2006 in partial fulfillment of the requirements for the Degree of Doctor of Philosophy in Materials Science and Engineering

ABSTRACT

Over the past 10-15 years, there have been tremendous research efforts in the synthesis of nanomaterials with unique electronic properties. Much less work, however, has focused on the incorporation of the nanomaterials into electronic devices. In order for nanomaterials to have a technological impact in electronic devices, nanomanufacturing techniques must be established for the reliable and reproducible creation of devices with nanomaterials as the active component.

In this thesis, the incorporation of 3-20 nm diameter ligand coated gold nanoparticles into an electronic device is studied. Ligand coated nanoparticles provide great control over their solubility and electronic properties through the choice of protecting ligand molecule. The use of an isolated nanoparticle in electronic devices presents two major difficulties which are studied in detail in this work. In order to use the electrical properties of a single particle or a few particles, insulating gaps in metallic electrodes must be fabricated with dimensions of 5-50 nm. Several methods including direct patterning with electron beam lithography, physical methods of gap formation, and electrical methods of gap formation are described, studied and evaluated for use in nanomanufacturing.

A second major challenge is the specific assembly of nanoparticles into the nanogaps. The use of chemically directed assembly to pattern particles on templates generated by Dip Pen Nanolithography is described using several different surface chemistries. An electrical based method, dielectrophoresis, is found to be better suited for assembly of particles into the gaps and the forces which affect assembly are studied in detail. Electrical characterizations of networks of 10-200 nanoparticles are studied as a function of protecting ligand molecule.

Preliminary results on the use of nanomanufactured devices consisting of gold nanoparticles-oglionucleotide conjugates bridging a nano-gap for DNA sensing are presented.

Thesis Supervisor: Dr. Francesco Stellacci

Title: Finmeccanica Career Development Assistant Professor of Materials Science and Engineering

Table of Contents

Nanomanufacturing for Biological Sensing Applications

List of Figures

List of Tables

Chapter 1: Literature Review

1.1 Introduction

Over the past 15 years, there has been a tremendous deal of excitement in the scientific community concerning the promise of nanotechnology. Much of this excitement has been due to the synthesis of exciting new materials. These materials are composed of elements which have been readily used for decades, such as Au, Si and C, but the size, structure and morphology of these novel nanomaterials has led to an exciting new set of properties. Much of the excitement concerning nanotechnology has been generated over the unique electronic properties of materials such as gold nanoparticles, silicon nanowires and carbon nanotubes.

The potential for electronic applications of nano-materials seems limitless. Due to the small size of the materials, nanotechnology applications in microelectronics have the potential to extend Moore's law for many years. The ballistic conductivity of metallic carbon nanotubes make them ideal candidates for interconnects. Devices which show single electron charging, such as metallic or semiconducting nanoparticles, would allow for low power logic devices. Incorporation of nano-materials into biological sensing devices also has tremendous possibilities. For the first time, scientists have a class of materials which are on the same size scale as the molecules they which to detect. Hybrid materials consisting of nano-objects bound to biological "probe" molecules have been made. The binding of a single target molecule (complementary to the probe molecule) to

these materials may have a large effect on their electronic properties, allowing for detection of target molecules with outstanding sensitivity.

While there have been tremendous research efforts in the synthesis of these materials and the characterization of their properties, there has been much less work undertaken thus far in the incorporation of the materials into electronic devices. Many of the devices which have been fabricated incorporating nano-materials have been done so in a manner suitable to basic research, but not to manufacturability. In order for the promise of nanotechnology in electronic devices to be realized, methods must be developed to incorporate nanomaterials into devices on silicon based platforms using methods which are technologically scalable. While there are many challenges to be met in nano-manufacturing here I chose to focus on two of the biggest challenges: 1.) the fabrication of metallic leads separated by a nanogap in order to electrically address the nano-objects 2.) the directed specific assembly of nano-objects into the gap.

In this particular work, I chose ligand-coated gold nanoparticles as the nanomaterial to be incorporated into a device. Au nanoparticles can be prepared in solution with diameters ranging in size from 0.84 nm to 200 nm in diameter.[1, 2] The metal nanoparticles are synthesized by adding a reducing agent such as $NaBH_4$ to a metallic salt solution $HAuCl_4$ with thiolated capping ligands (R-SH).[2] These nanoparticles are protected by ligands bonded to their surface. (figure 1.1) Functionality can be given to the nanoparticles by tailoring the type and ratio of the ligands attached to the nanoparticle. Alternatively, the particles can be synthesized using citric acid, where the resulting particles are

electrostatically stabilized by citrate ions.[3] With either type of particles, ligands with differing chemical functionality can be controllably substituted onto the particles through a place exchange reaction.[4, 5] The choice of ligand molecule allows for control over the solubility, electronic and optical properties of the particles. The ligand functionality also allows for further chemistry to be done to the nanoparticles, including their directed assembly on patterned surfaces or the incorporation of biologically significant molecules. As a model system, I have chosen to look at the possible use of nanomanufacturing for DNA detection.

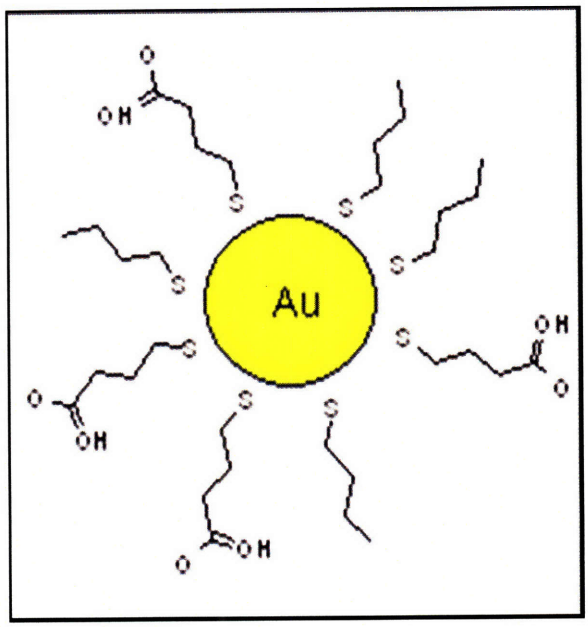

Figure 1.1: Gold nanoparticle stabilized by thiolated ligands with CH_3 and COOH head groups.

In this thesis, I begin by outlining the relevant background research in Chapter 1. This includes brief reviews of progress made on the fabrication of nanogaps, chemically directed assembly, electrically directed assembly, the electronic properties of nanoparticles, and efforts made at incorporating DNA and nanoparticles into hybrid

materials. Chapter 2 is devoted to finding technologically scalable methods for nanogap formation. In Chapter 2, I describe and evaluate the technological scalability of techniques to form nanogaps, with an emphasis on results showing the use electromigration of to form sub-20 nm gaps. Chapter 3 and 4 look at methods for the controlled assembly of nanoparticles. In Chapter 3, my work in chemically directed assembly is described, highlighting assembly using ionic and covalent bonds on substrates patterned by Dip Pen Nanolithography (DPN). In Chapter 4 an experimental and theoretical study of the use of dielectrophoresis for the controlled assembly of nanoparticles into nanogaps is presented. Electrical characterization of nanoparticles assembled in gaps with different stabilizing ligands is also presented. Finally, in chapter 5, preliminary efforts to use these devices for electrically based detection of DNA are described.

1.2 Fabrication of Nanogaps

In order to utilize the unique electronic properties of nano-objects as the active elements in logic or sensing devices, the nano-object must be electrically contacted to the outside world by two metallic wires. Different nano-objects therefore will impose different constraints on the size of the insulating gap into which the nanomaterial must be assembled. Long asymmetric nano-objects, such as carbon nanotubes and semiconducting nanowires stretch microns in length, making gap formation a trivial problem which can easily be achieved with standard lithography techniques. Nanoparticles, however, pose a much more difficult challenge. In this particular work ligand-coated gold nanoparticles, 4- 20 nm in core diameter, are used. In order to address

a single isolated nanoparticle, insulating gaps with dimensions of 3-20 nm must be achieved. Previous research on nanogap formation has been carried out for the study of the electrical properties of nano-objects,[6-14] molecules[15-20] and the formation of josephson junctions.[21, 22]

Fabrication of sub-50 nm nano-gaps on silicon-based platforms has been attempted using techniques which can be classified into 6 categories: 1.) direct patterning of gaps using electron beam lithography;[14, 23, 24] 2.) lithographic patterning of gaps followed by electrochemical etching/ electrochemical deposition to tune the size of gaps;[13, 19, 20, 25-28] 3.) "break" junctions formed by mechanical deformation of wires;[17, 18, 29, 30] 4.) physical methods of forming a gap after a continuous wire is patterned (deformation with atomic force microscopy, focused ion beam, or electron beam irradiation)[21, 31] 5.) use of conventional lithography and etching combined with shadow masking and angled evaporation to define nano-gaps;[6, 10-12, 16, 32-34] 6.) electrical methods of creating a gap after a narrow, thin wire is lithographically patterned. [7-9, 15, 35-39] All of these methods have certain advantages and disadvantages. The first four techniques, however rely on serial process techniques which have more application to basic research than to manufacturing. Electron beam lithography is a high resolution but slow technique for the formation of nano-gaps. Electrochemical deposition or etching is a fairly non-uniform process, so gaps must be individually monitored to achieve desired gaps sizes. Break junctions rely on complicated lithographic techniques not well-suited for manufacturability. Physical deformation techniques are serial techniques not suitable for technologies and also often cause contamination to the surfaces. As the last two

techniques can be more easily envisioned as technologically scaleable, the remainder of this section will focus on these methods.

Creative optical lithographic solutions have been devised for the fabrication of nano-gaps. In one approach, the first lead is patterned via optical lithography followed by coating the lead with a self-assembled monolayer[16]. This self-assembled monolayer (SAM) serves as a mask to prevent electrical contact when a second lead is overlapped. The length of the SAM molecule was used to tune the gap size. A second approach involves the creation of mesas or metallic wires (which serve as one lead), followed by the etching of the underlying SiO_2 substrate.[12, 32] This creates an undercut in the SiO_2 layer. A second deposition step results in the formation of a nano-gap. (figure 1.2) Similar approaches rely on the etching of a GaAs mesa,[11] angled-evaporation[6, 10] or the overhang of the photoresist (using positive lithography) to define the gap.[34] Finally, aligned carbon nanotubes have been demonstrated as shadow masks.[33] The use of optical lithography and the uniformity of gap sizes may allow these techniques to be transferred to a manufacturing environment. The gaps described have been used to study the electronic properties of molecules[16] and nanoparticles.[6, 10-12, 34]

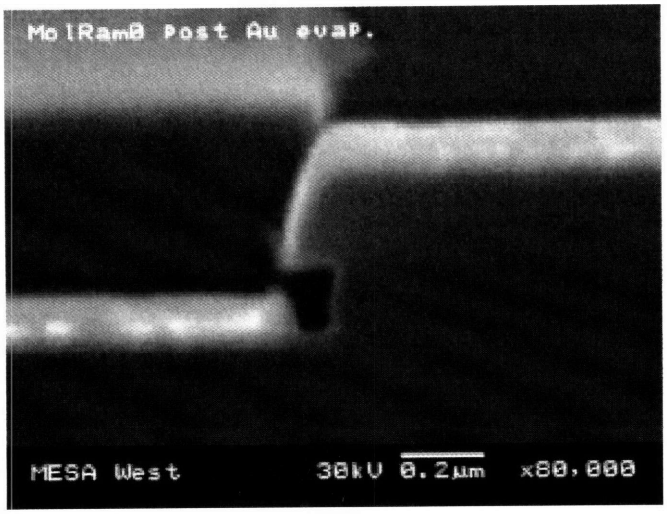

Figure 1.2: Undercut etching of SiO_2 substrate and subsequent deposition used to form a 60 nm gap. Courtesy of reference 12.

Electrical based methods of nano-gap formation are a second technique that is technologically scaleable. The promise of this technique is that gaps with separation of only a few atoms have been realized. A second advantage is that real time feedback via the electrical properties of the gap allows the process to be monitored in-situ. In this method narrow, thin metallic wires are patterned using either optical or electron beam lithography. The wire is usually patterned with a pre-defined neck or narrow section via either wire geometry, angled-evaporation or shadow masking. It is at this pre-defined weak point where controlled breaking will occur. While electron beam lithography is used in many of these works, it is not the enabling technology for this technique. (The dimensions patterned in many cases are 50-100 nm, well within the reach of state-of-the-art optical lithography techniques). After wire patterning, a voltage or current sweep is applied across the wire. The voltage or current is increased until wire failure is realized by the change in the electrical properties of the device. There remains a debate in the

literature whether failure is due to localized melting,[35] electromigration,[7, 15, 36, 38, 39] or perhaps thermally assisted electromigration.[8, 37]

In the localized melting explanation, the localized temperature increase due to joule (I^2R) heating is calculated by approximating the increase in resistance of the junction.[35] The localized temperature is found to be above the melting temperature of gold. Gap size is found to be below the resolution of SEM imaging (5nm).

Electromigration is the motions of atoms due to the momentum transfer from conduction electrons. According to the empirical Black's law the medium time to failure (MTF) in electromigration is proportional to current density (J):

$$MTF \propto J^{-n} e^{(E_a/kT)}$$

where E_a is a material dependent activation energy, k is Boltzman's constant, T is temperature and n is an empirical constant related to the type of defect formed.[35, 37] As current densities increase in the narrow section of the wire, atoms begin to migrate and eventually form defects. Failure in gold wires has been seen at current densities of $1.1*10^8 - 5.0*10^8$ A/cm^2. [8, 36] Electromigration has been performed at very low temperatures (4K or 77 K),[8, 9] room temperature[7, 36] and at elevated temperature.[39] Conductance measurements and SEM images of the gap post-break indicate that gaps ranging from a few Angstroms to 20 nm are formed. (figure 1.3) Increased control over the electromigration has been obtained by using feedback loops that increase voltage until a certain decrease in resistance is realized.[37, 38] Voltage is then decreased by 50-100 mV before being increased again. (figure 1.4) This technique has been used to see jumps in

conductance equal to integrals of the conductance quantum (G_0), corresponding to the movement of a few atoms. Gaps formed by electromigration have been used to study the electrical properties of nanoparticles.[7-9] Wide wires (~2 μm) defined by optical lithography have also been broken with electromigration and used for the study of molecular conduction.[15]

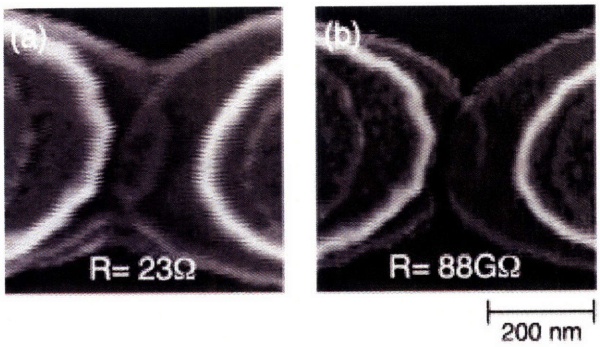

Figure 1.3: Nano-gap formed by electromigration, courtesy of reference 7.

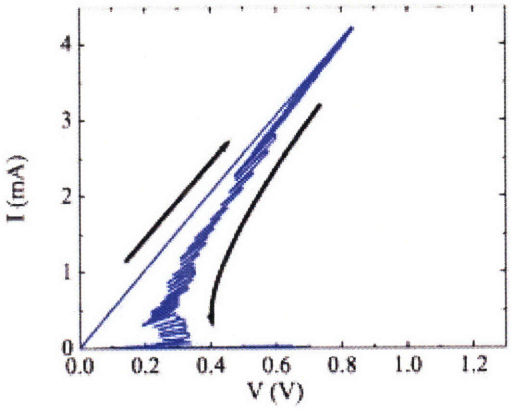

Figure 1.4: Voltage ramp method used for controlled electromigration. Courtesy of reference 38.

In order to pattern gold wires on SiO_2 substrates, a thin Cr or Ti adhesion layer must first be deposited. The role of this adhesion layer in the electrical breaking process has not been studied, although due to the higher melting points of Cr (1907 ° C) and Ti (1668 °C) as compared to gold (1064 °C), it may serve to hinder the formation of insulating gaps. In

order to avoid this problem, a self-assembled monolayer of mercaptopropyltrimethoxysilane (MPTMS) has been used to replace the Cr or Ti adhesion layer.[36, 40] (figure 1.5). Using ~ 2.2 μm wide wires defined by optical lithography, electromigration is used to form gaps ranging from 1-20 nm. The small gap sizes are attributed to the smaller grain size on films evaporated on MPTMS as compared with either Cr or Ti.

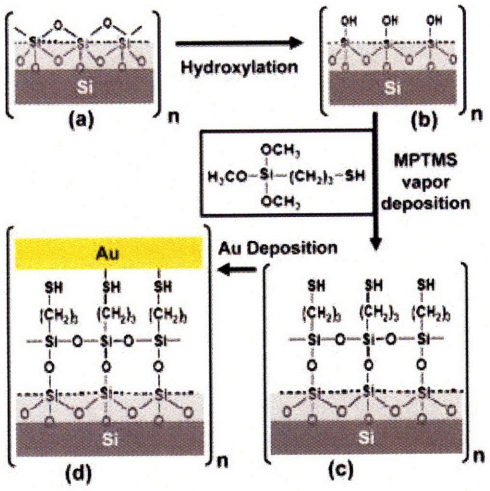

Figure 1.5: Method for molecular adhesion using an MPTMS monolayer. Courtesy of reference 40.

1.3 Chemically Directed Assembly

Nanotechnology requires the building of devices consisting of multiple materials onto surfaces. Chemically directed assembly of nano-objects is one strategy that has been developed for the construction of such devices.[41] Chemical directed assembly is an approach to building multi-material substrates and/or devices that uses molecular recognition to direct the assembly of objects onto lithographically defined patterns. A substrate is patterned with molecules with specific functional groups. When the substrate

is immersed into a solution of the desired object to be assembled, the patterned functional groups can guide the assembly of the nano-object through chemical interactions.

Chemically directed assembly has several major advantages. It is easily scaleable to large surfaces, giving it the potential to be used for technological applications. Chemically directed assembly allows for traditional lithographic approaches to be extended to the patterning of materials not compatible with such lithographies, such as nanoparticles, proteins, etc. Once an initial pattern is generated using scanning probe lithographies or more traditional top-down lithographies, nano-objects or proteins can be assembled onto this pattern using molecular recognition. Chemically directed assembly, however is not yet completely understood. Issues such as non-specific absorption, chemical reactions at interfaces, and the kinetics of such reactions have yet to be fully studied.

Conventional lithographic methods along with newer soft lithographic techniques have been used for the first step of chemically directed assembly, defining molecular templates on surfaces. Dip Pen Nanolithography (DPN) is a relatively new tool that is becoming increasing widely used in chemically directed assembly as it allows for patterning of molecules on surfaces with nanoscale resolution. In the following subsections a literature review of DPN (1.3.1), surface chemistries (1.3.2) , and chemically directed self-assembly (1.3.3) of Au nanoparticles on micron (*1.3.3.1*) and nanoscale templates (*1.3.3.2*), as well as onto devices (*1.3.3.3*) is presented.

1.3.1 Dip Pen Nanolithography

Dip Pen Nanolithography (DPN) was first demonstrated by Chad Mirkin's group at Northwestern University in 1999.[42] DPN uses an atomic force microscope to pattern molecules on specific areas of a surface. (figure 1.6) In DPN, molecules are first absorbed through weak van der Waals bonds onto the AFM tip and then released onto a surface on which they typically form stronger bonds; this was first demonstrated by patterning octadecanethiol (ODT) and mercapatohexadecanoic acid (MHA) on Au surfaces (using the strong thiol-Au covalent bond). DPN is performed by first coating a contact mode AFM tip with the molecule to be patterned ("ink"). This can be done using a solution or vapor deposition method.[42, 43] In the solution method a tip is dipped into an almost saturated solution of the molecule for 15-60 seconds.[42] In the vapor deposition method, the tip is suspended 1-2 cm above the solid form of the molecule, which is then heated to a temperature above its melting point but below its boiling point for 20-30 minutes, (65° C for ODT, 95°C for MHA).[43] Many molecules sublime and then condense on the AFM tip, coating it with the molecule. The coated tip is then used in contact mode AFM. It is known that as the tip is lowered towards the substrate, a water meniscus forms between the tip and the surface. The water meniscus serves as a means of transport to bring the molecules from the tip to the surface.[42, 44-46] When the AFM tip is scanned at slow speeds, (writing speeds vary tremendously from molecule to molecule but a general range is 0.5-20 μm/s), molecules flow from the AFM tip to the substrate. The concentration gradient established between the coated tip and the surface drives diffusion of the molecules towards the substrate. If writing time is sufficiently slow and

there exists an attraction between the molecule and the surface (thiol on Au), the molecules organize into a self-assembled monolayer.[42, 43] Patterns can be imaged ("read") by increasing the scanning rate (to a speed where little writing can occur) and using lateral force microscopy (LFM). LFM generates a map of the frictional forces between the tip and the substrate. The DPN patterned SAMs locally change the surface properties by either increasing (MHA SAMs) or decreasing (ODT SAMs) the frictional force felt by the tip as compared to the surrounding gold surface, making the patterns obvious in a frictional force map.[42] Imaging of written patterns can also be accomplished using contact AFM height mode for larger molecules or for short molecules on very flat substrates.

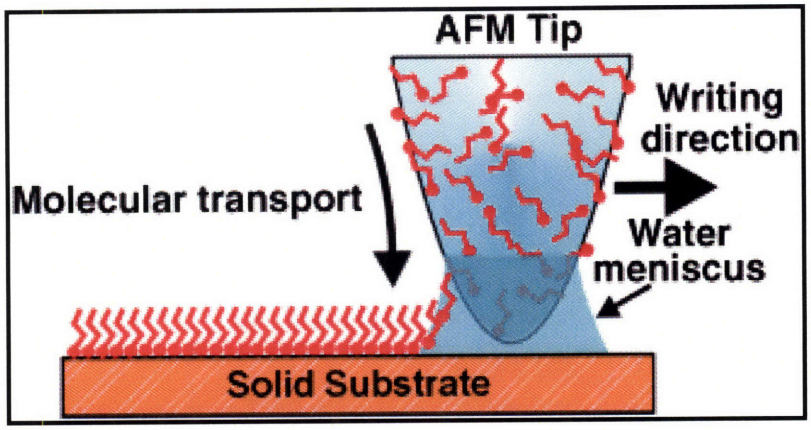

Figure 1.6: Schematic of Dip Pen Nanolithography showing molecular transport from the tip to the surface via the water meniscus. Courtesy of reference 43 .

One of the major advantages of DPN is its versatility.[47] It can be used to deposit many types of molecules on many different substrates usually with sub-100 nm resolution. DPN has been used to pattern alkane thiols,[42, 43] silazanes,[48] alkoxysilanes,[49, 50] metals salts,[51, 52] DNA,[53] conductive polymers,[54] magnetic material precursors,[55] dendrimers,[56, 57] and organic dyes[58].

Much work has been done on studying and improving the resolution of DPN. The type of molecule and substrate can drastically affect the resolution. If a strong attraction exists between the molecule and substrate, the molecule is likely to bond immediately to the surface, whereas molecules without that attraction will diffuse on the surface, decreasing resolution. Tip-surface contact time (t) has been shown to affect the resolution of DPN; in fact, when writing dots, a classical diffusion model has been used to show that the dot diameter grows linearly with $t^{1/2}$.[46, 48, 54, 58, 59] Relative humidity plays a role in the writing of hydrophilic molecules, because of higher solubility in the water meniscus. The radius of curvature of the tip (which is directly related to the size of the water meniscus) defines how wide of a line is deposited. Currently, the best resolution achieved is a linewidth of 15 nm by patterning ODT on Au.[47]

Currently, the major limitation of DPN is that it is a serial technique, not suitable for manufacturability. Recent work has focused on transforming DPN into a parallel technique. The resolution of molecules patterned via DPN has been shown to be relatively independent of the contact force applied to the AFM tip. This has allowed micromachined AFM cantilevers with up to 250 tips to be used to generate patterns in parallel while monitoring the contact force on only one tip of the array.[60, 61] Patterns have been written at a rate of 0.935 cm/min and spread out over a distance of 1.25 cm. Sub-100 nm resolution is maintained using the tip arrays. Work has also been done to create active tips, so each tip an array can be independently turned on and off. Resistive heating of tips with a metallic bilayer allows for thermal activation of tips.[62] Due to the differences in the coefficients of thermal expansion of the two metals, the tips are bent off

of the surface when they are heated, allowing writing to be stopped on selected tips in an array. A second method, dubbed thermal DPN, involves the use of inks that are solid at room temperature.[63] Heating the tip melts the molecule and allows for patterning.

1.3.2 Chemical reactions at surfaces

Self assembly of nanoparticles onto patterned surfaces can be accomplished using many different types of surface chemistries. Covalent and ionic bonds along with specific biological interactions can be used to direct the self-assembly of nanoparticles, proteins or dedrimers.[41] Amide bonds, formed when an activated carboxylic acid reacts with an amine; these are a strong covalent bond used for self-assembly. (figure 1.7) Different activation chemicals, triflouroacetic anhydride and triethanolic acid,[64] n-hydroxysuccinimide,[65] or ethyl chloroformate[50] have been used to activate the carboxylic acid group to form amide linkages. Without activation, an electrostatic attraction still exists between the amine and carboxylic acid group, but no covalent bond is formed.[50, 66] A urethane linkage, formed between an isocyanate group and an alcohol group has been used for self-assembly.[67, 68] A double bond at the head group of a SAM can be transformed using photochemical reduction into either a thiol group or an amine group.[69, 70] If a thiol group forms the top of the monolayer than self-assembling a nanoparticle onto the patterned area can be achieved through the strong thiol-Au bond.[70, 71]

Electrostatic attractions have also been used for self-assembly. When terminal amine groups are protonated in solution, self assembly of nanoparticles can be directed by the electrostatic attraction between a positively charged ammonium ion and negatively charged Au nanoparticles.[69] Negatively charged (deprotonated) terminal carboxylic acid groups can be used to self assemble positive Cd^{2+} ions.[50] This strategy has also been employed to assemble Cu^{2+} on MHA monolayers.[72, 73] The process is highly pH dependent; if the terminal carboxylic acids groups are protonated and therefore not negatively charged, no self-assembly can occur.[72] Gold nanoparticles stabilized with mercaptoundecanoic (MUA) ligands can than be assembled onto the Cu^{2+} ions, as the negatively charged carboxylic acids on the MUA ligands complete the electrostatic "sandwich."[73]

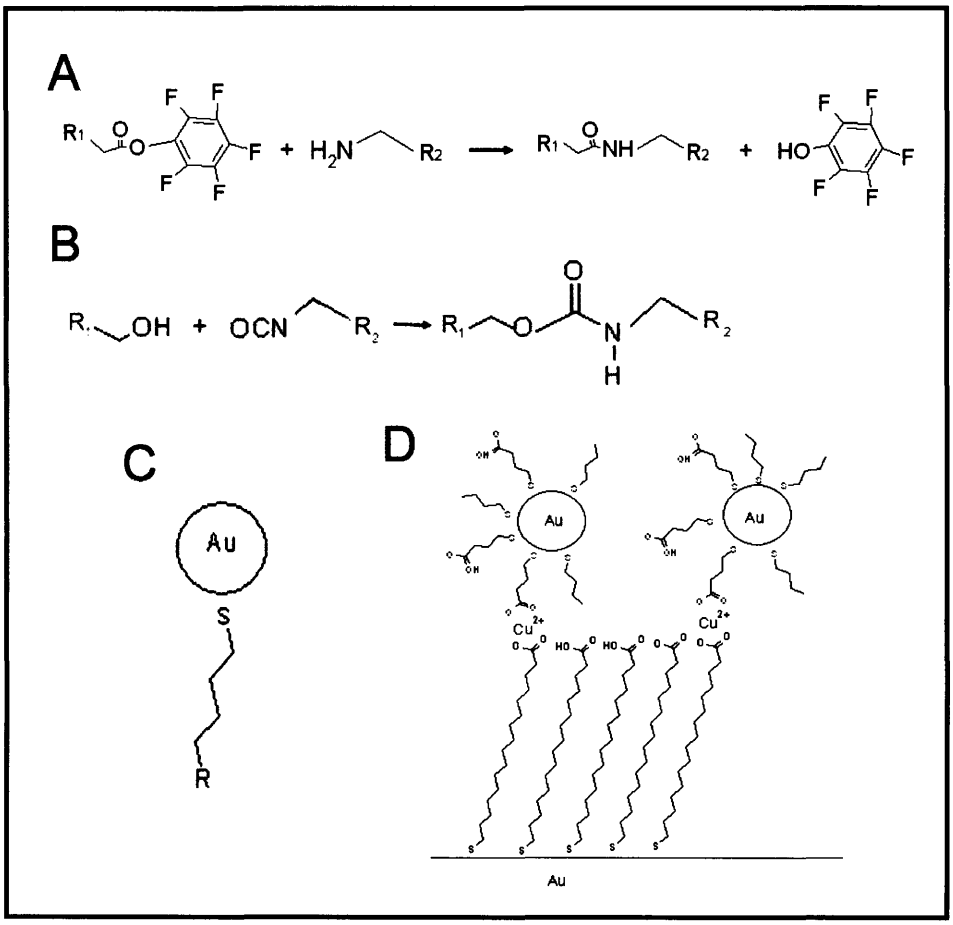

Figure 1.7: Chemical bonds for directed assemble of nanoparticles: (A) amide bond formed from a carboxylic acid activated with pentafluorophenol and an amine group; (B) urethane linkage formed by reaction of an alcohol and an isocyanate group (C) Au-thiol bond; (D) assembly of gold nanoparticles on an MHA SAM using Cu^{2+} ions.

DNA can be used as a tool for self assembly, through the use of single stranded DNA-nanoparticle complexes that hybridize to their pre-patterned complementary strands.[53, 74]

1.3.3 Chemically directed assembly of Au nanoparticles

The ability to direct the assembly of Au nanoparticles to particular locations on surfaces is critical for the fabrication of devices based on nanoparticles. Many applications will require the use of well-ordered, patterned arrays of nanoparticles. Several methods have

been used for patterning micron and nanometer sized features of molecules on a substrate for the chemically directed assembly of nanoparticles. Some work has also been done to chemically assembly nanoparticles onto devices.

1.3.3.1 Chemically directed assembly of Au nanoparticles onto patterned micron sized features

Methods for patterning molecules into micron size features include microcontact printing and optical lithography. In microcontact printing[75] a grooved PDMS stamp is "inked" by immersion into a supersaturated solution with the 1st molecule to be patterned. The inked stamp is brought into contact with the substrate. A SAM of this molecule is formed only where the stamp contacts the substrate. The substrate is then immersed into a solution of a 2nd molecule which forms a SAM on the remaining non-patterned surface.

Citrate stabilized, 12 nm Au nanoparticles have been assembled on surfaces patterned by microcontact printing of hexane thiol on Au surfaces.[76] Following microcontact printing, stamped substrates are immersed into solutions of either 4-Aminothiolphenol or hexanedithiol, forming a SAM with surface functionality in the remaining regions. In the former case, electrostatic attraction directs the assembly of the negatively charged, citrate stabilized nanoparticles to the positively charged NH_3^+ groups on the amino-functionalized substrates. In the latter case, covalent assembly occurs as the nanoparticles are bound to the surface by the Au-S bond between the nanoparticle core and dithiol functionalized regions of the substrates. The CH_3 terminated regions of the surfaces

resist absorption of the hydrophilic nanoparticles. Control of the density of nanoparticle assembly was demonstrated by using a very dilute solution of hexane thiol for μCP. Incomplete hexanethiol SAMs are formed, allowing for some dithiol molecules to assemble in the hexane thiol regions. These thiols can direct the assembly of isolated nanoparticles in the hexane thiol regions. Directed assembled of nanoparticle multilayers (MUA: alkane thiol stabilized, 1.6 nm diameter) on gold surfaces was demonstrated by μCP of hexane thiol followed by backfilling with mercaptoundecanoic acid.[73] The patterned substrates were immersed in a Cu^{2+} solution followed by immersion in the nanoparticle solution, creating the Cu^{2+} electrostatic "sandwich." Multilayer formation is realized by cycles of immersion in Cu^{2+} and nanoparticles. Assembly of Au nanoparticles (citrate stabilized, 20 nm diameter) on an activated carboxylic terminated SAM has been accomplished by μcp of hexadecylamine.[77] This is followed by reaction of the unpatterned areas with cysteamine ($HSCH_2CH_2NH_2$), where the amine groups reacts with the activated carboxylic acid group to form amide linkages while the thiol group give the surface a chemical functionality. The covalent specific assembly of nanoparticles on the thiol terminated regions is shown with SEM imaging. Directed assembly of hexagonally packed Au nanoparticles (dodecanethiol stabilized, 5 nm) on a GaAs surface by μcp printing of octanedithiol has been demonstrated.[78] A well-ordered nanoparticle film is generated by spreading a hexane solution of nanoparticles onto a water surface. The patterned GaAs substrate is briefly brought into contact with the surface of the film, where the nanoparticle core covalently binds to the surface thiol groups. The well-ordered nature of the nanoparticle assembly is shown with STM imaging.

Multilayers of gold nanoparticles have also been patterned using optical lithography.[79] Alternating films of positively charged nitrodiazoresin (NDR) and negatively charged Au mercaptobenzoic acid ligands nanoparticles (3nm) were assembled by ionic attraction to each other on a quartz slide or silicon wafer. Upon exposure to UV light through a photomask, a covalent linkage is formed between by NDR and mercaptobenzoic acid ligands. Unexposed regions could be developed away with a sodium dodecyl sulfate solution. AFM and SEM images show the regions of patterned nanoparticle assembly and elemental distributional images confirm the presence of Au only in the patterned regions. Patterning of gold nanoparticle multilayers was performed on top of lithographically defined gold on SiO_2 structures.[80]

Nanoparticles coated with DNA (*A'*) ligands were assembled onto the gold features that had SAMs of thiolated DNA (*A*).[80] Multilayers were formed by the assembly of nanoparticles with strands complementary to the first layer (*A*). The use of a polyethylene glycol siloxane molecule to passivate the SiO_2 substrate prevented non-specific binding of nanoparticles.

1.3.3.2 Chemically directed assembly of Au nanoparticles onto patterned nanometer sized features

In recent years, there has been a large effort to pattern nanoparticles on substrates with nanometer sized features that are generally difficult to pattern with traditional optical

lithography. New methods based primarily on scanning probe lithographies (such as DPN) have been developed that allow for the chemical patterning of monolayers on the sub-100 nm scale. Patterning molecules with specific functional groups allows for the directed assembly of nanoparticles via binding with either the nanoparticle ligand or directly to the nanoparticle core.

Constructive lithography is a scanning probe technique which allows for the transformation of a methylene group into a carboxylic acid by delivering electrical pulses through a conductive AFM tip.[69, 70, 76, 81] Au_{55} nanoparticles stabilized by phosphine ligands (2.3-2.4 nm) have been assembled onto a silicon substrate with feature sizes as small as 30-50 nm patterned using constructive lithography.[70] Starting with an octadecyltrichorosilane (OTS) SAM, carboxylic acid terminal groups are patterned with constructive lithography. A two step chemical assembly (figure 1.8) is used to generate a pattern of terminal SH groups to which the core of the Au nanoparticles are covalently bound. XPS images confirm the presence of Au, S, C, Si, O and P on an unpatterned substrate that has been assembled using a similar method. AFM images reveal the expected height change after each step of assembly and indicate that a single monolayer of particles is assembling. AFM images also reveal also that on the smallest features only 2-5 particles assemble. In a similar approach, citrate stabilized gold nanoparticles (17 nm or 2-6 nm in diameter) were assembled via electrostatic attraction onto a silicon substrate again patterned by constructive lithography.[69] In this case the COOH pattern is used to generate terminal amine groups. The positively charged NH_3^+ groups electrostatically bind and attract the negatively charged nanoparticles. AFM images again indicate a

single monolayer of particles is being assembled and complex patterns can be generated. (figure 1.9) The stability of the assembly is confirmed by exposing the pattern to organic solvents, acids, bases, and sonication. Smaller nanoparticles are even stable to the Scotch tape test.

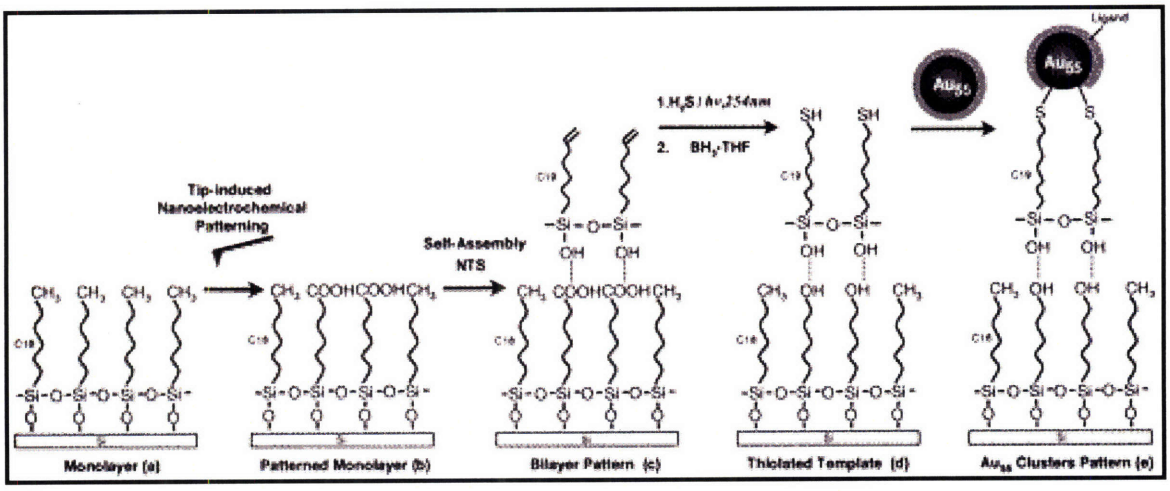

Figure 1.8: Schematic of steps to chemically direct the assembly of gold nanoparticles via a thiol head group in constructive nanolithography. Courtesy of reference 70.

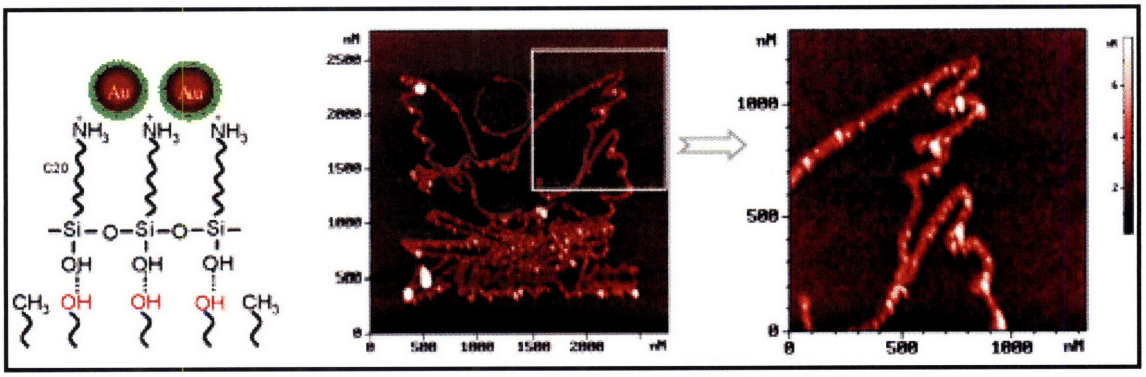

Figure 1.9: Constructive nanolithography used to pattern 2-6 nm diameter Au nanoparticles using the electrostatic attraction between negatively charged Au nanoparticles and positively charged amine head groups. Semicontact mode AFM images showing intricate pattern replication. Courtesy of reference 69.

Patterning of Au nanoparticles on Si surfaces has also been accomplished using nanooxidation.[82, 83] In this method, a Si substrate with an OTS SAM is patterned into regions of SiO_2 by applying a voltage pulse through a conductive AFM tip.

Aminopropyltriethoxysilane or aminopropyltrimethoxysilane is then assembled onto the unprotected SiO_2 regions. (figure 1.10) The terminal amine group is then used to electrostatically attract negatively charged gold nanoparticles 12-15 nm in diameter, while the nanoparticle will not absorb to the methylene terminated regions. SEM and AFM images confirm the directed assembly. The interparticle spacing, 35-80 nm, is found to be significantly larger than on amino-terminated SAMs, attributed to the incomplete degradation of the OTS SAM or incomplete surface medication with the amino-siloxane. Arrays of single nanoparticles were assembled on dots with diameters <70 nm.

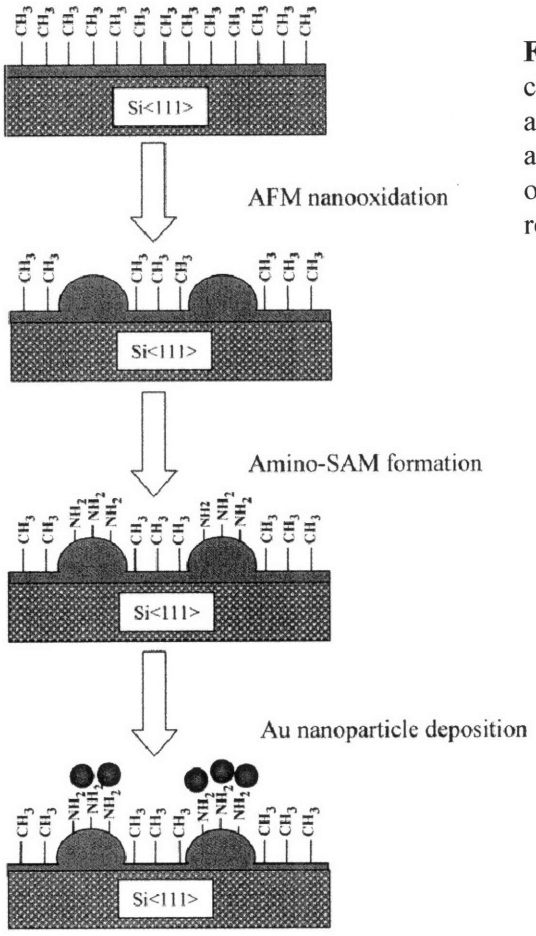

Figure 1.10: Method for chemically directed assembly of nanoparticles on a surface pattern by nano-oxidation. Courtesy of reference 84.

Substrates patterned by dip pen nanolithography have been used to direct the assembly of nanoparticles through covalent,[71] electrostatic[66, 71] and biological interactions.[53, 74, 84, 85] Covalent based nanoparticle assembly was realized on lithographically patterned gold on Si surfaces. MHA was patterned via DPN on a Au on Si surface, which then serves as a resist for the etching of nanometer sized Au features.[71] The MHA SAM is removed though UV irradiation. An hexanedithiol SAM is then formed on the patterned gold features, which directs the assembly of magnesium oleate capped Au nanoparticles (15 nm) via covalent bonds with the nanoparticle core, as evidenced by AFM imaging. Alternatively, an aminoethanethiol SAM is generated and electrostatically directs the assembly of negatively charged citrate stabilized nanoparticles (15 nm).[71] A similar etching strategy was demonstrated to direct the assembly of nanoparticles using highly specific DNA binding.[74]

The directed assembly of two types of nanoparticles on the same surface has been demonstrated using DNA interactions.[84] (figure 1.11) MHA is patterned using DPN on a Au surface, followed by passivation in ODT. Alkylamine-modified DNA (*A*) is then chemically assembled on the 1st MHA pattern. A second MHA pattern is generated is registry with the 1st, followed by assembly of DNA (*B*). A linker DNA (ends *A'* and *B'*)is assembled followed by the direct assembly of Au nanoparticles modified with DNA (13 nm particles with DNA *A* and 30 nm particles with DNA *B*). AFM images show that the nanoparticles assemble specifically in registry with one another on the complementary DNA.

The direct patterning of thiolated DNA via DPN on Au surfaces has also been used for the assembly of DNA modified Au nanoparticles (13 nm diameter).[53] AFM images show the assembly of isolated particles. The direct patterning of proteins via DPN has enabled the assembly of Au nanoparticles.[85] Rabbit immunoglobin-gamma (IgG) arrays were patterned with DPN followed by passivation with 11-mercapto-undecylpenta(ethylene glycol) disulfide (PEG). Au nanoparticles (10 nm) coated with anti-rabbit IgG were assembled on the patterned area, as proven by the changes in the AFM measured height of the patterned dots.

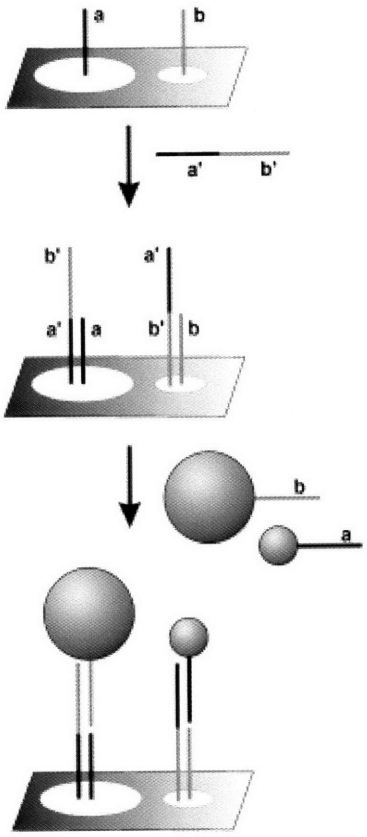

Figure 1.11: Method for chemically directed assembly of two different types of nanoparticles in registry with one another using complementary DNA interactions on a surface pattern by DPN. Courtesy of reference 85.

1.3.3.3 Directed Assembly of Au Nanoparticles in Registry for Device Applications: Assembly in a Gap

The directed assembly of gold nanoparticles on lithographically defined gold wires is a major step towards device applications using Au nanoparticles. Recent efforts have looked at the assembly of nanoparticles in fabricated nanogaps, often followed by the electrical characterization of the assembled nanoparticle. Chemically directed assembly in a gap has been performed using covalent binding and biological interactions.

Au nanoparticles (5.8 nm in diameter) have been assembled on nanogaps (1- 5 nm in width) formed by both electron beam lithography and electromigration.[6, 7] In the former case, the substrate with ebeam patterned wires and nanogaps was immersed into a hexanedithiol solution followed by immersion in a solution of nanoparticles.[6] (figure 1.12) One thiol group of the hexanedithiol molecule bound to the gold wires while the second thiol group could bind to the core of the Au nanoparticle. Using electromigration to form the gap allows for the dithiol and nanoparticle immersion step to be done before or after gap formation.[7] While this assembly results in the placement of a nanoparticle in the gap, it is not a specific placement. Gold nanoparticles will bind to all areas over the gold wires. Similar binding strategies have been used to assembly particles in nanogaps formed by electromigration[9] or unique optical strategies.[12, 34, 81]

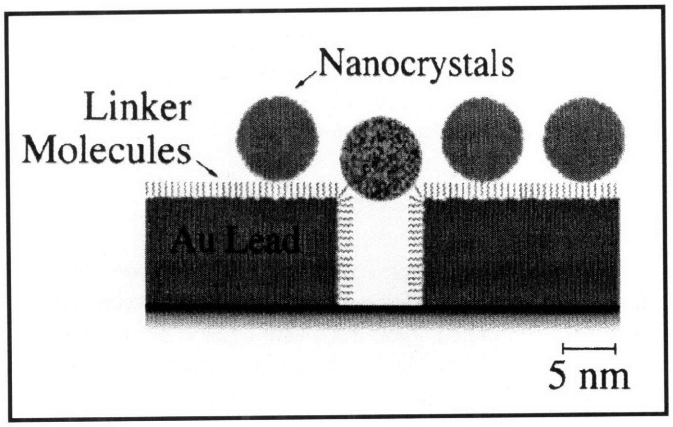

Figure 1.12: Schematic of a chemically assembled gold nanoparticle device using dithiol linker molecules. Courtesy of reference 6.

DPN nanolithography was used to pattern thiolated capture DNA strands directly onto the tips of gold wires.[86] These wires were patterned by ebeam lithography with nanogaps of dimensions 20-100 nm. The area patterned with capture DNA using DPN was $< 3 * 10^{-2}$ μm^2. Exposure to target DNA and Au nanoparticles (20 or 30 nm diameter) with thiolated DNA ligands was again performed. Complementary DNA resulted in gaps where individual Au nanoparticles selectively assembled as imaged by SEM. Using DPN to pattern the capture DNA allows for selective assembly of a only a few nanoparticles in a limited area of the chip. It also allows for many different sequences of DNA to be patterned on the same chip, to direct the assembly of different types of nanoparticles.

1.4 Electrically Directed Assembly

Dielectrophoresis (DEP) is the force felt by a polarizable object when it is placed in a non-uniform electric field.[87-89] In vacuum, when a polarizable object is placed into an electric field, polarization charge is induced at the surface of the object; if the applied electric field is non-uniform, it interacts with this polarization charge to attract the object

towards the point of strongest field. This also happens in solution, when an object with a larger polarizability than the solvent molecules interacts with a non-uniform field (positive DEP). When objects of lower polarizability interact with a field, the polarization charge aligns such that the object is pushed away from the region of highest field (negative DEP). For a spherical particle of radius R, in media of permittivity ε_m, acted upon by applied field $\mathbf{E}_0$, the DEP force is given by:

$$\mathbf{F}_{DEP} = 2\pi\varepsilon_m R^3 \,\mathrm{Re}\left\{\underline{CM}(\omega)\nabla\underline{E}_0^2(\mathbf{r},\omega)\right\}$$

Here, CM denotes the Clausius-Mossotti factor, in this case given by:

$$\underline{CM}(\omega) = \frac{\underline{\varepsilon}_p - \underline{\varepsilon}_m}{\underline{\varepsilon}_p + 2\underline{\varepsilon}_m}$$

where $\underline{\varepsilon}_p$ and $\underline{\varepsilon}_m$ are the complex permittivities of the particle and media, respectively. DEP has been demonstrated to manipulate micrometer-sized objects such as cells for over three decades.[90-95]

One of the major challenges for nanotechnology is the manufacturing of devices with easily scalable approaches. DEP offers the unique opportunity of selectively placing nano-objects inside electrically defined gaps with several potential advantages, mostly versatility and quick assembly time.[11, 88, 89, 96-118] One could envision DEP as a technologically scaleable approach to assemble many nanoscale objects in parallel.[111] In the following sections, early "proof of concept" efforts to use dielectrophoresis controllably assemble nano-objects (1.4.1) and specifically nanoparticles into gaps (1.4.2) are reviewed.

1.4.1 Dielectrophoresis of Nano-objects

Asymmetric nano-objects, such as nanotubes and nanowires, make ideal candidates for manipulation with DEP due to their high polarizability. Multi-walled (MWCNT) and bundles of single walled carbon nanotubes (SWCNT) have been assembled across gaps ranging in size from 200 nm to 5 μm using combination of AC and DC dielectrophoresis.[111-113, 119] (figure 1.13) The effect of frequency,[119] magnitude of the applied voltage[113] and the ratio of the AC to DC component of the electrical field[111, 113] on nanotube assembly via DEP has been studied. Real time feedback based on the electrical properties of the nanotubes has been used to monitor and controllably terminate the assembly once a desired number of nanotubes have bridged the gap.[112] Parallel assembly of DEP of nanotubes has been used to demonstrate the manufacturability of this approach.[111] A 100 device array showed 90% of gaps having a single MWCNT bridging the gap.

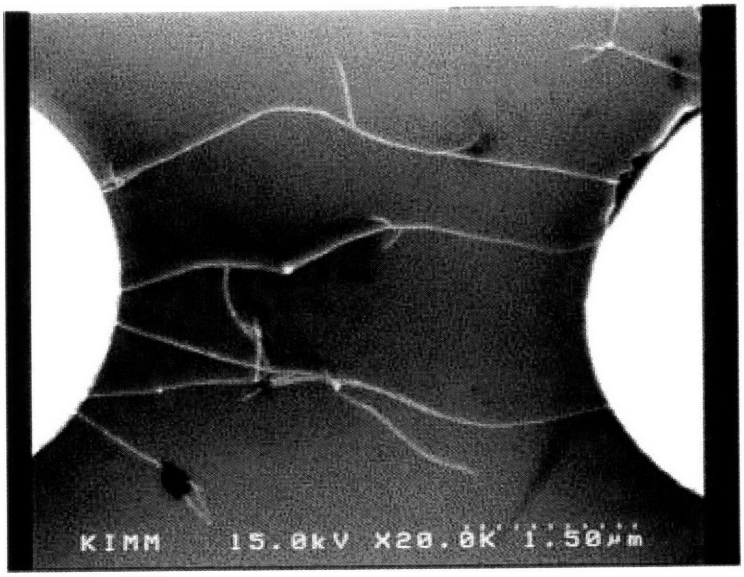

Figure 1.13: Use of DEP for the directed specific assembly of SWNT bundles nanotubes across a gap. Courtesy of reference 112.

Dielectrophoresis of metallic (Au, Pt and Ni wires) has also been demonstrated across gaps with control via frequency and the magnitude of the assembly voltage.[116-118] Alignment[117] and rotation[116] of nanowires has been achieved by the careful design of the electrodes and resulting electrical fields.

Insulating and metallic nanoparticles have also been manipulated by DEP. Significant research efforts have been made into the assembly of gold nanoparticles into conducting gold microwires which bridge gaps as large as 2 cm.[98, 99, 110] The effects of assembly voltage, frequency, nanoparticle concentration in solution, electrolyte concentration in solution and solvent viscosity have been studied. Particle-particle and particle-field interactions are discussed. Assembly of insulating particles as a function of frequency has been demonstrated to show that these particle can undergo both positive and negative dielectrophoresis.[96] Two-dimensional crystallization of large latex spheres has been achieved with DEP.[100] Finally, gold nanoparticles as small as 2 nm in diameter have been manipulated with large electrical field gradients generated by carbon nanotubes electrically contacted to gold electrodes.[97]

1.4.2 Directed Assembly of Nanoparticles into Nano-gaps

Preliminary experiments have shown it is possible to controllably assembly nanoparticles into nano-gaps. In these experiments, an aqueous drop of nanoparticle solution is placed over the nanogap. An AC or DC electrical field is applied across the gap, creating a localized strong electrical field at the nanogap. In positive DEP, particles are attracted to the nanogap. For charged nanoparticles, AC dielectrophoresis is found to be superior to DC electrophoresis for assembly in a gap. During DC dielectrophoresis charged particles

preferentially assembly on the oppositely charged electrode. 40 - 80 nm gold particle have been trapped in 40-60 nm nano-gaps using DEP and are found to have linear IV characteristics after assembly.[103-105] The electrical properties of thiolated SAMs used to link the gold electrodes to the gold nanoparticles have been studied using this technique. The assembly of 40 nm gold particles as a function of frequency has been observed.[11] Using a resistor in series with the nanogap, 20 nm neutral Pd colloids are assembled in 4 nm gaps using DC dielectrophoresis.[101] The use of a resistor in series with the gap allows for DEP to become self-limiting after the assembly of a single particle. Au nanoparticles have been fused together to create metallic bridges over small gaps using DEP.[106, 107] The use of DEP to assemble gold nanoparticles has enabled their electrical properties to be studied.[11, 101]

1.5 Electrical Based Sensing with Au nanoparticles

The unique structure and electronic properties of ligand functionalized gold nanoparticles make them excellent materials for sensing applications. The electronic properties of ligand coated gold nanoparticles can be influenced by either the size of the gold core or the chemical nature of the surrounding ligand molecules. These particles can be functionalized with molecules which serve as the probe to bind to the target molecule. The small size of the metallic core of these particles allows for the possibility of their electrical properties (capacitance, resistance) to be drastically affected by the binding of a single target molecule. The ability to control the number of each type of molecule bound to a ligand coated gold nanoparticle will also enhance the sensitivity of such devices. The unique electronic properties of the ligand coated gold nanoparticle are described in

the following section (1.5.1). In the subsequent section, preliminary sensing experiments using the electrical properties of ligand coated gold nanoparticles are reviewed (1.5.2)

1.5.1 Electrical Properties of Au Nanoparticles

The electronic properties of individual isolated ligand coated gold nanoparticles have been studied primarily with STM but also on Si based platforms at low temperatures.[1] The distinguishing feature of the electronic properties of isolated nanoparticles is the possibility of a non-linear IV characteristic. In the case of gold nanoparticles, this non-linear IV curve can be realized when the nanoparticle is placed in the following configuration: source electrode-insulating gap-Au nanoparticle-insulating gap-drain electrode (figure 1.14). The two insulating gaps are formed in part by the surrounding ligand shell. They are characterized by a large resistance and are usually between 1 and 10 nm. Electrons must tunnel through the insulating gaps to pass on and off the Au core. In order for an electron to tunnel onto the island it must overcome the columbic energy needed to charge the central island with one extra electron. It is known that in order for an electron to tunnel from a metallic lead (i.e. an infinite reservoir of electrons) into an object, an energy must be provided.[120, 121] For example, in the case of molecules, this energy equals the oxidation energy. For macroscopic objects, this energy is so small that it can be ignored. In between the molecular and the macro world, there is a size regime where the intrinsic capacitance of the isolated object plays an important role. It is in fact known that it takes energy to charge a capacitor. When this energy exceed kT, we have a region of non-zero voltage where electron flow is prohibited, known as the Coulomb

blockade. This is because only electrons with the threshold charging energy will flow from the source to the drain. The energy necessary to place a charge on a capacitor can be given as $W=q^2/2C$. [1, 121-125] In the case of the metal-insulator-nanoparticle junction, the lower limit of the capacitance is given by its self-capacitance of a metallic sphere: $C_s= 4\pi\varepsilon_0\varepsilon r$, where ε = is the dielectric constant of the insulator and r is the particle radius.[126] The capacitance of the metal-insulator-metallic island junction is given by $C= 4\pi\varepsilon_0\varepsilon r(1+ r/2L)$, where L is the junction thickness.[127] For macroscopic objects this energy is well below kT (kT= 0.04 eV at room temperature).

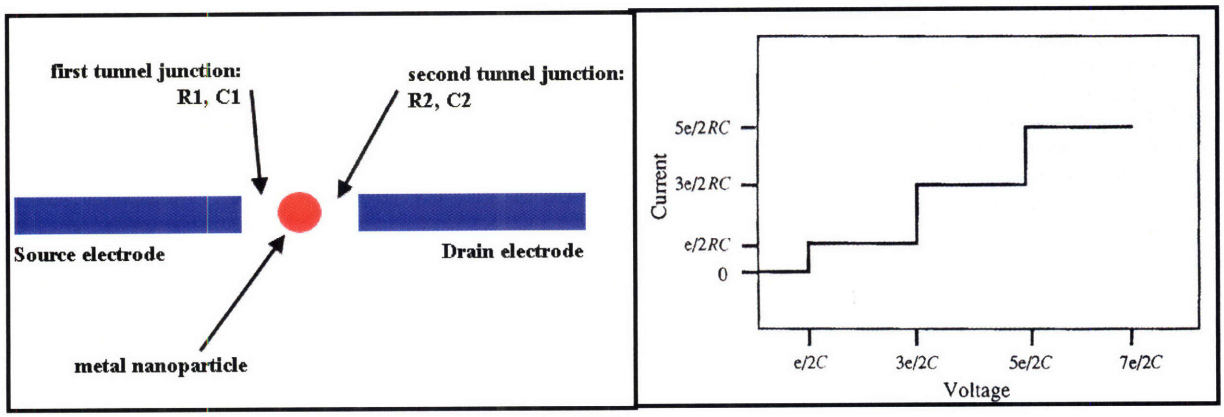

Figure 1.14: (left) Schematic of a nanoparticle device showing a Coulomb blockade. R1 and C1 (R2 and C2) are the resistance and capacitance of the 1st (2nd) tunnel junction. (right) Idealized IV characteristics of such a device, demonstrating the Coulomb staircase. Courtesy of reference 1.

The current-voltage (IV) characteristics of the nanoparticle device are affected by the energy needed to place an additional electron on a central island. For nanometer sized objects, the charging energy of the object is greater than kT, thus the tunneling of a single electron will generate a non-linear current-voltage characteristics. If an electron reaching the first insulating gap has less than the charging energy it will be unable to tunnel to the metallic island. At low source-drain bias therefore, no current flows through the

nanoparticle. This region of zero current, from bias voltages of $V=-e/2C_1$ to $V=e/2C_1$, (where C_1 is the capacitance of the tunneling junction having the greater capacitance) is known as the Coulomb blockade. Once the electron has enough energy to tunnel onto the nanoparticle, it can then tunnel through the second insulating junction to the drain electrode. Current flows through the circuit with a one electron difference between the number of electrons tunneling onto the nanoparticle from the source and those tunneling off the island to the drain (i.e. 10 electrons tunnel from the source to the island, while 9 electrons tunnel from the island to the drain). When the nanoparticle is being charged by one additional electron, (between source bias of $V=e/2C_1$ to $V=3e/2C_1$), the amount of current is constant; $I=e/2CR_1$, where R_1 is the resistance of the more resistive tunnel junction. Once a voltage of $V=3e/2C_1$ is reached, there is enough energy to charge the metallic core with 2 extra electrons, so the current steps to a level of $I=3e/2C_1R_1$. This step-like behavior in the IV curve of a single electron is referred to as the Coulomb staircase and is the result of capacitance charging being quantized in units of e. (figure 1.14)

Basic research on the electrical properties of isolated ligand coated gold nanoparticles shows that Au nanoparticles exhibit a Coulomb blockade and that their charging step is dependent on the particle radius and the length and type of surrounding ligand molecules. Andres and coworkers have studied the electrical properties of Au nanoparticles by forming self-assembled monolayers (SAMs) on gold surfaces.[128] Their approach uses the Au surface as one metallic lead, the alkyl dithiol as the first tunneling junction, the gap between the STM tip and the Au nanoparticles as the 2nd insulating junction and the

STM tip as the second lead (figure 1.15). They measured the IV characteristics of metallic nanoparticles as a function of tip-substrate distance, effectively changing the length of the second tunneling junction. Single gold nanoparticles with diameters of 1.7 nm demonstrated both a Coulomb blockade and a Coulomb staircase at room temperature. Rao has studied the effect of changing the diameter of Au nanoparticles on their electrical properties using the STM technique.[126] He finds the charging energy decreases with increasing nanoparticle diameter. This is as expected due to the increased capacitance of the larger nanoparticles.

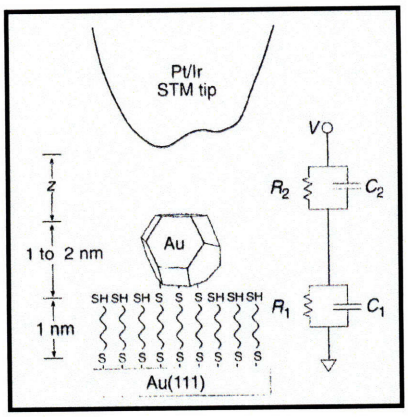

Figure 1.15: Schematic of a device showing a Coulomb blockade formed with an STM over a Au nanoparticle. Courtesy of reference 129 .

The use of the STM while interesting in an academic sense, is not an ultimate solution to new technologies. Research has shown that gold nanoparticles can be addressed by metallic leads on a silicon platform once the challenges of creating very small insulating gaps and positioning nanoparticles in these gaps have been met. As mentioned previously, several groups have fabricated gaps using electromigration or unique

lithography strategies for gold nanoparticle measurements on SiO_2 surfaces. After gap formation, chemical assembly of Au or CdSe nanoparticles was accomplished by functionalizing the electrodes with dithiol SAMs. Alternatively particles were assembled with DEP. These devices have shown Coulomb blockades at 1.5-4.2 K.[6-11, 101] Using the electromigration gap formation technique and dithiol linked assembly, Dhirani has studied nanoparticle charging energies and saw that they increased with decreasing particle diameter.[9] A significant voltage drop was found to occur over the insulating dithiol connecting molecules, causing a larger than expected Coulomb blockade. A similar method was employed by Vijayamohanan, who used the devices to study the effect of ligand molecules on the electrical properties.[129] It was found that the Coulomb blockade decreased as the length of the ligand molecule decreased and also decreased when the ligand molecules had larger π orbitals (phenyl groups). Several groups have also employed the use of physical force with an atomic force microscope to construct devices and study nanoparticle properties, a slow serial method suited only for basic research. Lorke, et al. patterned Au wires using ebeam lithography.[31] Plowing of the wire with tapping mode AFM tip was used to fabricate 20 nm gaps in the wire. 10 nm Au nanoparticles were then pushed into the gap by an atomic force microscope tip. The device produced showed a Coulomb blockade, but only at 4.2 K due to the large size of the Au nanoparticle. Carbon nanotubes (positioned on gold wires) have also been cut and manipulated by atomic force microscopy to be used as leads for a gold nanoparticle single electron transistor.[130] The nanotube was cut to have a 10 nm gap and a 7 nm Au nanoparticle was positioned between the leads. Periodic oscillations in current as a

function of gate voltage (a sign of single electron charging behavior) were seen from temperatures of 4.2 K up to 200 K.

The electronic properties of thin films of nanoparticles have also been studied. In typical experiments, interdigitated gold electrodes with large (100's of nanometers to micrometers) gaps are patterned using optical lithography on a SiO_2 substrate. The SiO_2 surface and gold surfaces are functionalized with molecules so they will chemically bind to the nanoparticles. The 1st layer of nanoparticles is formed by immersion into a solution of functionalized particle. The substrate is then immersed into a solution of cross-linking molecules which will bind to the 1st layer of the molecule and have a head group which can bind to the next layer(dithiol molecules are often used). The nanoparticle and crosslinking immersion cycles are repeated until the desired number of nanoparticle layers is deposited. The electronic properties of these films are then studied. In most cases, the films are completely insulating until a certain threshold number of layers (from 3- 6) has been reached.[131-133] After this threshold, ohmic IV characteristics are observed. Conductivity increases linearly with an increasing number of nanoparticle layers. The resistance of films has found to be highly dependent on the length of the surrounding ligand molecule; the films becoming more resistive with increasing molecule length.[73, 132] Larger core sizes have also resulted in lower resistance.[131, 134] Similar finding were made on films of gold particles bridging a 20 nm gap fabricated by electron beam lithography.[133] These electrical properties have generally been attributed to the formation of disordered 3-D films. The ligands form insulating barrier between

nanoparticles. Conduction can only been achieved when a percolation threshold has been achieved.

1.5.2 Electrical Sensing with Gold Nanoparticles

In order to achieve chemical sensing with gold nanoparticles, there must be a shift in the electronic properties of the nanoparticle after exposure to a molecule. Vapor sensing properties of films of nanoparticles have been presented.[73, 132] It has been shown when particles are soluble in the exposed vapor, the nanoparticle films swell. The distance between metallic cores increases causing a decrease in the conductivity of the film. Particles functionalized with longer alkanethiol molecules have shown greater sensitivity to vapors, attributed to the higher number of absorption sites.

Research has shown that a shift in the IV characteristics of a ligand-coated gold nanoparticle can also be realized via a chemical gate; for instance a charged molecule which is covalently bound to the Au nanoparticle. Feldheim and coworkers have done the proof of concept experiment showing that it is possible to shift the Coulomb staircase of a Au nanoparticle using such a gate.[123, 135] Au nanoclusters were coated with pH sensitive ligands. Their IV curves were measured in solution at varying pH values. Nanoparticles coated with galvinol showed a Coulomb staircase that shifted towards more positive bias as pH is increased, and the width of the charging steps also decreased. (figure 1.16) Gavinol is converted to anionic galvinoxide. The negative charge on the nanoparticle makes it more difficult for electrons to tunnel through the nanoparticle, pushing the IV curve to higher bias. The negatively charged ions also increase the

capacitance of the nanoparticle-insulator-metal junction, decreasing the size of the charging steps. Nanoparticles coated with amine ligands showed a similar effect.[123] As pH was decreased, the staircase shifted towards negative bias and the width of the charging steps decreased. The amine ligands are converted to cationic ammonium ions as the pH is decreased. This type of device could be used as a pH sensor and it proves that chemical changes can be detected by the changes in electronic properties of the nanoparticles.

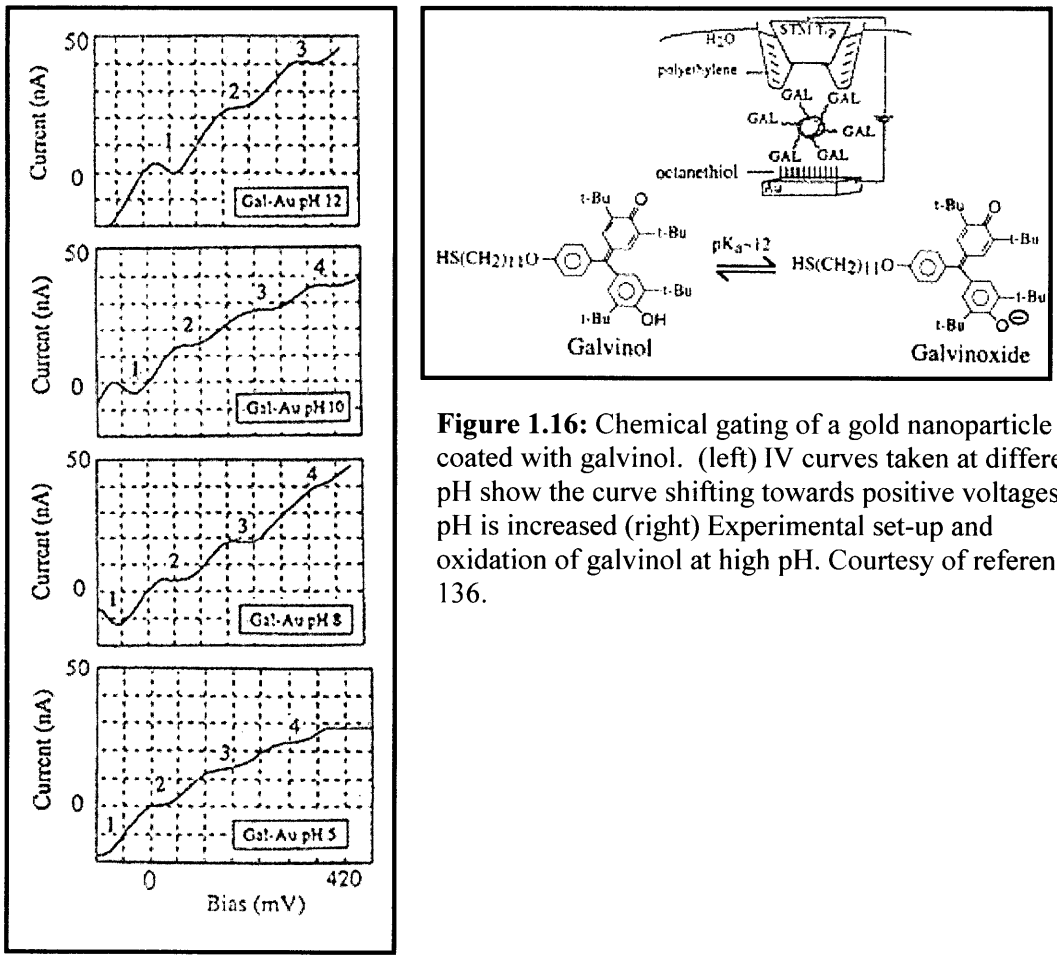

Figure 1.16: Chemical gating of a gold nanoparticle coated with galvinol. (left) IV curves taken at different pH show the curve shifting towards positive voltages as pH is increased (right) Experimental set-up and oxidation of galvinol at high pH. Courtesy of reference 136.

1.6 Nanoparticles and DNA

In this final section of this chapter we review the field of DNA sensing using gold nanoparticles. First the progress made in synthesizing Au nanoparticle coated with DNA and of DNA hybridization on surfaces are reviewed. Then DNA sensing based on nanoparticles is presented.

1.6.1 Au nanoparticle-DNA complex separation using gel electrophoresis

In order to create a DNA sensor using Au nanoparticles, it will be necessary to attach single-stranded DNA to the nanoparticles, first demonstrated by Mirkin[136] and Alivisatos.[137] To increase the sensitivity of the device, it will be critical to place a discrete number of strands on the nanoparticle with the ultimate goal of placing only one single strand of DNA on the active nanoparticle. Alivisatos group has done electrophoretic separations of phosphine ligand-coated gold nanoparticles with thiolated single-stranded DNA molecules.[138, 139] Gel electrophoresis separates particles by their mobility under an applied electric field. The mobility is therefore affected by both the size and the charge of the particles. Coating the Au nanoparticles with phosphine ligands places a high negative charge on the surface of the particles. The addition of negatively charged single stranded DNA therefore does not have a huge effect on the charge of the nanoparticles. Therefore, the mobility of the nanoparticles is only affected by their relative sizes; each strand of DNA attached to the nanoparticle increases it effective diameter, decreasing its mobility. Distinct bands in the gel electrophoresis indicated Au nanoparticles with1, 2, 3, 4 or 5 DNA strands.[139] (figure 1.17) This method was further extended to make dimmers or timers with nanoparticles.[138] Nanoparticle dimers were

made by attaching complementary strands of DNA to two different solutions of nanoparticles. Gel electrophoresis was then used to separate out the Au nanoparticles from each solution which had only 1 strand of DNA. The two solutions of nanoparticles with only 1 strand of DNA (complementary to each other; A and A') were then hybridized to form dimers. Nanoparticles with differing initial radii (5 nm and 13 nm) were used so the resulting dimers could be imaged with TEM.

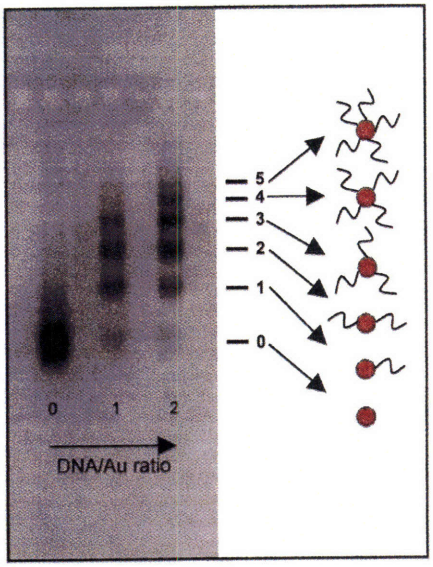

Figure 1.17: Gel electrophoresis of Au nanoparticle-DNA complexes allowing for the separation of nanoparticles with discrete numbers of DNA strands. Nanoparticles with more strands have a larger effective radius and a slower mobility. Courtesy of reference 140.

1.6.2 Hybridization of DNA on Au surfaces

Both steric considerations and the conformation of single-stranded DNA are significant factors in their ability to hybridize. Tarlov has found that the hybridization of thiolated DNA on flat Au surfaces is highly concentration dependent.[140] Monolayers made of only thiolated DNA showed low hybridization rates due to both steric considerations (not enough space in the tightly packed monolayers for complementary DNA to hybridize) and electrostatic factors (the two negatively charge single strands repel each other). DNA molecules may also bind non-specifically to the Au surface, adapting a conformation

parallel to the surface, unfavorable for hybridization. Mixed monolayers of thiolated DNA and mercaptohexanol (MCH) showed much greater hybridization rates. MCH allowed for the removal of non-specifically bound DNA and created space between DNA strands, lowering the steric and electrostatic repulsions. Keating has studied the hybridization efficiency of DNA-nanoparticle complexes, where many DNA strands surround each nanoparticle.[141] DNA binds to the surface of a nanoparticle via a thiolated linker compound. The nanoparticle was covered with both primer DNA strands (those strands which would be hybridized) and a diluent oglionucleotide which acted as a spacer. Hybridization efficiency was studied as a function of the primer/spacer concentrations, the length of the linker molecule and the complement/primer ratio. Steric effects proved to be the dominant effect on hybridization efficiency. Hybridization efficiency increased as the primer/spacer concentration decreased (more space between primer oglionucleotides), linker length increased (more space between the nanoparticle and the DNA) or complement/primer ratios decreased (as the complement:primer ratio is decreased (optimal at 1:10), their exists more room between hybridized DNA strands).

Hybridization efficiency may be affected more by conformation effects when only a few (1-5) strands of DNA are present on the nanoparticle. These nanoparticles, covered with phosphine ligands, rely on place exchange for attachment of DNA to the nanoparticle. With only short phosphine ligands coating the nanoparticle, DNA may wrap around the surface through non-specific interactions, lowering its hybridization potential. Alivsatos and coworkers have employed their electrophoresis technique to study the conformation of DNA molecules on the surface of the Au nanoparticle, reasoning that DNA strands

extending perpendicular to the surface will increase the effective radius of the nanoparticle significantly more than strands wrapped around the surface of the nanoparticle.[142] Low surface coverage of DNA results in DNA wrapping around the nanoparticle. At higher surface coverage, short DNA orients perpendicular to the surface. Longer DNA shows 30 bases oriented perpendicular to the surface, while outer bases still adopt a random coil configuration.

1.6.3 DNA sensing based on Au-nanoparticle DNA complexes

Here, several research efforts on devices designed to detect DNA based on Au nanoparticle-DNA complexes are reviewed. Nie, et. al. have used the ability of gold nanoparticles to quench fluorescence as a detection mechanism.[143] They found that when 1-2 fluorescently tagged single-stranded oglionucleotides were placed on 2.5 nm diameter Au nanoparticles, they adopted an arch conformation; the thiols on one end of the DNA bound to the gold nanoparticle and the fluorophore (the other end of the DNA) also absorbed on the surface. In this conformation fluorescence is completely quenched by the nanoparticle. When a complementary DNA hybridizes to the nanoparticle-oglionucleotide complex, a hybridized DNA adopts a rigid-rod double helix conformation and orients perpendicular to the nanoparticle surface. The tail group (the fluorophore) is separated from the nanoparticle by 10 nm. (figure 1.18) The fluorescence is no longer quenched, as nanoparticles quenching is a short range effect (1-2 nm) for small nanoparticles. Fluorescence then indicates the presence of a specific strand of DNA (the DNA complementary to the strand attached to the nanoparticle).

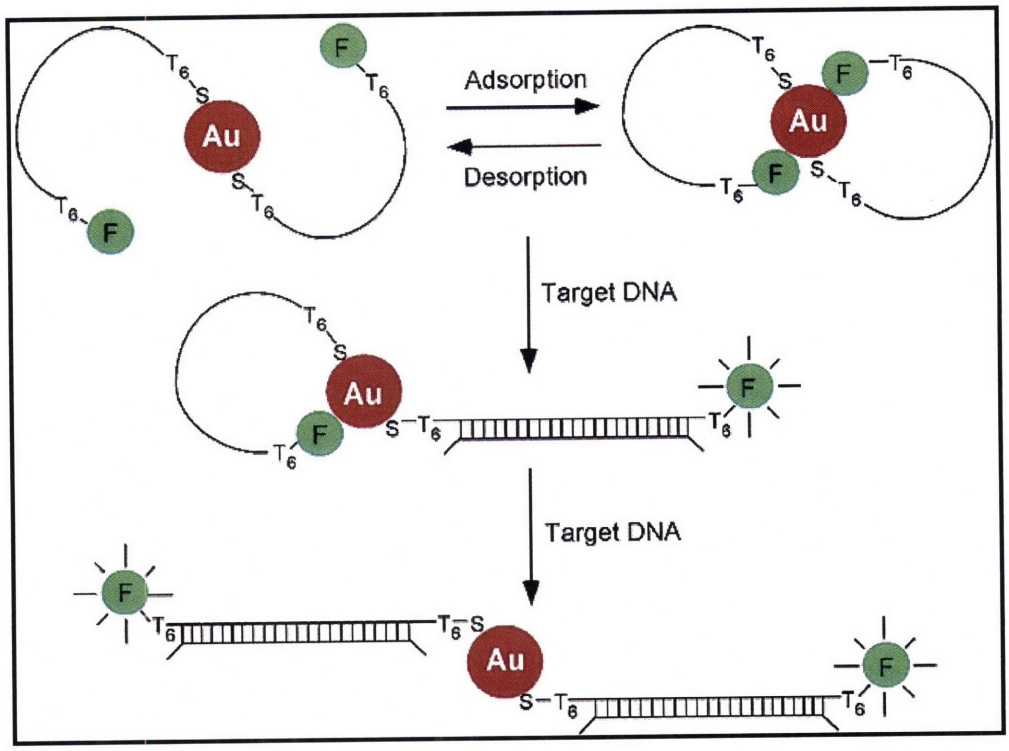

Figure 1.18: Conformation of DNA on Au nanoparticles before and after hybridization. Single-stranded DNA maintains an arch conformation, quenching fluorescence. After hybridization, the DNA takes on a stiff rod-like conformation. The fluorophore is now sufficiently far away from the nanoparticle to eliminate quenching effects. Courtesy of reference 144.

The optical properties of nanoparticle complexes have been used by Mirkin and Alivisatos for DNA detection.[144] Nanoparticles separated from each other by more than one diameter appear red in color. When the inter-particle distance is decreased to less than one diameter, a red to purplish/blue color change occurs. By linking nanoparticles, with specific DNA, a polymeric network of closely packed nanoparticles take on a purplish color. (figure 1.19) If non-complementary DNA is used, the nanoparticles do not bind and the complex does not form and the nanoparticles appear red in color. The use of nanoparticle-oglionucleotide complexes as sensing devices is significant due to the much sharper melting point (temperature where dehybridization of complementary DNA

occurs) of DNA when attached to Au nanoparticles.[144-147] As temperature is increased, DNA with fewer and fewer base mismatches dehybridizes, until the melting point (T_m) when even complementary DNA dehybridizes. In DNA attached to fluorophores, this melting point occurs over a range of temperatures, making the detection of a single base mismatch difficult. With a sharp transition temperature, the DNA may be tested at temperatures only tenths of degrees below T_m, so even singly mismatched strands dehybridize. This sharp transition also allows for a greater amount of tagged nanoparticle to remain after stringency washing steps are performed, increasing the sensitivity of the device over fluorophore based sensors, where a high amount of complementary DNA is washed away due to the broad range in melting temperature. This sharp transition temperature will also improve the sensitivity and accuracy of a DNA sensor based on a Au nanoparticle single electron transistor.

A scanometric DNA array also takes advantage of this sharp melting temperature.[147] In this method, glass surfaces were modified with different DNA strands. Complementary DNA was used to hybridize the surface DNA strands to a strand on a Au nanoparticle. The Au nanoparticles then reduced a Ag^+ solution, and were thus coated with silver metal, enhancing their optical signal. The resulting substrate could be optically scanned, and only the surface sites with DNA complementary to the linker strand appeared silver in color. A similar scheme used an electrical detection of DNA.[145] The surface DNA was patterned in an insulating gap between two metallic leads. When the nanoparticles were successfully linked to the DNA patterned on the surface, followed by silver enhancement, an electrical resistance drop of a magnitude of 10^6 was realized.

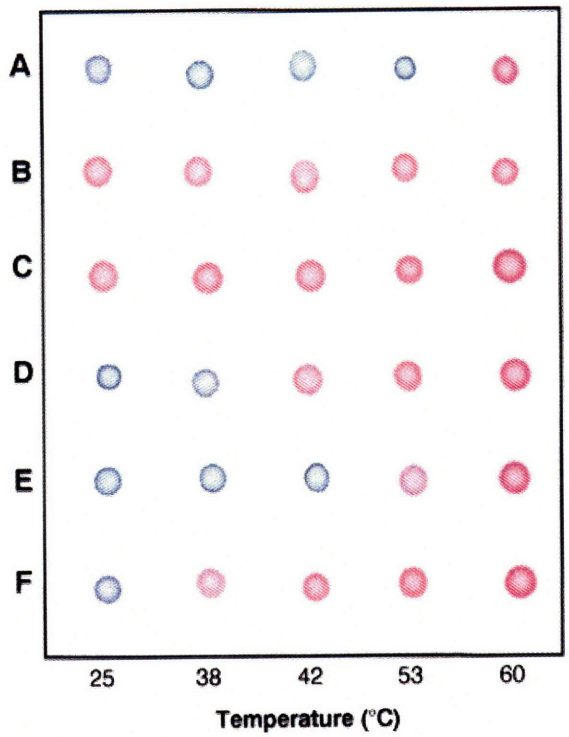

Figure 1.19: Colorimetric DNA detection. When the DNA is hybridized, forming an extended polymeric network, the nanoparticles appear blue. Above the hybridization temperature (58.5° C) or when mismatches in the target DNA do not allow for hybridization, the nanoparticles appear red. A-complementary target, B-no target, C-complementary to one probe, D-6 base pair (bp) deletion, E-1 bp mismatch, F-2 bp mismatch. Courtesy of reference 145.

Chapter 2: Nanogap Fabrication

Nanotechnology has caused a great deal of excitement over the past decade, in part due to the unique electrical properties of objects when they are reduced to the nanometer scale dimensions. In order to study these electrical properties and eventually utilize them in electronic or sensing devices, one must be able to electrically address these objects. While films of nano-objects can provide useful information on ensemble average properties and have device applications, one of the real powers of nanotechnology is be the sensing capabilities offered by individual nano-objects. Due to the size of nanoparticles, it is impossible to measure these objects by direct contact with microprobes or large metallic wires defined by optical lithography. Therefore, metallic wires with sub-100 nm gaps must be fabricated to study their electrical properties and to eventually use nano-objects in devices.

As reviewed in the previous chapter, many methods have been used for the formation of nano-sized gaps for the electrical characterization of nano-objects and molecules. Here, four methods of nano-gap formation were explored. Three of these methods fall into the category of being well-suited for basic research applications, but as serial techniques are not well suited for manufacturability. Two of these techniques, direct patterning by electron beam lithography, and physical deformation by contact mode AFM were selected primarily due to their simplicity and the availability of suitable equipment. Physical deformation by focused ion beam was chosen due to the promise of high resolution.

A 4th technique, gap formation by electrical breaking of a continuous wire, was chosen for several reasons. The technique is extremely simple, requiring the use of only common electrical characterization and lithography tools. It has the promise of extremely high resolution, with sub-10 nm gaps possible. Most importantly, however, is the promise of manufacturability. Due to its reliance on electrical current, one could easily envision arrays of devices which are all connected to voltage sources at the same time. The formation of many gaps could then be achieved in a manner suitable for a technology. In my opinion, this technique shows the greatest promise for nano-manufacturing.

In the following sections, experimental procedures and results for these four methods of nanogap formation are presented. Procedures for the use of a 2nd layer of overlapping optical lithography to connect wires to large contact pads are also described. Advantages and disadvantages of each technique are presented. An emphasis is paced on the understanding and control of nanogaps formed via electrical methods.

2.1 Direct Patterning of Nanogaps with Electron Beam Lithography

Electron beam (ebeam) lithography is a technique used to pattern nanoscale structures onto substrates. It involves coating a thin PMMA resist layer onto the desired substrate. A focused beam of electrons is then scanned across the resist on the areas which are to be patterned. The PMMA polymer chains are broken into small fragments only in the areas where the electron beam is scanned. Following the writing, the pattern is immersed in a

chemical developer which removes the exposed regions of PMMA. Electron beam evaporation is then used to deposit a thin metal layer. The final step is lift-off of the undeveloped PMMA (and the metal on top of it), done by immersion in a solvent such as acetone or N- methylpyrrolidone for 10-15 minutes. Using this method, the pattern generated by the electron beam in the PMMA resist is transferred to a pattern of metallic features on the substrate. Electron beam lithography is an extremely high resolution tool with the ability to pattern features sizes as small as 5 nm

In order to electrically address an isolated a single or a few nano-objects, the metallic leads should be sufficiently narrow (50-500 nm). These narrow wires need to be contacted with the outside world for electrical characterization. A microprobe station is a common research tool used to connect devices to the outside world. A microprobe consists of sharp metallic needles, or probes which are connected to various voltage sources, current meters, etc. The probes typically have radii of curvature of 5-10 μm. Large metallic contact pads (~50 μm by 50 μm or greater), therefore, must be patterned on the device to allow for easy connection with a microprobe. As electron beam lithography requires the scanning of an electron beam to pattern features in the PMMA resist, it is not a high throughput technique. While it is ideal for the patterning of nanoscale features, it is too slow for the patterning of large contact pads. Thickness requirements for the narrow wires and large contact pads impose a 2nd restraint. Ideally the wires would be very thin (<40 nm) to address isolated nano-objects. However, in order to ensure reliable contact with the microprobes (avoiding scraping away the metal with the probe) the pads should be made thick (>200 nm). The speed and thickness

restraints require that contact pads be patterned with a 2nd layer of lithography, using optical lithography.

Optical lithography relies on the use of ultraviolet light to pattern features in a polymer resist. After a polymer resist is spun onto the substrate, the substrate is exposed by UV light through a patterned mask. Light passes through the transparent regions of the mask. Certain polymer resists are used for positive lithography, whereby the polymer chains broken by the UV light. In positive lithography, then, the regions which are exposed to light are removed when the substrate is immersed in a chemical developer. In other resists, the polymer chain is made less soluble in the developer after being exposed to light. In this process, negative lithography, regions which are exposed to UV light remain, while regions blocked from the light are developed away. Following development, electron beam evaporation is used to deposit a metal layer and then lift-off is performed to remove the remaining resist.

The two layers of lithography must be aligned to form devices. This can be done in two ways. If the large contact pads are patterned first along with alignment makes, the ebeam patterns can be written in registry with the contact pads. If the electron beam wires are fabricated first, the mask can be aligned with the features. However, due to the need for thin wires but thick gold pads, the electron beam lithography layer must patterned first. When a resist is exposed, UV light is scattered as it travels through the thickness of the resist. This results in more of the resist being developed at the top of the resist than the bottom. The sidewalls of the resist are angled. After gold evaporation, the sidewalls of

the Au features are also angled. If the thicker gold pads are patterned first, their overhanging edges act a resist, not allowing the electron beam patterned wires to make electrical contacts with the pads (figure 2.1). This overhang method has actually been used to pattern nano-meter size gaps.[34] If the thinner wires are patterned first, the Au pads can be evaporated on top, allowing for good electrical contact.

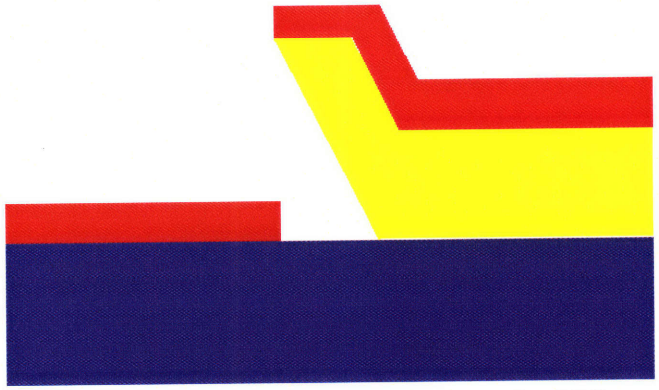

Figure 2.1: Insulating gap formed when the thicker lithography layer (yellow) is patterned before the thinner layer (red). Courtesy of reference 34.

Si wafers with 400-700 nm of thermally grown SiO_2 are used as the underlying substrate for the devices. The thick SiO_2 provides an insulating substrate which does not allow any current to leak through to the underlying Si. A PMMA resist is spun coated onto the substrate to be patterned with ebeam lithography. In order to achieve the best possible resolution with ebeam lithography, the thickness of the resist must be chosen carefully. Thinner resists allow for better resolution, as less scattering of the electrons occurs as they pass through the resist. The thickness of the resist, however, sets an upper limit on the thickness of the patterned metal features, usually 33% of the thickness of the resist. Polymethyl-methacrylate (PMMA) dissolved in anisole is a resist commonly used for electron beam lithography. 2% PMMA in Anisole is spun coated onto the SiO_2

substrates at a speed of 1000 rotation per minutes for 90 seconds. The resist is then baked at 135 °C for 90 minutes. These conditions are reported by the resist manufacturer to give resist thickness of 120 nm, limiting the wire thickness to ~40 nm.

During electron beam lithography, the PMMA resist is broken into small polymer fragments by a focused beam of electrons. After patterning, the small polymer fragments are dissolved away during development, leaving the written pattern in the PMMA resist. Patterning wires and gaps with sub-100 nm dimensions requires consideration of the scattering of electrons during writing, known as "cross-talk." If electrons scatter onto non-patterned spots, too much cross-talk may occur and the PMMA resist over these spots may be sufficiently fragmented, resulting in their removal during development. Features are then larger than desired. In these cases fewer electrons should be focused onto the patterned spots during writing (lower "electron doses" are needed.) If not enough electrons hit a given spot of PMMA (possibly due to not enough scattering from neighboring pixels; insufficient cross-talk) the spot will not be fully developed and a higher does of electrons is needed. In order to determine the optimal electron dose levels, a dose matrix is designed using NanoWrite software. The dose matrix consists of pattern of wires to be written at different electron beam current doses. The purpose of a dose matrix is to determine the optimal patterned dimensions and current levels (electron "dose" levels) to achieve the desired patterns. Dose matrices were designed to achieve nanogaps with spacings from 20-100 nm.

After the dose matrix is designed, ebeam lithography is performed at the Scanning Electron Beam Lithography (SEBL) facility at MIT. Development is then carried out in a 2:1 solution of Isopropyl Alcohol (IPA): Methyl Isobutyl Ketone (MIBK) for 80 seconds followed by immersion in an IPA bath. At this point, the substrate consists of the PMMA resist layer with exposed SiO_2 areas where the electron beam has patterned the resist. Evaporation of a layer of metallic gold is then performed. Au is chosen as it does not form a surface oxide; a surface oxide would cause additional resistance when making measurements of nano-objects. Au, however has poor adhesion to SiO_2, so it is necessary to first evaporate a Cr or Ti adhesion layer. 2-5 nm of Cr or Ti followed by 12.5-25 nm of Au are deposited using electron beam evaporation at a rate of ~0.1 nm/s. Lift-off is then used to remove the remaining PMMA resist (and the metal layer on top of it), leaving only the patterned Cr/Au wires. Lift-off is performed by immersing the substrate in N-methylpyrrolidone (NMP) at 85°C for 10-15 minutes followed by low power ultra sonication in a water bath for 30-60 seconds.

The optimal shape used for patterning nanogaps with ebeam lithography is shown in figure 2.2. Using this shape and varying the electron beam dose from 400 $\mu C/cm^2$ to 1000 $\mu C/cm^2$ allows for the fabrication of nanogaps with various sizes. As the does increase, the average gap size become smaller, as more "cross talk" allows for more of the PMMA to be developed. Unfortunately, small difference in the thickness of the PMMA resist causes inconsistencies in the exact size and shape of the resulting features patterned with ebeam lithography. As the dose is increased, on some devices the two leads overlap forming a continuous gold wire with a narrow neck. At higher dose levels,

a higher percentage of devices consist of this continuous wire with no nanogap. Device yield is sacrificed at the expense of resolution. The continuous wire features are however, utilized for the electrical method of nanogap fabrication and will be discussed in section 2.3.1.

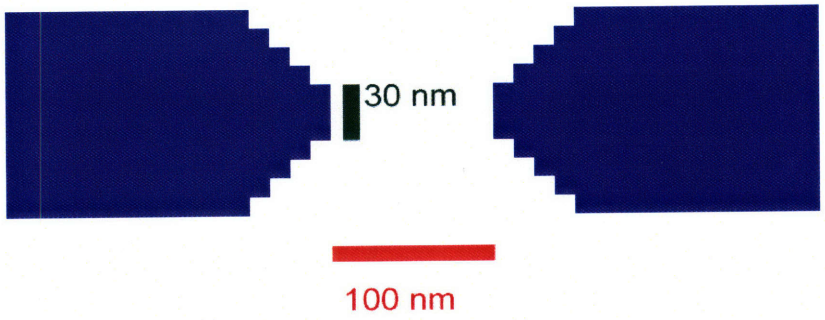

Figure 2.2: Optimized Pattern used for electron beam patterning of gaps.

Electrical characterization of wires (done after the optical lithography of the large pads, see below) is used to quickly determine the percentages of wires which are continuous (R ~ 100-200 Ω resistance) and which have insulating gaps (R >100 GΩ). Imaging of the wires and gaps was performed using contact mode AFM, tapping mode AFM and SEM. Characterization of sub-50 nm gaps using AFM suffers from tip convolution effects, where the radius of curvature of the AFM tip is on the same size scale as the gap or wire to be measured. This makes it difficult to determine whether the image reflects the size or shape of the gap, or, the size or shape of the AFM tip. Characterization by AFM is also very slow. More accurate and much quicker imaging of wires and gaps can be performed using high resolution SEM. Average gap sizes are measured by SEM imaging. Table 1 summarizes the results as a function of electron beam dose. Figure 2.3 show

representative SEM images of the different types of wires formed. Gaps with sizes of over 40 nm can be patterned with reasonable yield. Smaller gap (sub-35 nm) sizes can be achieved but at yields of <60%.

Table 2.1

Electron beam dose ($\mu C/cm^2$)	Average Gap Size	Yield of nanogaps
500	91.1 nm	100%
600	46.7 nm	75%
800	34.5 nm	52%
900	31.6 nm	29%
1000	-	0%

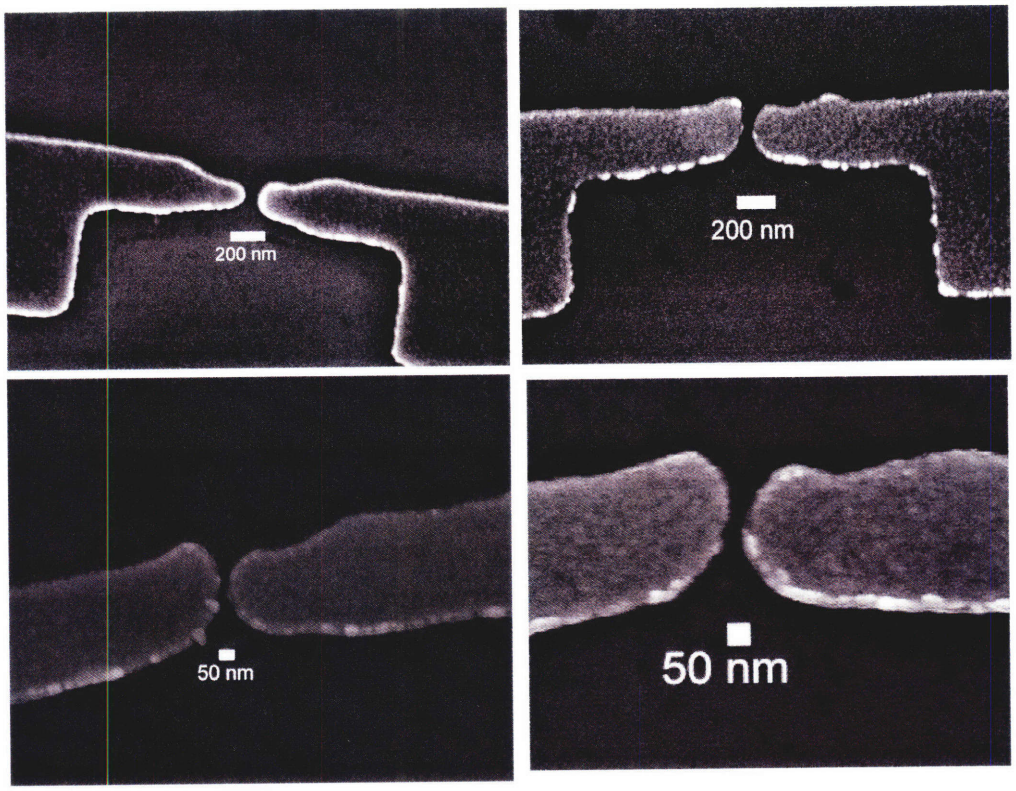

Figure 2.3: Gaps patterned directly with electron beam lithography. (top left) 79 nm gap patterned with 500 $\mu C/cm^2$, (top right) 52 nm gap patterned with 600 $\mu C/cm^2$, (bottom left) 29 nm gap patterned with 800 $\mu C/cm^2$ and (bottom right) 22 nm gap patterned with 900 $\mu C/cm^2$.

The second layer of lithography, optical lithography is used to pattern the large contact pads in registry with the ebeam patterned wires. The need for alignment of the optical

lithography step to the patterned wires places constraints on the optical mask. Although masks can be made on transparency paper, these flimsy masks can not be readily aligned. Due to the grain size of the paper, the patterned features have extremely rough non-uniform features. Masks composed of chromium features on glass allow for easier alignment and sharper edges. A clear field mask, where most of the mask is transparent and only the desired features are opaque, is also required for alignment so the features on the underlying substrate can be located. The clear field mask requires the use of negative lithography.

Optical masks were designed with NanoWrite software. A polymer resist overlying a Cr on glass plate is patterned via laser writing in the Microsystems Technology Laboratory at MIT. Immersion in a chemical developer removed the polymer resist in the areas which were to be transparent. Etching of the Cr which was not protected with the resist transferred the pattern to the mask. The remaining resist was then removed by washing in acetone.

A commercial negative resist, AZ-5214E was spun coated onto the SiO_2 substrates previously patterned with the electron beam defined wires at a speed of 3000 RPM for 30 seconds. The resist is baked at 85°C for 30 minutes. The wires patterned on the substrates are then aligned with the features on the clear field mask. The substrate is patterned by exposure to UV light for 10 seconds, followed by baking for 30 minutes at 85° C. A flood exposure, where the entire substrate is exposed to UV light, is then carried out for 90 seconds. Development in a commercially available developer (AZ422)

is carried out for 60-90 seconds, followed by washing in DI water. Optical microscopy of the large pads can be used to check that all of the resist has been removed from the patterned areas. At this stage, most of the substrate is still covered with resist with exposed areas only where the pads have been patterned. A metal evaporation and lift-off procedure is again used. 10 nm Cr and 200-500 nm Au are deposited using electron beam evaporation. Lift-off to remove the resist is carried out in N-methylpyrrolidone at 85°C for 30 minutes followed by pipetting away the resist (high pressure of solvent through a pipette tip directed onto the substrate will remove the resist) or low power ultrasonication.

At this point the devices are completely formed. The devices are imaged with optical microscopy (figure 2.4) to ensure overlap between the optically patterned contact pads and the wires patterned with ebeam lithography. Devices with major defects (gaps in the wires) can also be observed. Normally 10-50 devices are patterned on a 1 cm by 1 cm substrate. The devices can be electrically characterized using a microprobe station.. This allows for the quick determination of the percentage of continuous wires and the percentage of wires with gaps (as shown in Table 2.1).

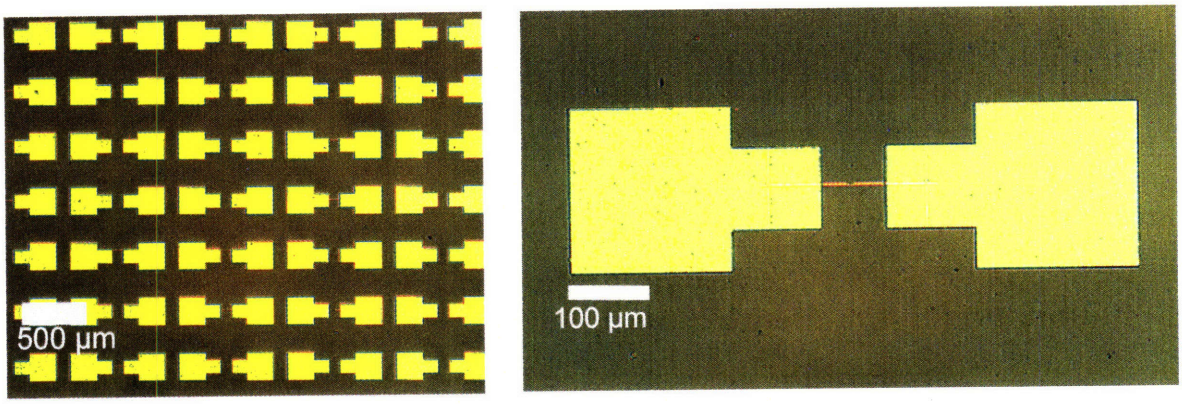

Figure 2.4: (left) Optical image of an array of devices consisting of optically defined contact pads and ebeam defined wires with nanogaps (right) magnified image of one device.

The use of electron beam lithography to directly pattern wires with nanogaps onto insulting substrates has advantages and disadvantages. Electron beam lithography is a well-studied and understood technique. Using the most simplistic techniques, as demonstrated above, gaps with 40-50 nm separation can be easily patterned with gap sizes as small as 20 nm possible. It is very easy to controllably pattern devices on the same sample with different gap sizes by programming different electron beam doses for each device. Geometries of different devices can also be easily changed. Resolution of electron beam lithography can be improved with the use of bilayer resist, angled evaporation of metals or lithography tools with a more focused electron beam.

The major disadvantage of the electron beam lithography technique is the slow speed. Devices have to be written in a serial manner and the patterning of a single substrate with 50 devices takes ~30 min. This speed is far too slow for manufacturability. Resolution of gaps sizes using simplistic methods is also not sufficient for the measurement of isolated nanoparticles. Using more complicated techniques may improve resolution but further decrease speed.

Due to the ability of the electron beam lithography to pattern gaps of various sizes with good uniformity, it is a valuable basic research tool for this thesis. Nanogaps formed by directed patterning with electron beam lithography are used to study dielectrophoresis of nanoparticles and for initial attempts to use nanoparticle devices for DNA sensing.

Electron beam lithography and optical lithography have also been used to fabricate structures for other projects ongoing in the Stellacci group. Appendix A describes this work.

2.2 Physical Methods of Nanogap fabrication

2.2.1 Focused Ion Beam patterning

Physical deformation using a focused ion beam (FIB) is a method that can be used to decrease the width of wires and for the fabrication of insulating nanogaps. Continuous gold wires (400 nm wide) or overlapping triangular leads were patterned using electron beam lithography. Optical lithography is used to pattern large contact pads in registry with the ebeam defined wires, as described in section 2.1. For gap formation, a dual beam SEM/FIB, (located at the Elletra lab in Basovizza, Italy) is used. The wire is imaged with the SEM, allowing for the imaging of the sample, while only the beam of electrons hits the sample. If the ion beam is used to both image and cut the sample, unwanted damage to the wires will occur while the sample is imaged. When the desired spot for gap formation is found, the electron beam is turned off, and the focused beam of

Ga^+ ions is enabled. The number of ions (measured as current) and the duration of the cut were varied to find the optimal parameters. Figure 2.5 shows cuts made on devices with overlapping triangular leads. 2 pA of current were focused onto a line 2μm in length for 1 second. This was found to be the optimal parameters for gap formation. Cuts varying in width from 15 to 100 nm (as measured by SEM images) were formed.

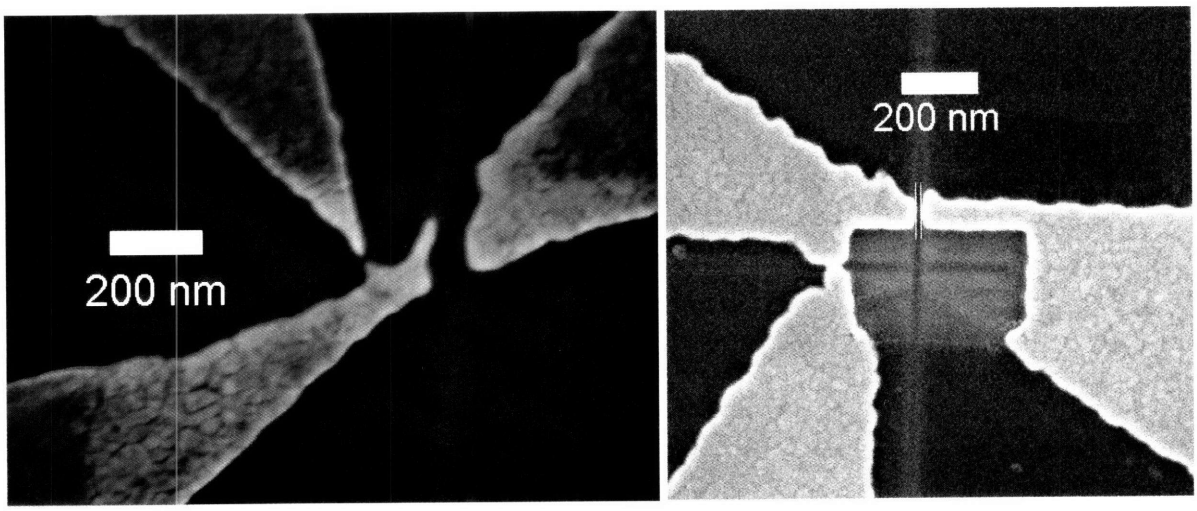

Figure 2.5: SEM images of sub-20 nm gaps formed with a focused ion beam.

The focused ion beam was also used to thin the 400 nm wires patterned with electron beam lithography prior to gap formation. The focused ion beam was used to remove large squares of Au, narrowing the Au wires down to widths of 30 - 50 nm. (Figure 2.6) Boxes of 0.15 μm^2 were cut by rastering the ion beam with 2 pA of current for 2 seconds. Gaps of 20 to 50 nm were then cut by rastering the ion beam over a 2 μm long line with 2 pA of current for 1 second.

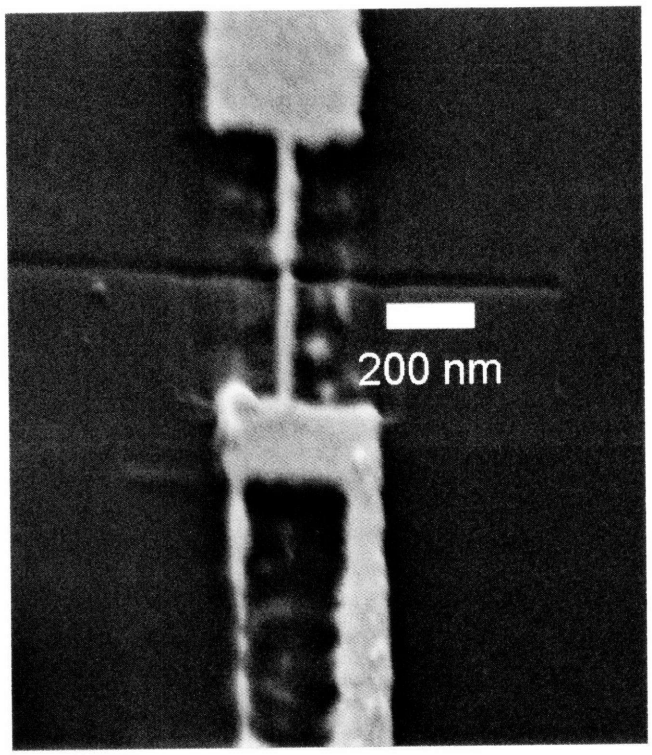

Figure 2.6: SEM image of a 400 nm wire thinned to a 30 nm width and then cut by FIB.

Electrical characterization of the gaps was performed. Gaps showed non-linear IV curves with resistance 0.1-5 GΩ at 250 mV bias. Current due to tunneling across an insulating gap would be expected to reach these levels only if the gap is <5nm.(McCarty) The current, therefore is likely due to the contamination of the surface with Ga^+ ions (from the FIB) and the formation of amorphous carbon from SEM imaging.[148]

The FIB has the ability to pattern gaps with very small sizes. Unfortunately, there are several major disadvantages of this technique. Surface contamination presents two major problems. The current due to the contamination may be greater than the current flowing through the nano-object, making it impossible to characterize the electrical properties of the nano-object. Surface contamination may make it difficult to pattern the surfaces with molecules for chemically directed assembly, as described in chapter 3. To further

improve the cutting resolution of the FIB, the ions must be focused into a very narrow beam. Improving the focus, however, will likely result in higher levels of surface contamination as more ions strike a localized spot of the surface, possibly damaging the insulating oxide layer. A final disadvantage of the technique is its extremely slow speed, taking 10-20 minutes to form a single gap.

As this was one of the first gap formation techniques I used, attempts at chemically directed assembly were made on the tips of these wires, with inconsistent results as described in section 3.2.3.

2.2.2 Contact Mode AFM Patterning

A second method of physical deformation of a continuous gold wire uses force generated by contact mode AFM. Wires were fabricated using electron beam lithography with aligned optically defined contact pads as described in section 2.1. A second set of wires fabricated using a molecular resist defined with Dip Pen Nanolithography (see Appendix B) were also cut using contact mode AFM. In these experiments, a contact force is applied to an AFM tip as it scans a line perpendicularly across the wire, breaking the wire to form a nanogap.

A straight gap across a 300-400 nm wide wire will allow for many nanoparticles to be electrically addressed in parallel. In order to attempt to electrically address an isolated particle, cuts were also made in a 'X' shape, two cuts made at 45° and 135° to the wire.

Cutting two gaps in an 'X' pattern forms two sharp metallic leads separated by nanogap at the intersection of the two cuts.

Cutting experiments were done by using a tapping mode tip (Nanodevices, TAP300) in contact mode AFM (Nanoscope IIIA) while varying the contact force in an attempt to cut the gold wires. Si tapping mode tips are used because they have a higher stiffness, needed for cutting through, than SiN contact mode tips. Systematic tests done on ebeam patterned solid gold pads tested the forces, speeds and times required for successful cutting. Little correlation was found between the depth of the cut and the number of traces or the cutting speed. The depth of the cut however increased considerably as the cutting force was increased. A contact force of 14 μN produced cuts 10 nm in depth, which would be sufficient to cut through 10 nm thick wires patterned by ebeam lithography. Figure 2.7 shows the effect of varying the contact force applied for performing the cuts. An additional problem to be addressed is the presence of the conductive chromium adhesion layer. The silicon tapping mode tip will not be able to cut through the much harder chromium. If the Cr adhesion layer is sufficiently thin, however, it should completely oxidize after the Au wire is cut.

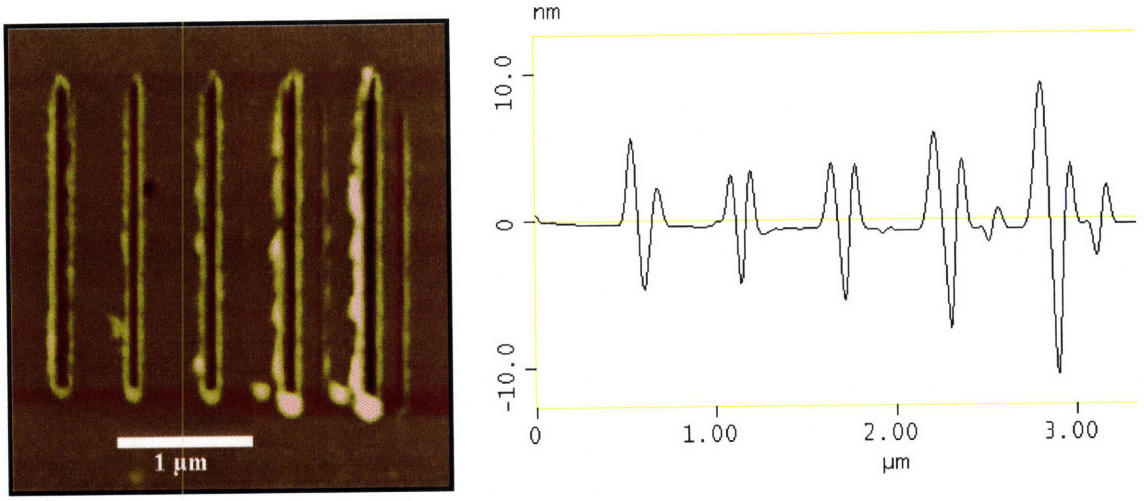

Figure 2.7: (left) Contact mode AFM images of trenches formed in a gold pad by varying contact force (increasing force from left to right). (right) height profile of AFM image, showing a deeper cut as contact force is increasing.

To form a nanogap in the wire, the tapping mode tip is able to images the wire (in contact mode) by operating at very low contact force (0.4 µN). When the desired position to be cut is scanned, the slow scan axis is disabled, so the tip continually traces over the single line to be cut. Upon the application of 14 µN of contact force, a typical wire is cut 10 nm deep at its edges, but only scratched 1-2 nm in its center. (figure 2.8) Electrical conductivity tests on scratched wires reveal no loss in conductivity, indicating that no significant gap had been created in the wires. This is likely due to the fact that the 14 µN contact force is placed on the tip while it is near the Au wire, but actually on the SiO_2 surface. The feedback of the AFM system causes the tip to remain on the surface, going over the 12-18 nm wire. Ideally we would like the tip to find the height of the SiO_2 surface and remain at that height as it plows through the Au wire. This can be accomplished using the Nanoscript lithography program. The tip is moved 100-200 nm past the wire on the SiO_2 surface. The feedback is then disabled, and the tip is moved

back and forth through the wire. A better but still not complete cut is realized. This may again be due to difficulties with feedback, this time due to the large force pushing the tip slightly off the surface when the tip first encounters the gold wire (indicated by the complete cutting of the sides of the wires but incomplete cutting of the center). A solution to this problem is to cut the wire in small increments moving the tip slightly further into the wire with each trace (a "saw" cut method). Results show a significant drop in conductivity when using this approach. (figure 2.8) Unfortunately, the cuts using this technique are 50 -100 nm in width.

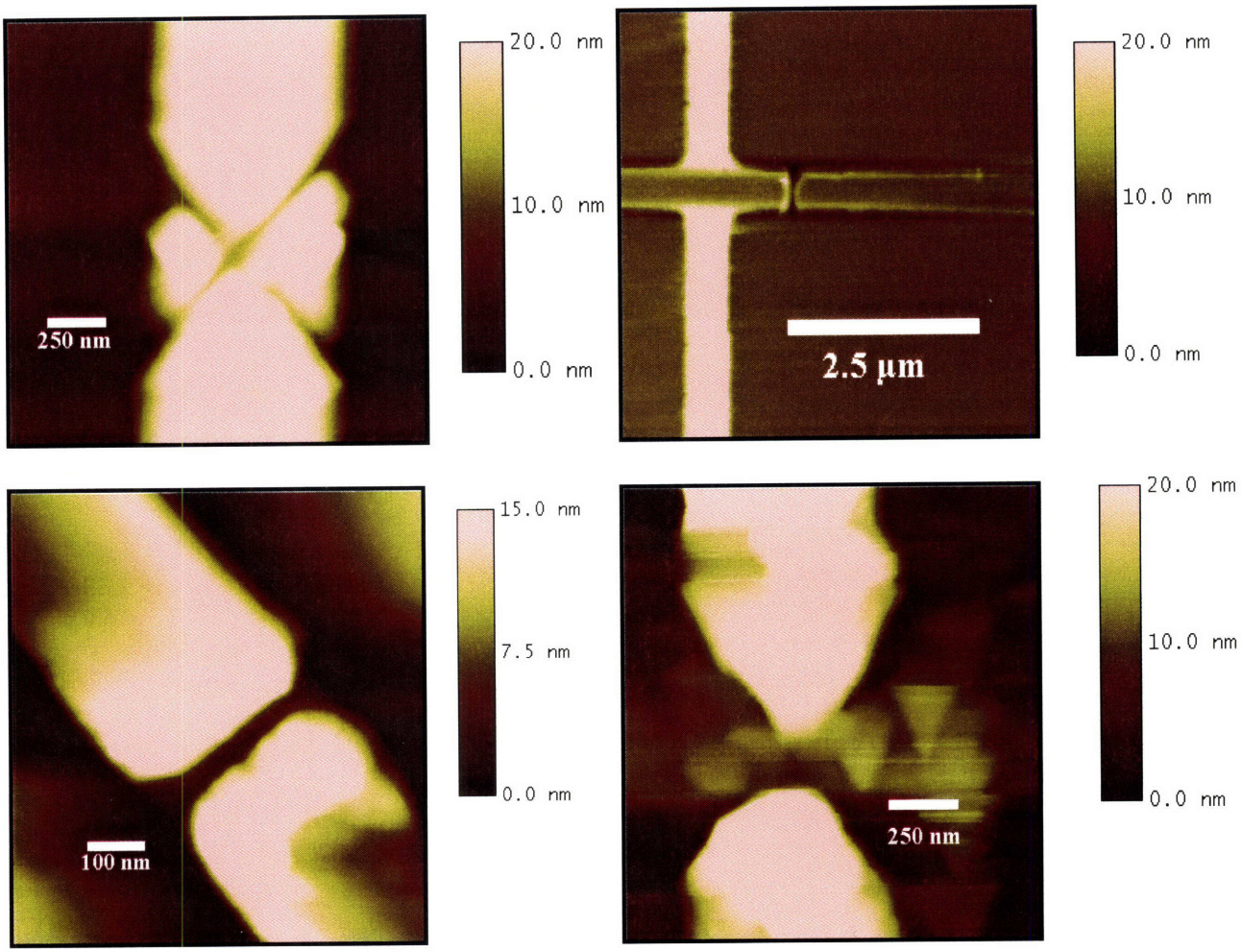

Figure 2.8: Contact mode AFM images of nanogap cut in gold wires using atomic force microscopy. (upper left and right) 'X' and straight cuts on ebeam patterned Au wires. These incomplete cuts showed little change in conductivity. (lower left) Disabling the feedback and using the "saw" cutting procedure allows for more complete cuts. (lower right) 'X' cut showing a 1-2 order of magnitude decrease in conductivity but having a 150 nm width..

Wires patterned by dip pen nanolithography lithography could be cut at lower contact forces. Only 5µN was needed to cut 20 nm nanogaps in these wires. (figure 2.9) This is likely due to the smaller grain size present in the DPN patterned sample. A 3µm by 3µm box of the contact pads was analyzed for both types of sample. The root mean square roughness was 2.832 nm for the DPN patterned substrates and 0.192 nm for the ebeam patterned sample, one indication of the larger grains in the ebeam patterned sample. The

tip may have been able to cut through the many grain boundaries in the DPN patterned sample more easily, especially as these grain boundaries were likely weakened by the ferrocyanide etchant. (See Appendix B) Due to the poor initial conductance of the DPN patterned wires, it was impossible to see differences in electrical properties after nanogap formation.

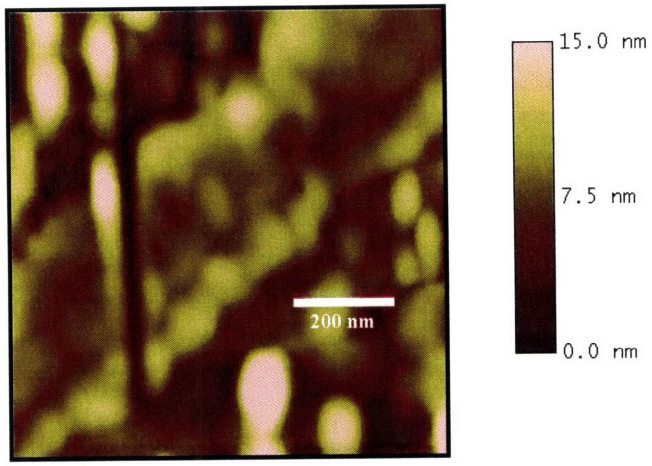

Figure 2.9: AFM image of 20 nm gap cut on a Au wire patterned by a DPN defined resist using 5μN of force.

Nanogap formation by cutting with contact mode AFM suffers both major resolution and speed problems. Reasonable gap sizes were fabricated in the DPN patterned wires, but due to the unreliable conductance of these wires, they could not be used. The smallest insulating gaps patterned in wires defined by electron beam lithography were 50 nm. 10-20 minutes were required for the formation of each gap. These nanogaps were not used further in this work.

2.3 Electrical Methods of Nanogap fabrication

2.3.1 Electrical methods of nanogap formation on wires defined by electron beam lithography

The use of electrical methods to form nanogaps has the potential advantages of both extremely small gap size and parallel processing suitable for manufacturability. Continuous wires for electrical breaking can be patterned using electron beam lithography. Wires are patterned with a pre-defined weak point or "fuse" where breaking will occur first. The wires can be patterned using the same design used to generate nano-gaps (figure 2.2) with higher electron doses. For the best control over the location of the break, the wires should overlap in a very narrow neck. Optimal geometry can again be achieved by varying the electron dose. Due to small differences in the thickness of the PMMA resist there exists variation in the shape obtained using the same dose. Again there is a tradeoff between the optimal geometry and device yield. Lower doses provide some devices with extremely narrow necks, ideal for breaking with electrical methods, but many devices with a directly patterned gap. Higher doses provide a better yield of devices with overlapping leads but these devices have large overlap. (figure 2.10) Table 2.2 summarizes the yield of overlapping wires for given electron dose levels. After development of the pattern in the PMMA resist, 2-5 nm of Cr and 10-25 nm of Au are deposited using electron beam evaporation. Lift-off in 85°C NMP completes the wire fabrication. After gold wires are patterned using electron beam lithography, contact pads are aligned to the wires using optical lithography as described in section 2.1.

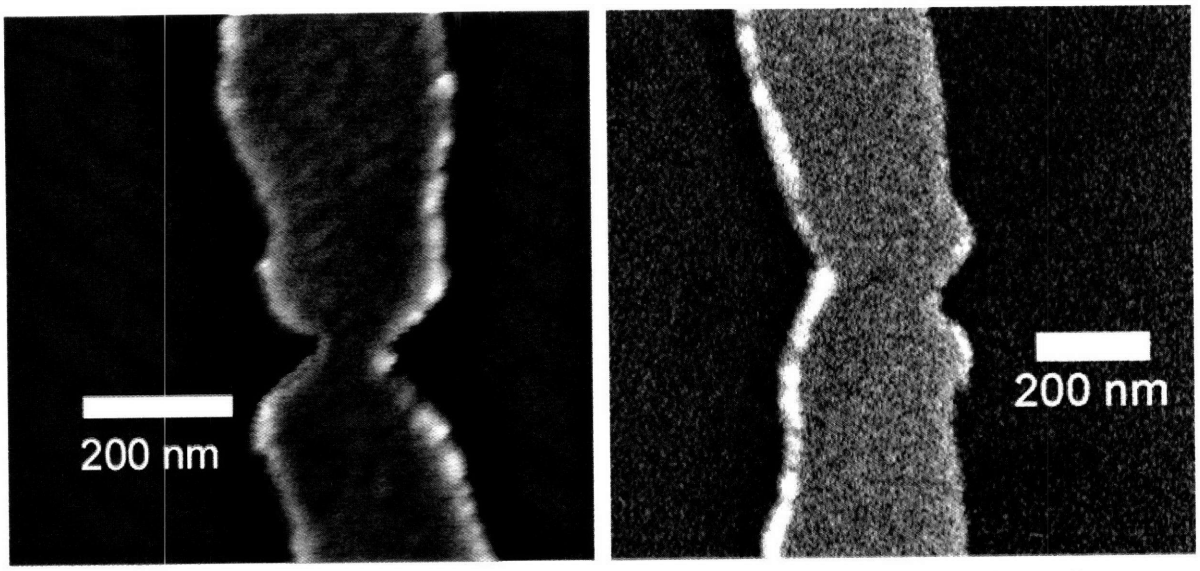

Figure 2.10: SEM images of overlapping leads patterned by electron beam lithography. (left) Wire patterned at 900 $\mu C/cm^2$ with ~100 nm wide neck. (right) A dose of 1000 $\mu C/cm^2$ increases the overlap to ~200 nm.

Table 2.2

Electron beam dose ($\mu C/cm^2$)	Yield of overlapped wires
600	25%
800	48%
900	71%
1000	100%
1100	100%

In a typical breaking experiment, microprobes are contacted to pads on both sides of the gold wire. The voltage is swept from 0 Volts to 2 Volts in increments of 2.5 mV, while the current is monitored. A typical IV curve of the break is shown in figure 2.11. Once a sharp decrease in current is realized, signifying the formation of a nanogap, the voltage sweep is stopped. Wire failure generally occurs between 0.75 -1.5 V and 5.5-9 mA. The gap is characterized electrically post break by sweeping voltage from 0 to 300 mV and measuring the current which passes though the gap. Nanogap sizes are measured by SEM imaging. Examples of gaps broken by electrical methods are shown in figure 2.12.

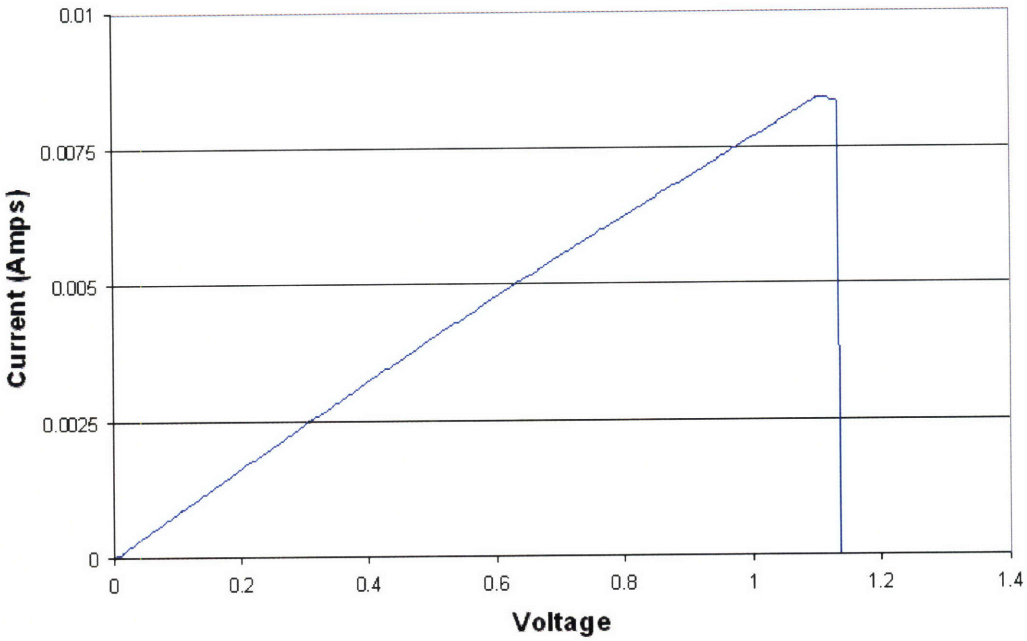

Figure 2.11: Typical current-voltage characteristics of a wire broken using the rapid electromigration method. The sharp decrease in current (1.14 V, 8.3 mA) indicates when gap formation has occurred.

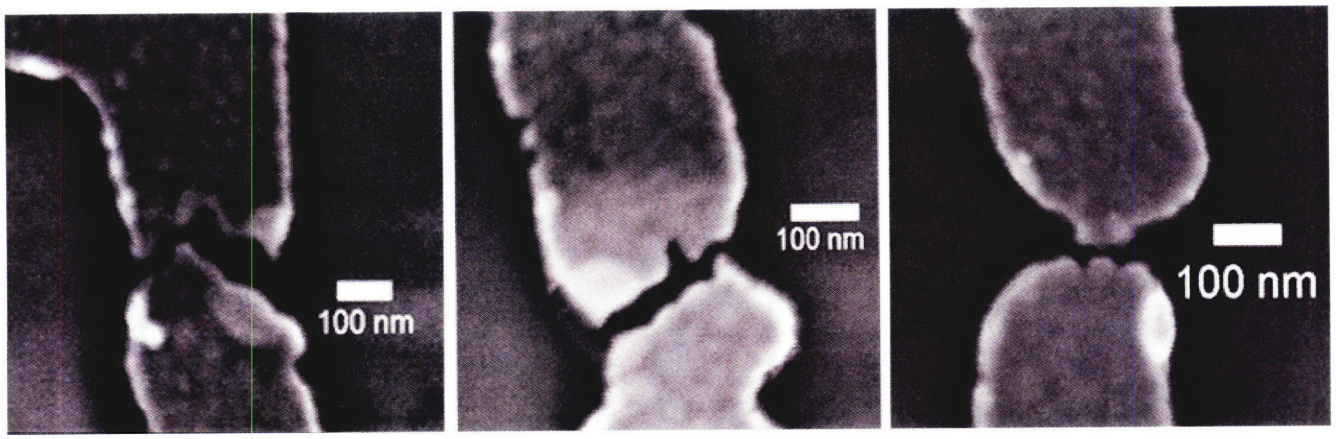

Figure 2.12: SEM images of gaps formed by electrical methods (left) 25 nm (center) 18 nm and (right) 11 nm.

SEM imaging of 50 gaps broken with electrical method shows an average gap size of 25.6 nm with a distribution as shown in figure 2.13. Electrical characterization of the 85% of the gaps post break showed resistances > 100 GΩ. Literature reports that only gaps having sizes < 6.2 nm will show appreciable tunneling current.[16] The 15% of gaps with residual current are likely caused by the incomplete breaking of the Ti or Cr adhesion layer and will be discussed further in section 2.3.2.

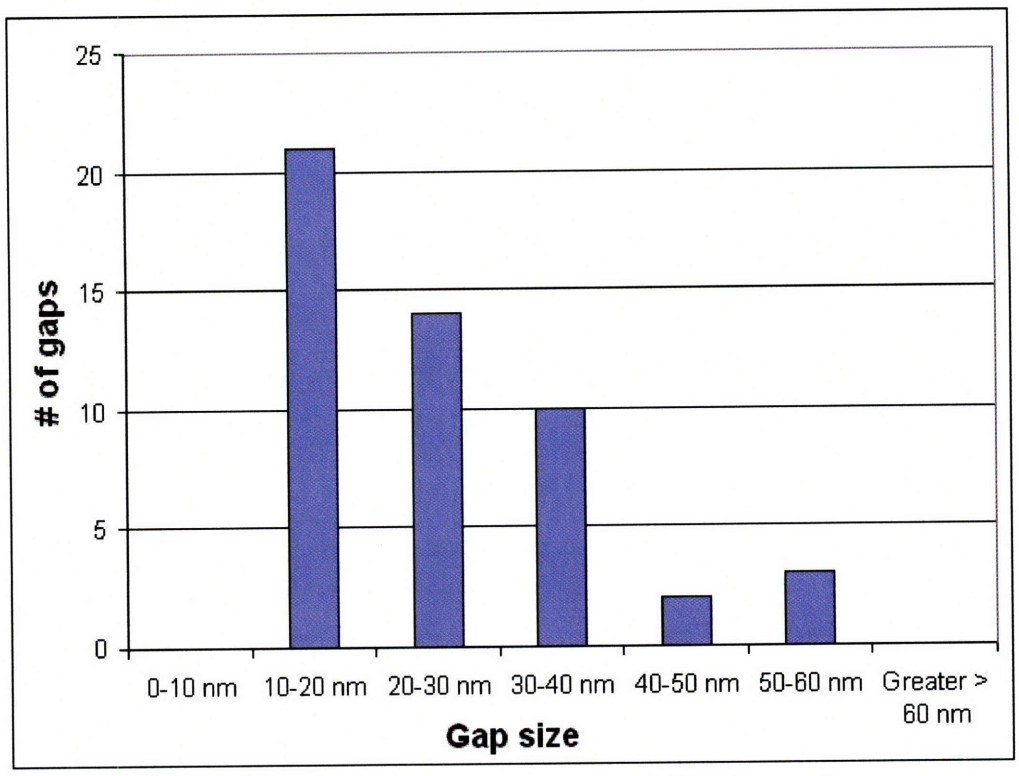

Figure 2.13: Distribution of gap sizes in wires formed by electron beam lithography.

In order to be able to better control the position and size of the gaps formed by electrical methods, it is necessary to understand the mechanism causing the gap formation. As described in chapter 1, two competing processes may cause the gap formation. The wire may fail by electromigration, where at high current density, the momentum of the conduction electrons is transferred to the gold atoms, causing their diffusion and the

formation of a gap. The electromigration force is proportional to the current density passing through the wire. The second mechanism of failure may be due to the joule heating of the wire caused by its resistance. If the local temperature at the junction exceeds the melting temperature of gold, the wire will fail due to melting. The heat produced in the wire is proportional to IR^2.

Following a model suggested by Richter, et. al,[35] we can predict whether localized melting can occur in these wires. This model looks at the ratio of the heat generated in a section of the wire (Q, proportional to its resistance by I^2R), compared with the volume (V) of the wire in order to determine where the maximum temperature increase will occur. The well-formed wires with narrow overlap can be divided into four sections all with thickness (t) of 32 nm. Calculating the relative Q/V ratio of each section as compared with the junction can be done by the following relationships: $Q=I^2R$, $R=\rho l/A$, $V=l*A$, $A=w*t$ and with I, ρ, t the same for each section of the wire, $Q/V \alpha 1/w^2$. Therefore the relative Q/V ratio to the junction Q/V ratio can be defined as $(Q_1/V_1)/(Q_{junction}/V_{junction})= w_{junction}^2/w_1^2$ and summarized in table 2.3.

Table 2.3

Wire section	Width (w) (nm)	Relative Q/V ratio to junction Q/V
Junction	100	-
Thin wires	300	0.11
Medium wires	1000	0.01
Thick wires	2000	0.025

As shown in the table 2.3, 9 times more heat/volume is generated in the junction than in the thin wires, 100 times more than in the medium wires and 400 times more than in the wide wires. This would indicate most of the temperature increase occurs at the junction, leading to localized melting at that point. When well formed narrow junctions are fabricated, the gap almost always occurs at the junction of the wires. (figure 2.12 right) However, in devices which suffered from overexposure, too much overlap occurs (figure 2.12, left), and leads to the formation of continuous gold wires poorly defined wide junction points. In these wires the maximum temperature increase happens all across the 2 μm long 300 nm wide wire. This causes gaps which do not form in the center of the two leads. All gaps were still found in the thin wires, as opposed to the larger 1 and 2 μm wide wires.

Again, following Richter's model,[35] the localized temperature change can be calculated using the following equation and the temperature coefficient of resistance (TCR= 0.002 $^{\circ}C^{-1}$ for pure gold, TCR=0.0037 $^{\circ}C^{-1}$ for the device reported by Richter):

$$(\Delta R_{junc}/R_{junc}) * (1/\Delta T)=TCR$$

An increase in resistance of 6-9 Ω has been seen in the electron beam defined devices immediately before failure. Using geometrical arguments to calculate the resistance of the well-formed narrow junctions as a percentage of the overall resistance yields a junction resistance of 1.2-1.5 Ω. Assuming the entire resistance increase occurs at the junction and taking the TCR value of 0.0037 $^{\circ}C^{-1}$, this would indicate a temperature increase of 1080-

2027 °C, above the melting temperature of gold (1064°C). For wires with larger overlap, the assumption that all of the resistance and subsequent temperature increase occurs at the junction is no longer valid. For these devices, larger changes in resistance (12-19 Ω) are realized before failure. Heat is now spread throughout the thin 300 nm wire. For wires with no geometrically defined weak points, the localized melting may occur at defect sites in the wire.

The average value of the current density at the point of wire failure (J_b) was found by dividing the current at failure (I_b) by the cross-sectional area of the wire at the point of failure (thickness known from evaporation, width of wire measured from post-break SEM images). The average current density for the wires studied was found to be $1.02*10^8$ A/cm^2. This value is 10% lower than the lowest values seen in the literature for electromigration of Au wires.[36] This suggests that the current density has not reached sufficient strength to break the wires by electromigration alone. SEM evidence of a differing grain structure near the gap further supports gap formation by localized melting (figure 2.14).

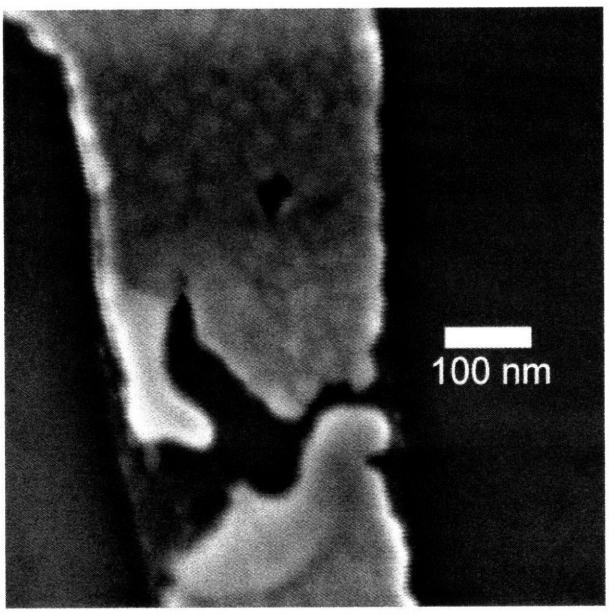

Figure 2.14: Smoother grain structure near break suggests gap formation by localized melting.

The influence of the certain parameters on the gap size can also give an indication of the gap formation mechanism. The gap size was plotted against J_b and I_b^2 and average gap sizes were calculated for devices the lowest 1/6, middle 2/3 and highest 1/6 current densities and currents at failure (figure 2.15 and table 2.4). Ideally to look at the effect of melting, gap size should be plotted against $I_b^2R_{junc}$. However it is difficult to isolate from the resistance of the junction from the resistance of the overall device. The data shows a trend between I_b^2 and the gap size. This indicates as more heat is generated the wire fails more catastrophically, leading to a larger gap size. No such trend is seen in J_b vs. gap size, as would be expected if the failure were purely due to electromigration.

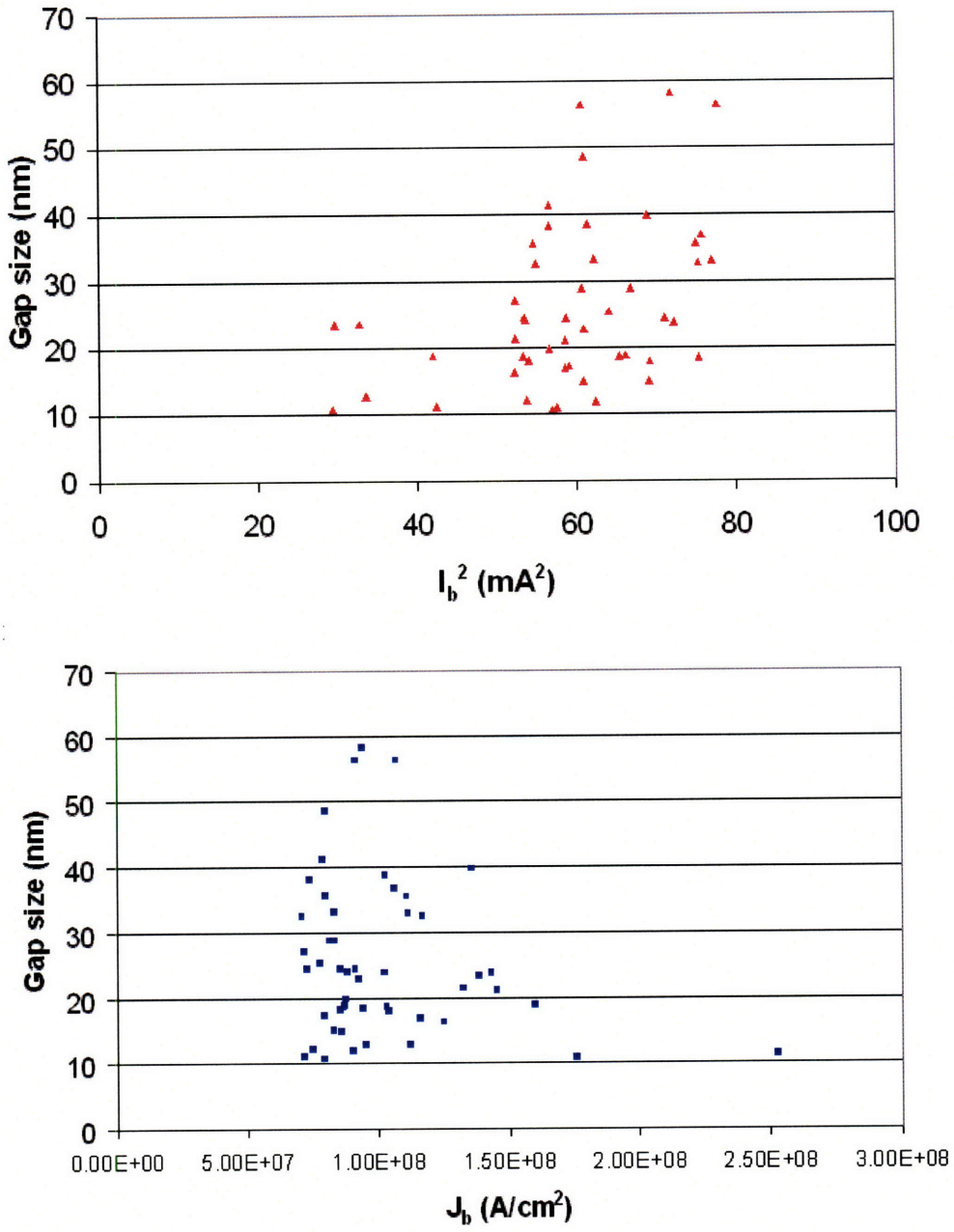

Figure 2.15: Correlation between gap size and (top) I_b^2 and (bottom) J_b.

Table 2.4

I_b^2 (ma^2)	Average Gap Size (nm)	J_b (A/cm^2)	Average Gap Size (nm)
29 - 50	**16.30**	**7E7 - 7.8E7**	**24.47**
50 - 70	**25.10**	**7.8E7 - 1.15E8**	**27.48**
70 - 80	**35.57**	**1.15E8 - 2.6E8**	**21.33**

The data presented above suggests gap formation by localized melting. It does not however rule out possibility that the gap formation begins due to thermally assisted electromigration. In thermally assisted electromigration, the high localized temperatures allows for electromigration to occur at lower current densities After gap formation begins due to electromigration, the extremely narrow section of remaining wire leads has an extremely high resistance. Joule heating than takes over, as the rest of the wire fails due to melting. The ultimate failure of the wire by melting would offer an explanation for the grain structure near the gap and the dependence of gap size on I_b^2 even if failure had begun due to electromigration.

In either mechanism, it is clear that control over the fabrication of sub 20 nm gaps can be obtained by causing wire failure at lower I_b. In the localized melting mechanism, lower currents translate into a more localized region of temperature increase and smaller gap sizes. In thermally assisted electromigration, lower currents mean that more of the wire can fail due to electromigration before the more catastrophic melting process begins. Device geometry and the rate of voltage increase have been used to lower the current at failure, as demonstrated in figures 2.16 and 2.17 and in tables 2.5 and 2.6.

As mentioned previously, controlling device geometry through patterning with electron beam lithography at different dose levels leads to a narrower neck. This narrow neck is able to fail at lower currents, producing more narrow gaps. A second method of control is offered by the rate of voltage increase during the experiment. Decreasing the rate leads to failure at lowest possible current levels. Higher speeds with larger voltage steps forces to failure to occur at higher currents, generating larger gap sizes. Slower rates allow for the system to reach a thermal equilibrium before more current is forced through the junction.

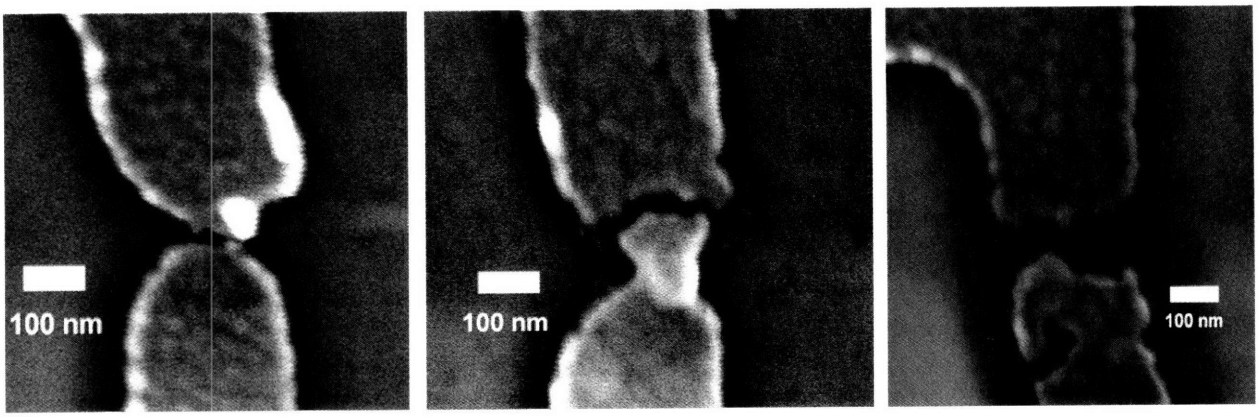

Figure 2.16: SEM image of nanogaps formed on wires patterned at different doses: (left) 11 nm gap on wire patterned at 600 $\mu C/cm^2$ (center) 18 nm gap on wire patterned at 900 $\mu C/cm^2$ (right) 58 nm gap on wire patterned at 1100 $\mu C/cm^2$

Table 2.5

Electron beam dose	I_b (mA)	Average Gap size (nm)
600- 800 μC/cm2	6.36	18.00
900 μC/cm2	7.28	24.05
1000 μC/cm2	8.02	27.80
1100 μC/cm2	8.08	28.71

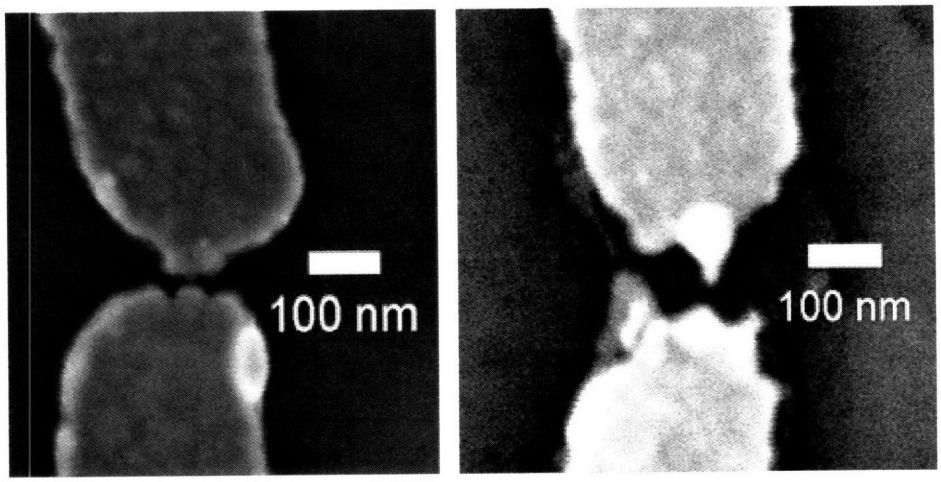

Figure 2.17: SEM image of nanogaps formed with different rates of voltage increase: (left) 11 nm gap formed at 4.63 mV/s increase. (right) 40 nm gap formed at 17.83 mV/s increase.

Table 2.6

Rate of voltage increase	I_b (mA)	Average Gap size (nm)
4.63 mV/s	7.38	23.80
8.63 mV/s	8.04	26.25
17.83 mV/s	8.66	39.78

2.3.2 Electrical methods of nanogap formation on wires defined by optical lithography

Devices with 2-3 μm wide, 10 μm long, 15 nm thick Au wires connecting larger wires and contact pads have been patterned using only optical lithography. The wires are patterned using a dark field mask and positive lithography followed by the evaporation of 2-5 nm Cr and 15 nm of Au. It is possible to form sub 30 nm gaps in these wires using electrical methods. (figure 2.18) Similar experimental procedures for breaking wire are used as described in section 2.3.1. The melting, however, is not localized to a central point on the wire, as no pre-defined weak point exists. The break is likely to occur at any point in the 10 μm long wire.

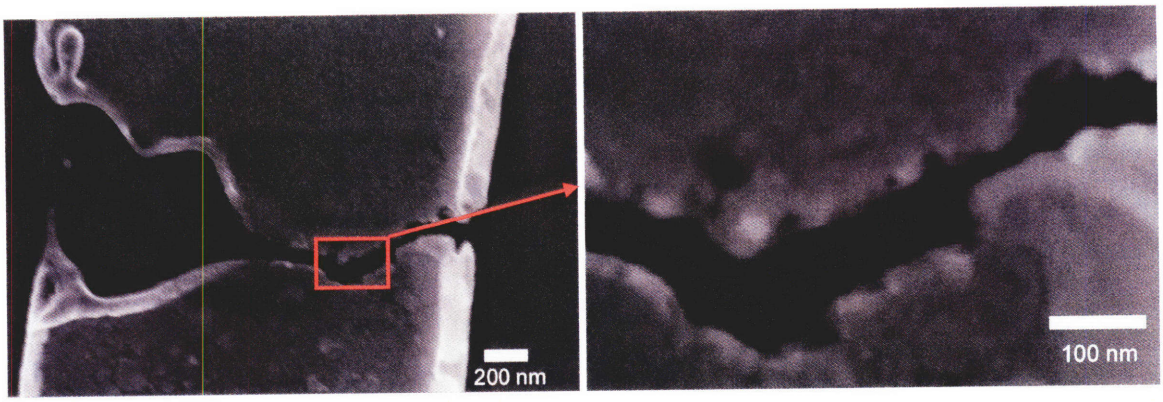

Figure 2.18: SEM image of a nanogap formed on a 2.5 aμm wire wires patterned by optical lithography.

Electrical characterization of the gaps pots break reveals that 85% of the gaps are insulating (R>100 GΩ at 300 mV) but 15% of gaps show linear IV characteristics with R<100 GΩ. The size of the gap (and the shape of the IV curves) indicates that this current is not due to tunneling through the insulating gap. The residual current is likely due to the incomplete breaking of the Cr adhesion layer as shown in figure 2.19.

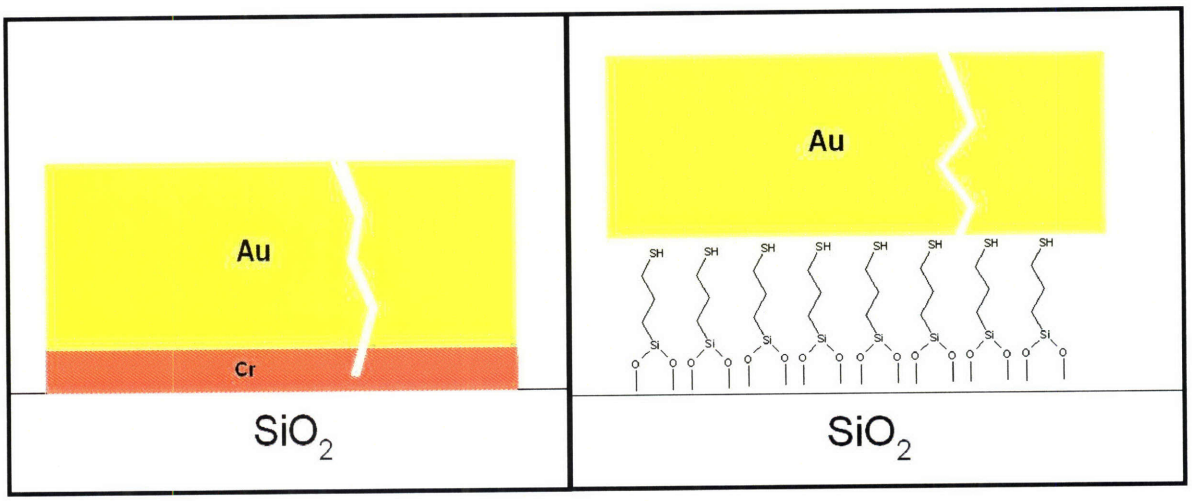

Figure 2.19: (left) Residual current can pass through the Cr adhesion layer. (right) The use of a mercaptopropyltrimethoxysilane monolayer eliminates the chance of residual current.

Modifying a procedure first reported by Janes,[36, 40] a molecular adhesion layer can be used to avoid the use of a metallic adhesion layer. Mercaptopropyltrimethoxysilane (MPTMS) can bind to dangling oxygen bonds on a SiO_2 substrate. The surface of the

MPTMS monolayer is composed of thiol groups which can bind to gold. In this way the gold adheres to the substrates through an insulating molecular monolayer.

Before lithography is performed, the SiO_2 substrates are cleaned in piranha solution (30% HCl: 70%H_2O_2), followed by cleaning in a 5:1:1 DI water:H_2O_2:NH_3OH solution to ensure the removal of any organic contamination that would affect monolayer formation. Following optical lithography, the sample is placed into an oxygen plasma cleaner for 5 minutes to remove any residual resist and form dangling oxygen bonds on the surface of the substrate. The sample is then exposed to HCl vapor for 60 seconds to protonate the oxygen bonds. Finally a vapor phase deposition of MPTMS creates a monolayer on the patterned area of the surface. 15 nm of gold are evaporated onto the surface followed by ultrasonication in 85°C NMP. The adhesion layer is strong enough to prevent removal of the gold even after high power ultrasonication.

Transferring this strategy to electron beam patterned wires has been more problematic. The much thinner PMMA resist is unable to withstand the oxygen plasma cleaning step, destroying the pattern in the polymer.

Over 98% of gaps formed in optically defined wires have shown resistances of >100 GΩ at 300 mV. Wire failure generally occurs at 2.5-4 V and 25-45 mA. 48 of these gaps have been studied. Their average gap size is 28.8 nm with a gap size distribution as shown in figure 2.20. A typical examples of a gap patterned on wires with a MPTMS monolayer is shown in figure 2.21

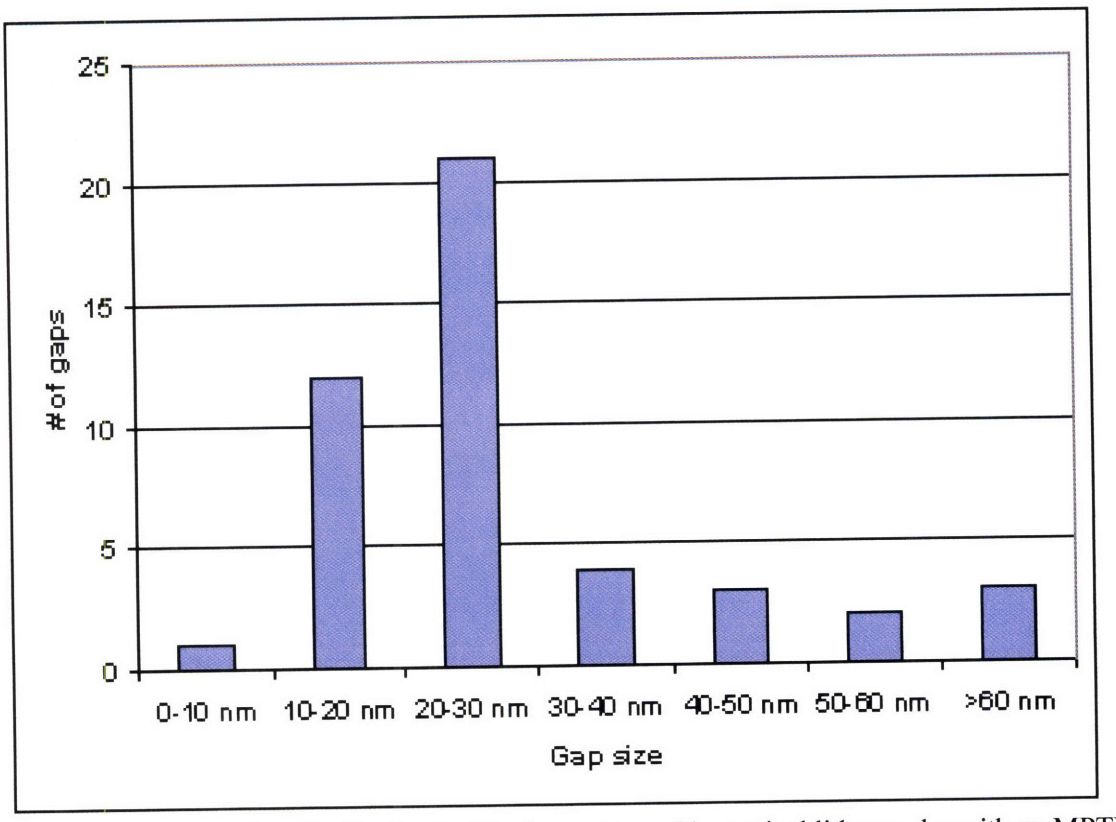

Figure 2.20: Gap size distribution in 48 wires patterned by optical lithography with an MPTMS adhesion layer and then broken with electrical methods.

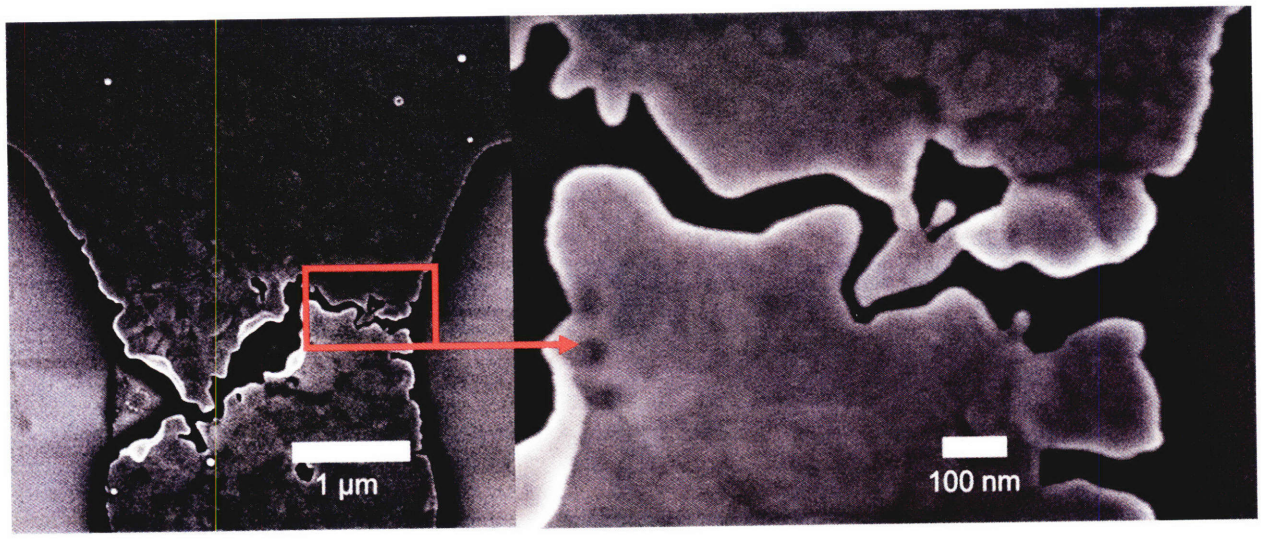

Figure 2.21: Nanogap with a 17.6 nm minimum size formed by electrical methods on a wire defined by optical lithography with an MPTMS monolayer.

It is again important to understand the mechanism by which gap failure is occurring in these wires. Using the thermal analysis model suggested by Richter and described in section 2.3.1, the localized temperature in the 2.5 μm wide wires can be calculated. The increases in resistance in this case are generally only 2-6 Ω. This would indicate a very small, <50°C temperature increase. This makes the onset of gap formation by localized melting very unlikely. Average current densities for these wires are 1.11 $*10^8$ A/cm^2, within the range described for failure by electromigration for similar devices in the literature.[36] This suggests that the onset of failure for the optically defined wires is due to electromigration. Further proof is found by studying the temperature dependence of the breaking conditions, as shown in Table 2.7. As the temperature increases, the current and current density needed for wire failure decreases drastically. This is again indicative of electromigration. The medium time to failure for electromigration is dependent of the current density and exponentially dependent on temperature. Increasing the temperature gives more mobility to the atoms, allowing electromigration to occur at lower current densities.

Table 2.7

	I_b (mA)	J_b (A/cm2)
25° C	35.48	1.12*108
100° C	30.23	9.44*107

Gap sizes were plotted as a function of J_b and I_b^2 and average gap sizes were again calculated for devices the lowest 1/6, middle 2/3 and highest 1/6 current densities and currents at failure. Different results are seen for the optically defined wires than the case

for the thinner ebeam defined wires. (figure 2.21 and table 2.8). Here, gap size is correlated to J_b, indicating that electromigration is controlling the gap formation. Little dependence is seen between gap size and I_b^2.

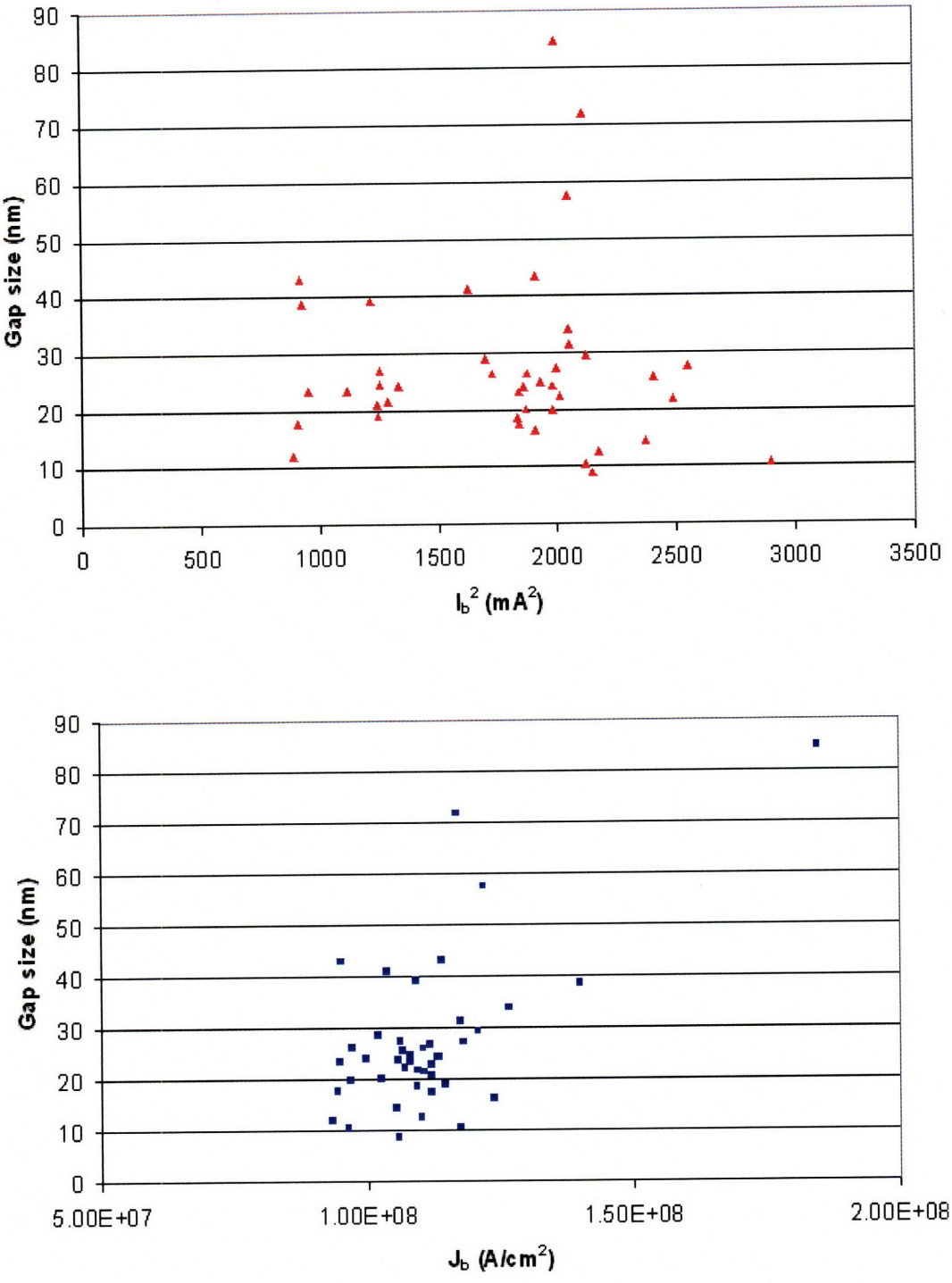

Figure 2.22: Correlation between gap size and (top) I_b^2 and (bottom) J_b.

Table 2.8

I_b^2 (ma^2)	Average Gap size (nm)	J_b (A/cm^2)	Average Gap size (nm)
850-1170	26.42	8.8E7 – 9.8E7	21.88
1170-2120	30.08	9.8E7 – 1.22E8	25.74
2120-2900	18.97	1.22E8 – 1.85 E8	46.34

Many of the gaps formed show a rather unusual shape as demonstrated in figure 2.23. A narrow gap is present across ~50-70% of the wire. The remaining section of the gap is much larger, often > 1 μm. This suggests a two part breaking mechanism. Failure begins by electromigration. As the gap propagates across the wire, the resistance of the remaining wire quickly increases. A large amount of joule heating occurs in that remaining section. Once the melting point of gold is reached, the remaining piece of wire fails catastrophically, leading to the larger gap seen on many wires.

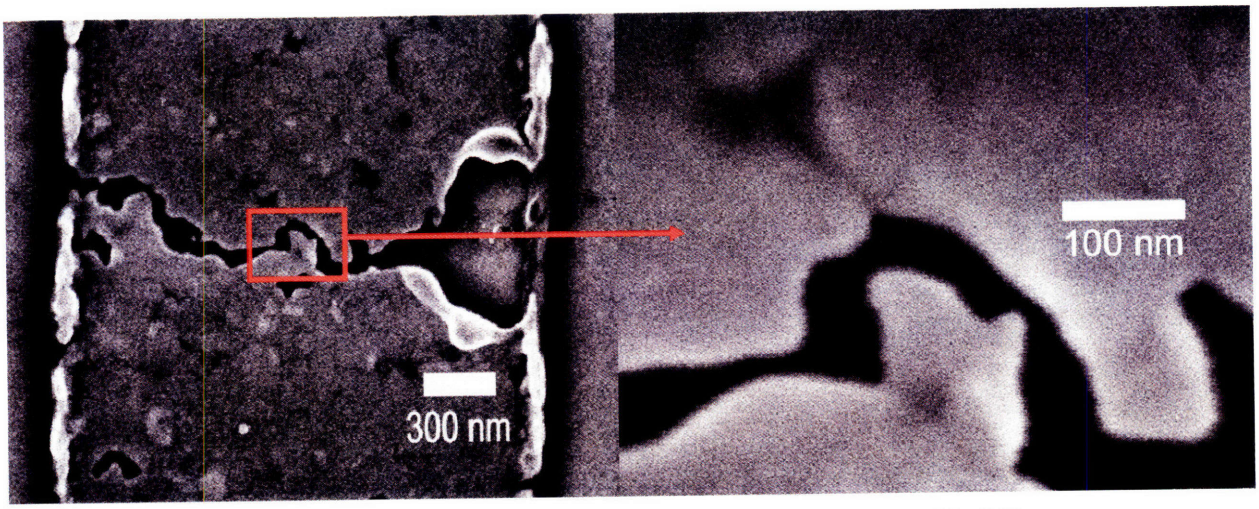

Figure 2.23: Nanogap with a 16.5 nm minimum feature size but catastrophic failure on one piece of the wire opens a 715 nm gap.

The use of electrical methods of gap formation has important scientific and technological implications. Controlled breaking using electromigration allows for the easy fabrication of sub 30 nm gaps. Optimization of the process could potentially enable gaps as small as a 1 nm to be routinely patterned. The use of electrical circuits allows for the potential for many gaps to be formed at the same time, giving this method the best potential for nanomanufacturing of all the techniques presented. Fabrication of nanogaps in large wires which require only basic optical lithography further enhances the appeal of this technique.

In this work, I chose to focus on electrical methods of gap formation due to their simplicity, ease of incorporation on a silicon based platform and potential for scalability. These gaps are used for the dielectrophoretic assembly of nanoparticles (Chapter 4) and in attempts for DNA sensing. (Chapter 5)

Future work in this field should concentrate on a better understanding of gap formation and a better control of gap location, size and shape. While interesting on a basic research level, electrical based gap formation on wires patterned with electron beam lithography or wires patterned with complicated lithography techniques will not easily scale for nanomanufacturing, Efforts should focus on electrical means of gap formation in optically defined wires. Due to break initiation by electromigration for these wires, simple methods of lowering current levels do not affect the gap size or shape. Controlled techniques of ramping voltage or current might be used to prevent run-away melting. Work exploring the effect of varying grain shape (perhaps a bamboo grain structure) or

size may also be significant, as electromigration proceeds fastest along grain boundaries. Once a complete understanding and control of gap formation on optically defined wires is achieved, devices based on isolated nano-objects or even molecules bridging nanogaps will more readily be achieved.

Chapter 3: Chemically Directed Assembly of Nanoparticles

In the following chapter, work on the chemically directed assembly (CDA) of nanoparticles is explored. Due to the promise of parallel placement on nano-objects onto precise locations of substrates, CDA is a valuable tool for nanomanufacturing. First, work understanding monolayer formation using Dip Pen Nanolithography (3.1), an important method of patterning molecules on surfaces with sub-100 nm resolution, is described. Then, different chemical strategies to assembly nanoparticles onto surfaces using ionic (3.2.1) and covalent (3.2.2) bonds are reported with an emphasis on controlled specific assembly and a description of the advantages and disadvantages of each strategy. Finally, early efforts to use chemically directed assembly to position nanoparticles in a gap are described (3.2.3).

3.1 Dip Pen Nanolithography

Dip Pen Nanolithography is a valuable tool for the patterning of molecules on surface with nanoscale resolution. As DPN can be done using many molecule-substrate combinations, it offers the ability to pattern surfaces with specific functional groups that can direct the assembly of nano-objects, It is therefore a valuable tool for chemical directed assembly. A better understanding and control over the quality of SAMs patterned via DPN will lead to better assembly. Another motivation for studying the science behind DPN comes from the current debates and lack of scientific studies on the enabling mechanisms and kinetics of the technique. While there have been many papers published on applications of Dip Pen Nanolithography, only a very few have looked at the science behind DPN.

The most common molecules used in DPN patterning are octadecanethiol (ODT, CH_3-$(CH_2)_{17}$-SH) or mercaptohexadecanoic acid (MHA, COOH-$(CH_2)_{15}$-SH) on Au surfaces. Solution and vapor deposition methods, as described in section 1.3.1, were used to coat tips with molecules for subsequent writing. Both methods produced tips that would pattern ODT and MHA. It was also determined that cleaning the tips with an overnight soak in dichloromethane increased the tip patterning success rate. Substrate type and preparation is also critical for successful patterning. To image ODT and MHA monolayers in both height and friction mode, flame annealed Au (111) thermally evaporated on freshly cleaved mica was used as a substrate. This type of substrate is composed of atomically flat terraces that have height mismatches of up to 2 nm. The substrate is used immediately after opening to avoid contamination by organics. For technological applications using DPN it is desirable to work on a Au on Si substrate. After looking at several types of Au on Si, substrates with a 2-5 nm Cr or Ti adhesion layer and 25-30 nm of Au thermally evaporated on a Si substrate were selected. Gold samples should be either used immediately after evaporation or stored under an inert gas atmosphere until use to avoid contamination by carbonaceous compounds. It is difficult to pattern on samples that have been left in air for longer than a few days. Older Au on Si samples can be treated by soaking overnight in ethanol followed by cleaning for 5 minutes in a UV ozone cleaner immediately prior to writing, but patterning is still far worse than what can be achieved on freshly evaporated surfaces. Au on Si surfaces allow for lateral force microscopy (LFM) images of DPN patterns, mapping the frictional

forces of the surface. Height images are more difficult to obtain on Au on Si due to the rough nature of the surface.

1 μm^2 boxes of MHA and ODT were patterned by scanning the AFM tip at speeds of 2-4 $\mu m/s$. 256 lines per box were traced 4-8 times each by the AFM tip. The scan size was then increased to 16-25 μm^2 and the scan speed was increased to 40-50 $\mu m/s$. A rapid scan speed is used for imaging patterns to prevent further writing with the coated tip. The patterned box is seen by looking at frictional forces images with LFM. It is well documented that frictional forces are lower in hydrophobic molecules and higher in hydrophilic ones when compared to the surrounding bare gold substrate.[42, 43] Boxes written with ODT, a hydrophobic molecule therefore appear as low friction. Boxes patterned with well ordered MHA SAMs, which contains a hydrophilic carboxylic head group appear as high friction. In a similar method, lines were patterned with DPN by disabling the slow scan axis and allowing the tip retrace the same line 20-40 times at speeds of 3-10 $\mu m/s$. The scan angle was then changed to create two lines intersecting each other at 45°. The Nanoscript (Digital Instruments) lithography program was used to pattern other features with the AFM including the letter "X," 5 parallel lines, and the letters "MIT." (figure 3.1) Patterning dots with DPN involves holding the tip stationary on the substrate for a given period of time. Arrays of dots were patterned with the Nanoscript lithography program. A plot of dot diameter vs holding time follows the $t^{1/2}$ dependence expected from a diffusion based mechanism and reported in the literature.[46, 48, 54, 58, 59] (figure 3.2)

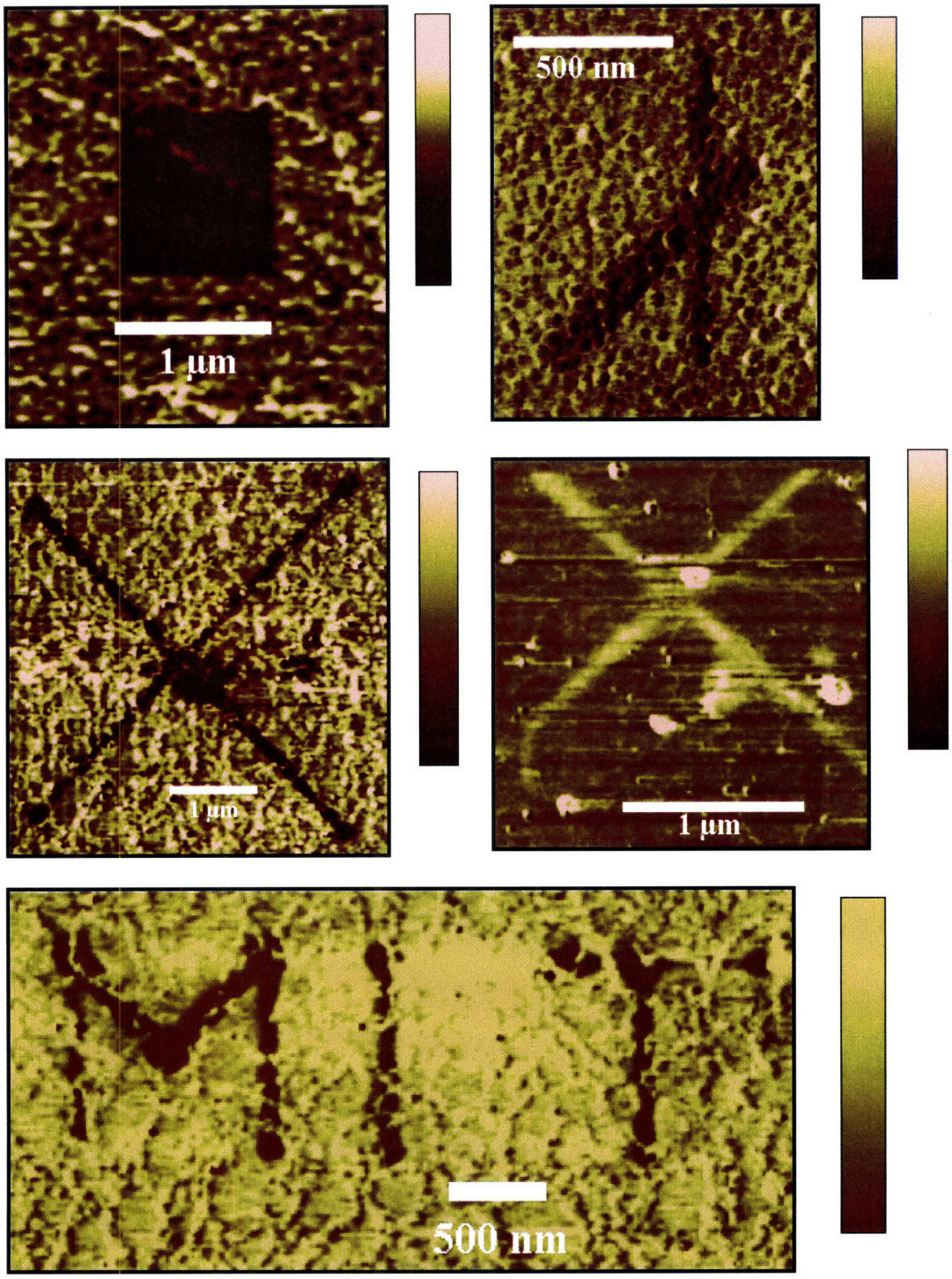

Figure 3.1: Lateral force microscopy images of patterns generated by Dip Pen Nanolithography. (Top row) ODT boxes and lines, (middle left) ODT "X" (middle right) MHA "X" (bottom) ODT "MIT."

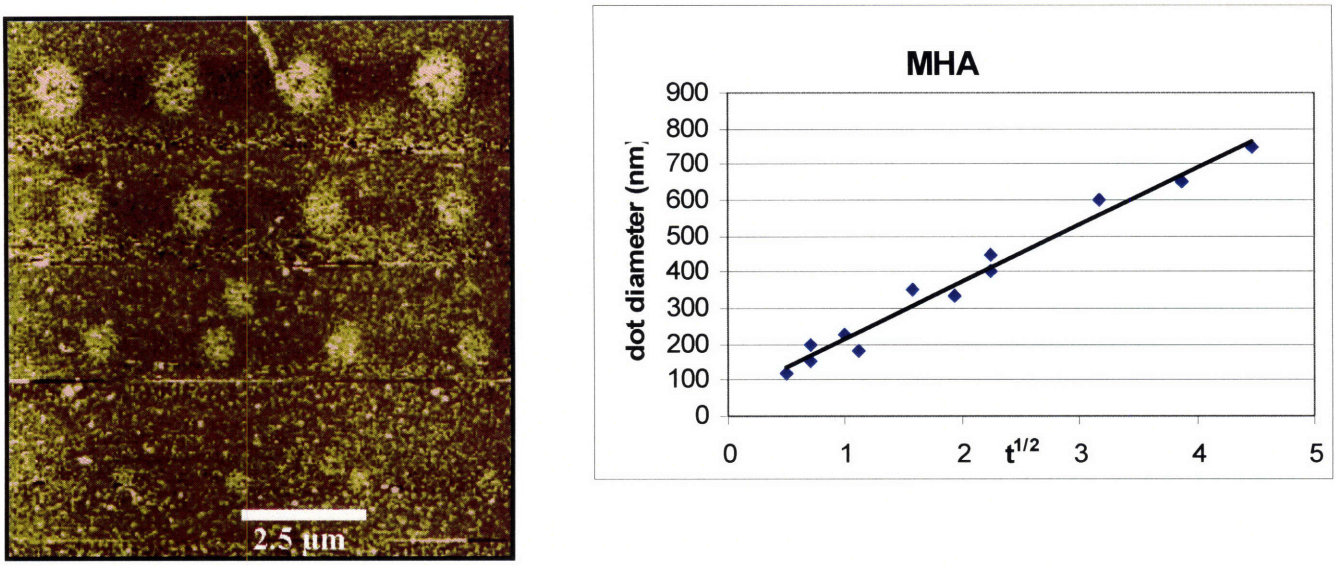

Figure 3.2: (left) MHA dots patterned with DPN by holding the tip stationary for differing amounts of time. (right) Plot of MHA dot diameter vs. time showing the expected $t^{1/2}$ dependence.

3.1.1. Self-Assembled Monolayer Formation using DPN

Much of the fundamental research on the enabling mechanism of DPN[44-46, 59] has focused on understanding the phenomena that allow the transfer of molecules from the tip to the surface, with the goal of improving its lateral resolution. We focused on the subsequent assembly of such molecules on the surface, showing that they can form homogeneous and dense self SAMs as long as they are given enough time to nucleate and grow.[149] The analysis of AFM height images of monolayers written via DPN proves that the writing speed determines the quality of the written SAMs.[149] The patterned SAM quality is of critical importance for application of DPN, such as self-assembly of nanoparticles or patterning resists for the etching of nanometer sized wires.

SAMs of thiolated molecules on metal surfaces have been extensively studied[150, 151] and it has been established that they form through a multiple step mechanism.[152, 153] The first step is always a fast adsorption on the surface, in which the molecules assume a flat lying conformation. (figure 3.3) The second step occurs when the surface is almost completely covered; at this stage new molecules can only bind to the surface by inducing a reorientation of the flat-lying molecules more normal to the surface. This step, nucleation, is characterized by the formation of isolated densely packed pockets. The third step consists of the growth of these pockets into a continuous and uniform film made of molecules all forming the same angle to the surface normal. This angle is the one that maximizes the density of the monolayer; indeed the height of a monolayer is directly related to its density. While it is proven that DPN produces monolayers following such mechanism,[154] it was unknown whether DPN allows for the control of the density of the patterned SAMs and consequently of the orientation of the written molecules. We have shown that it is possible to stop the formation of the SAM at any point, starting from SAMs made of flat lying molecules all the way to densely packed SAMs made of molecules almost normal to the surface.

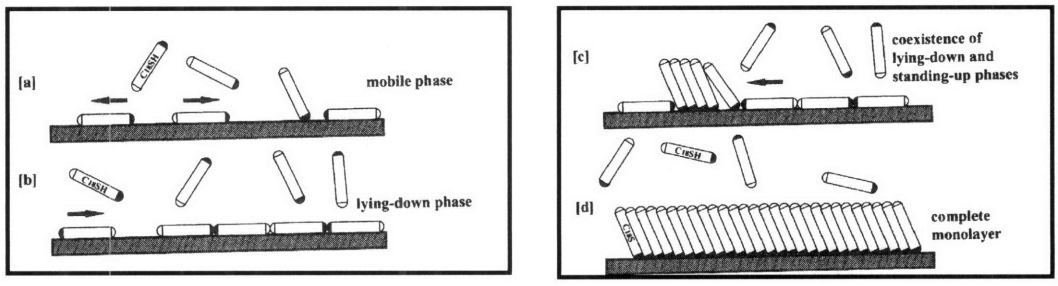

Figure 3.3: Schematic of monolayer formation. Molecules first assemble on the surface in a parallel conformation. As more molecules bind to the surface, the molecules reorient more parallel to the surface to maximize the number of energetically favorable bonds between the tail groups of the molecule and the surface.

In order to understand the relationship between DPN kinetics (i.e. writing speed) and monolayer formation kinetics, the height of the written SAMs was investigated. In particular, to include both monolayer density and molecular height in a single figure of merit, the concept of relative height is introduced. Relative height is defined as the measured height of a monolayer divided by the height of the densely packed monolayer assembled on a large and flat surface. To assure consistency when comparing height of monolayers all our experiments were performed on the same type of surface, flame annealed Au (111) thermally evaporated on freshly cleaved mica. Height information of the written features on the substrate (see for example figure 3.4) were obtained using a feature of our microscope analysis software that allows for averaging the height of areas specified by the operator. Thus the difference between the average height of the patterned areas and the averaged height of the surrounding gold substrate was measured. Internal controls were used to avoid errors or image artifacts and to quantify the error margins of our measurements. For instance, the height of the surrounding gold substrate was calculated in multiple spots of the image. For any given analyzed line, its height was calculated by selecting both the whole line and segments of it. Data was used only when all measurements agreed within 3 Å.

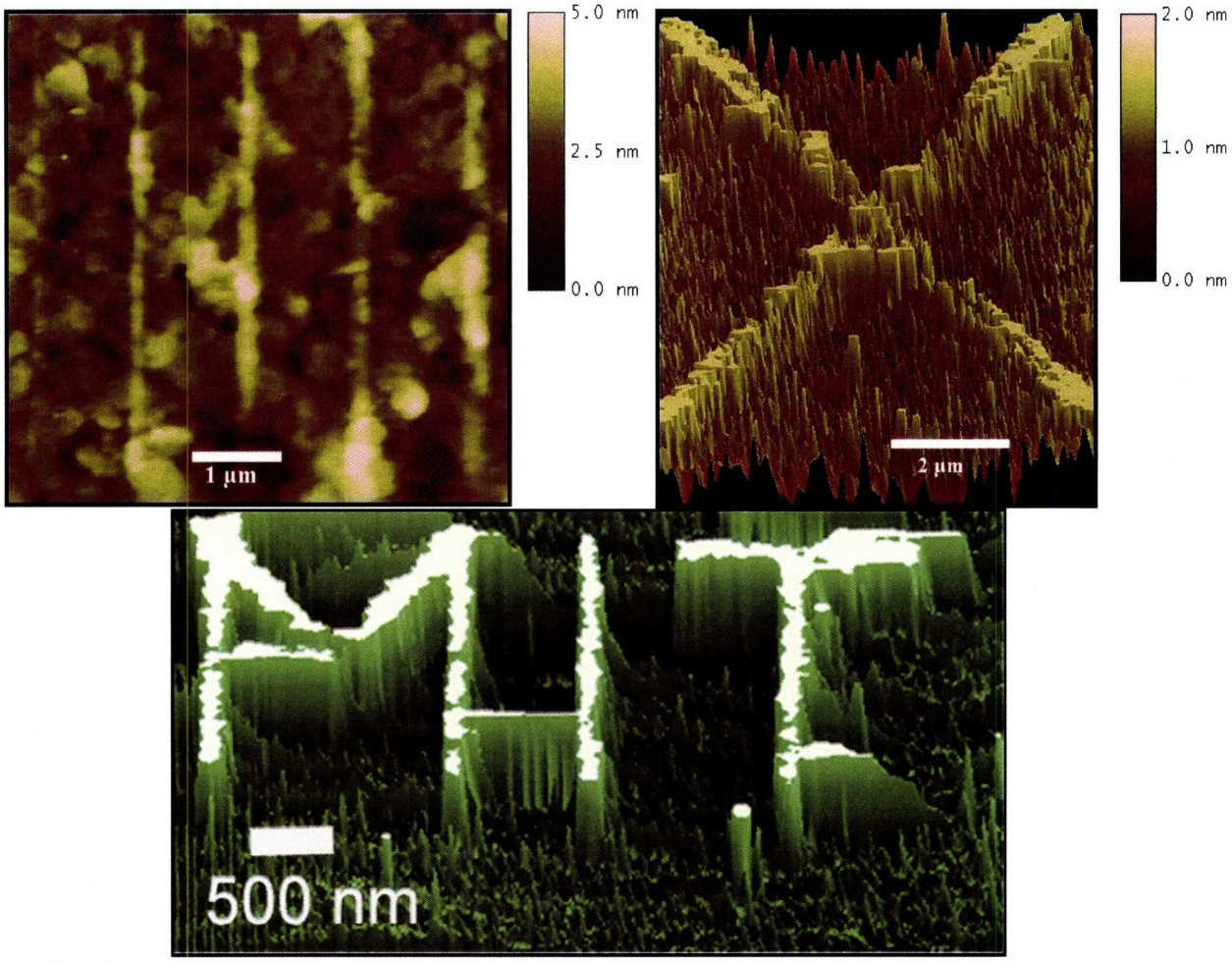

Figure 3.4: Examples of AFM contact mode height images of SAMs written via DPN on Au on mica substrates. (left) 5 parallel lines of ODT (right, bottom) 3-dimensional view of an "X" and "MIT" patterned with MHA.

As shown in figure 3.5 the height of dodecane thiol (DDT, CH_3-$(CH_2)_{11}$-SH) monolayers written in DPN strongly depends on the writing speed (inverse of time). An explanation for this behavior is that at high writing speeds there is not sufficient time to allow for either the nucleation of dense islands or their growth. Conversely when the tip moves slowly the monolayer is allowed more time to nucleate and grow. To date, we have never seen complete monolayer formation upon writing with the tip passing over the feature only once (i.e. single pass writing). The kinetics of this process are quite involved. The combined effect of the diffusion of molecules from the tip to the surface, $t^{1/2}$, together

with the monolayer formation kinetics[155, 156] is observed. Indeed, the height of the written features decays as $v^{-1/3}$ ($t^{1/3}$), with v= writing speed. Diffusion dominates at high velocities (short times; when $t^{1/3}$ is similar to $t^{1/2}$) while the Langmuir kinetics of monolayer formation[155, 156] become important at slow velocities (long times; when $t^{1/3} < t^{1/2}$). A reasonable consequence of these results is that most of the SAM formation happens when the water meniscus is above the written feature.

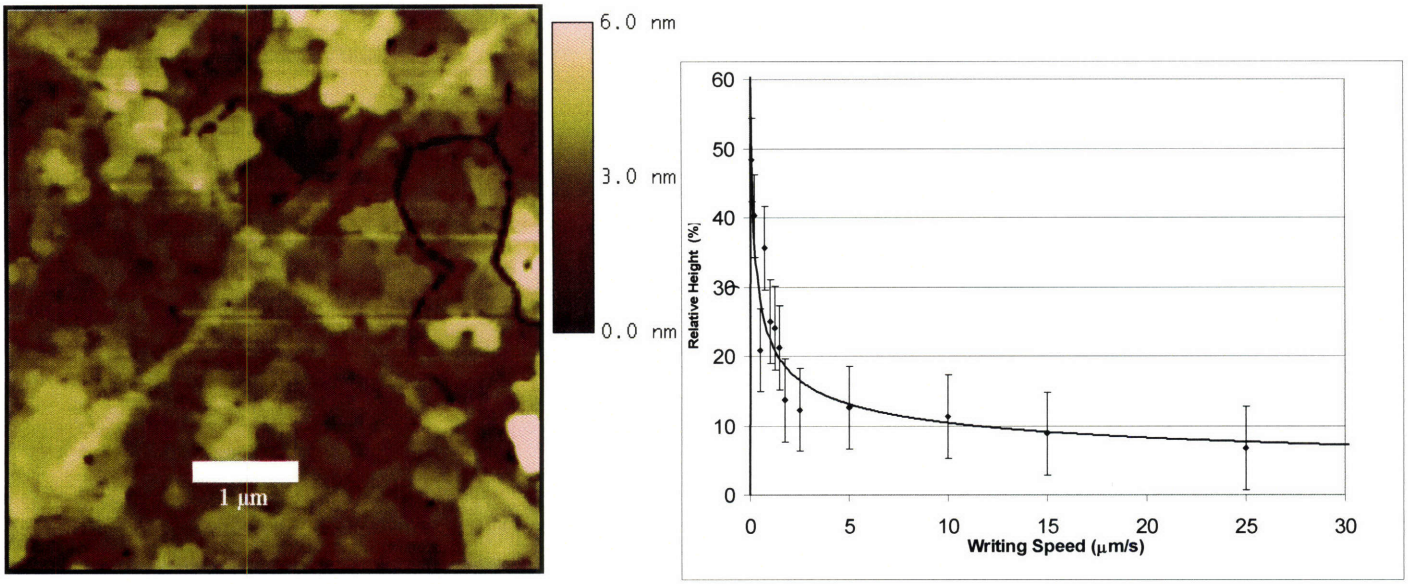

Figure 3.5: (left) AFM contact mode height image of an "X" patterned with DDT on Au on mica. (right) Plot of the relative height of DDT versus writing speed. The dots represent averages of the measured data and the line is a fit to $v^{-1/3}$. 100% relative height for DDT is 1.666 nm as given by reference 152.

Additional evidence for the proposed mechanism can be found in LFM images of features written with MHA, (HS-$(CH_2)_{16}$-COOH). LFM images of MHA wires patterned by DPN show high friction for wires written at slow speeds and low friction for those written at rapid speed. (figure 3.6) The reason for this behavior is that when quickly written, MHA monolayers consist of flat lying molecules,[1] and thus the AFM tip

[1] A similar interpretation of higher friction halos surrounding lower friction ODT (hydrophobic molecule) dots written by DPN has been given in reference 50. The higher friction part of the image was credited to prone lying molecules not as effective at reducing friction as the low friction standing molecules in the center of the dot. I also saw this

perceives the monolayer as composed of mostly hydrophobic methylenes. At slower speeds the written SAM is more dense and thus the AFM tip interacts primarily with the molecular end groups, the hydrophilic carboxylic acids.

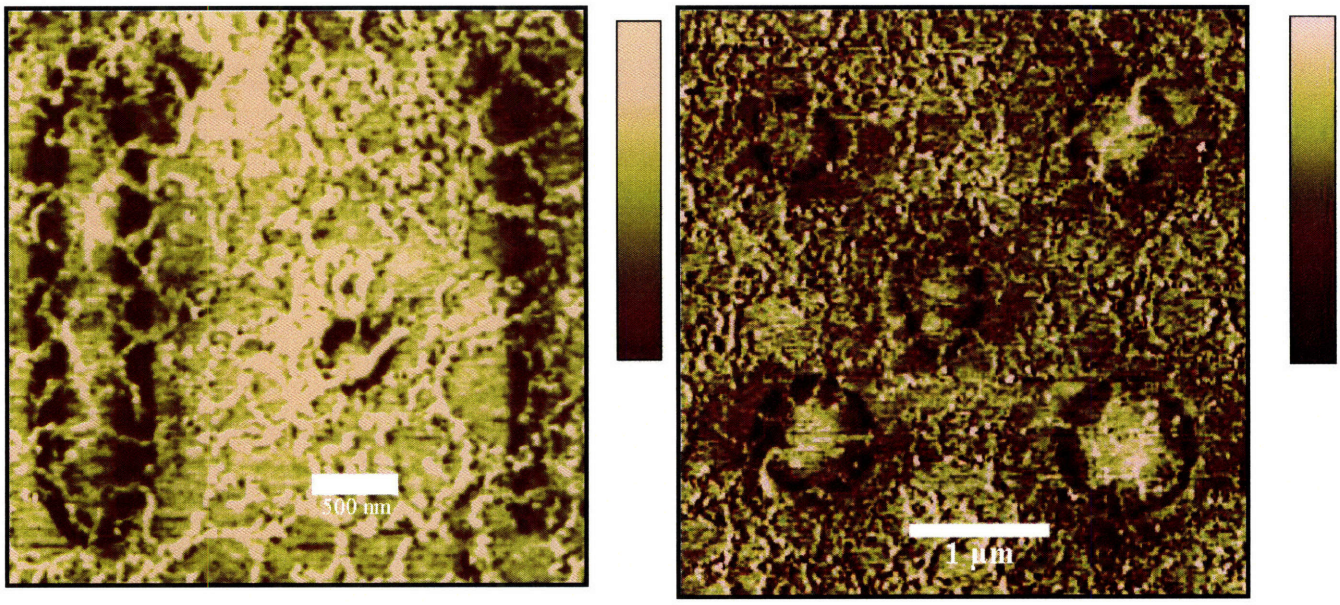

Figure 3.6: (left) Lateral force microscopy images of MHA patterns on Au on silicon. Two lines patterned with MHA by DPN at 0.25 µm/s (left) and 3 µm/s (right). The left line consist of densely packed molecules so the tip interacts with the hydrophilic carboxylic acid groups; the line appears high friction. The right line consists of molecules lying parallel to the surface so the tip interacts with the hyrdrophobic methylene groups; the line appears low friction.
(right) Dots patterned with MHA showing a densely packed interior (high friction); only a few molecules diffuse to the outer ring (low friction) and these loosely-packed molecules have a conformation parallel to the surface.

To further test this idea, the kinetics of SAM formation in DPN for different molecules were compared. (figure 3.7) These molecules were chosen to have similar diffusion rates but different rates of monolayer formation. First ODT, (CH_3-$(CH_2)_{17}$-SH) was compared to DDT, (CH_3-$(CH_2)_{11}$-SH) and octanethiol (OT, CH_3-$(CH_2)_7$-SH). It is known that shorter thiolated molecules form better monolayers more rapidly;[152] due to the fact that the energetic difference between an all *trans* conformation and a conformation with one

behavior in our own lab with the writing of MHA dots, where the core appeared high friction and a low friction halo surrounded the dot. (Figure 3.7)

gauche defect gets larger as the molecule gets shorter. SAMs are composed of mostly *trans* molecules, thus they form faster when starting from molecules that are already in such conformation, i.e. shorter ones. Compared to ODT we noticed that DDT forms shorter SAMs at higher speed and the opposite at slower speeds. At low writing speeds the shorter molecule, DDT, forms SAMs with higher relative height, i.e. better packed. At high speed SAMs composed of flat lying molecules will always form, but the ODT SAMs appear higher because of the conformational defects in the molecules that do not allow for perfect alignment to the surface plane. In the case of OT, writing was almost impossible due to the fact the molecules tend to crystallize either on the tip or on the substrate, showing that it is not easy to write in DPN with molecules that are too short. Results similar to the DDT, ODT comparison were obtained when comparing MHA to mercapto-undecanoic acid (MUA, HS-$(CH_2)_{10}$-COOH). It should be noted that alkane thiols achieve better relative heights when compared to carboxylic acid terminated molecules, probably due to the fact that the latter have slower kinetic rates of formation due to their head group interactions.

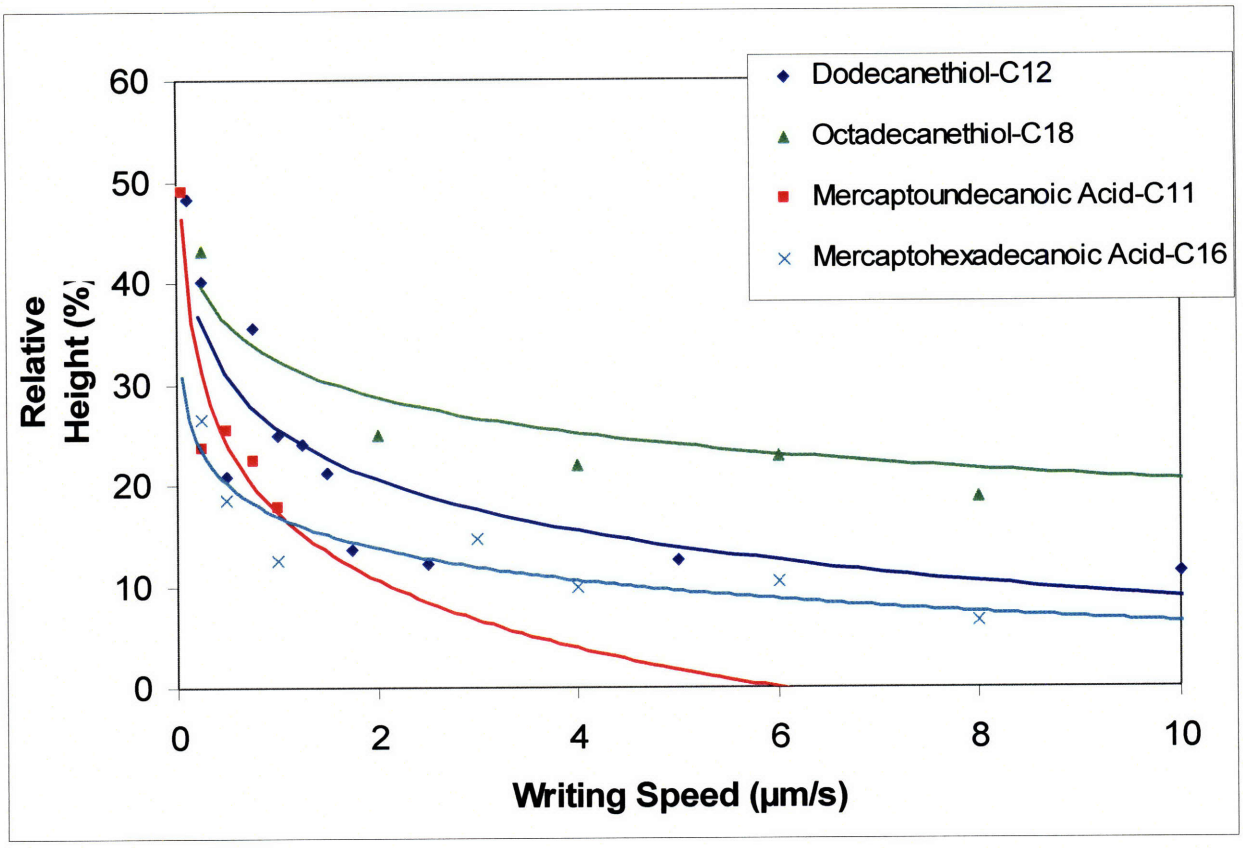

Figure 3.7: Plot of the relative height of written patterns in DPN versus writing speed. The dots represent averages of the measured data and the continuous line is a fit. 100% relative height is 1.666 nm for DDT, 2.326 nm for ODT, 1.591 nm for MUA and 2.117 nm for MHA as found in reference 152.

In order to better understand the mechanism of monolayer formation in DPN we analyzed AFM height images of features written in multiple passes. As shown in figure 3.8, the height of lines written at different speeds plateaus at the same value at high number of passes. At slow speeds, most of the monolayer formation happens in the first few passes and it looks like additional passes do not affect the height of the monolayer. The only observable effect is that the lines become wider and wider at every pass. At high writing speeds the nucleation and growth keeps happening at every pass up to the moment when the plateau relative height is achieved. An additional insight in this writing mechanism has been studied looking at the height of features written in two passes in which the speed

of the first and the second pass is different. As shown in figure 3B when the first writing pass is slow the monolayer height achieved is almost independent of the speed of the second pass. The faster the first pass, the more the height becomes dependent on the second pass speed, consistent with a nucleation and growth mechanism.

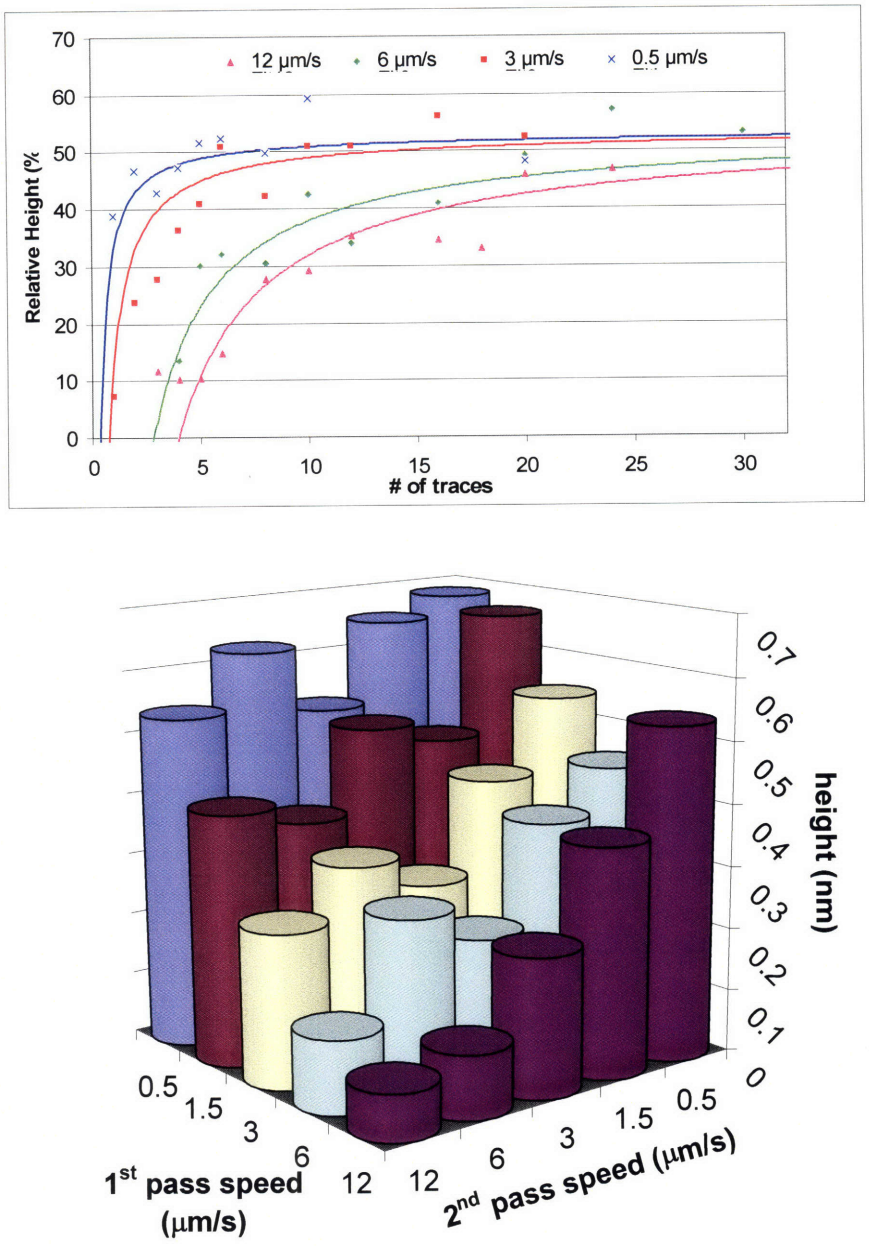

Figure 3.8: (top) Plot of relative height vs number of traces for a series of ODT wires (5 µm in length) written via DPN. The curves are present to guide the eye when comparing lines written at different speeds. This plot shows that at a large number of traces the same relative height is achieved when writing at different speeds. (bottom) Height of ODT wires written in two traces plotted against the speed of the first and the second trace. When the first writing trace is at a slow speed most of the nucleation occurs in that stage, thus the additional height gained during the second trace is almost independent of writing speed. This shows that the growth occurs more rapidly than the writing speeds we tried.

DPN can be used to write features that further direct the assemblies of other molecules or materials.[53, 74, 157] To further test the idea that writing speed determines molecular orientation, we have studied the ability of DPN written monolayers to direct the assembly of suitably terminated nanoparticles. A densely packed monolayer has the upper surface homogeneously composed of the molecular end groups, while, at lower densities, the end group concentration varies along the surface. MUA coated nanoparticles were used as probes for the homogeneity of the carboxylic acids terminal groups in MHA monolayers. Such assembly can happen only through the interaction of the carboxylic acids that compose the outer layer of the nanoparticles with the carboxylic acids end groups of the MHA monolayer. MUA coated nanoparticles, 3.8 nm in diameter, were assembled on wires written at different speeds by placing the substrate in an ethanol solution of such particles for 72 hours. It was found that they assembled selectively on patterns written at speeds lower than10 μm/s. Moreover, the slower the speed the more uniform the coverage (as show in figure 3.9), clearly confirming the nature of the underlying uniformity of the SAM orientation.

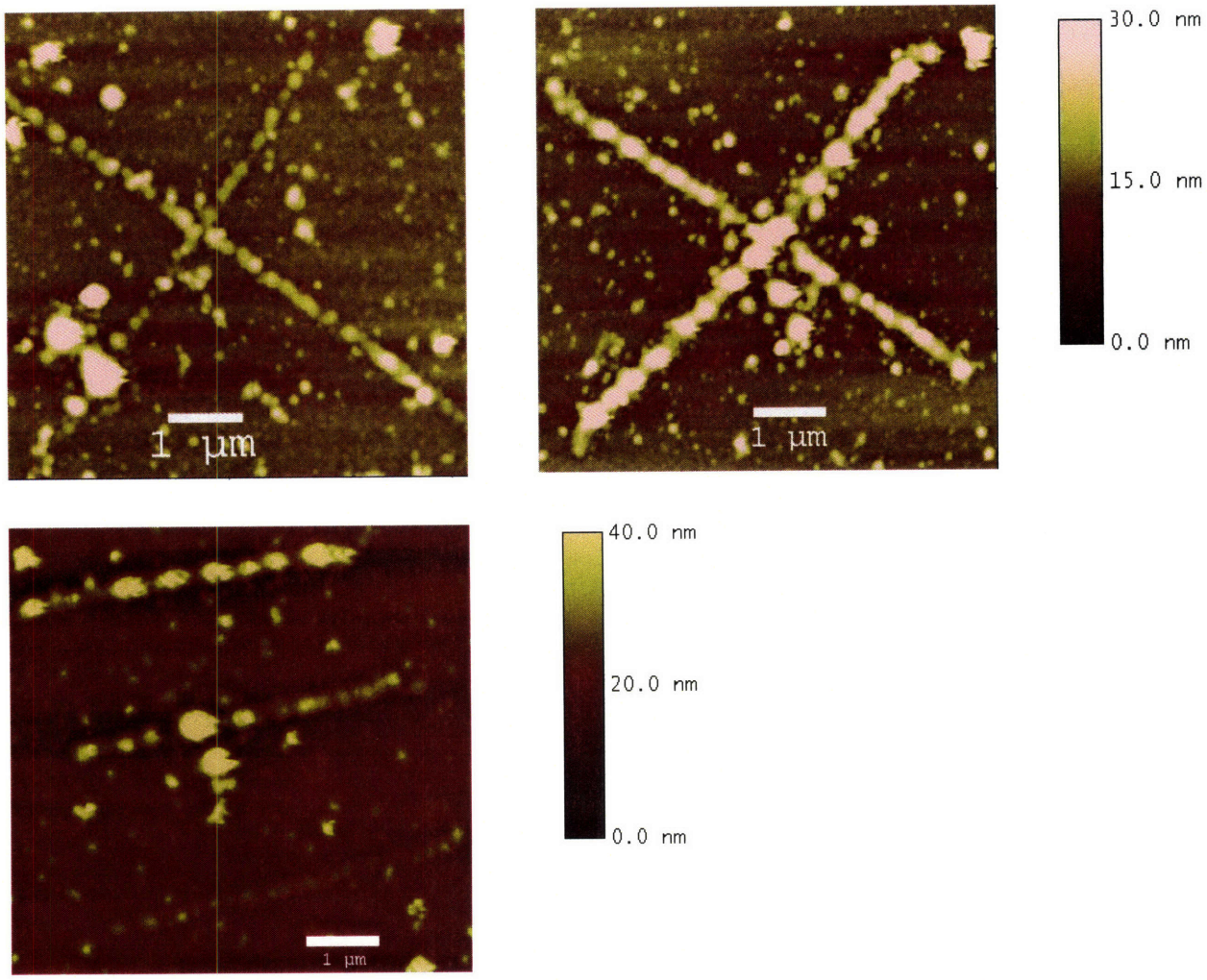

Figure 3.9: Tapping mode AFM height images of patterns of self-assembled Au nanoparticles on top of identically shaped features of MHA written with DPN. (upper left) "X" patterned at 5 µm/s, (upper right) "X" patterned at 1 µm/s. (Bottom left) Lines written at (top) 1 µm/s, (middle) 3 µm/s, and (bottom) 5 µm/s. These images clearly show the effect of writing speed and consequently of SAM quality on the ability to direct further self-assembly of the nanoparticles.

Controlling the morphology and the density of the written self-assembled monolayers is critical for the efficient etching of Au nanostructures. This method consists of using written ODT monolayers as masks against gold etching in a ferrocyanide solution. Patterning the ODT at different writing speeds on the same substrate results in monolayers of different densities. After patterning, the substrate is etched in a ferri/ferrocyanide etchant.[158] Tapping mode of AFM images of the resulting gold features reveal that features that were patterned slowly, i.e. were covered by a more dense SAM had a higher remaining thickness (due to less etching through the dense resist) than those covered with a more disordered SAM. (figure 3.10) In order to fabricate conductive metal wires, it is necessary to start with a SAM that is as dense as possible. In the case of less dense SAMs, wires that are either not percolated or with resistivities that are orders of magnitude higher then bulk gold are obtained. This is probably due to the etchant attacking at the boundary between dense nucleation centers and regions of flat lying molecules. A 43 μm long wire with a 1 μm x 20 nm cross section obtained by etching a gold film protected by a dense ODT SAM written at 5 μm/s with 20 retraces[2] showed a resistivity of $3*10^{-8}$ Ωm, just 30% more then bulk gold.[159] (figure 3.11)

[2] This is a condition that was known to form best possible relative height SAM.

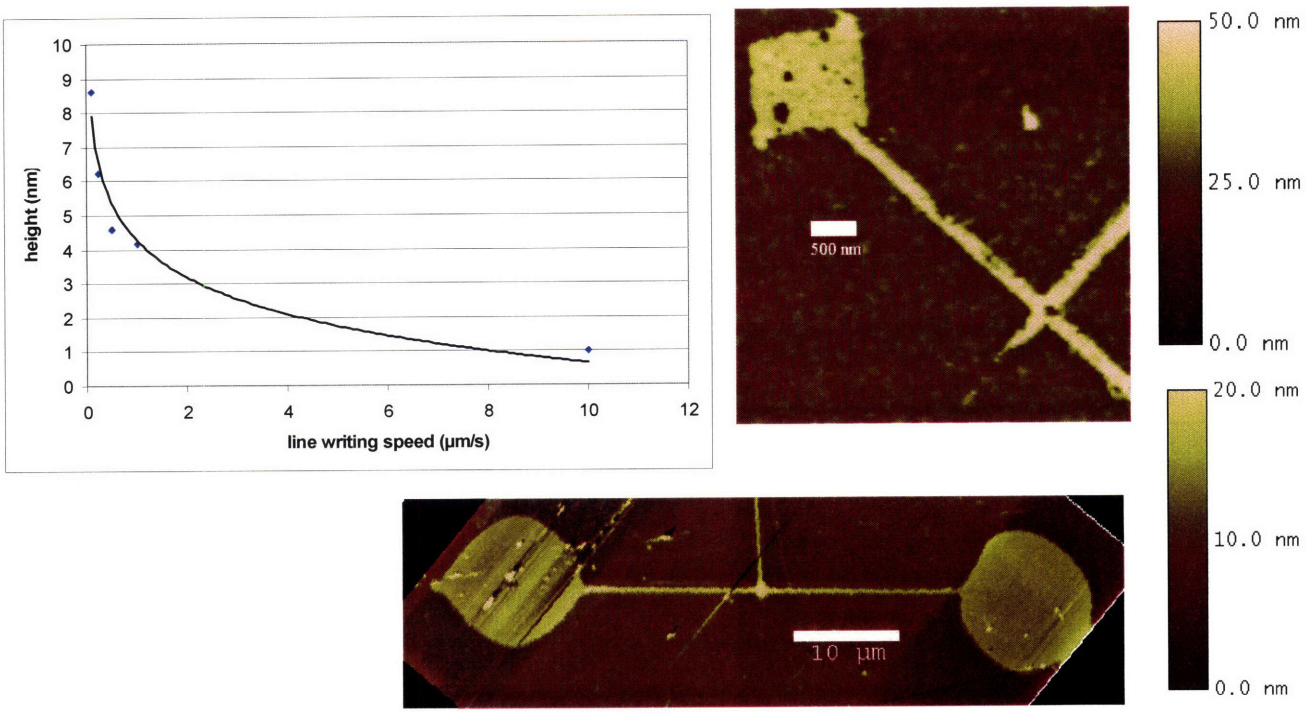

Figure 3.10: (Upper left) Plot of the height of the remaining Au after etching as a function of the writing speed used to pattern the ODT resist with DPN. SAMs written at lower speeds were more dense and served as better resists; more Au remained after etching. (Lower left, upper right) Tapping mode AFM images of gold wires formed by patterning an ODT resist with DPN and etching with a ferrocyanide etchant.

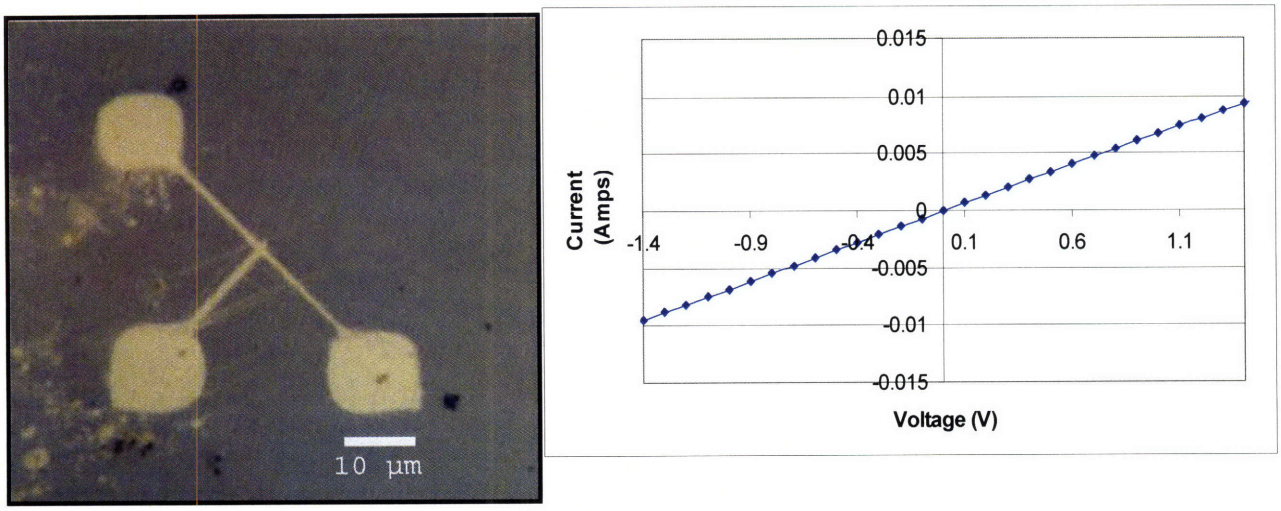

Figure 3.11: (left) Optical image of conductive Au wires formed by patterning an ODT SAM with DPN that served as a resist on a Au on Si substrate. (right) Current-Voltages characteristics for the wire showing a resisitivity of $3*10^{-8}$ Ω–m.

3.1.2 Effect of humidity and contact force on DPN

While writing speed is the most critical factor in the patterning of a good SAM, relative humidity and the contact force between the AFM tip and the substrate also play a major factor in the writing of SAMs. The importance of relative humidity and transport through the water meniscus is a topic of great debate in the DPN community.[44, 59] A consensus has been reached that for the transport of hydrophobic molecules, such as ODT, the transfer rate of molecules form the tip to the surface is unaffected by relative humidity. Whether or not the presence of a water meniscus is necessary for the writing of these molecules is still highly debated. It is well agreed that humidity has an effect on writing hydrophilic molecules, such as MHA at very high relative humidities (>50%) where transport through the large water meniscus is the dominant mechanism. At lower relative humidities, however, the transport mechanism is debated.

We have used a humidity box manufactured by COY laboratories to test the effect of humidity on DPN. Tests writing dots, lines and boxes have shown little difference when writing MHA at humidities ranging from 17% to 43%. The major effect induced by humidities in this range is their effect on the attractive forces between the tip and the substrate. When a sharp tip is evenly coated with MHA, their exits a very low attractive "stiction" force between the tip and the substrate, usually between 5-10 nN. This "stiction" force is quantified by measuring the force on the tip felt as it retracts from the surface. The force is caused by the pull of the water meniscus on the tip. With hydrophilic molecules on the tip, the force is increased. Certain tips show huge attractive forces, 50-100 nN, possibly due to a blunt tip or an uneven coating with MHA. When using these tips to pattern boxes of MHA or ODT is it common to see large regions of negative height where the image has been patterned. These trenches are likely caused by the rapid deposition of molecules that are then pushed to the edges of the box by the scanning AFM tip. The resulting pattern consists of piled multilayers at the edges of the box. (figure 3.12) They may also be the result of surface contamination. Surfaces that have an excess amount of organic contamination are plowed by the AFM, even at low forces. The organic film above the gold surface is pushed to the edges. It is unclear whether the box itself is patterned with a SAM in either scenario. The result of AFM plowing can be seen in both etching and self-assembly applications. When a "plowed" patterned substrate is etched, tiny gold channels appear where lines were patterned. The AFM has deposited excess monolayer/organic film, which serves as a resist for etching. The line itself, however, is etched away as it is not covered with an adequate SAM. When self-assembling on top of a plowed substrate, gold nanoparticles preferentially

absorb at the edges of the boxes where the most MHA molecules are located. The patterned box appears significantly lower in height than the immediate surrounding substrate.

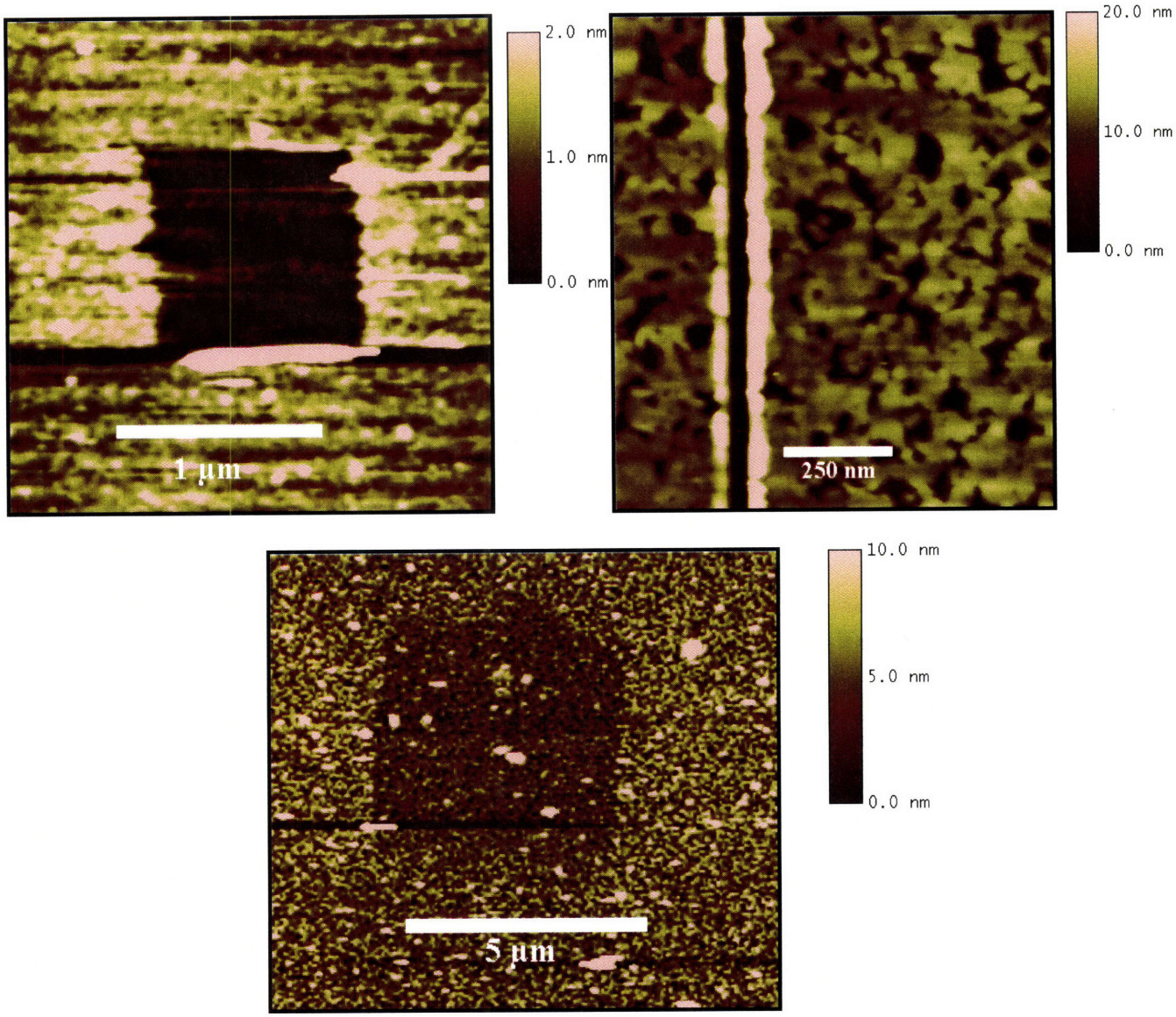

Figure 3.12: Effect of AFM plowing in DPN. (upper left) Contact mode AFM image of MHA patterned box showing negative height due to the piled MHA molecules and organic contamination pushed to the sides of the box by the AFM tip. (upper right) Effect of etching a plowed line patterned with ODT by DPN, creating a channel in the substrate; tapping mode AFM image. (bottom) Self-assembly of Au nanoparticles on a plowed box patterned with MHA; tapping mode AFM image. Nanoparticles assemble on the edges of the box, making the box appear negative in height.

DPN has been used for other applications including a molecular stamping method, directed assembly of viruses, directed assembly of Au nanorods, directed assembly on

SiO_2 surfaces, and the patterning of nanometer scale gold wires. This work is described in Appendix B.

3.2 Directed Assembly on Au Surfaces

Chemically directed assembly (CDA) is a potentially valuable technological tool for the placement of nanoscale materials on surfaces and devices. The formation of thiol based monolayers on Au surfaces has been well-studied.[150] There exits thiol molecules with a variety of functional groups which can be used for CDA. This makes the use of gold surfaces with patterned thiolated molecules a great system to study the chemically directed assembly of nanomaterials. Potential patterning on devices with Au wires makes this technique technologically relevant.

There are two approaches to CDA; one in which assembly is driven by ionic or weaker van der Waals attractions,[69, 71, 73, 79, 82, 84, 86, 160-162] the other in which the formation of covalent bonds is the driving force.[6, 70, 77, 162-167] The former strategy has faster kinetics due to long range electrostatic attractions and allows for the assembly of ordered arrays, due to the reversibility of the bonds formed. These reversible bonds may be necessary for sensing applications. The latter has the advantage of being based on strong bonds that are more durable. Electronic applications involving high electric fields may require this type of assembly.

3.2.1 Assembly using Ionic and Van Der Waals Attractions

Due to the relative ease of patterning MHA and the number of different chemistries which could be applied to its carboxylic acid head group, MHA was chosen as the first molecule to be used for CDA of nanoparticles. In section 3.1.1, self-assembly based on Van Der Waals attractions of two neighboring carboxylic acid groups was demonstrated. This type of bond, however, produced very inconsistent assembly, resulting in nanoparticle multilayer formation on some surfaces but no assembly on others. An ionic bond provides more reliable assembly. The ionic bond between carboxylic acid groups (COO-) and M^{2+} ions, where M is a divalent metal such as Ni or Cu can be used to direct assembly of nanoparticles.[72] (figure 3.13) MHA SAMs were patterned by DPN on a Au surface. The gold surfaces were then immersed in a 0.1 M $Ni(NO_3)_2 \cdot H_20$ water solution for 24 hours. The surfaces were soaked in DI water for 5 minutes to remove excess Ni^{2+}. At this point, the surfaces consist of Ni^{2+} ions attached to carboxylic acids by ionic bonds. The substrate was then immersed in an aqueous solution of nanoparticles with mercatoundecanoic acid (MUA) ligands for 5 hours. The goal is to sandwich the Ni^{2+} ions with two carboxylic acid groups, one from the MHA monolayer, one from the ligands of the nanoparticle. Figure 3.14 shows the patterned lines and boxes of Au nanoparticles. Patterns imaged by tapping mode AFM before and after self-assembly showed average heights of the features range from 0.2 nm - 1 nm. A large amount of non-specific binding of nanoparticles on the surrounding gold surface makes the heights much lower than would be expected. Before self-assembly, the pattern could be visualized in the phase image only, while after subsequent nanoparticles assembly, the patterns are clearly visible in the height image, proving that the height of the feature comes from the nanoparticles and not the MHA pattern.

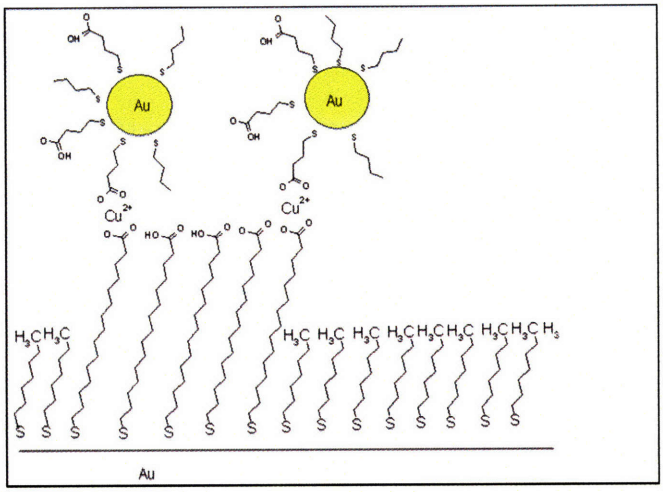

Figure 3.13: Strategy for chemically direct assembly of nanoparticles on an MHA monolayer using divalent metal ions.

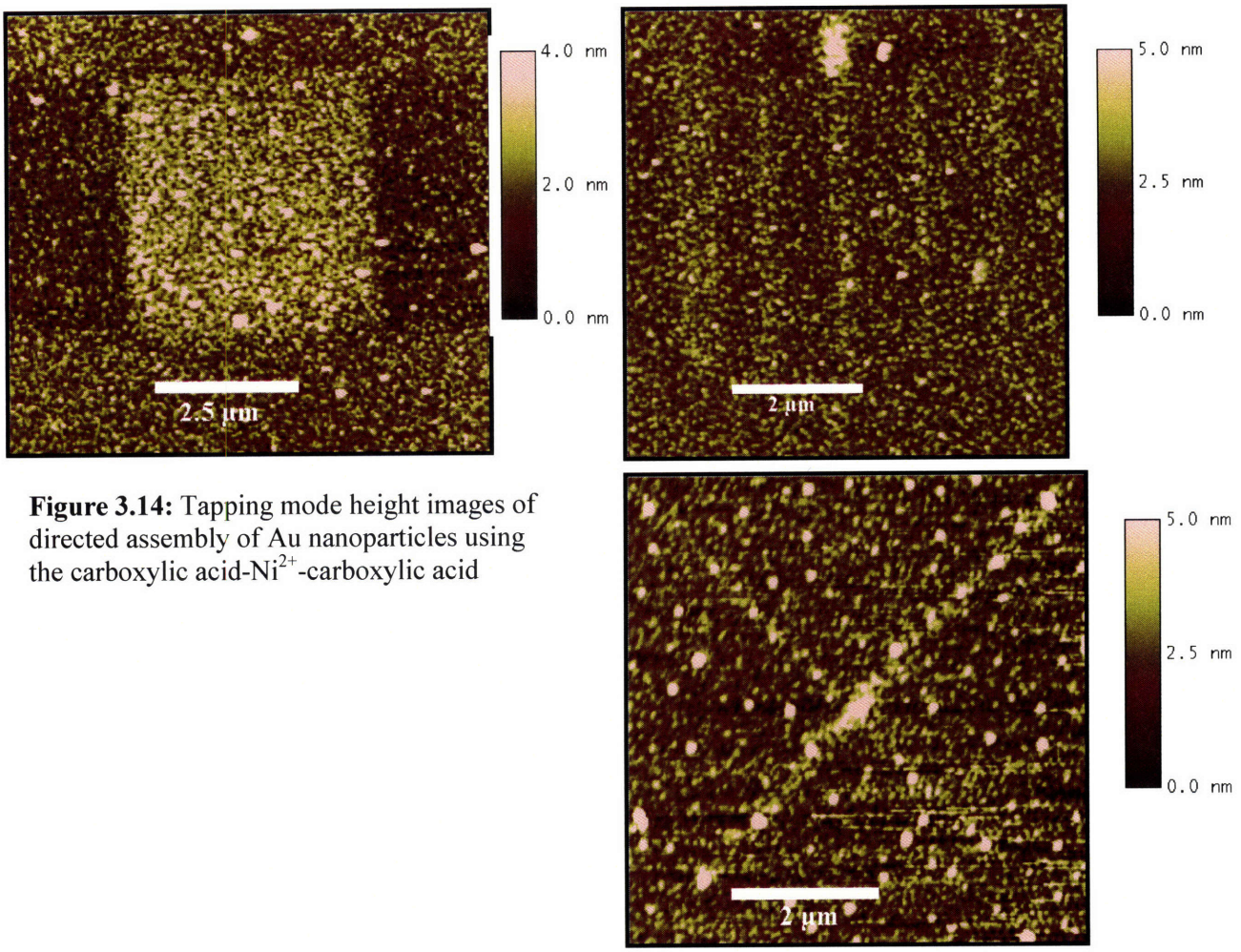

Figure 3.14: Tapping mode height images of directed assembly of Au nanoparticles using the carboxylic acid-Ni^{2+}-carboxylic acid

Five steps were made to improve the ionic bond directed self-assembly. 1.) An octane thiol monolayer was formed around the patterns immediately following the DPN of MHA, by immersion in a 4 mmol solution of OT in ethanol for 1-3 hour. After this passivation step, the remainder of the Au surface is covered by the non-reactive $-CH_3$ groups, which resist the non-specific binding of nanoparticles. The short SAM formation time (1-3 hours) allows for a decent SAM to be formed but is too short of a time for significant place exchange between the patterned MHA SAM and the OT molecules. The immersion in the solvent may also allow for the reorientation of the patterned MHA molecules, allowing for a better quality monolayer with more carboxylate groups on the surface. 2.) The amount of immersion time in the metal ion solution was reduced to10 minutes and the amount of time in the nanoparticle solution was reduced to 25 minutes to further reduce non-specific binding. 3.) Cu^{2+} ions were also substituted for the Ni^{2+} ions used previously, as Cu^{2+} has a higher binding affinity to carboxylic acid groups. 4.) The nanoparticles used were treated with HCl before being patterned. The HCl protonated the carboxylic acid groups. This made it difficult for nanoparticles to bind to each other through an MUA-alkaline ion-MUA assembly. The Cu^{2+} ion still had the necessary strength to remove the hydrogen atom from the carboxylic acid group when the nanoparticle was close enough to the surface to self-assemble. 5.) Gold on silicon surfaces were patterned with DPN immediately after the Au evaporation on Si. This prevents contamination of the Au surface with carbonaceous compounds, allowing for the formation of better MHA monolayers and thus more consistent assembly.

The MHA patterned features were imaged with contact mode AFM after passivation with OT. (Figure 3.15and 3.16) The patterned MHA features appear 1 nm higher than the OT background, in good agreement with the difference in length of the two molecules. After Cu^{2+} ion and nanoparticle assembly, the features are re-imaged with contact mode AFM. The features increase in height by 3-4 nm. Based on the size of the gold nanoparticles (core size plus twice the ligand length, ~8 nm total size for the nanoparticles used in this study) and a simple geometrical arguments, it can be concluded that a 37.5-50% nanoparticle monolayer is assembled on the MHA features. (figure 3.17) Very little non-specific assembly is seen on the passivating OT layer. Figure 3.16 demonstrates that assembly can be directed on features as small as ~100 nm. Figure 3.18 shows tapping mode height images of nanoparticles assembled on a 1 μm by 1 μm square and an array of dots. Individual nanoparticles showing limited hexagonal packing could be imaged with tapping mode phase imaging.

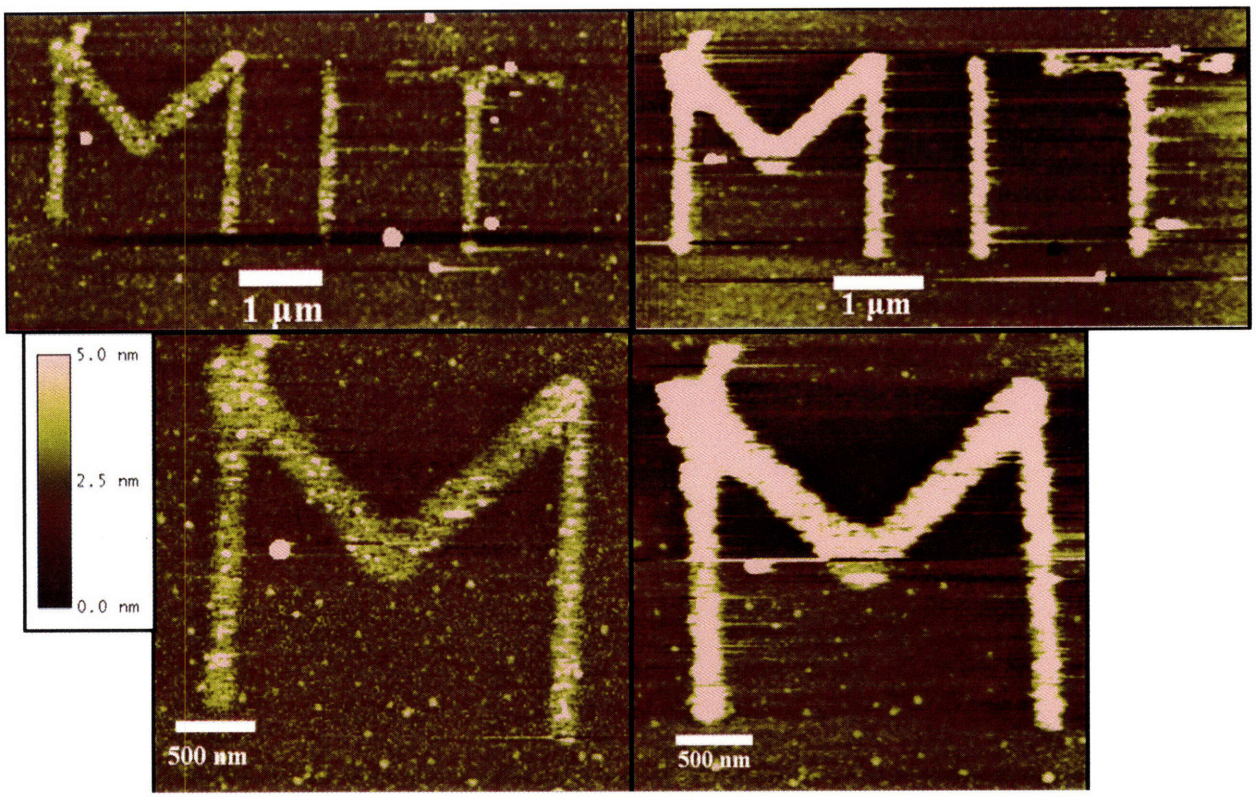

Figure 3.15: (left) MHA features patterned by DPN surrounded by an OT SAM. (right) Feature height increases by 3-4 nm after specific assembly of nanoparticles on Cu^{2+} ions assembled on the MHA features.

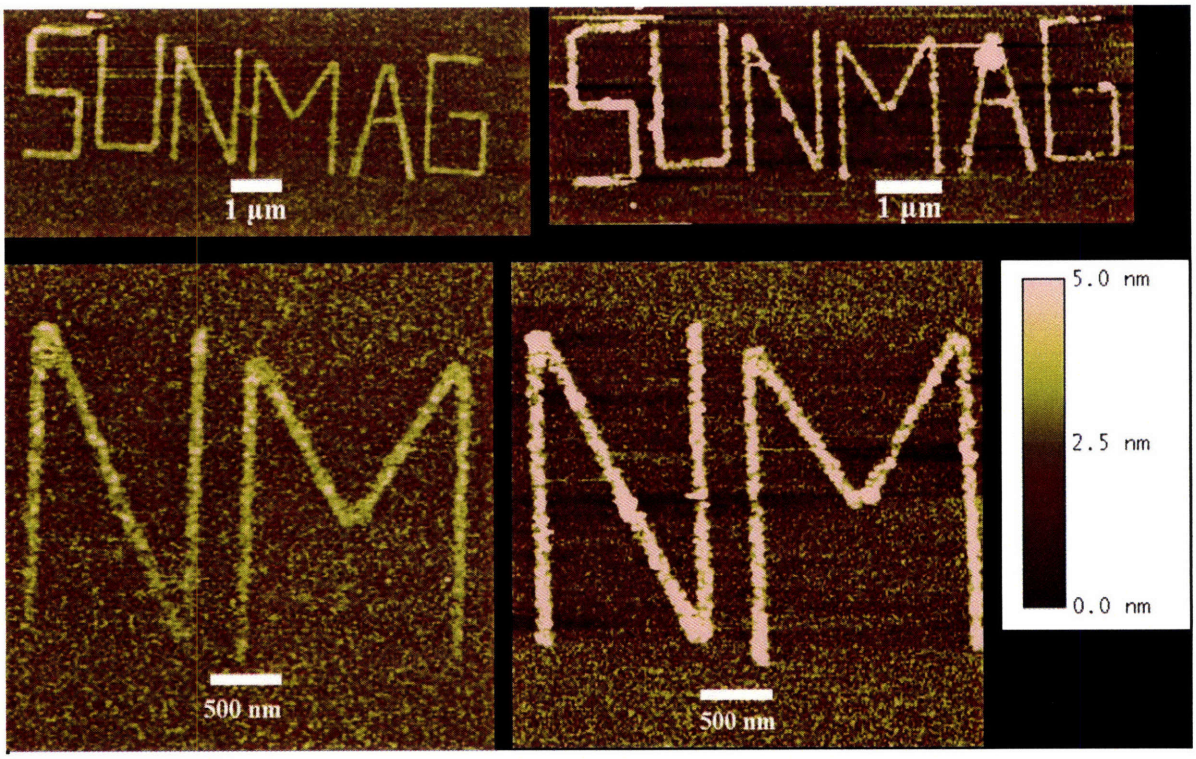

Figure 3.16: Sub-100 nm MHA features patterned by DPN surrounded by an OT SAM (left) before and (right) after nanoparticle assembly using Cu^{2+} ions.

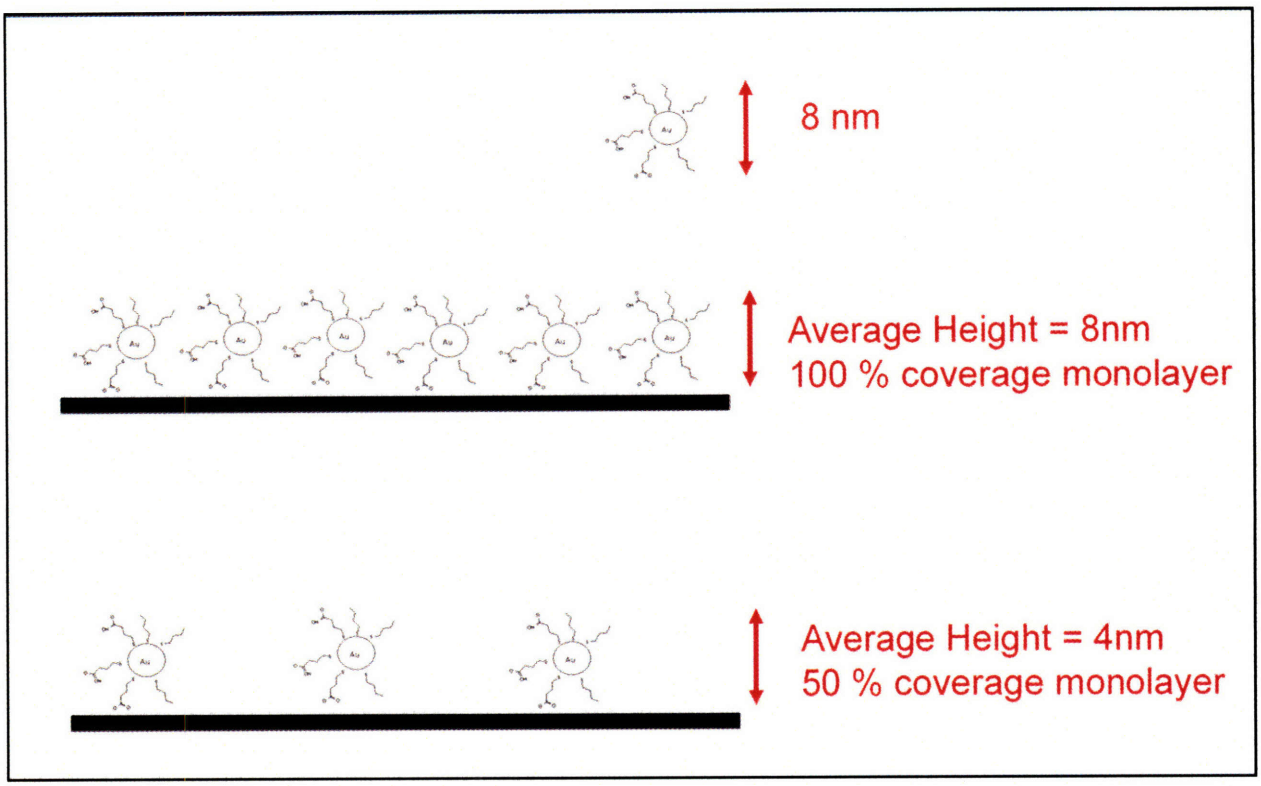

Figure 3:17: Schematic of geometrical argument used to determine nanoparticle monolayer coverage from the AFM average height measurements of assembled features.

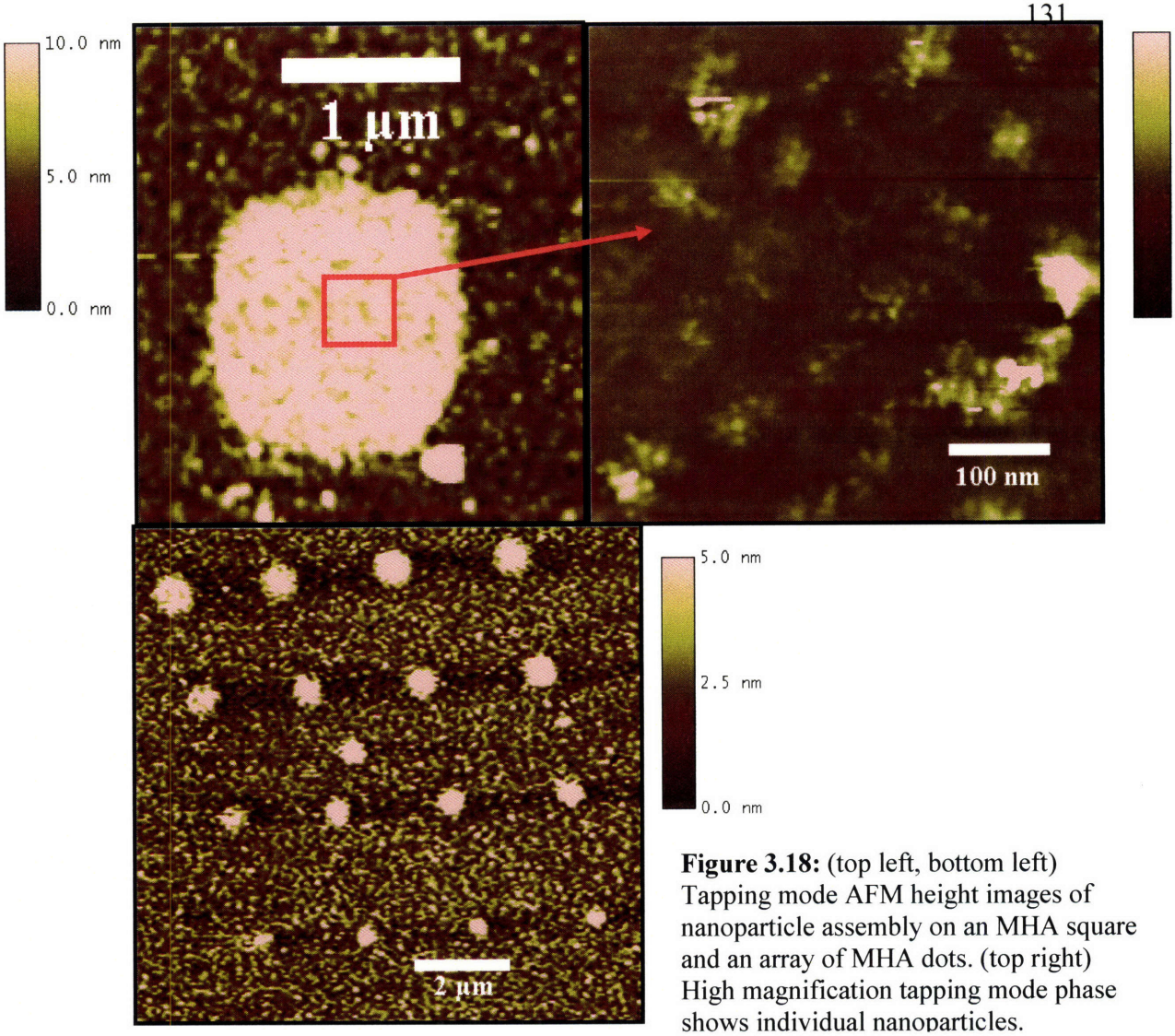

Figure 3.18: (top left, bottom left) Tapping mode AFM height images of nanoparticle assembly on an MHA square and an array of MHA dots. (top right) High magnification tapping mode phase shows individual nanoparticles.

While ionic based CDA has the advantage of high speed due to electrostatic attraction, two major disadvantages may hinder its use for some applications. Weak ionic bond strengths may not withstand the high electrical fields needed for some applications. Due to the use of charged particles, there exists an electrostatic repulsion, between particles. This limits the amount of nanoparticle assembly; in fact, no ionic based assembly with > 50% nanoparticle coverage monolayer has been realized.

3.2.2 Assembly Using Covalent Bonds

3.2.2.1 Assembly using urethane linkages

Highly reactive isocyanate groups can be used in combination with surface bound alcohol groups to form urethane linkages. In this method, mercaptoundecanol (MUD, HO-$(CH_2)_{11}$-SH) is patterned on the surface using DPN. A diisocyanate molecule is then assembled. One isocyanate group on the molecule reacts with the surface bound alcohol group to form a urethane linkage. The second isocyanate group now forms the surface of the monolayer and can react with a nanoparticle functionalized with an alcohol terminated ligand such as MUD or mercaptohexanol. (MH, HO-$(CH_2)_6$-SH). (figure 3.19). Isocyanate reactions must be carried out in an aprotic dry solvent to avoid unwanted reactions, so all reactions were carried out in dry DMF.

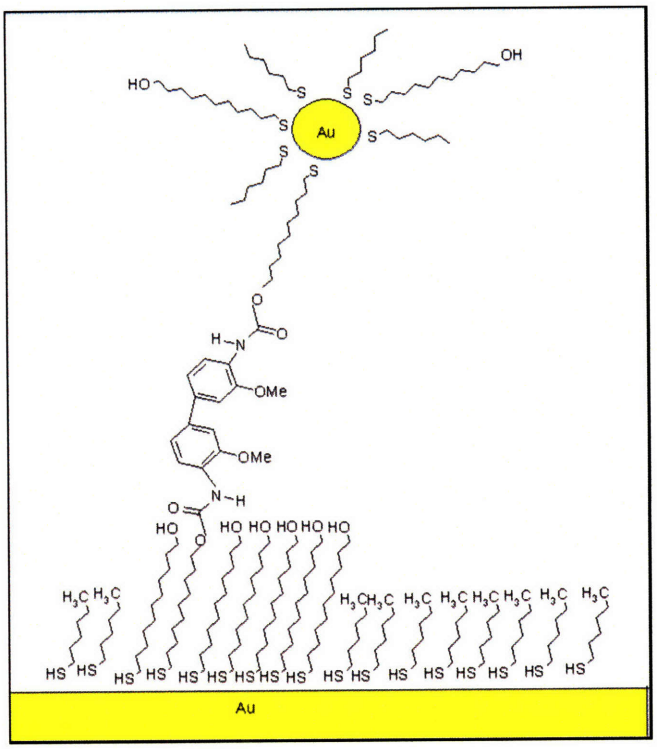

Figure 3.19: Schematic of covalent based nanoparticle assembly on a MUD monolayer using Dimethoxybiphenyldiisocyanate (BPDI).

This assembly strategy required the patterning of MUD using DPN. DPN patterning MUD had not been previously reported in the literature. The solution method of patterning proved impossible with MUD. Vapor deposition at a temperature of 50°C for 30-35 minutes with tips very close to the solid molecule (<1 cm) allowed for loading of the tip with MUD. Patterning of sub-100 nm features of MUD, and patterning of MUD features in registry with MHA features is shown in figure 3.20. The ability to pattern features of different molecules in registry with one another allows for the patterning of two types of nano-object on the same substrate using different assembly chemistries. While this method is not explored further here, it has valuable research and technological applications.

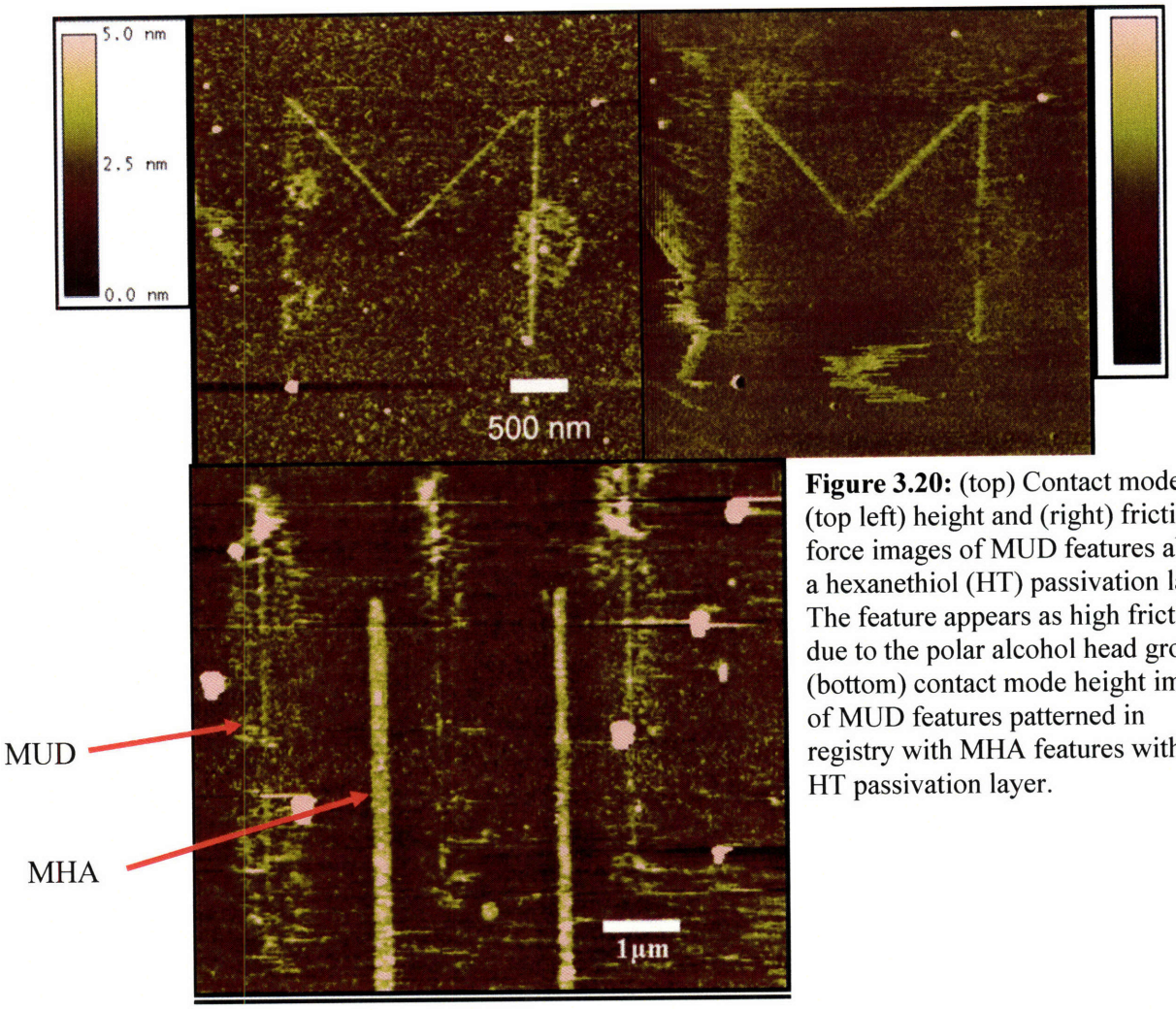

Figure 3.20: (top) Contact mode (top left) height and (right) frictional force images of MUD features above a hexanethiol (HT) passivation layer. The feature appears as high friction due to the polar alcohol head group. (bottom) contact mode height image of MUD features patterned in registry with MHA features with an HT passivation layer.

After passivation with a hexanethiol (HT) monolayer to prevent non-specific absorption,. the surfaces are exposed to a concentrated solution of dimethoxybiphenyldiisocyanate (BPDI), followed by immersion in solution of nanoparticles functionalized with mercaptohexanol. A large amount of non-specific absorption is found on the surface. A possible explanation is that both isocyanate groups of BPDI may bind to the surface, linking two MUD molecules but leaving few groups for the assembly of nanoparticles.

An improvement to this method was made by first immersing the nanoparticles into a solution of BPDI. The concentration of BDPI was selected so there would be a large excess of BPDI for every mercaptohexanol ligand on the nanoparticle. Every MH ligand should quickly encounter a BPDI molecule and bind to one of its isocyanate group. BPDI groups will not have the opportunity to bind to two MH ligands on the same nanoparticle or to crosslink nanoparticles, as all the MH groups will have already reacted. The patterned surface is then be immersed into the nanoparticle-BPDI solution, allowing for surface bound alcohol groups to react with the nanoparticles which now ligands terminated with isocyanate groups.

While this method showed less non-specific absorption of nanoparticles, only weak nanoparticle coverage (10-20%) monolayers are observed. (figure 3.21) Ultrasonication removes an even higher percentage of nanoparticles, which suggests that strong covalent bonds are not realized. A likely cause of the failure is due to the high reactivity of isocyanate groups with water. Unless solvents can be kept completely dry, the isocyanate group will be transformed before any reaction with surface bound alcohol groups can occur. This leads to poor assembly by weak non-covalent interactions, as evidenced on flat Au surfaces here and in the device based assembly described in section 3.2.2. Due to the difficulty of operating under extremely dry conditions, other means of covalent assembly were explored.

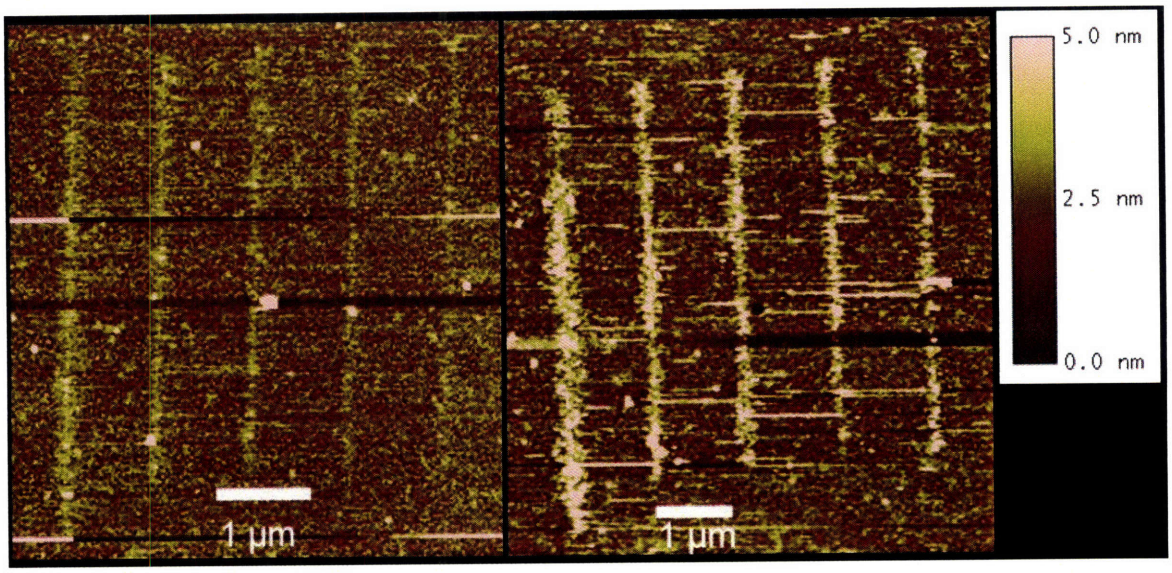

Figure 3.21: (left) Contact mode AFM image of MUD features surrounded by a hexanethiol passivation layer. (right) After nanoparticle assembly feature height increases by 0.5- 1nm, suggesting a poor coverage nanoparticle monolayer.

3.2.2.2 Assembly using amide linkages

The chemically directed assembly of gold nanoparticles via covalent amide bonds is a second strategy used in this work. Gold surfaces were patterned with mercaptohexadecanioc acid (MHA) using dip pen nanolithography (DPN) and micro-contact printing (µcp). A diamine molecule was using to link the surface bound carboxylic acid group to nanoparticle ligands with terminal carboxylic acid groups via two amide linkages.[168]

Surfaces were patterned with MHA by either µcp or DPN. µCP generated patterns were produced by inking a grooved PDMS stamp with a 10-20 mMol MHA acetonitrile solution. The stamp was brought into contact with the surface for 20-30 sec. The substrate was then passivated by immersion in a 5 mMol solution of octadecanethiol

(ODT) in toluene or ethanol for 60-90 min. This passivation layer created a hydrophobic surface surrounding the patterned MHA molecules to help limit non-specific absorption. μcp has the advantage that surfaces can be quickly patterned, making it easier to study the effect of variables such as time and nanoparticle concentration on the resulting particle assembly. Once the experimental procedure is optimized, DPN can allow for assembly on sub-100 nm features. As previously mentioned, patterning of MHA on Au surfaces using DPN has been studied extensively.[42-44] With this molecule, it is straightforward to achieve high resolution (sub-100 nm). Following patterning, the substrates used in this work were passivated by immersing them in a 2-5 mMol ethanol or toluene solution of ODT, dodecanethiol (DDT) or octanethiol (OT) for 90 min.

Covalent attachment of Au nanoparticles via amide linkages requires a carboxylic acid group and an amine group. Patterning amine terminated thiolated molecules onto surfaces has proven to be difficult due to the formation of coordination bonds between the amine group and the gold surface. Molecules often lie flat on the surface, as both the amine and thiol groups bond to the gold surface. Likewise, Au nanoparticles with amine terminated ligands tend to aggregate in solution as the amine group on the ligand shell of one nanoparticle binds to the Au core of second nanoparticle as illustrated in figure 3.22. Thus, we chose to use a diamine molecule to link surface bound carboxylic acid groups to nanoparticle ligands terminated with carboxylic acid groups (figure 3.22). The surface bound carboxylic acid groups were activated by immersion in 0.1 M *N*-(3-dimethylaminopropyl)-*N'*-ethylcarbodiimide (EDC) and 0.2 M pentafluorophenol (PFP) solution in dimethylformamide (DMF) for 20 min. followed by washing in DMF.[167] This transformed the carboxylic acid groups into activated esters, necessary for amide

bond formation. The substrates were then immersed into a 2 mMol solution of diamine (diaminoheptane (DAH) in toluene or hexamethyl diamine (HXDA) in DMF) at 50°C for 60 min. followed by washing.

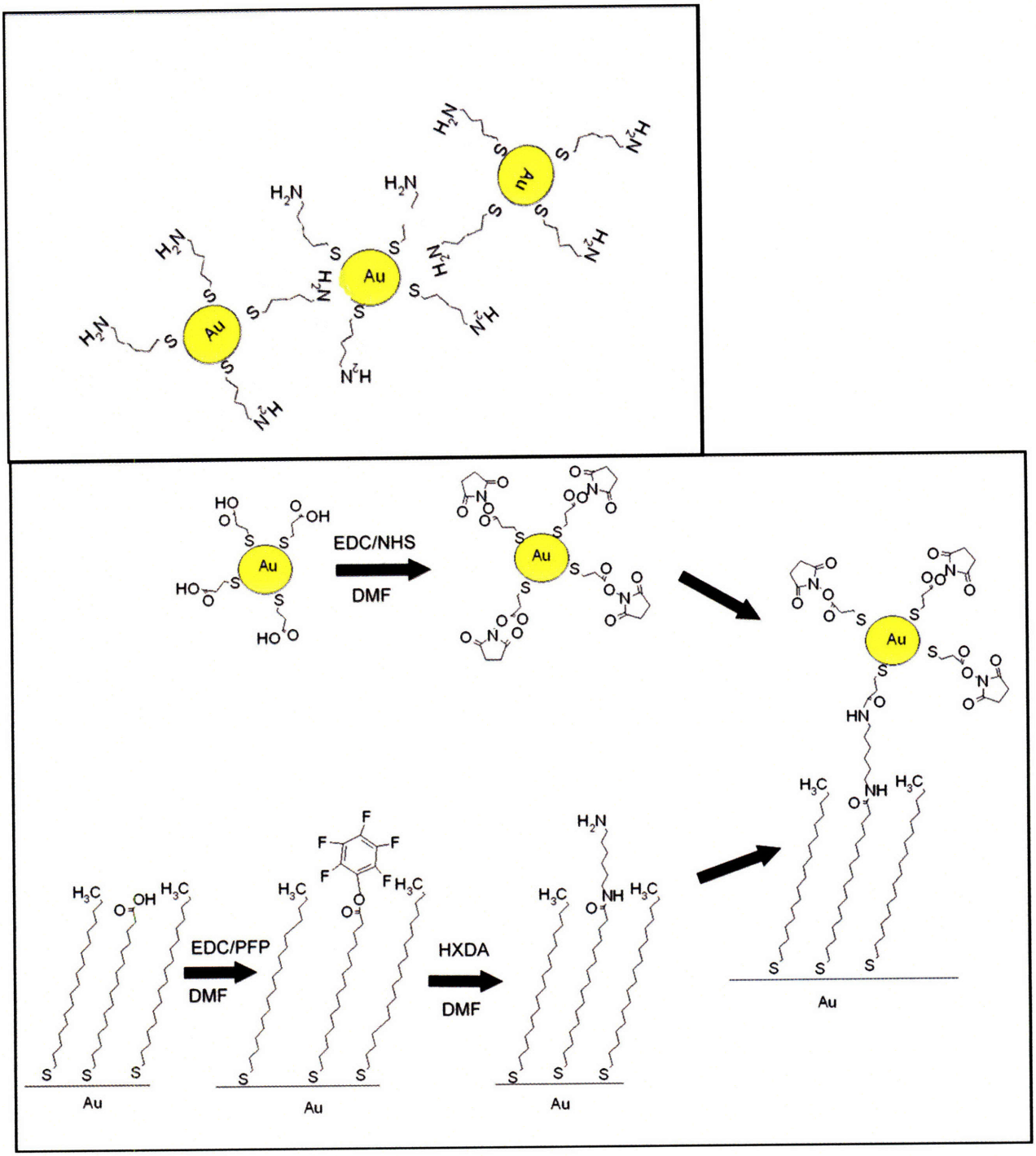

Figure 3.22: (top) Nanoparticles functionalized with amine terminated thiols aggregate and become insoluble. (bottom) A three part strategy is needed to assembly nanoparticles using a diamine molecule to form two amide linkages.

Figure 3.23 shows a typical substrate patterned by μcp before and after diamine assembly. The height image before assembly (figure 3.23a) shows almost no difference in the height of the feature relative to the background. This is due to the similar molecular length of ODT (background) and MHA (features). Lateral force microscopy (LFM) better distinguishes the two regions (figure 3.23b). After the HXDA assembly the height image shows a 0.4 - 0.6 nm increased in the height on the MHA regions, indicating that HXDA has been specifically assembled. If a complete monolayer of HXDA molecules had been formed, a 1.0 nm height change would be expected. The lack of a complete SAM may be attributed to (1) imperfect MHA monolayer formation with μCP, or (2) incomplete HXDA monolayer formation, or (3) the presence of a fraction the diamine molecules lying prone, bound by both amide linkages. To prevent the latter phenomenon a concentrated (2mMol) solution of HXDA molecule was used during the assembly.

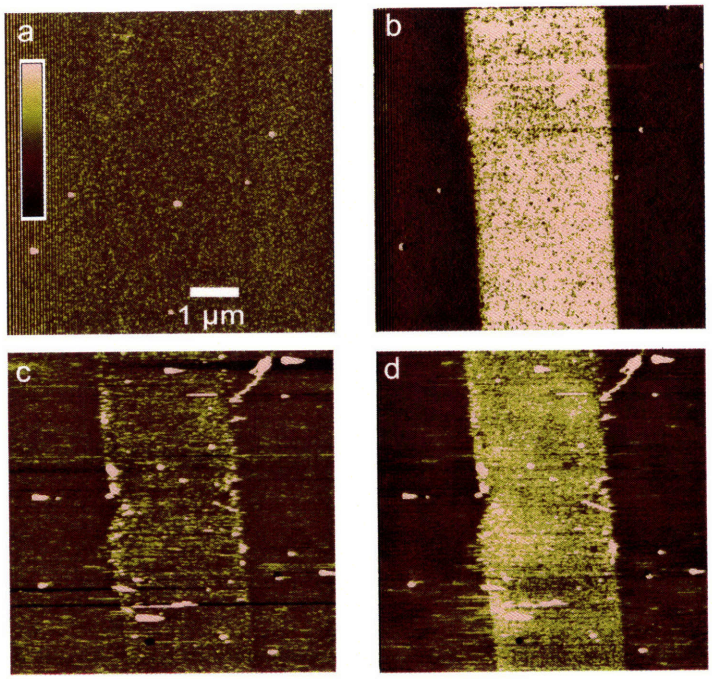

Figure 3.23: (a) Contact Mode AFM (CMAFM) height images of a 3 µm wide line of MHA patterned by µCP and passivated with ODT. (Inset: height scale-5 nm) (b) Lateral force microscopy (LFM) image of the same MHA line shown in (a) which appears as a high friction region due to their highly polar terminal carboxylic acid groups. (c) CMAFM height image of the same pattern after specific assembly of HXDA on the MHA feature. Height of the feature is 0.4- 0.6 nm. (d) LFM image after HXDA assembly showing a high friction region over the MHA patterned lines, indicating the surface is coated with polar amine groups which are higher friction than the surrounding apolar methylene groups. This serves as further evidence that a high percentage of the diamine molecules are bound with only one amide linkage while the other amine group is on the surface of the monolayer. If all of the amine molecules were bound to the surface via two amide linkages, the surface would be composed of the low friction methylene groups that form the HXDA backbone.

The nanoparticles used here were synthesized using a one-phase method,[2, 169] with a 3:1 ratio of MUA:OT. TEM images showed particles with an average core diameter of 4.8 nm. This means that the total particle average diameter (taking in account the core and the ligands in an *all trans* configuration) is 8.4 nm.[150] The carboxylic acid groups on the protecting ligand shell of the gold nanoparticles were activated into esters by the addition of a 5-10 fold excess (relative to the ligand molecules) of EDC and N-hydroxysuccinimide (NHS) molecules in a DMF (1 mg nanoparticle/ml) solution. The EDC/NHS/nanoparticle solution was heated at 40°C for 4 h. Unreacted EDC/NHS molecules were removed via centrifugation in deionized water. UV-Visible spectra of the

nanoparticles were taken along this process. They were almost identical, all showed the characteristic gold surface plasmon peak at 520 nm. (figure 3.24) Thus we conclude that no substantial change to the particles happens during the process. In order to test the ability of diamine molecules to bind to the activated carboxylic acid groups on the nanoparticles, a solution containing 50 diamine molecules per nanoparticle was prepared. Complete precipitation of nanoparticles was observed in less than 80 min., due to the cross-linking of nanoparticles via the diamines. Non-activated solutions of nanoparticles showed no precipitation 80 min after the addition of diamines.

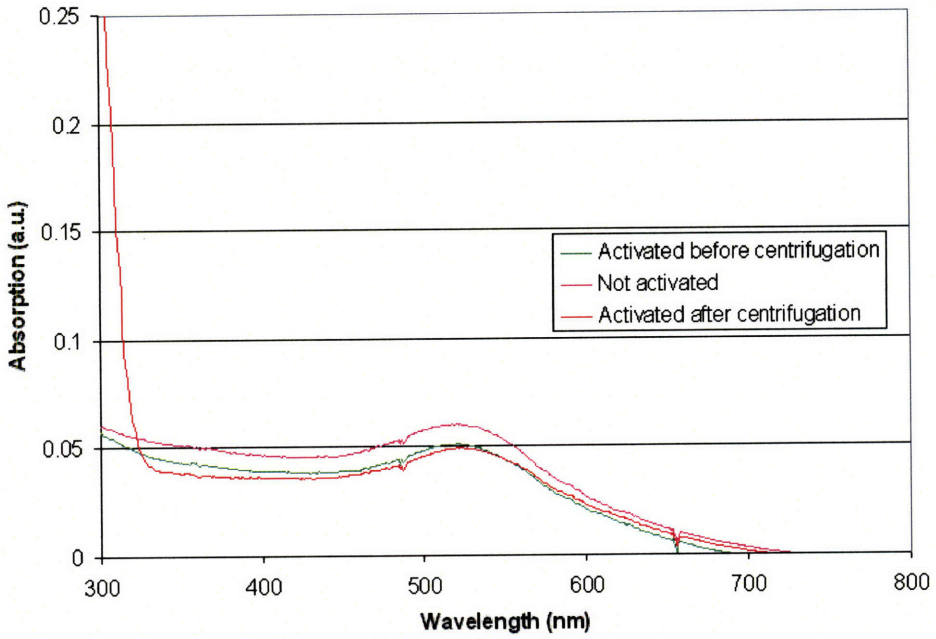

Figure 3.24: UV-Vis spectra showing the strong surface plasmon peak at 520 nm associated with Au nanoparticles with diameters < 10 nm. The peak remains strong after activation with EDC and NHS and after centrifugation. The new peak at 300 nm is attributed to the solvent.

To complete the chemically directed assembly of Au nanoparticles, patterned samples were immersed in activated nanoparticle DMF solutions (0.01-0.1 mg nanoparticles/ml) at 40 °C for 6-24 h. After assembly, samples were typically sonicated in DMF for 30-60

min. to remove nanoparticles non-specifically adsorbed to the surface. AFM images showed height increases of 2-6 nm on the MHA/ diamine regions after nanoparticle assembly. (Figure 3.25). Optimized assembly conditions (18 hrs, nanoparticle concentration of 7.0 $*10^{-2}$ mg/ml) showed a 6 nm height increase of the MHA/ diamine region, indicating a 70-75% coverage nanoparticle monolayer is assembled. Optical microscopy and SEM were also used to image the assembled nanoparticle features. (Figure 3.26) In the optical microscopy images, the nanoparticle regions appear dark due to the increased scattering of light by the nanoparticles as compared with the gold regions coated only by ODT.[73] These regions of different contrast in optical microscopy are further proof of nanoparticle assembly, as this contrast is not seen on samples where only diamine assembly has been performed. Likewise, in SEM nanoparticle regions appear dark,[77, 79, 163] due to the increased scattering of secondary electrons.

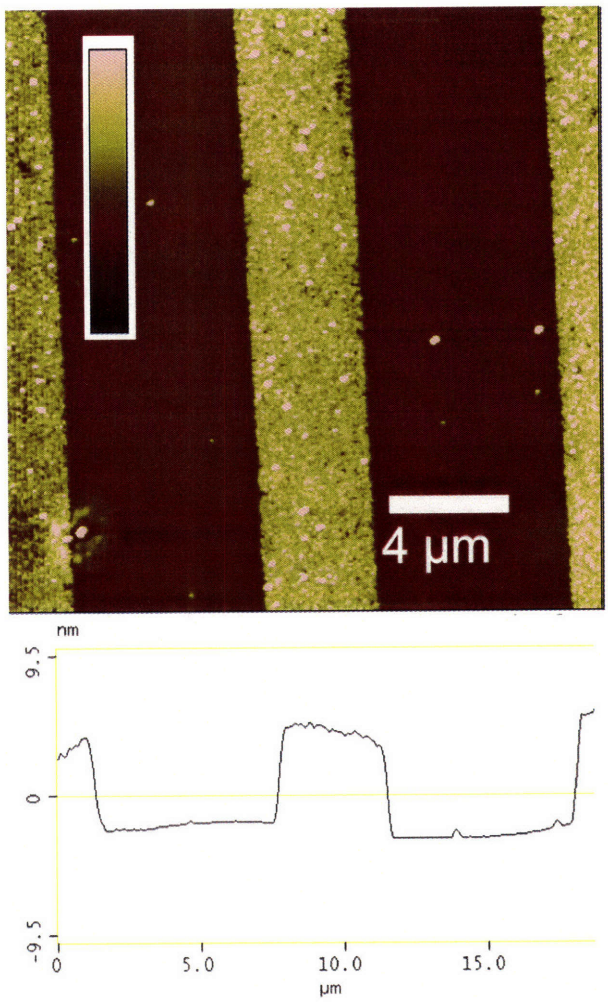

Figure 3.25: CMAFM height image (top) and average height profile (bottom) of gold nanoparticles chemically directed onto MHA features patterned by µCP. Sonication removes the non-specifically absorbed nanoparticles. The lines show an average height of 6.5 nm (see average height profile on the bottom), a 6 nm increase over the feature height after HXDA assembly. (Inset: height scale-20 nm)

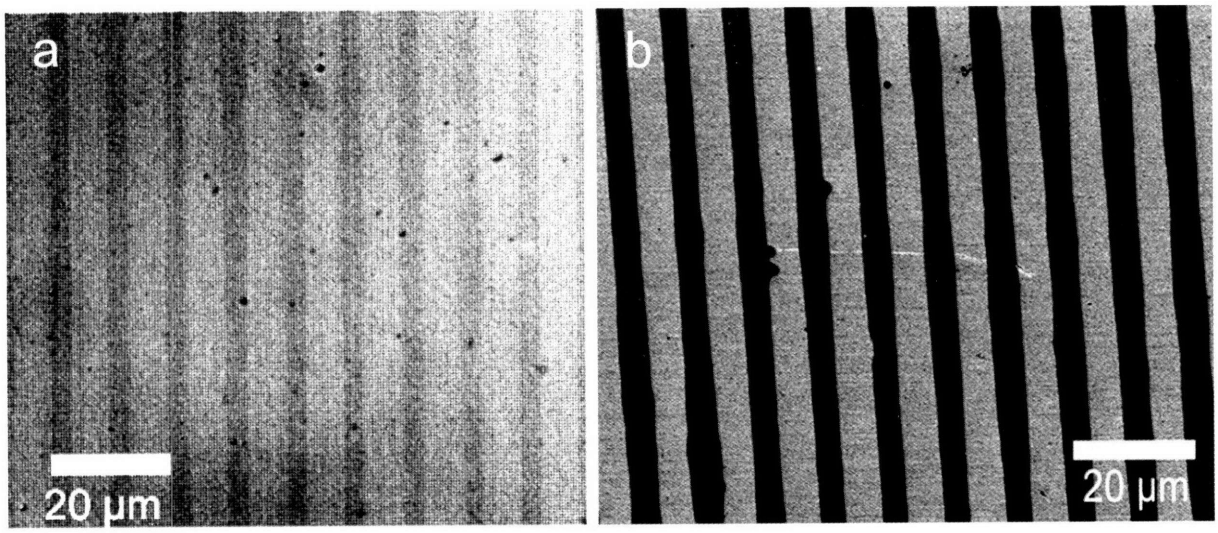

Figure 3.26: (a) Optical microscopy image of patterned features after nanoparticle assembly. The nanoparticle regions appear dark due to the increased scattering of light as compared with the gold regions coated only by ODT.[73] This contrast is not seen on samples where only diamine assembly has been performed, giving further proof of nanoparticle assembly. (b) SEM image of patterned features after nanoparticle assembly. As explained in the literature,[11] the nanoparticle regions appear dark in SEM as well.[77,79,163]

The CDA of nanoparticles was demonstrated also on much smaller features, patterned by DPN. Figure 3.27 shows 5 MHA lines before assembly, after nanoparticle assembly and after sonication. Even the narrowest feature patterned, 85 nm in width, is able to chemically direct the assembly of gold nanoparticles, as demonstrated by the increased height after nanoparticle assembly and sonication.

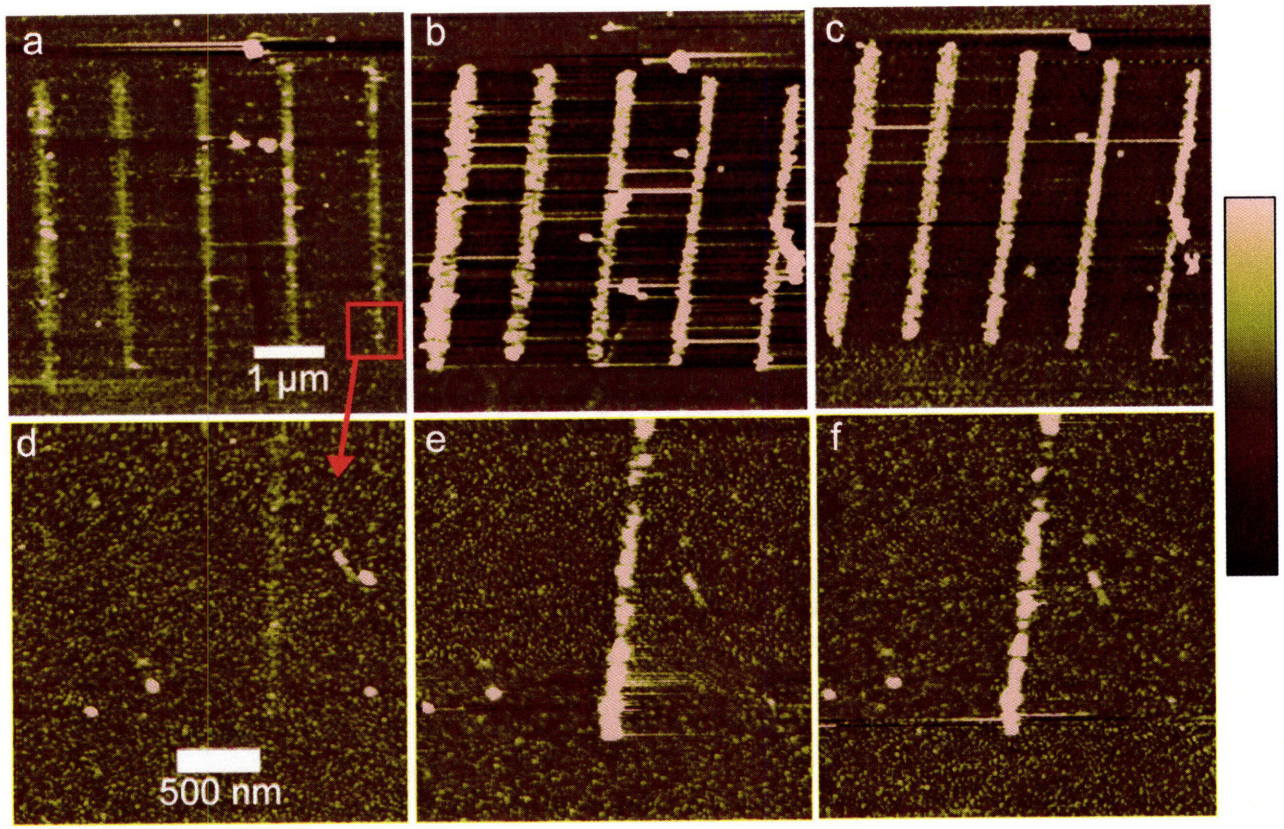

Figure 3.27: CMAFM height image of all MPA gold nanoparticles chemically directed onto MHA lines patterned by DPN. (a+d) MHA pattern before assembly, (b+e) pattern after nanoparticle assembly and (c+f) after sonication. The narrowest line (magnified: d-f) has a width of 85 nm. (Right: height scale-5nm)

Several factors were found to be critical for the CDA of nanoparticle monolayers with good coverage. Assembly times of 8 and 12 hours at a nanoparticle concentration of 3.5 * 10^{-2} mg/ml resulted in a poorly formed monolayer with height increases of 1- 1.5 nm when using DAH. 18 hours was found to yield monolayers that showed 3-4 nm height. No further increases in height were observed after immersion for longer times. Time dependence of nanoparticle assembly has been explained by a diffusion model, where the nanoparticle must come into contact with surface bound amines before assembly can occur.[170] Nanoparticle concentration was found to have a linear effect on the amount of

assembly within the range of concentrations tested. As shown in figure 3.28, a two fold increase in concentration leads to a two fold increase in nanoparticle assembly.

The kinetics rates of assembly are also changed when different types of nanoparticles are assembled. Nanoparticles coated with mercaptopropionic acid (MPA) ligands, with an average core diameter of 4.9 nm (and therefore a total diameter of 6.4 nm, assuming an *all trans* configuration of the MPA molecules[150]), as measured with TEM, were assembled on samples patterned with MHA via μcp and DPN. After only 8 hours of assembly, features of similar height to the ones observed after 18 hours of assembly of MUA:OT nanoparticles were observed. (figure 3.29) We believe that this is due to the difference in the overall particle diameter. The shorter MPA ligands allow for faster diffusion rates (the diffusion coefficient of nanoparticles has been reported to scale as either $(1/r)$[171] or $(1/r^2)$ [172]) and therefore quicker assembly. The amount of nanoparticle assembly was also affected by the choice of diamine, HXDA being better that DAH, probably due to its solubility in the same solvents, such as DMF, that dissolve the particle and MHA. The use of ethylene diamine, phenylene diamine and hydrazine as the linking diamine resulted in almost no particle assembly. Interestingly, when using shorter diamines, partial nanoparticle assembly was observed at the interface between the MHA and the ODT regions. Interface assembly has been noticed in other nanoparticle systems.[162]

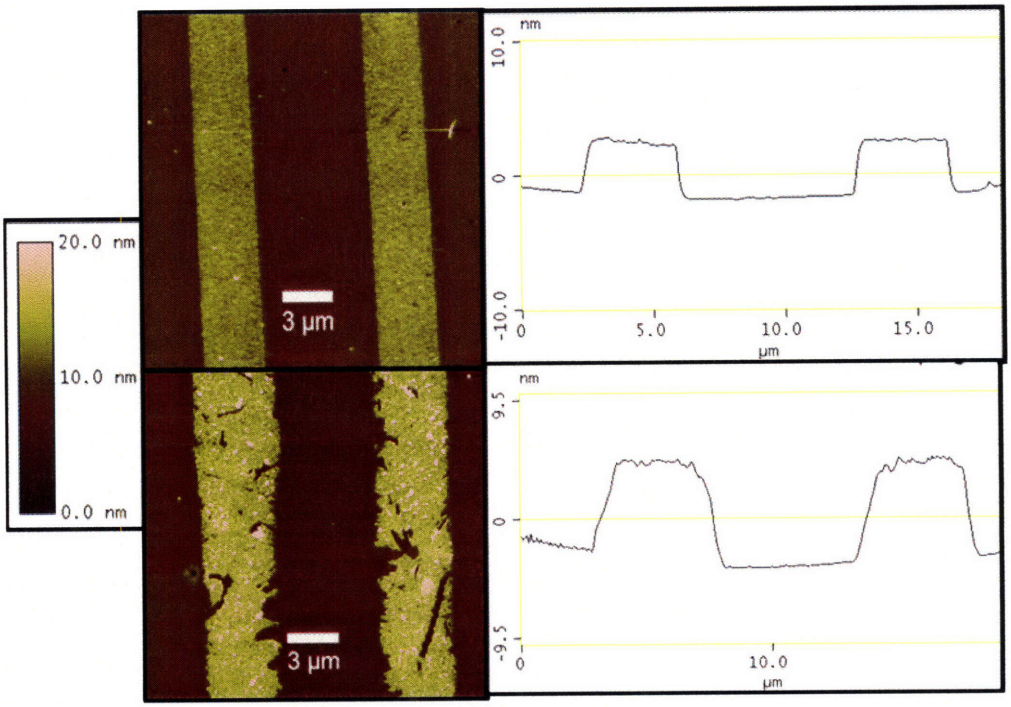

Figure 3.29: Contact mode AFM images and average height profiles of nanoparticles assembled from a concentration of (top) 0.035 mg nanoparticles/ml giving a 35-40% coverage monolayer and (bottom) 0.07 mg nanoparticles/ml giving a 70-80% monolayer.

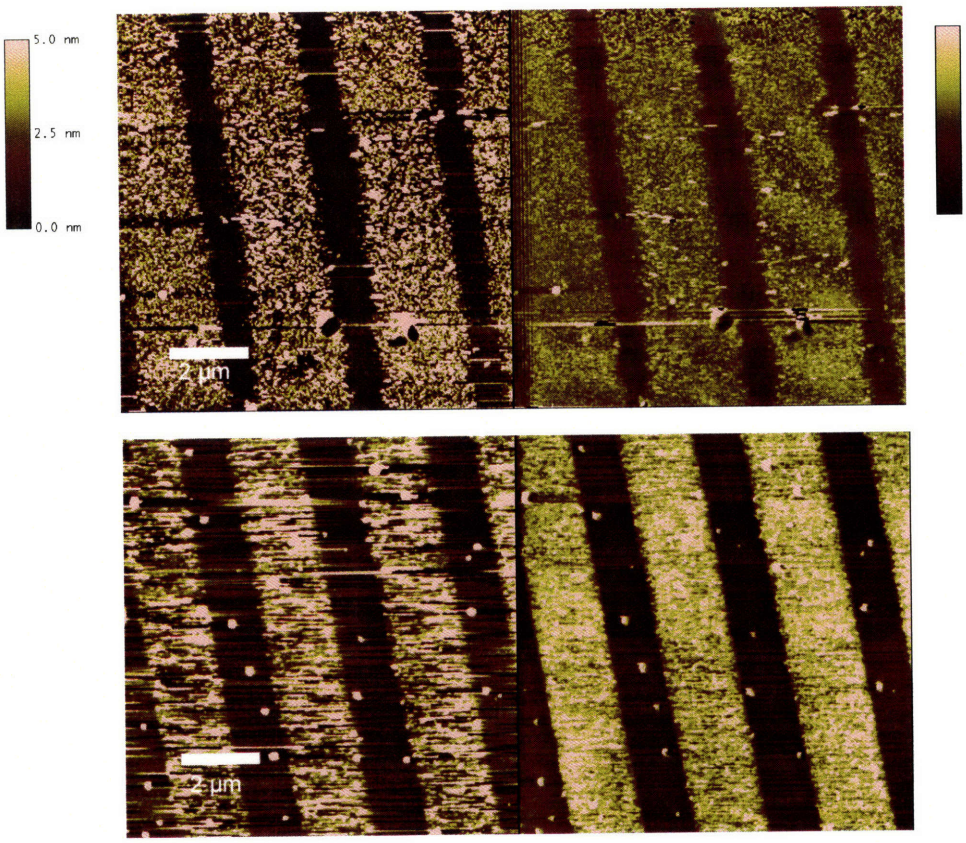

Figure 3.29: CMAFM height images (left) and LFM images (right) showing the difference in kinetics of assembly of two different nanoparticles. The wider lines are the MHA/DAH regions. Both assemblies were done using DAH and a nanoparticle concentration of 0.035 mg/ml. The all MPA nanoparticles (top) take only 8 hours to achieve the same amount of assembly for which the MUA:OT, 3:1 nanoparticles take 18.5 hours.

Control experiments were done to confirm the covalent nature of the assembly. No assembly was observed when no diamine was used. To rule out the role the formation of ionic attractions to guide the assembly, a MHA patterned surface was immersed in an HXDA solution for 1 h at 50 °C and subsequently in a solution of nanoparticles, $3.5 * 10^{-2}$ mg/ml, for 18 hours. Only non-specific assembly was observed, predominantly on the ODT regions. When the same experiment was repeated in the same condition but after activation of both the MHA on the surface and the MUA on the nanoparticles a 60% coverage nanoparticle monolayer was observed.

The chemically directed assembly of gold nanoparticles using covalent bonds can be easily achieved using diamine molecules. CDA using covalent bonds has the disadvantage of slower speeds, but major advantages of bond strength and higher coverage nanoparticle monolayers.

3.2.3 Assembly on Lithographically Patterned Wires

CDA is one possible strategy to direct the assembly of nanoparticles into nanogaps. In this method, a SAM is patterned on the ends of the gold wires adjacent to the insulating gap. (figure 3.30) Ligands on the nanoparticle would bind to the reactive head groups of the patterned monolayer. The sides of both wires would be patterned, and the nanoparticle would be bound to both sides of the gap. DPN would allow for very small area immediately surrounding the gap to be patterned. The rest of the gold wire could be coated with a methylene terminated thiol to avoid the non-specific absorption of nanoparticles on the rest of the device.

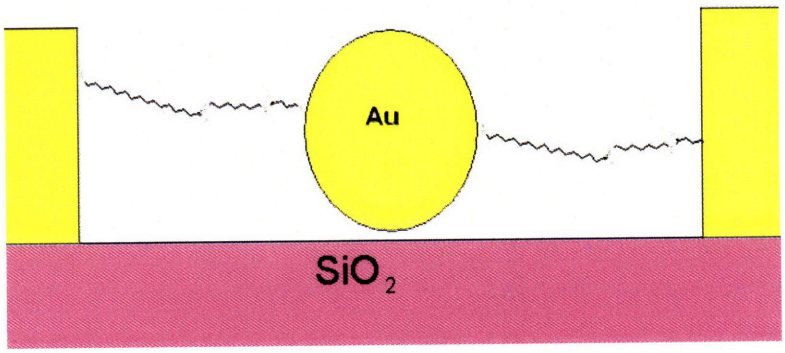

Figure 3.30: Schematic of CDA of a nanoparticle inside a nanogap.

The tips of wires forming nanogaps cut by FIB were patterned with MUD to attempt the covalent chemically directed assembly of nanoparticles onto a device using urethane linkages.[173] (Both FIB and urethane linkages were later found to be sub-optimal for gap formation and nanoparticle assembly, respectively. Unfortunately, electrical based methods of gap formation and amide linkages had not yet been used at the time of these experiments. By the time these techniques had been optimized, DEP replaced CDA as the method of choice for nanoparticle assembly, for reasons explained below and in Chapter 4.) A small 250 nm by 250 nm square surrounding the gap was patterned with DPN. The strategy used to form covalent bonds with BPDI as outlined in section 3.2.2.1 was followed. Figure 3.32 shows the gap before assembly and electrical characterization of the device before and after assembly. 60% of devices showed a decreased resistance of 10-100% after nanoparticle assembly. Unfortunately after 4-5 voltage sweeps the current level going through the nanoparticle device began to decrease until it reached or became slightly lower than the pre-nanoparticle level. This is likely due to the lack of covalent bonds formed using the urethane linkages, as described in section 3.2.2.1. High electrical fields at the gap may push the nanoparticle out of the current pathway.

A larger problem concerning CDA on devices involves the patterning of molecules on the lithographically patterned features via DPN. Due to the carbonaceous compounds and residual photoresist, it is difficult to impossible to pattern consistent well-formed monolayers using DPN on lithographically patterned surfaces. The contamination prohibits the thiol group from reaching the gold surface where it can form a bond. AFM height and LFM images after DPN patterning on lithographically defined wires does not show the presence of features of the patterning molecule. As shown in section 2.1.1, well-formed monolayers are need for good self-assembly. Without these well-oriented SAMs, the head groups of the molecule, needed for CDA, are not accessible. While CDA has the potential to direct the assembly of nano-objects onto flat surfaces, until a better method is found to pattern molecules on lithographically defined features, electrical methods of nanoparticle assembly are better suited for device applications.

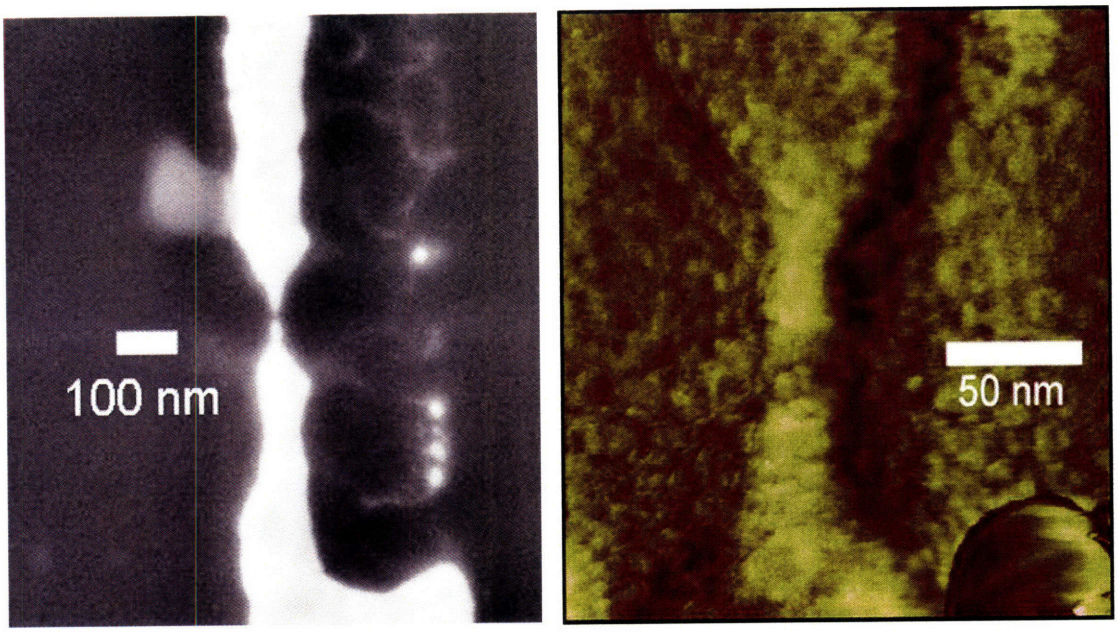

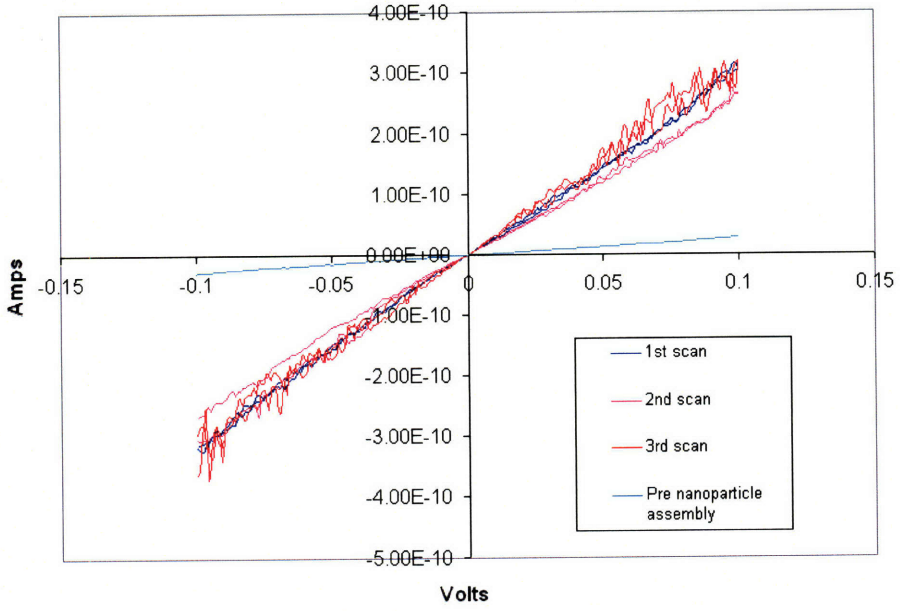

Figure 3.31: (top) SEM and tapping mode AFM phase image of nanogap formed by physical deformation with FIB. (bottom) IV curve of gap before nanoparticle assembly and for the 1st 3 measurements after assembly, showing a ~10% decrease in resistance. Increased current levels were only stable for 3 measurements.

Chapter 4: Electrically Directed Assembly of Nanoparticles

The directed assembly of nanoparticles and nanoscale materials onto specific locations of a surface is one of the major challenges in nanotechnology. Here we present a simple and scalable method and model for the assembly of nanoparticles into a nanogap between electrical leads using AC dielectrophoresis (DEP).[174] The forces and experimental variables affecting DEP-based assemblies have been well-studied in the case of assembling nanoparticles into microwires.[98, 99] However, much less is known regarding the manipulation of nanomaterials into nanoscale gaps. The technological understanding of DEP on the nanoscale could lead to the scalable integration of isolated nano-objects into electronic devices.

Gold nanoparticles were assembled inside electrical gaps ranging from 15 to 150 nm with the use of positive AC DEP. In this method, an alternating current is used to create a gradient of electrical field that attracts particles in between the two leads used to create the potential. Assembly is achieved when dielectrophoretic forces exceed thermal and electrostatic forces; the use of anchoring molecules, present in the gap, improves the final assembly stability. We demonstrate with both experiments (section 4.1.1) and theory (section 4.1.2) that nanoparticle assembly inside the gap is controlled by the applied voltage and the gap size. Experimental evidence and modeling suggest that a gap size dependent threshold voltage must be overcome before particle assembly is realized, as discussed in section 4.1.3. Assembly results as a function of frequency and time are also presented. Assembly of fewer than 10 isolated particles in a gap is demonstrated. The assembly of nanoparticles with core diameters of 7-20 nm stabilized with thiolated

ligands having different functional groups are presented in section 4.1.4. Electrical characterization of the assembled particles is presented in section 4.2 with emphasis of the effect of ligand length and type on particle resistance.

The work presented here is the result of a collaboration I initiated and led. I would like to acknowledge Ryan Wartena for the help with the experimental set-up and analysis of the results and Michael Vahey for the theoretical modeling. Section 4.1.2 is a summary of Mike's theoretical methods and results. The theoretical methods are further described in reference 174.

4.1.1 Controlled Assembly of Nanoparticles into Nanogaps

Gaps used in this work were formed either by direct patterning with electron beam lithography or by electrical methods of breaking a continuous gold wire patterned with electron beam lithography. Gaps formed by direct patterning have widths of 30 to 150 nm (controlled via the electron dose level during electron-beam lithography) and the wires are 300-nm wide with almost hemispherical ends. Electrical methods of gap formation were carried out as described in section 2.3.1. SEM imaging reveals gaps with widths which range from 10-70 nm.

Citrate-stabilized gold particles[3] were chosen for this study partly because of their unique optical and electronic properties, but mainly because of their solubility in water,

monodispersity and commercial availability. 20 nm diameter particles were used so assemblies could be visualized analyzed with SEM images. Citrate-stabilized gold particles were purchased from British Bio Cell International and used at the as-purchased concentration ($7*10^{11}$ particles/ml) or diluted with DI water to a concentration of $7*10^{10}$ particles/ml.

Prior to DEP assembly of nanoparticles, the substrates were immersed in a toluene solution of hexanethiol and nonanedithiol. Both molecules bind (through their thiol group) to the metallic leads. The dithiol molecules (once 'diluted' in the well-packed hexanethiol molecules) chemically bind to the surface with one thiol group. The 2nd thiol group stays on the surface on the self-assembled monolayer (SAM), ready to bind to the nanoparticles once they are brought into the gap by the DEP force.[103-105, 109] The SAM, therefore, serves as a molecular glue, binding the nanoparticles to the wires. Control experiments where the dithiol molecules were not used resulted in inconsistent nanoparticle assembly.

The experimental set-up used for dielectrophoretic assembly is shown in figure 4.1. A 0.1- 0.25 ml drop of aqueous nanoparticle solution was placed over the sample, covering all devices on the chip. An alternating voltage of a given magnitude and frequency was applied for a set amount of time. An oscilloscope was used to monitor the changes in conductivity of the nanoparticle bridge when testing for the conditions of fused vs. isolated particle assembly (see below). After these conditions had been established, experiments were performed without the oscilloscope; the 2nd electrode was connected directly to ground.

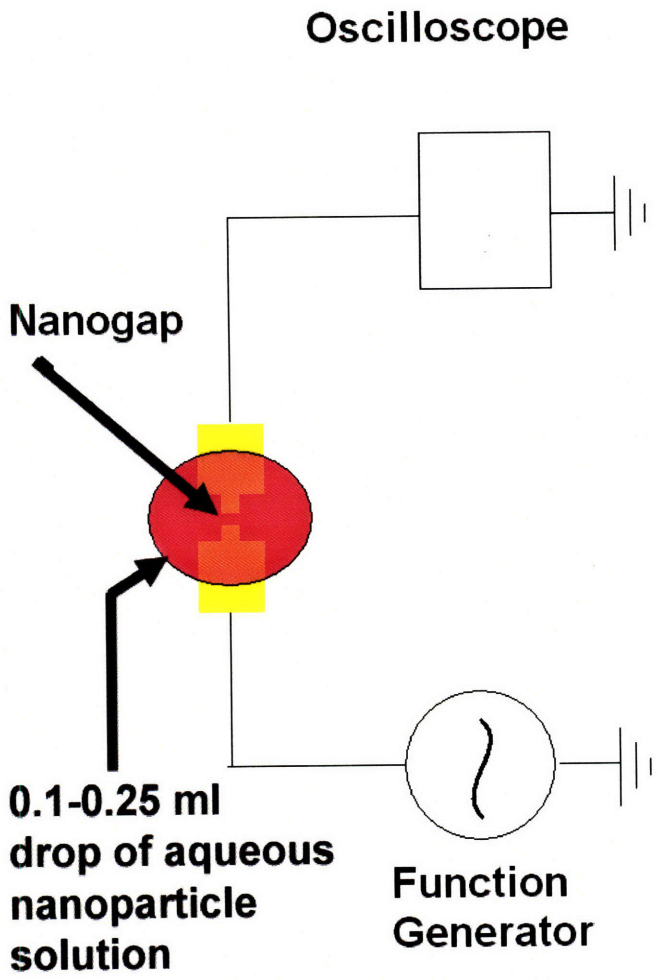

Figure 4.1: Schematic of experimental set-up for DEP assembly of nanoparticles in nanogaps.

4.1.1. Assembly vs. Voltage and Concentration - Fused vs. Isolated Particle Assembly

The assembly of nanoparticles into nanogaps has been shown for isolated individual particles[101, 103-105, 109] and for fused metallic particles[106, 107] using similar conditions. Using our experimental set-up it was possible to achieve both types of assembly (figure 4.2) and to detect the creation of a fused metallic wire bridging the gap in real time. When a gap is present, the circuit is open and no voltage signal is seen on the oscilloscope. When a metallic bridge forms, a highly conductive pathway forms across

the gap, and the applied peak-to-peak voltage (V_{pp}) waveform is seen on the oscilloscope. Fusing of particles occurred anywhere from 2-60 seconds after the voltage was applied. The post-assembly DC characteristics of the fused nanoparticle bridges show linear IV curves and low resistances (150-600 Ω) similar to those reported previously.[106, 107]

The key controlling factors differentiating the two types of assembly are found to be the applied peak-to-peak voltage and the nanoparticle concentration in solution. At a nanoparticle concentration of 7×10^{11} particles/ml, 15 out of the 17 gaps (~88%) assembled at voltages of 3 V_{pp} and higher were found to be filled with fused particles. When V_{pp} was below 3 V, fused wire assembly was not observed (0/6) and isolated particles could be seen in subsequent SEM images. At a more dilute nanoparticle concentration (7×10^{10} particles/ml), the voltage required for fusing increases. Voltages larger than 4.5 V_{pp} were needed to observe fused particles in the gap (~69%, 9/13) while at voltages equal to or lower than 4 V_{pp} almost all gaps (28/29) showed isolated particle assembly. As our goal was to study the assembly of isolated particles, we performed experiments in these latter conditions (with nanoparticle concentrations of 7×10^{10} particles/ml and lower voltages).

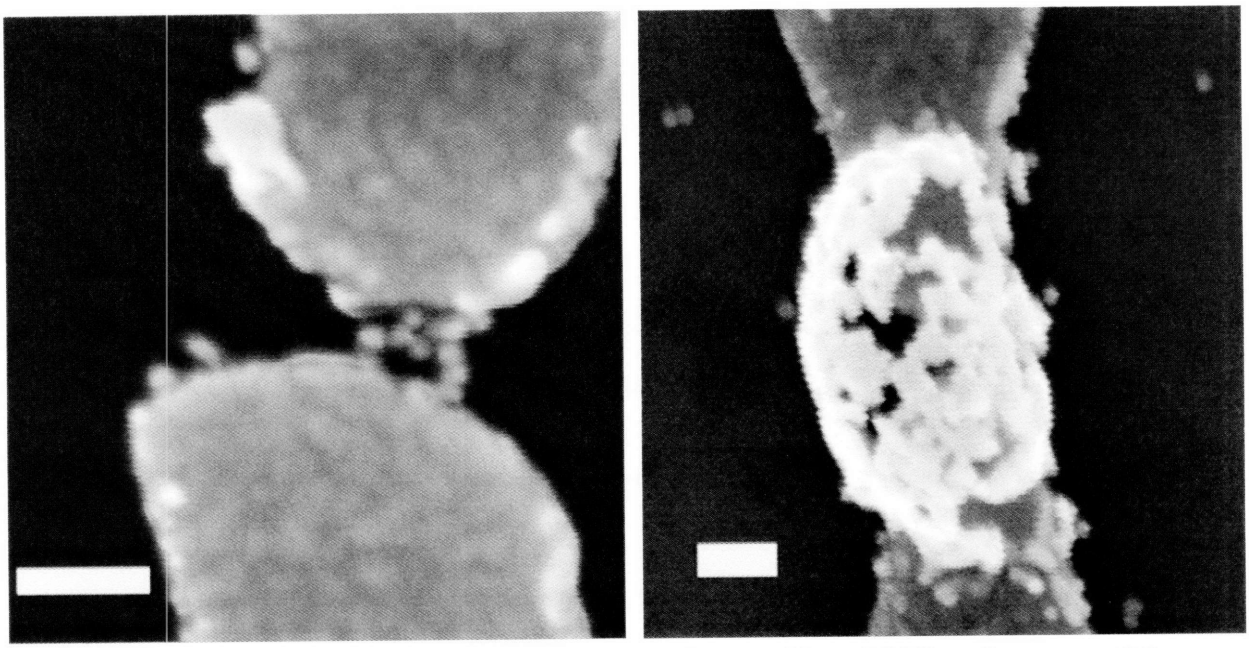

Figure 4.2: SEM images of the two modes of nanoparticle assembly at 1 MHz and a nanoparticle concentration of 7×10^{11} particles/ml. Assembly of isolated particles at 2 V_{pp} for 60 seconds (left). Assembly of a fused nanoparticle bridge occurs at 4 V_{pp} in 3 seconds (right). Assembly appears to be out of the surface plane. This type of assembly was described by Velev for assemblies on much larger gaps.[101] Scale bar=100 nm.

4.1.1.2 Assembly vs. Voltage and Gap Width

To investigate assembly as a function of voltage and gap width, assemblies were carried out for 120 seconds at a given alternating V_{pp} and a frequency of 1 MHz. After the assembly of isolated particles, the samples were imaged by SEM and the number of particles captured in each gap was counted. A 400 nm diameter circle centered on the middle of the gap was drawn and only nanoparticles within this circle were considered as captured. SEM images were also used to measure the gap width. Gap widths were measured at their narrowest points.

Figure 4.3 demonstrates the effect of voltage and gap width on nanoparticle assembly. A threshold voltage must be reached before any nanoparticle assembly is realized, as seen

in previous works.[11, 100, 110] As the gap width is increased, the threshold voltage required for nanoparticle assembly increases. At an average gap width of 30 nm (widths from 15 to 50 nm) and voltages below 2 V_{pp}, no assembly was observed. For slightly larger gaps (85 $nm_{average}$; widths from 50- 110 nm) assembly was not observed until 3 V_{pp}, and for the largest gaps tested (125 $nm_{average}$, widths from 110-150 nm), assembly was not observed until approximately 4 V_{pp} on 8/9 gaps tested. The use of larger gaps was also observed to increase the voltage necessary for fusing. Isolated nanoparticle assembly was achieved on gaps >70 nm at V_{pp} = 4.5 and on gaps >105 nm at voltages of 5 and 6 V_{pp}. The number of assembled particles captured in the gap increased with increasing voltage for all gaps widths when voltages larger than the threshold voltage were applied.

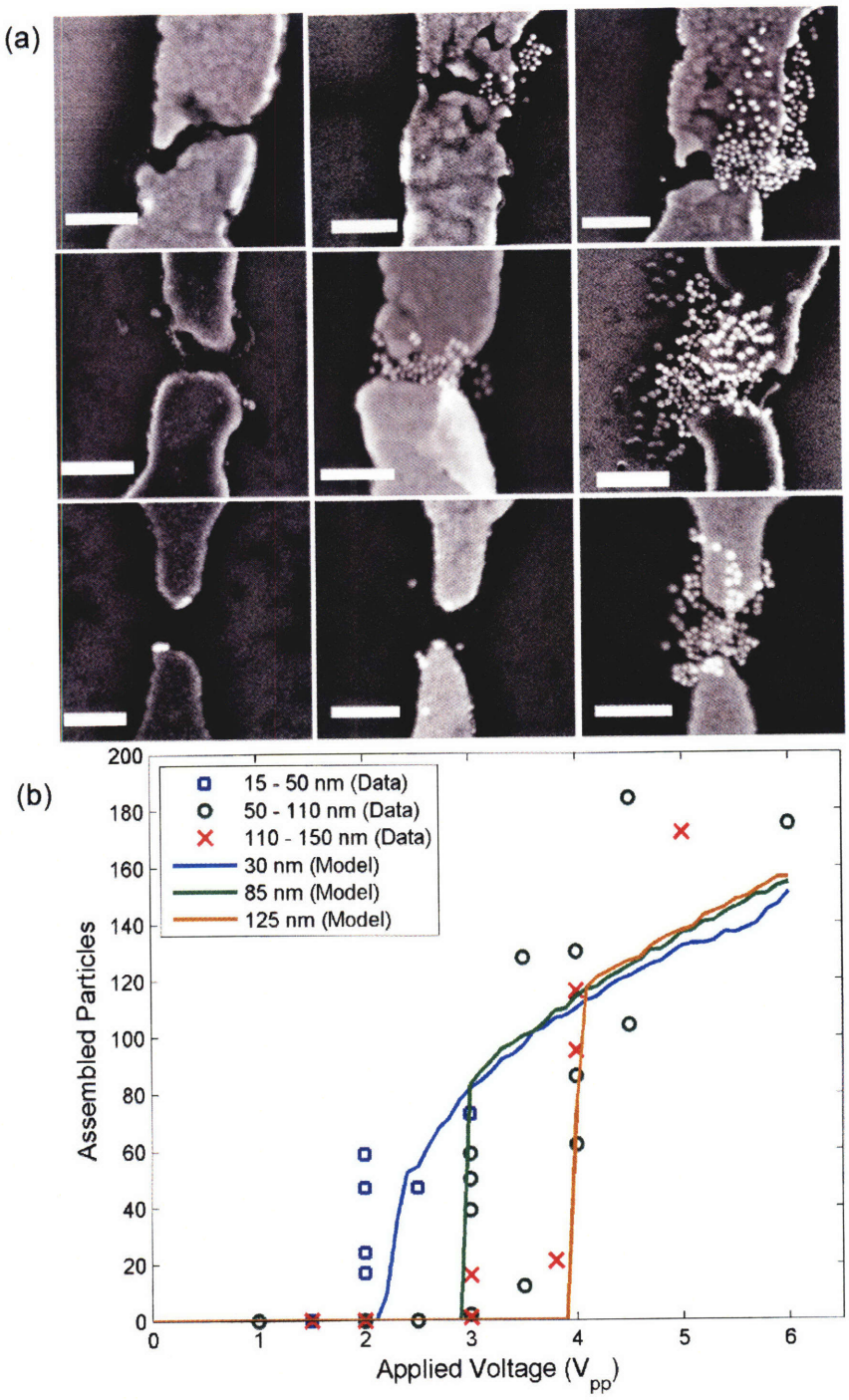

Figure 4.3: (a) SEM images of assembly as a function of voltage and gap width after 120 seconds assembly at 1 MHz and a nanoparticle concentration of 7×10^{10} particles/ml. (a) Top Row: Small gaps at V_{pp} = 1.5 V (left), 2 V (center) and 3 V (right). Middle Row: Medium gaps at V_{pp} = 2 V (left), 3 V (center) and 4 V (right). Bottom Row: Large gaps at V_{pp} = 2 V (left), 3 V (center) and 4 V (right). Scale bar=200 nm. (b) Plot of experimental data and theoretical model for nanoparticle assembly using DEP as a function of voltage and gap width. Data is plotted as a function of voltage for three different gap width ranges: 15-50 nm, average=30 nm; 50-110 nm, average=85 nm; 110-150 nm, average=125 nm while the theoretically predicted number of particles is shown at the average gap widths.

4.1.1.3 Assembly vs. Time

To achieve the assembly of a very few (<10) isolated particles in the gap, it was necessary to limit the assembly time. Operating at a frequency of 1 MHz and at voltages near the threshold for a given gap size resulted in the capture of a few nanoparticles. For small electrode gaps, ~15-40 nm, 2 V_{pp} assemblies were performed for 5, 10, 30, 60 and 120 seconds, while on larger electrode gaps, ~55-90 nm, 3 V_{pp} assemblies were performed for similar durations. As illustrated in figure 4.4, the shortest assembly times resulted in the assembly of fewer than 10 particles in the gap. Increased assembly time resulted in more nanoparticles in the gap for all gap widths at voltages above the threshold value.

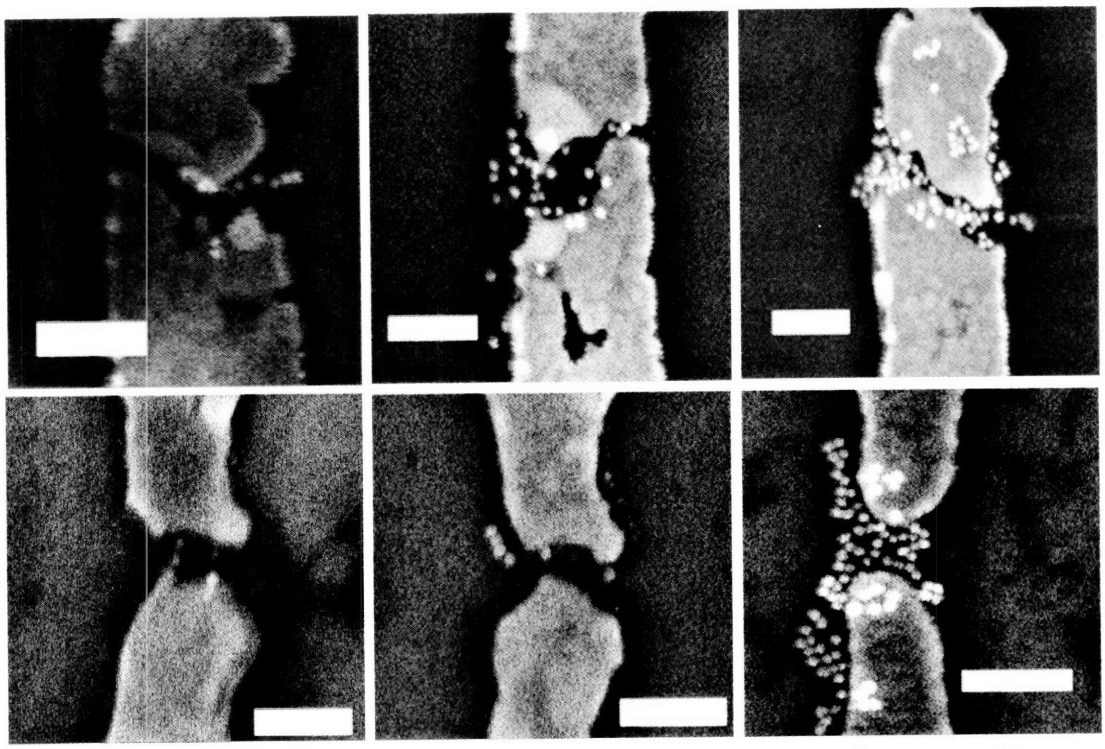

Figure 4.4: SEM images of assembly as a function of time. The top row shows assembly on small (15-40 nm) gaps at $2V_{pp}$, 1MHz, and 7×10^{10} particles/ml for 5 seconds (left), 30 seconds (center), and 120 seconds (right). The bottom row shows that assembly of only a few particles can also be achieved with the use of medium (55-90 nm) gaps at 3 V_{pp}, 7×10^{10} particles/ml, for short times. 5 seconds (left), 30 seconds, (center) and 120 seconds (right). Scale bar = 200 nm.

4.1.1.4 Assembly vs. Frequency

To study the effect of frequency on nanoparticle assembly, peak-to-peak voltages near the threshold (2.5 V_{pp} - 4 V_{pp}) were applied. Assemblies were carried out for 120 seconds at frequencies of 10 kHz, 100 kHz and 1 MHz. Figure 4.5 shows a strong dependence of nanoparticle assembly on frequency.[11, 98, 100, 110] At lower frequencies more nanoparticle assembly is seen and fusing occurs more readily. As frequency is increased, fewer nanoparticles assemble and the particles remain isolated.

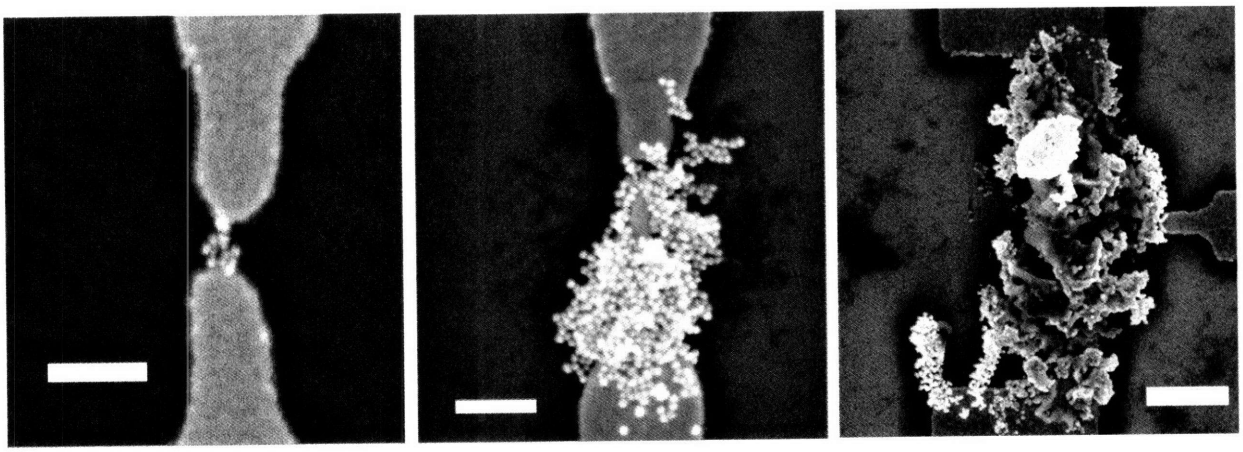

Figure 4.5: SEM images of assembly as a function of frequency. Assembly increases drastically with decreasing frequency. 120 seconds, 3.5 V_{pp}, ~100 nm gap size, 7×10^{10} particles/ml, 1 MHz (left), 100 kHz (center), 10 kHz (right). Scale bar = 200 nm (left and center). Scale bar =500 nm (right).

4.1.2 Theoretical Modeling of Dielectrophoresis of Nanoparticle Assembly

Control over the number of nanoparticles assembled in a gap as a functional of experimental variables can be better achieved with an understanding of the forces which effect particle transport during dielectrophoretic assembly. Here, we explore the effect of several key forces on particle transport; the dielectrophoretic force, the electrostatic repulsive force between the particles and the substrate and the thermal force. We explore the regions of space over which each force becomes dominant.

In modeling the assembly of nanoparticles in the gap we consider the concentration of particles as a function of time and radial distance from the gap. The flux of nanoparticles is related to their diffusion due to thermal motion and the effect of forces acting on these particles. In our system, the dielectrophoretic force and electrophoresis force and electrostatic repulsive force affect nanoparticle transport.

For each of these forces, it is helpful to look at their relative importance and the region of space over which the force becomes dominant. As described previously, for a spherical particle of radius R, in media of permittivity ε_m, acted upon by applied field $\mathbf{E}_0$, the DEP force is given by:

$$\mathbf{F}_{DEP} = 2\pi\varepsilon_m R^3 \,\mathrm{Re}\left\{\underline{CM}(\omega)\nabla\underline{E}_0^2(\mathbf{r},\omega)\right\}$$

Here, $\underline{CM}$ denotes the Clausius-Mossotti factor, in this case given by:

$$\underline{CM}(\omega) = \frac{\underline{\varepsilon}_p - \underline{\varepsilon}_m}{\underline{\varepsilon}_p + 2\underline{\varepsilon}_m}$$

where $\underline{\varepsilon}_p$ and $\underline{\varepsilon}_m$ are the complex permittivities of the particle and media, respectively. For the case of perfectly conducting spheres, as for the gold particles here, the CM factor reduces to unity. The gradient of the electrical field is calculated using idealized gap geometries and a finite element model. For the gap geometries used in this experiment, the field decays as r^{-4}. The DEP force is found to be significant compared to the thermal force for a few hundreds of nanometers.

The effect of the electrophoretic force is mostly offset by the use of AC dielectrophoresis at high frequencies. The negatively charged particles do not move significantly towards either electrode as the field polarity changes rapidly.

The negative zeta potentials of the citrate-stabilized Au nanoparticles,[175] the gold electrode[176] and SiO_2 surface[177] creates an electrostatic repulsion between the particles and the substrate. This electrostatic force will hinder the assembly of the particles. In

contrast to DEP however, it is found to be a more localized force, affecting the particles at distances of only a few tens of nanometers from the substrate.

Modeling the assembly of particles as a function of voltage indicates the presence of a threshold voltage for particle assembly. The DEP force is a function of electric field gradient so it is ultimately a function of assembly voltage. The electrostatic repulsive force is constant as it depends only on the charges of the particles and surfaces. When the electrostatic repulsive force is greater than the DEP force, assembly is blocked. When the DEP force exceeds the electrostatic force, nanoparticle assembly is achieved. For this latter case, it is necessary to look at the region of space where the DEP force is greater than the thermal force, a region dubbed the region of influence (ROI). Once a particle reaches the ROI, it is quickly swept into the gap. This reduces the model to a diffusion problem. When a particle diffuses into the ROI, it is quickly assembled. For a more detailed description of the theoretical models and detailed procedure please see reference 174.

4.1.3. Correlation of Experiment to Theoretical Model

4.1.3.1 Assembly as a function of Voltage and Concentration - Fused vs. Isolated Particles

The observation of fusing as a function of voltage and nanoparticle concentration suggests that nanoparticle melting is due to Joule heating. Once a critical number of

nanoparticles is reached, high currents are able to pass through the assembly. The high current passing through these particles causes localized melting and the formation of conductive metallic bridges. At lower V_{pp}, the current is not large enough to cause melting. At lower nanoparticle concentrations, a larger DEP force (higher peak-to-peak voltages) is needed to assemble the number of nanoparticles necessary for the current density required for melting.

4.1.3.2 Assembly as a function of Voltage and Gap Width

Figure 4.3 shows experimental data points for the number of particles assembled as a function of V_{pp} and gap width along with the predictions of the model at the average gap width of each experimental range (30 nm, 85 nm and 125 nm). Given the many differences between the set-up assumed in the model (idealized gap geometries, no inter-particle interactions, induced flows, or electrochemical reactions) and that used in experiments, good agreement is achieved mostly in predicting the threshold voltages required for assembly.

The appearance of a voltage threshold for particle assembly in both the experimental and theoretical work shows the significance of electrostatic repulsion between the particles and the electrode/substrate surfaces. In the absence of any electrostatic force, nanoparticle assembly would occur down to very low voltages, since the DEP force only needs to overcome the random thermal motion of the particles. Also, in the absence of electrostatic forces our model predicts that the number of particles assembled should be independent of gap size at this length scale (see discussion below). The dependence of

this voltage threshold on the size of the gap supports the idea that the DEP force must reach a critical value to overcome the electrostatic repulsion between charged particles and surfaces.

For voltages exceeding the threshold, the number of particles assembled appears to be largely independent of the gap size. In terms of the model we propose, this represents the relatively weak dependence of the size of the ROI on the size of the gap; while smaller gaps produce a stronger, more confined DEP force for a given voltage, larger gaps produce a weaker DEP force which acts over a larger area. Simulations show that this independence of gap size, after the threshold voltage is reached, is approximately true for gaps up to 150 nm, and is corroborated by experimental observation.

The model slightly over-predicts the observed threshold for the smallest gap sizes. Gap sizes were measured at their narrowest width. In many cases, this smallest gap size is not the average gap size. The model assumes a uniform gap at the smallest size. This would overestimate the electrostatic repulsion felt by the particles from the electrode surface as compared with the experimental reality, causing the shift seen in the threshold. This effect would be expected to be greatest for the narrowest gaps, as small changes in gap width result in large changes in the electrostatic repulsive force.

The model also seems to slightly under-predict the number of assembled particles at V_{pp}=4.5 and above. At higher voltages, irreversible water dissociation may become a

factor, leading to the generation of protons which weakens the electrostatic repulsion term.[178]

4.1.3.3 Assembly as a function of time

Previous works have used a resistor in series with the gap to make DEP assembly self-limiting.[11, 101, 103, 104] In these works, the assembled particles were significantly larger than the gaps onto which they were assembled, allowing for a single particle to bridge the gap. This creates a low resistance bridge. Preliminary experiments using a 1 kΩ to 1 MΩ resistor in series with our gaps have shown no self-limiting behavior. This is likely due to the ratio of gap size to nanoparticle radius in our system. Our gaps are larger or the same size as the diameter of our particle, making it difficult for a single particle to bridge the gap. The nanoparticle bridges we formed have higher resistances (2.5 MΩ to 60 GΩ) than the resistors we placed in series with the gap. Future experiments will use smaller gap sizes to enable single particle assembly.

To achieve assembly of a small number of particles we decided to operate near the threshold voltage. As seen in figure 3, there is a rather steep increase in the number of assembled particles assembled when operating for 120 s. Hence it was necessary to limit the assembly time to achieve the assembly of <10 nanoparticles.

4.1.3.4 Assembly as a function of frequency

At low frequencies, assembly was found to drastically increase. A counter ion cloud surrounds the particles, which at low frequencies can respond to changes in the electrical field.[98, 100] This counter ion cloud increases the effective radius of the particle, thereby increasing the DEP force, which scales as r^3.

Another potential factor contributing to the frequency dependence is the existence of induced charge electroosmosis (ICEO) flows, caused by the movement of counterions which form the double layer on the electrode surface by the applied electric field.[174] At low frequencies, where greater amounts of charge accumulate in the double layer around the electrodes, ICEO flows would be expected to play a larger role. These flows potentially change the system dynamics and increase nanoparticle assembly.

We have modeled and demonstrated the effect of voltage and gap size on the assembly of 20 nm diameter gold nanoparticles into nanogaps. The model accurately describes our experimental results with regard to the threshold voltage required for nanoparticle assembly. The assembly as a function of time and frequency has been discussed. The fabrication of smaller gaps will allow for the assembly of single particles. Future improvements to the theoretical study will include consideration of induced flows, inter-particle repulsions and electrochemical reactions. Future experimental studies on controlled assembly will analyze parameters such as temperature and electrode geometry. The controlled assembly of citrate coated particles has both interesting basic research and technological implications. It also serves as a model system to understand which forces are dominant in the DEP of nanoparticles into gaps. This understanding can be used for

the controlled assembly of smaller nanoparticles and nanoparticles stabilized with ligands with different chemical functionalities or biologically significant molecules.

4.1.3 Assembly of Ligand Coated Nanoparticles

In order to use nanoparticles for technological applications, ligand functionalized particles must be assembled in the gap. For electronic applications the choice of ligand may allow for metallic, semiconducting or insulating particles to be assembled in the gap. For biological sensing applications, nanoparticles functionalized with selective probe molecules must be assembled in gaps. The ability to selectively assemble different types of particles in different gaps on the same substrate will also be critical for technological applications.

In this particular work, as biological sensing applications were targeted, water soluble nanoparticles were studied. Nanoparticles with 20 nm core diameters were synthesized and subsequently functionalized with a 1:1 ratio of mercaptoundecanoic sulfonate (MUS, SO_3-$(CH_2)_{11}$-SH): mercaptopropionic sulfonate (MPS, SO_3-$(CH_2)_3$-SH). Particles with 7 nm core diameters were also functionalized with a 1:1 ratio of MUS:MPS. A third set of nanoparticles with 13 nm core diameters were synthesized using the Frens method.[3] After synthesis, single-stranded thiolated 18 mer DNA was place exchanged onto the particles.[179] The nanogaps used for this study were either 1.) directly patterned by electron beam lithography and having gap sizes of 60-100 nm or 2.) formed by electrical methods of breaking a 2 μm wide optically defined wire having gap sizes of 20-50 nm. DEP was used to assemble particles into nanogaps as described in section 4.1.1.

Ligand functionalized particles could successfully be assembled in nanogaps and showed similar behavior to the citrate stabilized nanoparticles. Figures 4.6-4.8 show the assembly of particles as a function of peak-peak assembly voltage.

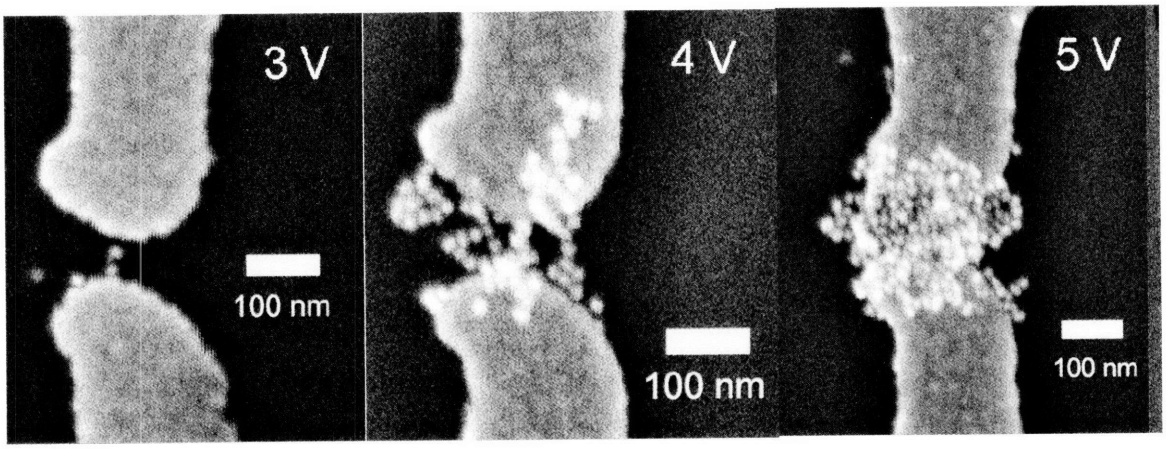

Figure 4.6: DEP assembly of 20 nm particles functionalized with a 1:1 ratio of MUS to MPS as a function of assembly voltage. Assemblies were carried out at 1MHz for 240 seconds.

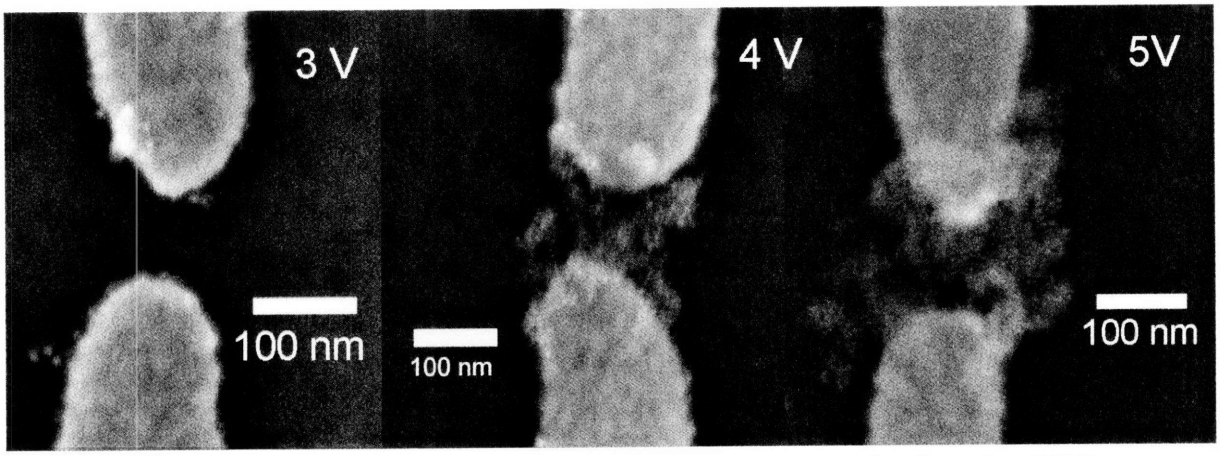

Figure 4.7: DEP assembly of 7 nm particles functionalized with a 1:1 ratio of MUS to MPS as a function of assembly voltage. Assemblies were carried out at 1MHz for 120 seconds.

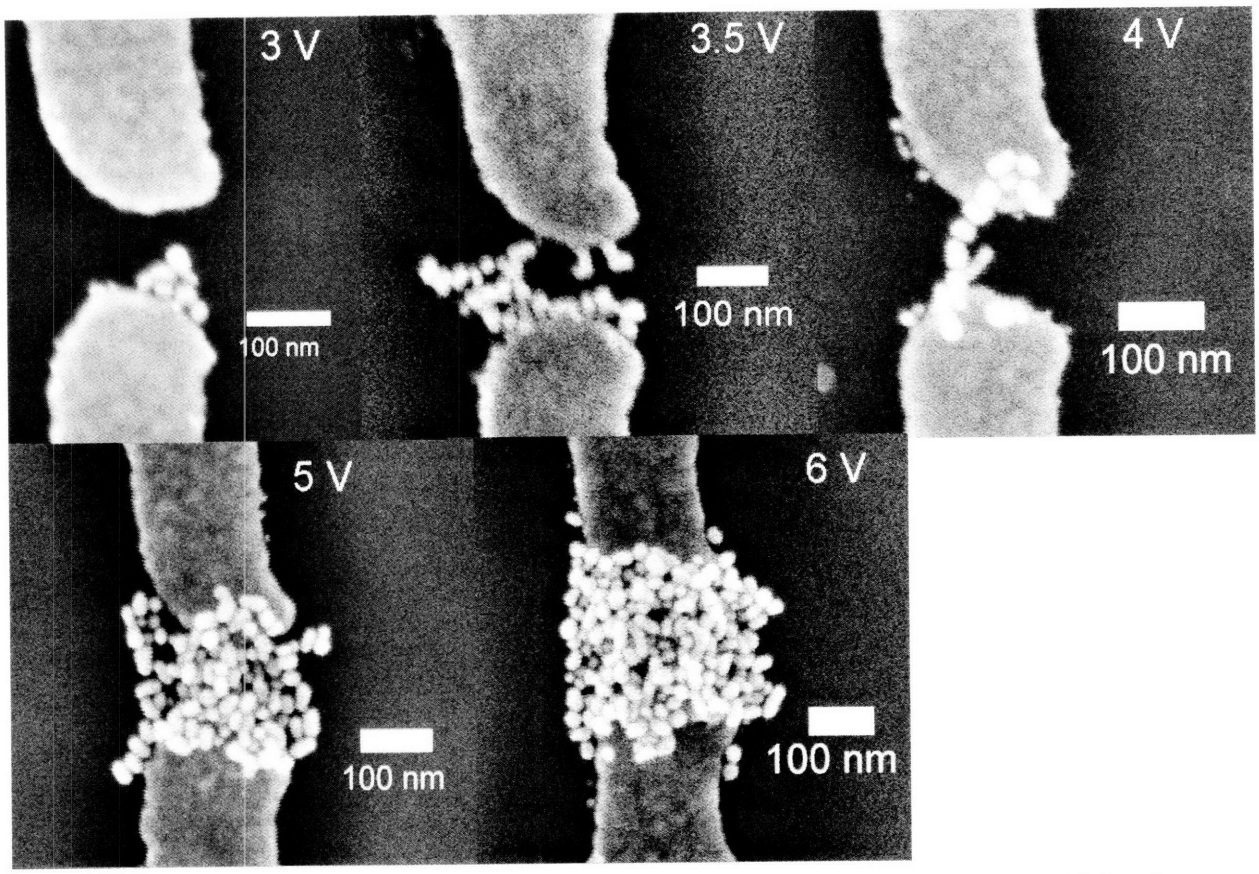

Figure 4.8: DEP assembly of 13 nm particles functionalized with 18 mer single-stranded thiolated DNA as a function of assembly voltage. Assemblies were carried out at 1MHz for 60 seconds.

Two characteristics of the assembly are worth noting. Similar to the citrate stabilized particles, the number of particles assembled increases as a function of assembly voltage. As voltage is increased, the electric field and gradient of the electric field increases. As the DEP force is proportional to the gradient of the electric field squared, assembly will increase as the applied AC voltage increases.

The ligand coated particles also show a threshold voltage which must be reached in order to begin to see assembly. For these three types of particles, the threshold for assembly is between 3 and 4 V_{pp}. For citrate stabilized particles, the threshold voltage for these size

gaps is found to be 3 V_{pp}. For the smaller particles, the radius of the particle can explain the increased threshold voltage. The DEP force on a sphere depends on r^3, so the smaller particles will feel a smaller DEP force.

Electrostatic interactions will also play a significant role in determining the threshold voltage. As the ligands placed on these particles are negatively charged, they will feel a substrate particle repulsion and particle-particle repulsion. As the 20 nm MUS:MPS particles have a larger threshold voltage than the 20 nm citrate particles, it is likely they have a more negative zeta potential. This can be explained in part by the location of the charge in relationship to the particle center. In the citrate particle, negative charge is on the surface of the particle, while the negatively charged SO_3^- sits 1.5 nm away from the core due to the MUS molecule. This may increase the effective zeta potential of the MUS:MPS particles. As the 7 nm and 20 nm MUS:MPS particle show similar threshold voltage, electrostatic interactions may dominate over size effects in determining the threshold voltage for these particles.

Ligand coated nanoparticle could also be achieved on gaps formed by electrical breaking of optically defined wires. Figure 4.9 shows the assembly of 7 nm MUS: MPS particles and 13 nm DNA functionalized particles in such gaps. Due to the irregular shape of these gaps, voltages series do not produce such predictable results, although particle assembly is still seen to increase with increasing voltage. Nanoparticle assembly occurs first at areas of the gap with smaller gap sizes, where the electric fields are the strongest. As gap sizes and thus electrical fields are generally smaller on these 20-30 nm gaps, assembly

can usually be achieved with lower threshold voltages than on the larger gaps defined by electron beam lithography.

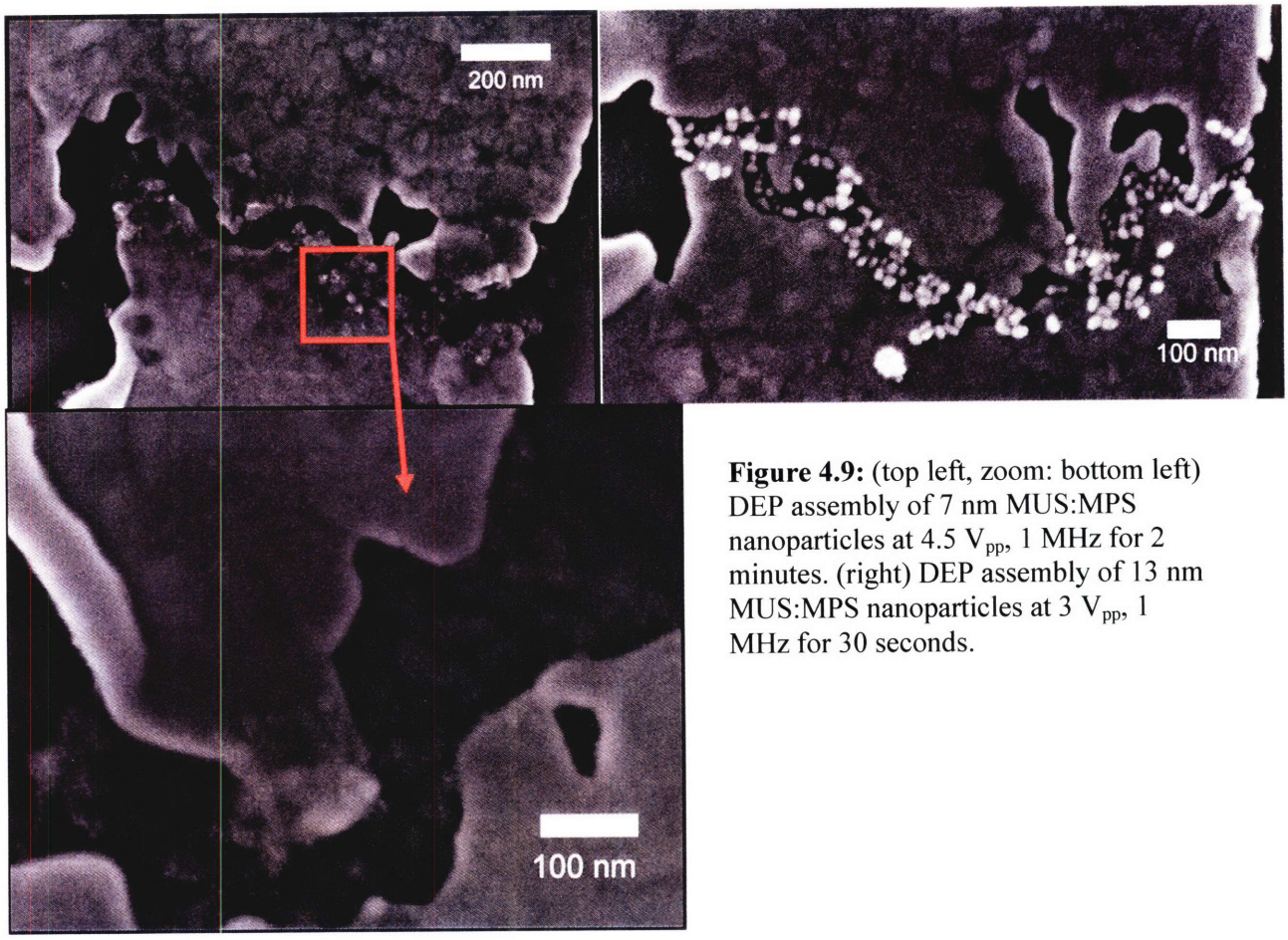

Figure 4.9: (top left, zoom: bottom left) DEP assembly of 7 nm MUS:MPS nanoparticles at 4.5 V_{pp}, 1 MHz for 2 minutes. (right) DEP assembly of 13 nm MUS:MPS nanoparticles at 3 V_{pp}, 1 MHz for 30 seconds.

Assembly of two different types of nanoparticles into different devices on the same substrate has been achieved. The 20 nm and 7 nm MUS:MPS particles were chosen so

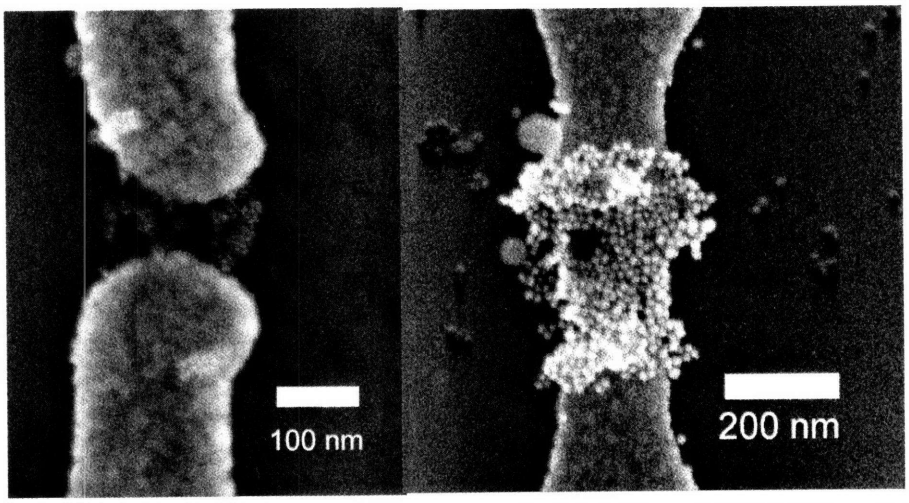

Figure 4.10: DEP assembly of (left) 7 nm and (right) 20 nm MUS:MPS particles on two devices on the same substrate. 7 nm particles were assembled at 4 V_{pp}, 1 MHz for 2 minutes. 20 nm particles were assembled at 6 V_{pp} for 4 minutes.

the assembly of the two types of particles could be easily confirmed by SEM imaging. After the assembly of the 20 nm particles into device A, the drop of 20 nm particles was removed. A drop of 7 nm particles was placed onto the substrate and an alternating voltage was applied across gap B. Figure 4.11 shows the assembly of the two types of particles into different gaps on the same substrate. The 20 nm particles show some degree of hexagonal packing. Spacings between the particle cores due to the ligand shell can be seen.

4.2 Electrical Characterization of Nanoparticle Assemblies

The electrical characterization of the nanoparticles bridging the nanogaps is critical for device applications. In order to use these assemblies in devices, methods to make reliable

contact to the particles and achieve the desired electronic properties are extremely important.

The assembly of nanoparticles in a gap was characterized in the dry state at room temperature with DC IV measurements between 0 and 300 mV prior to SEM imaging. Many of the early attempts at DEP assembly of citrate stabilized nanoparticles in a gap showed puzzling electrical characteristics. Even though SEM images revealed hundreds of closely packed particles bridging the gaps, resistances of the devices at 300 mV were greater than 300 GΩ. Surface contamination of the gold electrodes likely played a large role in the high resistance. Before being coated with the self-assembled monolayer, electrodes were cleaned for 10 minutes in an O_2 plasma cleaner, followed by soaking for 90 minutes in ethanol. This removes some of the organic contamination, allowing the dithiol molecules to bind to the electrode surface and removing the additional organic contamination which serves as an insulating tunneling barrier. This cleaning procedure resulted in a much greater percentage of conductive devices after particle assembly. The 20 nm citrate stabilized particles generally showed a resistance of 500 kΩ to 60 GΩ.[103, 104] (figure 4.11) (Fused particle assemblies showed much lower resistances generally 100-1000 Ω, as discussed in section 4.1.1.1, but these type of assemblies do not consist of isolated particles and are not considered here) Using higher applied voltages led to more nanoparticle assembly and lower-resistance devices. These devices were measured in the dry state 16 hours after assembly. The current levels of the devices were stable up to 20 electrical sweeps.

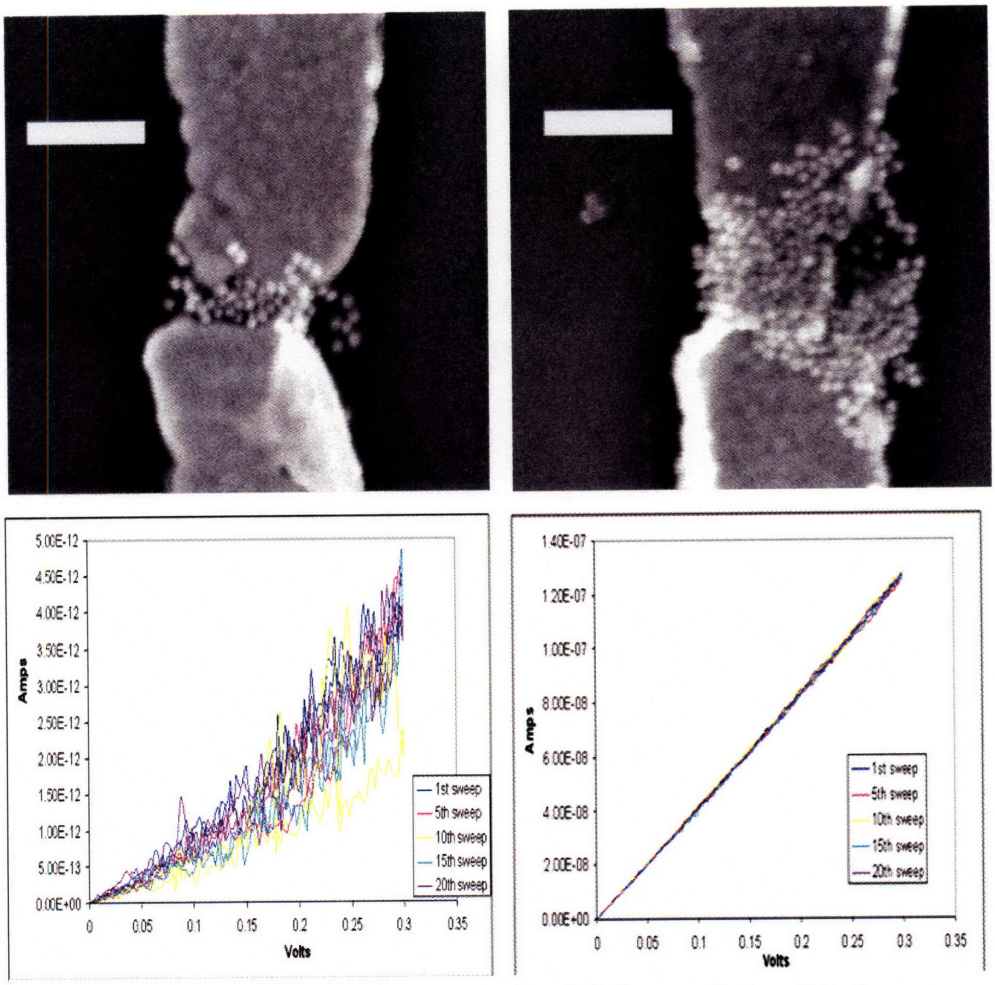

Figure 4.11: SEM images and corresponding IV characteristics of devices assembled using DEP of citrate stabilized particles. Stable current levels are seen through 20 electrical sweeps. Scale bar=200 nm.

Electrical characterization of ligand coated nanoparticles showed different results. Nanoparticle assemblies of 7 and 20 nm MUS:MPS particles are shown in the preceding section in figures 4.6, 4.7, and 4.10. Even though hundreds of densely packed bridge the gap in many of these assemblies, resistances in all of the pictured devices were found to be higher than what could be measured on our probe station (300 GΩ) for these 60-100 nm gaps. The use of the smaller gaps formed by electrical methods allowed for some characterization of the electrical properties of these particles, but the assembly of

electrically "live" devices was inconsistent. 9/32 (28%) of devices assembled with 7 nm particles showed resistances ranging from 500 kΩ to 60 GΩ. This type of poor conductance from a single layer of ligand coated nanoparticles has been seen previously.[132, 133]

Electrical characterization of 13 nm DNA functionalized particles showed similar results to those of the citrate particles, but generally having resistances 1-2 orders of magnitude higher. (300 GΩ – 30 MΩ at 300 mV). IV curves showed linear behavior and were stable for multiple measurements. As more particles assembled at higher applied peak-peak voltages, resistance of the assemblies decreased. Figure 4.12 illustrates this trend for the voltage series seen in figure 4.8. Assemblies on electrically broken gaps generally showed higher current levels, likely due to the smaller gaps.

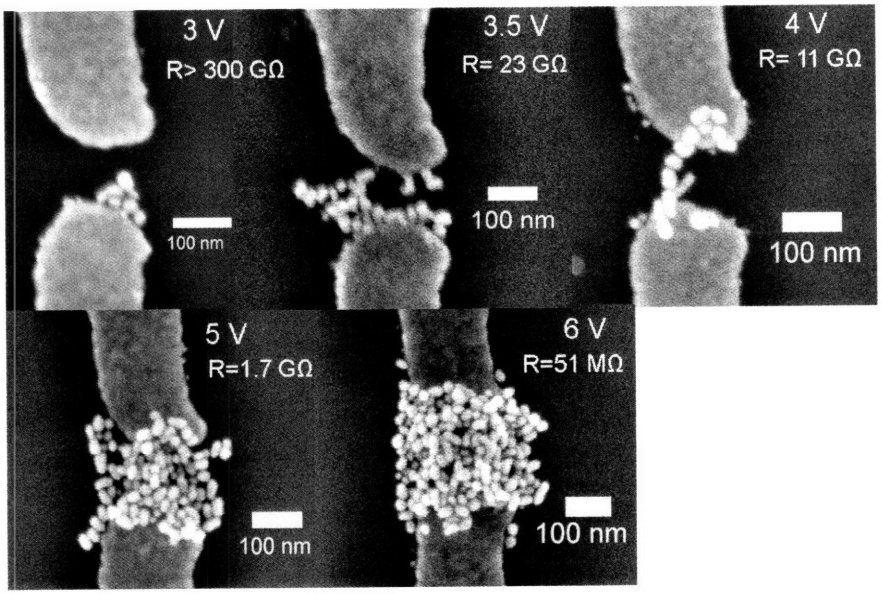

Figure 4.12: Electrical characterization of 13 nm DNA functionalized nanoparticles showing decreased resistance with an increased number of assembled particles.

It is interesting to note that after SEM imaging resistance of these devices dropped by 3-5 orders of magnitude. This maybe due to the build-up of amorphous carbon when high magnification SEM images were taken.[148] The amorphous carbon may bridge the space between electrodes and the adjacent nanoparticles, allowing for electrons to travel through the device. Gaps without nanoparticles did not show similar improvements in conductance, suggesting that the deposited amorphous carbon can only bridge short distance between assembled nanoparticles.

The different resistances of the different types of particles can be explained based on the ligand length and conformation. Citrate ions are very small molecules (figure 4.13) which bind electrostatically to the particle core, lying flat along its surface. This gives a very small barrier in between particles and explains the higher conductance of these assemblies. This weak type of ionic stabilization may be removed during assembly in solution, thus allowing for some gold core- gold core contact further lowering resistance. MUS, the longer of the two ligands on the 7 and 20 nm particles, has a length of ~1.5 nm. Thiolated molecules form well-packed monolayers on gold nanoparticles, with the thiol group binding to the gold core and the molecule extending radially outwards. MUS is composed primarily of an insulating alkane thiol backbone. If no inter-digitation occurs between ligands, the metallic cores of the nanoparticles would be separated by 3 nm. (Little inter-digitation would be expected due to the electrostatic repulsion between neighboring sulfonate groups.) Electron tunneling through a series of 3 nm insulating barriers would be negligible, explaining the high resistance (for the 7 nm particles, a

minimum of 6 gaps would need to be traversed to cross a 60 nm gap). On the basis of length alone, therefore, the DNA coated nanoparticles should show the lowest conductance, as an 18 mer DNA has a length of ~6 nm. DNA, however, does not form a well packed monolayer on nanoparticle surfaces.[142, 143] The DNA backbone wraps around the particle. This considerably shortens the distance an electron must tunnel through to get from one metallic core to the next. The disordered DNA also may allow for some gold core-gold core contact.

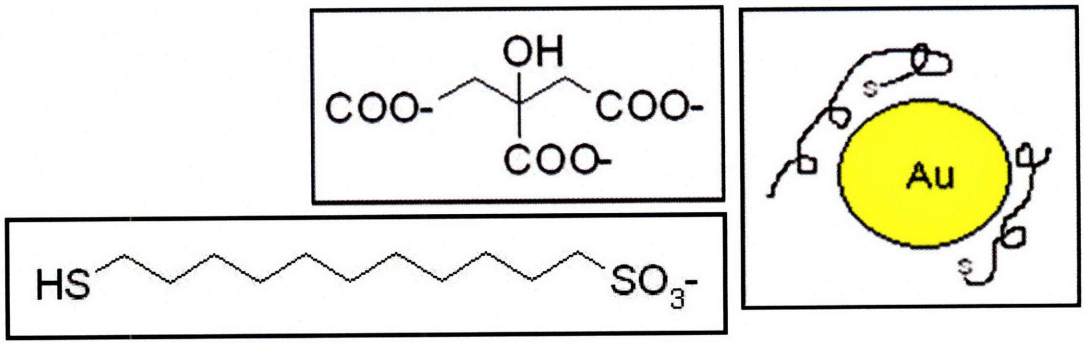

Figure 4.13: (top left) The small prone-lying citrate ion allows for short core-core separation. (bottom left) The long radially oriented MUS molecules may cause a core to core spacing of up to 3 nm. (right) The spaghetti-like conformation of DNA allows for short electron tunneling distances.

As small changes in gap sizes and arrangements of nanoparticles may produce large changes in electrical properties of the assemblies, it is useful to look at trends in series of assemblies. Figure 4.14 shows the resistances of DNA functionalized 13 nm diameter nanoparticles assemblies in nanogaps as a function of the DEP peak-peak voltage used for assembly. The graph shows that for both ebeam and electrically patterned gaps, an increase in assembly voltage leads to more particles and lower resistance. For a given V_{pp}, the small electrically defined gaps show a lower resistance. For biological sensing applications, described in chapter 5, it was desired to have nanoparticle assemblies with

resistances of 3MΩ – 300 MΩ, with values as high as 3 GΩ acceptable. Using the optimized voltages ranges for each type of gap (4-5 V for electrically patterned gaps , 5.5-6.5 V for ebeam patterned gaps), 33/60 (55%) assemblies were within the target range and 42/60 (70%) of devices were within the acceptable range. While this yield and the large acceptable current range are not yet ready for manufacturability, DEP assemblies do hold the promise of controllable electrical properties from functionalized particles.

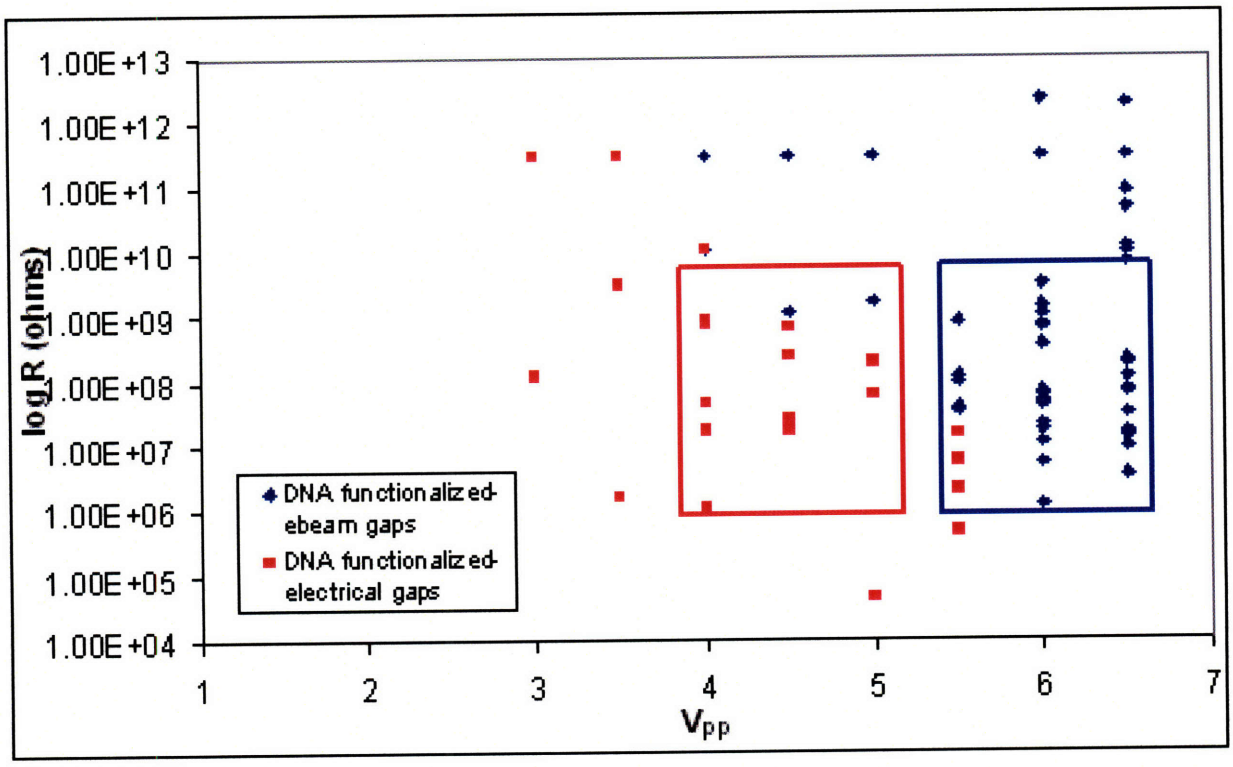

Figure 4.14: Plot of post assembly device resistance at 300 mV vs DEP peak-peak voltage. Red square shows device with acceptable R values in the optimized voltage range for electrically patterned gaps. Blue square shows device with acceptable R values in the optimized voltage range for ebeam defined gaps.

Chapter 5: Potential for Biological Sensing

The ability to nanomanufacture devices with nano-objects bridging a nanogap will allow for significant improvements in logic and sensing devices. In this chapter, the use of nanomanufactured devices incorporating ligand stabilized gold nanoparticles for DNA sensing is described. Experimental conditions are discussed, preliminary results are presented and strategies for future experiments and devices are outlined.

DNA sensing today relies on the use of microarrays. While microarrays are a mature and valuable technology, due to their reliance on optical based detection, they have several intrinsic limitations. The ultimate sensitivity of such a device is limited by the need for large spot sizes required for optical based detection. Optical signals also must be transferred into electronic "0 or 1" signals for computer analysis, limiting the speed of such a device. Finally, the large fluorescent microscopes needed for microarrays make the portability of the sensing device poor. Electrical based detection of DNA could offer potential advantages in sensitivity, speed and device portability.

Several groups have used AC impedance spectroscopy of DNA monolayers on gold surfaces in an attempt to electrically detect DNA.[180-184] While this approach may provide speed and mobility advantages, due to the large number of probe molecules attached to the gold surfaces, sensitivity improvements may be minimal. As described in chapter 1, other groups have shown DNA detection based on the optical properties of ligand coated gold nanoparticles.[143, 144, 146] While these devices offer some sensitivity

advantages, they are ultimately hampered by the previously mentioned limitations of optical based sensing.

DNA sensing via the electrical properties of ligand coated gold nanoparticles may potentially offer the ultimate in sensing capabilities. Feldheim demonstrated that nanoparticles electrical properties can be altered by changing the charge on the ligand molecule.[135] The hybridization of a strand of DNA, with its highly negatively charged phosphate backbone, may produce similar effects on the nanoparticle properties. The conformational change that DNA undergoes upon hybridization (random coil to rigid rod) may have large effects on the resistance or capacitance of the Au-nanoparticle conjugates. Due to these large changes that would occur in the ligand shell upon the hybridization, nanoparticle electrical properties may be significantly altered by the hybridization of a single strand of complementary DNA.

Nanoparticle based electrical detection also offers the ability to directly interface with the binary computer based logic. The change of the relevant property could be monitored, giving a "0 or 1" detection scheme. Finally, smaller electrical characterization equipment may allow for portable field-based DNA detection.

In a very recent work, Brousseau showed that the electrical properties of a 5 nm diameter gold nanoparticle-oglionucleotide conjugate could be used for DNA sensing.[185] Single electron charging was seen in these devices. Upon DNA hybridization a 50% reduction in the charging voltage needed to overcome the Coulomb blockade was observed and

attributed to the presence of additional negative charge from the complementary oglionucleotide. (figure 5.1) The device, however was made of large electrodes and gold beads, with a nanogap size controlled by piezoelectric actuators. It would be difficult to imagine a technologically scaleable array of devices constructed in such a manner. The combination of Au nanoparticle based DNA sensing with nanomanufacturing techniques could allow for sensing devices which have a large technological impact.

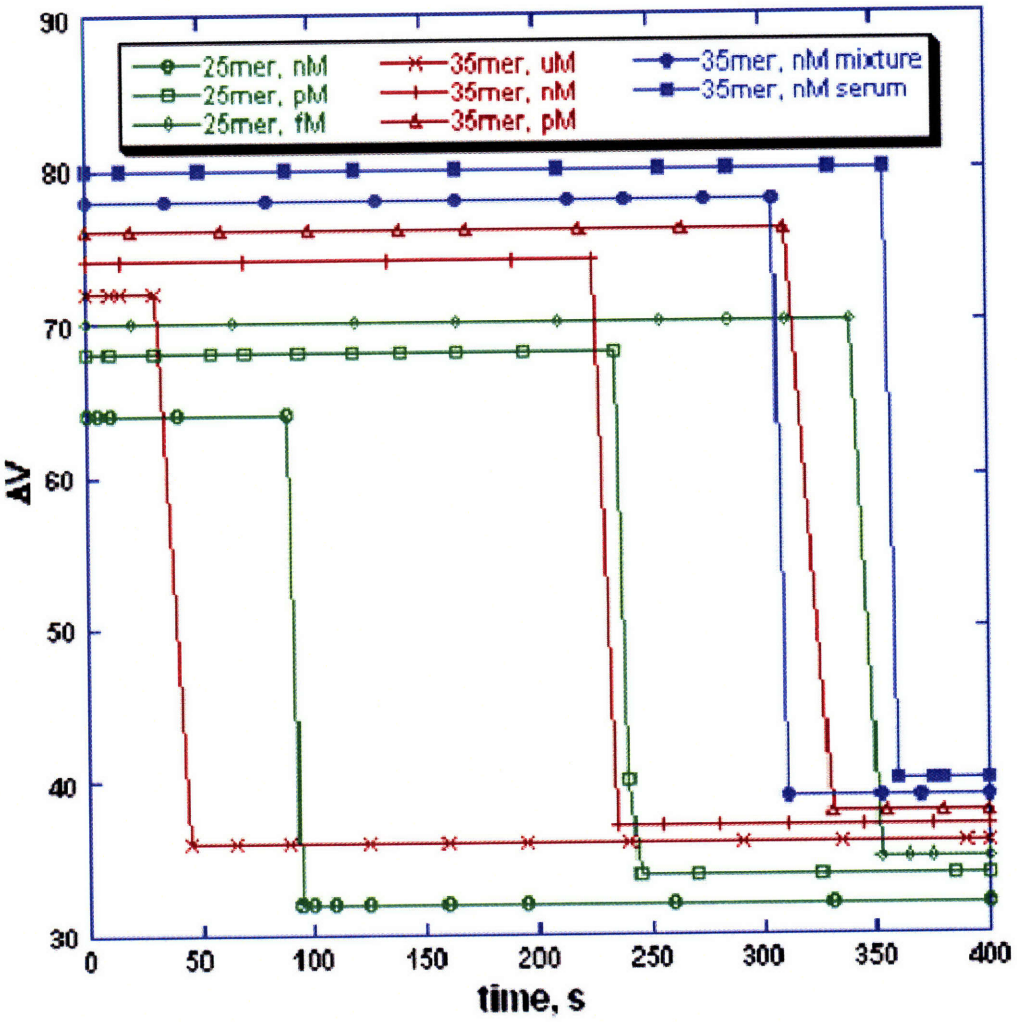

Figure 5.1: Brousseau's results showing reduction in charging energy (in mV) of a single electron transistor consisting of a nanoparticle-DNA conjugate as a function of a.) time after the introduction of the complementary strand and b.) concentration of the complementary strand in PBS. Figure courtesy of reference 185.

5.1 Experimental Considerations

13 nm diameter, citrate stabilized gold nanoparticles were prepared using the Frens method. Water soluble nanoparticles were required for functionalization with DNA.

Citrate stabilized nanoparticles were chosen due to their higher conductivity as compared to their water soluble thiol stabilized counterparts, as described in section 4.2.

Citrate particles were functionalized with oglionucleotides following procedures from the literature.[179] Briefly, the concentration of the as synthesized citrate stabilized particles was determined using UV-Vis. The absorbance of the nanoparticles at 510 nm is directly proportional to concentration. The absorbance strength was compared to commercially purchased citrate particles with known concentrations. The particle was then diluted to 6 nM with DI water. A 40 μM solution of 18 mer thiolated single stranded DNA in DI water was further diluted and then added to the particles with to achieve a certain oglionucleotides: nanoparticle ratio. For one set of nanoparticles, a huge excess of DNA/ per particle was added ($>10^5$ oglionucleotide strands/ nanoparticle) to achieve the maximum number of DNA strands per particle. DNA-nanoparticle conjugate ratios were also made with a 4:1 oglionucleotide: nanoparticle ratio.

The effect of oglionucleotide functionalization on the nanoparticles can be seen with UV-Vis. As shown in figure 5.2, the surface plasmon peak at ~520 nm remains strong, indicating the particle core has not been affected. The additional peak at 260 nm can be attributed to the presence of DNA.

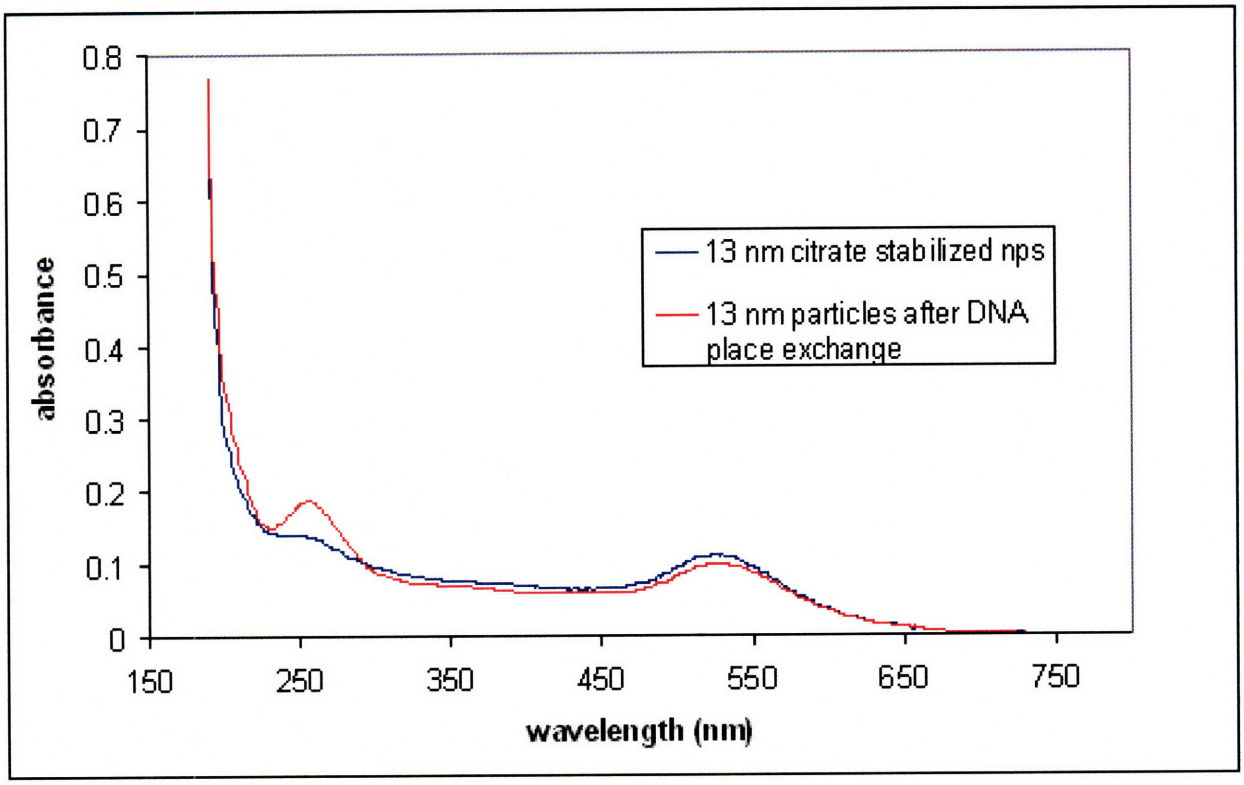

Figure 5.2: UV-Vis absorbance curves of citrate stabilized particles before and after functionalization with DNA.

Additional evidence of the successful functionalization of the particles with excess DNA can be obtained through solubility studies. Adding a 0.3 M aqueous NaCl solution to the citrate particles causes a change in the color of the solution from red to purple to a murky black to a clear solution with a black precipitate. This change occurs with 2-3 minutes of the addition of the NaCl solution. The electrostatically stabilized particles are no longer soluble in the high ionic strength salt solution. After functionalization with DNA however, the particles remain completely soluble when the NaCl solution is added. The thiol protected particles are stable against precipitation in the salt solution.

A major consideration for devices to be used for biological sensing is the ability to make measurements in an aqueous environment. DNA hybridization occurs best in a high ionic

strength pH buffered aqueous solution. Real-time detection of DNA will only be possible in the electrical properties of the nanoparticle can be measured in the aqueous salt solution. This prevents difficulties due to ionic conductance through the salt solution. If the solution conductance is significantly large than the conductance of the nanoparticle-DNA conjugates, the electrical properties of the solution will dominate, making detection of hybridization impossible. Conduction through aqueous media is dependant on the amount of the metal surface in contact with the solution. More surface area contact results in higher solution conductance. Using the original device design (as described in chapter 2) even the smallest drop of aqueous salt solution covers the contact pads, making it necessary for the microprobe to also be in contact the with the drop of solution. This large amount of surface-drop contact results in currents from 100 nA – 5 μA at 300 mV bias, significantly higher than the currents passing through the particle assemblies.

In order to circumvent this problem a new design was needed for the devices ("spider" design, Figure 5.3) In this design, the nanogap is connected to contact pads which are 4-5 mm away from the gap via a 20-50 μm wide Au wires. Many gaps are positioned in the center of a substrate, with contact pads located on the edges. This allows for a 10-50μl drop of aqueous solution to be placed on the center of the substrate, wetting the gaps but not the contact pads. This allows for the microprobes to contact the device without being in contact with the salt buffer solution.

Two variation of this design have been used. In one variation, the thin wires and gaps are patterned by electron beam lithography with 5 nm Cr and 25 nm Au evaporated. An

optical mask is aligned to these features to pattern large, thick contact pads. For devices with narrow wires patterned by optical lithography and broken with electromigration, a single layer lithography process can be used. Both the 2 μm wires and the large 400 μm pads are patterned with a single exposure. An MPTMS adhesion layer is used followed by evaporation of 15 nm Au. Due to the strength of the MPTMS adhesion layer, it is possible to reliably contact the thin pads with microprobes, making the one step process possible.

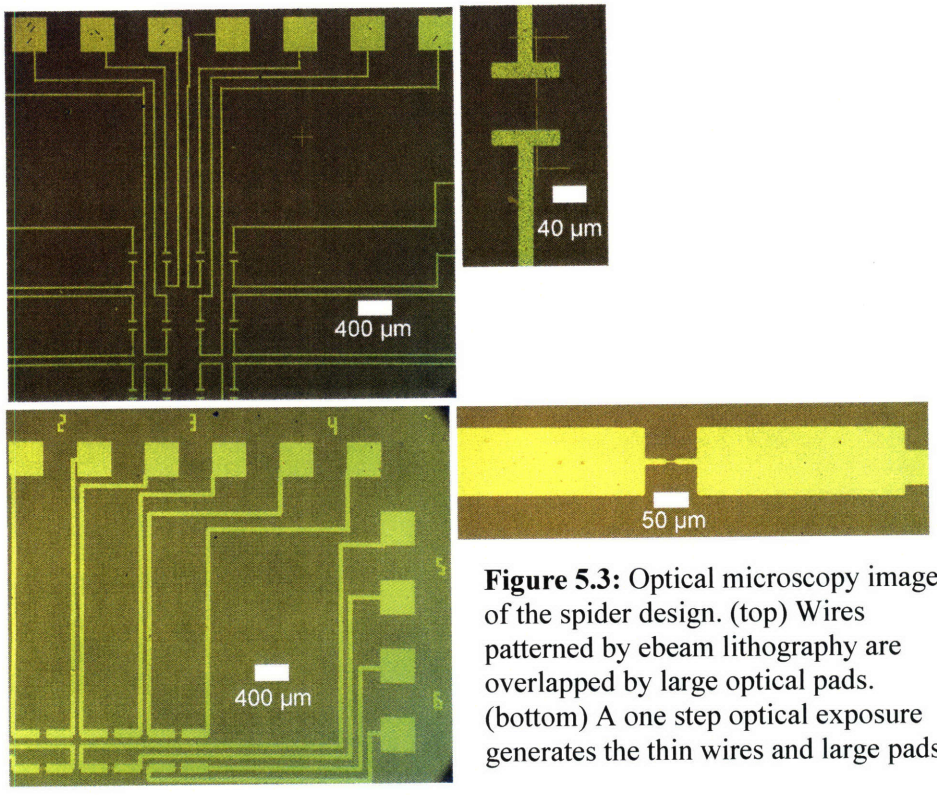

Figure 5.3: Optical microscopy images of the spider design. (top) Wires patterned by ebeam lithography are overlapped by large optical pads. (bottom) A one step optical exposure generates the thin wires and large pads

This "spider" design allows for 16 devices to be patterned on a 1 cm by 1 cm substrate. Figure 5.4 shows the decreased current levels through this design. Current levels drop to 100- 500 pA at 300 mV bias.

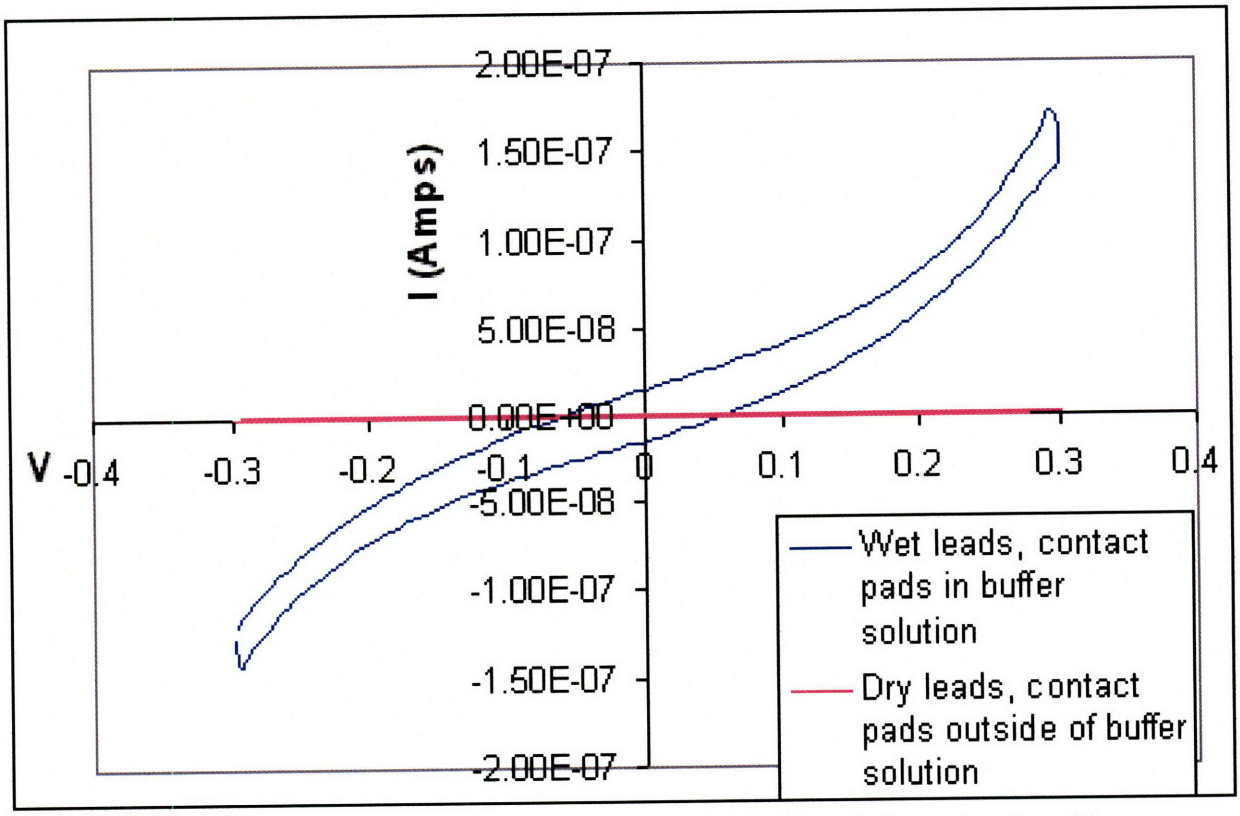

Figure 5.4: Decreasing the surface area in contact with the buffer solution using the spider design results in a 3-4 order of magnitude decrease in conductance.

Nanogaps for DNA detection were created by both direct patterning of gaps with electron beam lithography or by electrical methods of gap formation, primarily on optically defined wires. Optical lithography was performed as described previously. (Chapter 2) After gap formation, surface cleaning via UV-ozone (Chapter 4) and the formation of a dithiol monolayer to bind the particles to the leads, particles were assembled using dielectrophoresis as described in chapter 4. In order for the nanoparticle conductance to dominate over the solution conductance, assemblies with resistances of 3 MΩ- 300 MΩ

were targeted. Lower conductances were avoided as this was generally an indication of nanoparticle melting.

5.2 Electrical characterization of Au-DNA conjugates

5.2.1. AC Impedance spectroscopy

Several groups have used AC impedance spectroscopy of DNA monolayers to detect hybridization.[180-184] Detection of the hybridization event has been attributed to conductivity changes of single vs double stranded DNA, conformation changes and the ability to restrict the movement of ionic species. AC impedance spectroscopy can be used on our nanoparticle assemblies to measure the impedance at increased frequencies. Figure 5.5 shows the AC impedance and phase as a function of frequency for three devices assembled with DNA-nanoparticle conjugates. The electrical properties are stable to three sweeps taken at 30 minute intervals. The impedance of the device at low frequencies is equal to its DC resistance. As frequency increases, impedance decreases. The phase-frequency plot begins at 0° phase as expected for a conducting channel. As frequencies increases, phase decreases to -90°C, indicating capacitive behavior. A possibility for future detection schemes is the use of AC impedance spectroscopy to monitor the electrical properties of DNA-nanoparticle conjugates at high frequencies during hybridization.

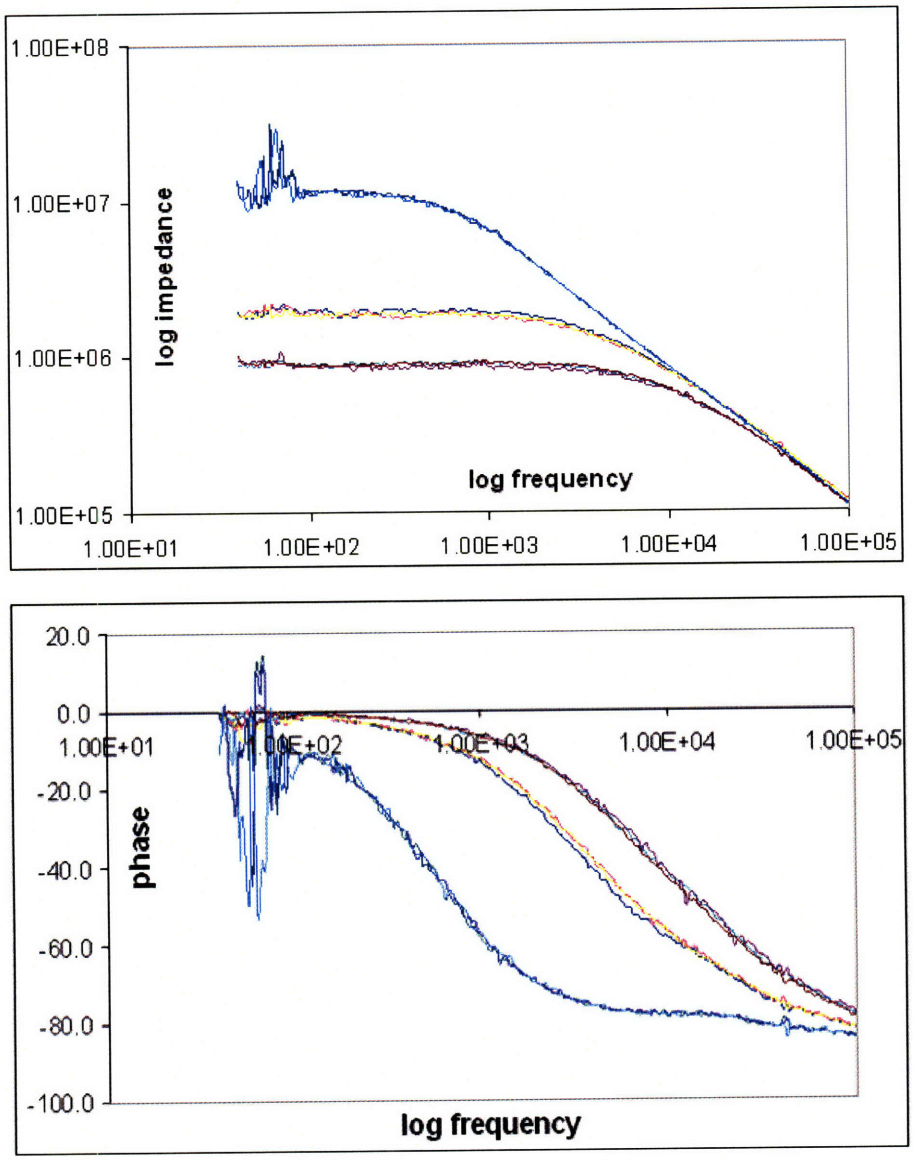

Figure 5.5: AC impedance spectroscopy on three gold-DNA conjugate assemblies. Three overlapping sweeps taken at 30 minute intervals confirm the stability of the device.

5.2.2. Electrical properties in solution

As described above, in order for real time detection of DNA hybridization, measurement of nanoparticle-oglionucleotide conjugates in solution must be performed. This has proved to be a significant challenge. Citrate stabilized nanoparticles and DNA-nanoparticle conjugates are assembled in nanogaps using DEP. Their dry electrical properties are measured at 300 mV bias. A 10- 50 μL drop of either DI water or 1 M NaCl pH buffered aqueous solution is then placed over the nanogaps. Electrical properties are then measured at 300 mV.

20 nm and 13 nm diameter citrate particles show a 10-75 % decrease in conductance (as compared to the dry value) when measured in either water or buffer solution. This is somewhat unexpected as the aqueous solution which now occupies the gaps between the particles has a higher conductivity than air. The use of particles functionalized with an excess DNA results in at least a 2-3 order magnitude decrease in conductance. (Figure 5.6) The decrease causes the gaps with particles to appear electrically identical to gaps without particles. After the drop is blown off, the assemblies remain conductive but increase in resistance by 100-1000%.

The loss of conductance in aqueous solution is likely attributable to the swelling of the nanoparticle network in solution. The particle network expands in the solvent increasing the distance between gold cores and eliminating any possible gold-gold contact. Some (but not all) particles likely re-dissolve in solution, explaining the increased resistance after drying. This effect is increased with the particle-oglionucleotide conjugates. These

particles are more soluble in the NaCl solution. The oglionucleotides may also undergo a conformational change in solution. The oglionucleotide strand may have been wrapped tightly around the particles in the dry state. In solution the DNA strand can extend, pushing away neighboring particles and making electron transport more difficult.

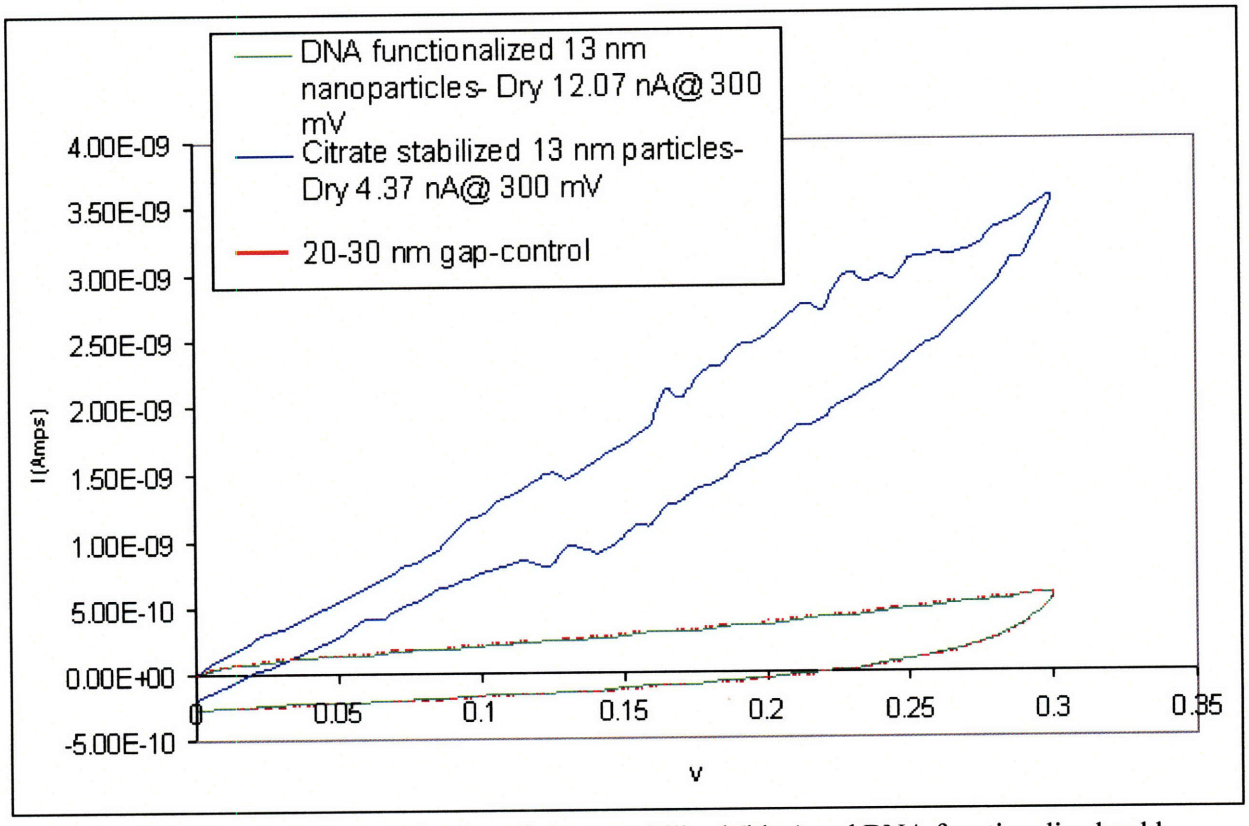

Figure 5.6: Electrical characterization of citrate stabilized (blue) and DNA functionalized gold nanoparticles in a 1M NaCl solution

A potential solution to this problem is the use of molecules which will bind the gold nanoparticles to each other, preventing the network swelling. Dithiol molecules were chosen for their ability to bind to the gold core. Longer dithiols provide the advantage of chain flexibility, increasing the likelihood of crosslinking two nanoparticles. Shorter molecules, however, might bind the particles into a tighter network. After DEP assembly was performed, substrates were immersed into a 10 mM ethanol or toluene solution of a

dithiol molecule for 12-36 hours, followed by immersion for 30-60 minutes in the same solvent.

Electrical characterization of these assemblies was again carried out while the gap was under a 10-50μL drop. Figure 5.7 shows the results of these measurements. A control open gap was measured on each sample. Due to the effect of surface area on the electrical properties, control measurements show currents from 100- 500 pA @ 300 mV bias. Only 1 such control (showing 500pA of current) is shown. Some measurements were carried out from -300 mV to 300 mV while others were performed from 0 mV to 300 mV.

Ethanedithiol, hexanedithiol, nonanedithiol and 1, 4 benzenedimethanethiol had no effect on the electrical properties of the assembly. For each molecule, the electrical properties of assembled particles are identical to the control gap on that sample. It is possible that the dithiol molecules bind both of its thiol groups to the same particle, thus having no crosslinking effect. Alternatively, the thiol-gold bond may not be able to withstand the high electric fields or the nanoparticle's thermodynamic driving force to re-dissolve.

1,4 benzenedithiol (BDT) showed an interesting electrical behavior, with the presence of steps in current levels (the steps occur at 100 mV and -100 mV in the curve below.) The presence and position of these current steps were dependent on the measurement rate and on the amount of contact between the drop and the gold wire, suggesting an electrochemical charging event. The presence of the step, however, was not found to be dependent on the presence of nanoparticles. Open gaps with large amounts of electrode

surface contacting the drop also showed the charging step. This indicates that the effect is dependent on the presence of BDT. Some BDT molecules bind to the gold electrodes. The current step may be due to the charging of the benzene group with an extra electron. A conductive pathway of nanoparticles slightly enhanced the step (allowing it to occur with less electrode-drop contact) but this effect was inconsistent and unreliable.

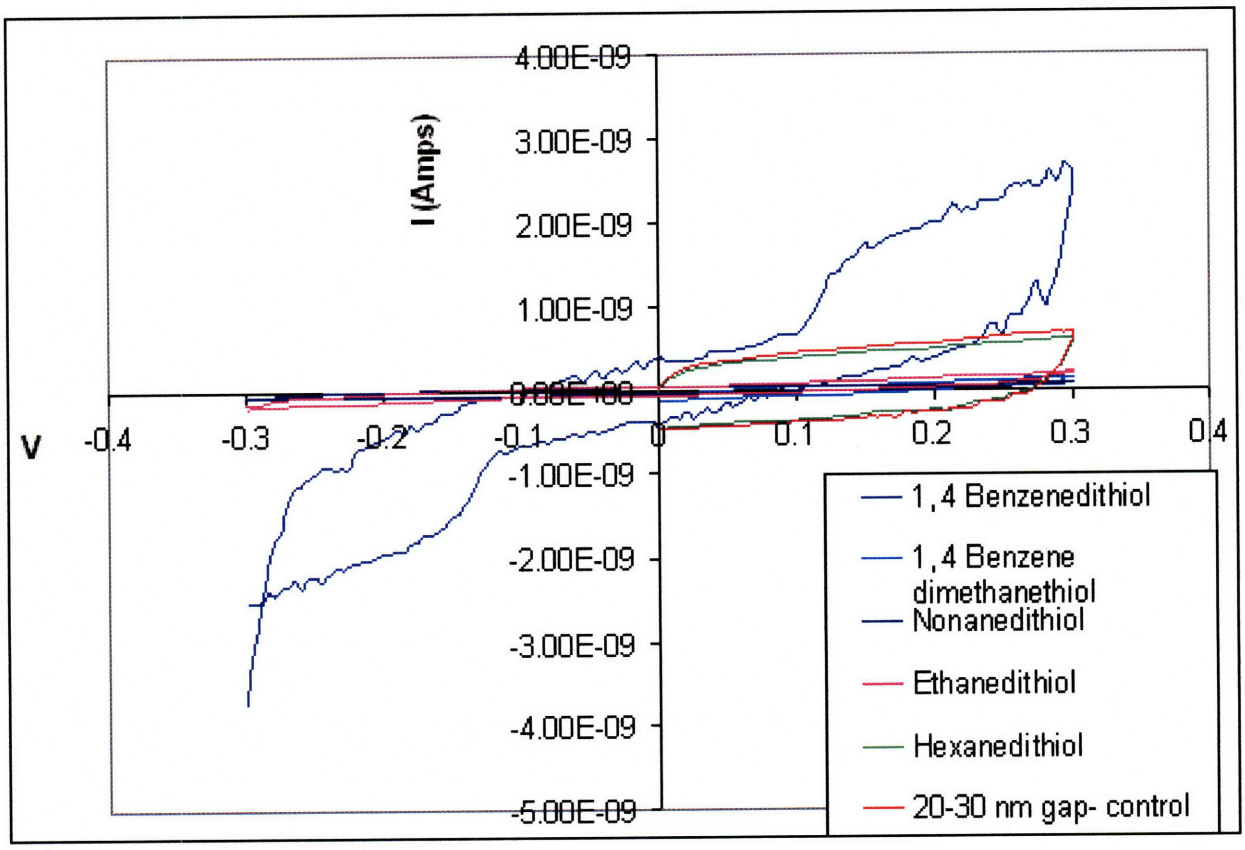

Figure 5.7: IV characteristics of nanoparticle assemblies after attempted crosslinking with various dithiols.

A second strategy to create nanoparticle assemblies which are electrically stable in aqueous solution is to decrease the number of oglionucleotides per particles. Fewer oglionucleotides creates particles which are less soluble in the buffer solution. The "stretching out" of only a few DNA strands will have a smaller swelling effect on the particle network. Particles were place exchanged with a solution of DNA having only 4

oglionucleotides per particle. The resulting IV curves in buffer solution are presented in Figure 5.8. As seen from these results, the nanoparticle assemblies decreased in conductance by 85-95%. This decrease is greater than what was seen for the particles with no DNA (10-75%) but much less than particles fully covered with DNA. If the assemblies have dry resistances of 3-60MΩ, the nanoparticle conductance will still dominate over the conductance of the salt buffer solution.

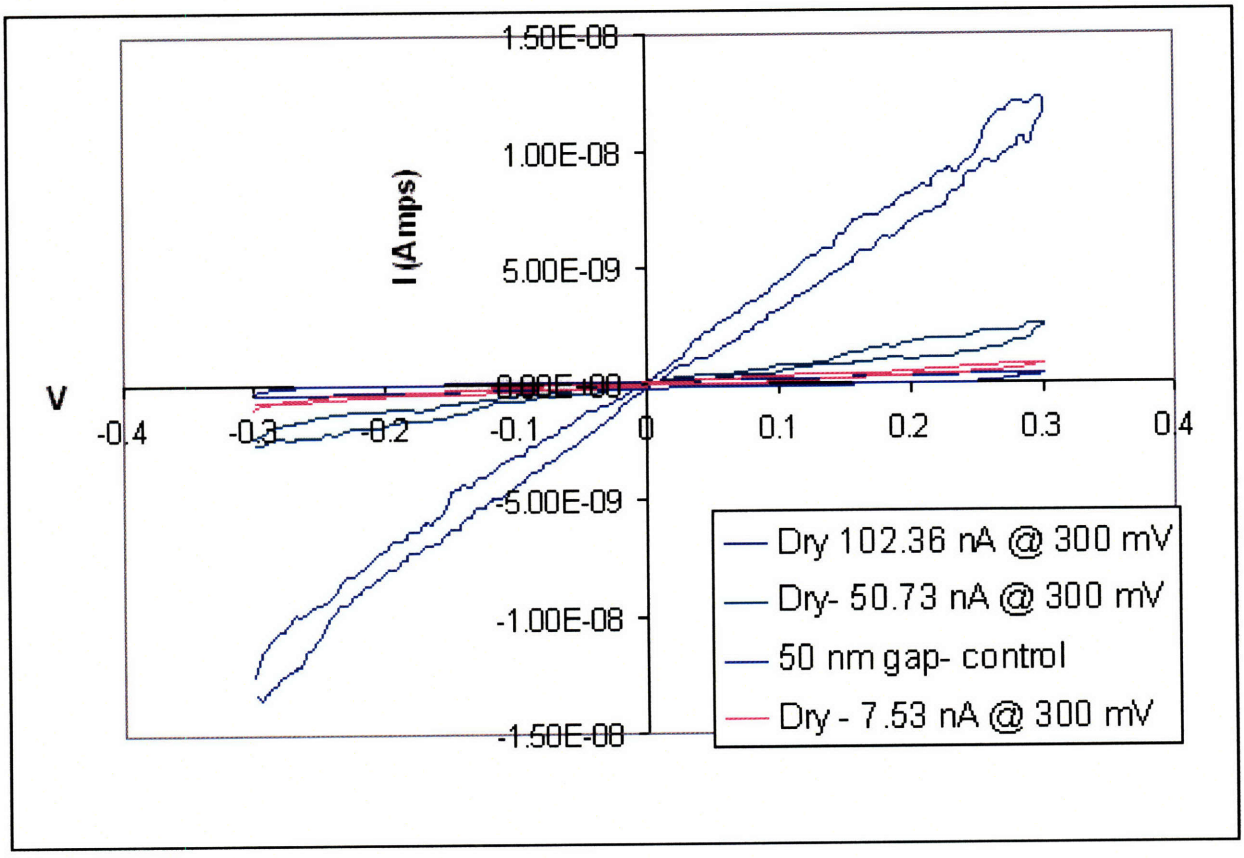

Figure 5.8: The use of particles with only 4 DNA strands/particle allows for the measurement of properties in aqueous solution.

5.3 Hybridization Experiments

In order to test the effect of hybridization on the electrical properties of the nanoparticle assemblies, it was necessary to assemble particle with both complementary and non-complementary strands of DNA. Some particles were placed exchanged with DNA A while some were exchanged with DNA B. These two types of particles were assembled onto different devices on the same substrate using DEP. Hybridization was performed with DNA A', complementary to DNA A but non-complementary to DNA B.

The 1st method used to attempt to detect DNA was to measure the dry assembly conductance before and after hybridization. The conformation change of DNA to a rigid rod upon hybridization will hopefully cause the particle core-core distance to increase even after drying, leading to a change in resistance. In a typical experiment, the assembly resistance was measured initially, after drying for 30 min at 70° C, and after an additional 30 min at 70°C. The drying step is necessary to remove any water in the assembly which causes swelling and decreases conductance. The first drying cycle produces significant decreases in resistance. The resistance remains fairly stable after the 2nd drying procedure, indicating most of the water has been removed. Hybridization is performed by placing a 20 μl drop of a 1 μM solution of DNA A' in the 1M NaCl pH 7 buffered solution over the particle assemblies. The drop is allowed to sit over the assembly for 160 minutes. The drop is removed by washing with cold DI water (cold water is used to prevent spontaneous dehybridization) followed by blowing the assembly dry with compressed air. Drying is again carried out for 30 min at 70° C followed by and

additional 30 minutes at 70° C. Control experiments were performed where assemblies with DNA A were allowed to sit in a buffer solution with no DNA and assemblies with DNA B were exposed to a solution of DNA A'.

Figure 5.9 shows the results of this experiment. Unfortunately, no significant trends in resistance change after hybridization are detected in comparison with changes in the control experiments. The random reorganization of particles after exposure to the salt buffer solution and subsequent swelling may dominate any changes in resistance caused by hybridization.

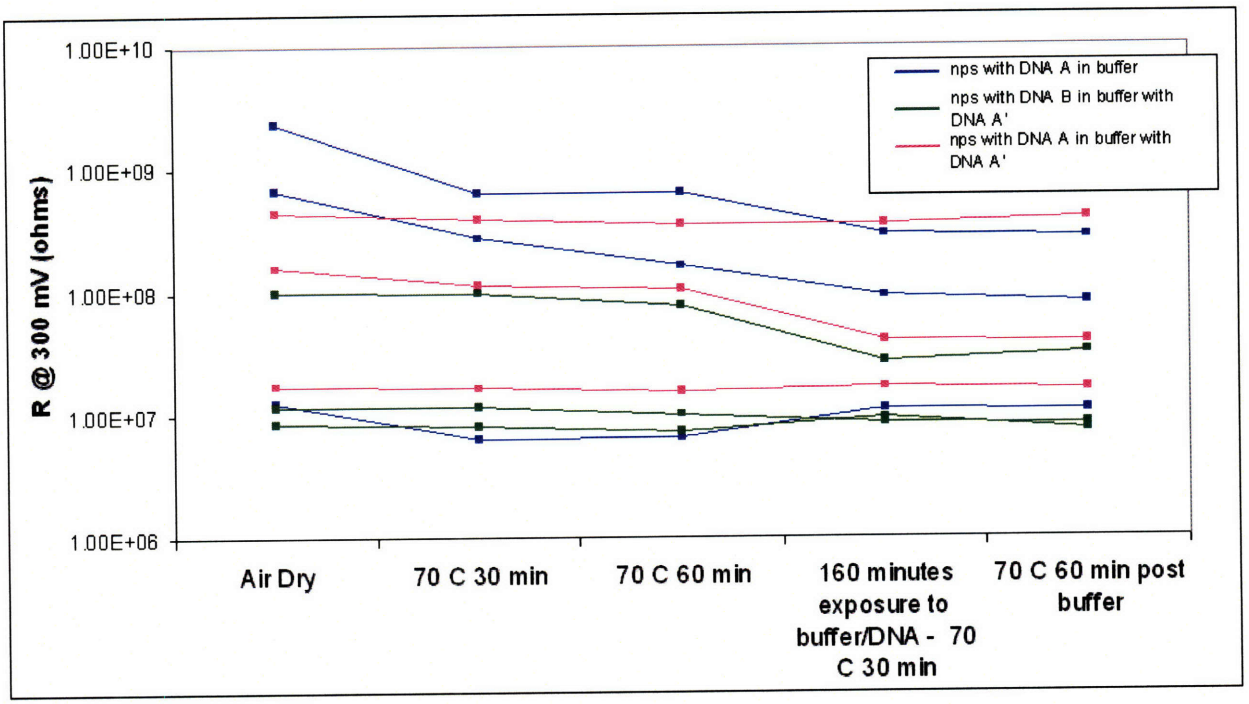

Figure 5.9: Resistance measurements at 300 mV bias of particle assemblies after various stages of drying and hybridization. No significant changes after hybridization are seen when compared with random changes seen in control experiments.

In a very recent experiment, the ability to detect DNA hybridization real time using the DNA-particle conjugates with a 4:1 oglionucleotide: particle ratio was tested. A 20 µL drop of buffer solution (without DNA) was placed over the assemblies. The electrical properties of assemblies with both DNA A and DNA B were measured. A 10µl drop of 1 µM DNA A' was then added to the original drop. Electrical measurements were performed again on the gaps at 5 and 40 minutes.

As shown in figure 5.10, a significant increase in resistance (10-55%) is seen after the DNA drop is added. Resistance continues to increase with time. Unfortunately, a similar increase is also seen in assemblies with DNA B. The effect therefore can not be attributed solely to hybridization. Swelling of the particle network may continue with longer immersion times in the buffer solution, leading to the observed decrease in assembly

conductance. Using simple resistance measurements, it has not been possible to electrically detect hybridization events.

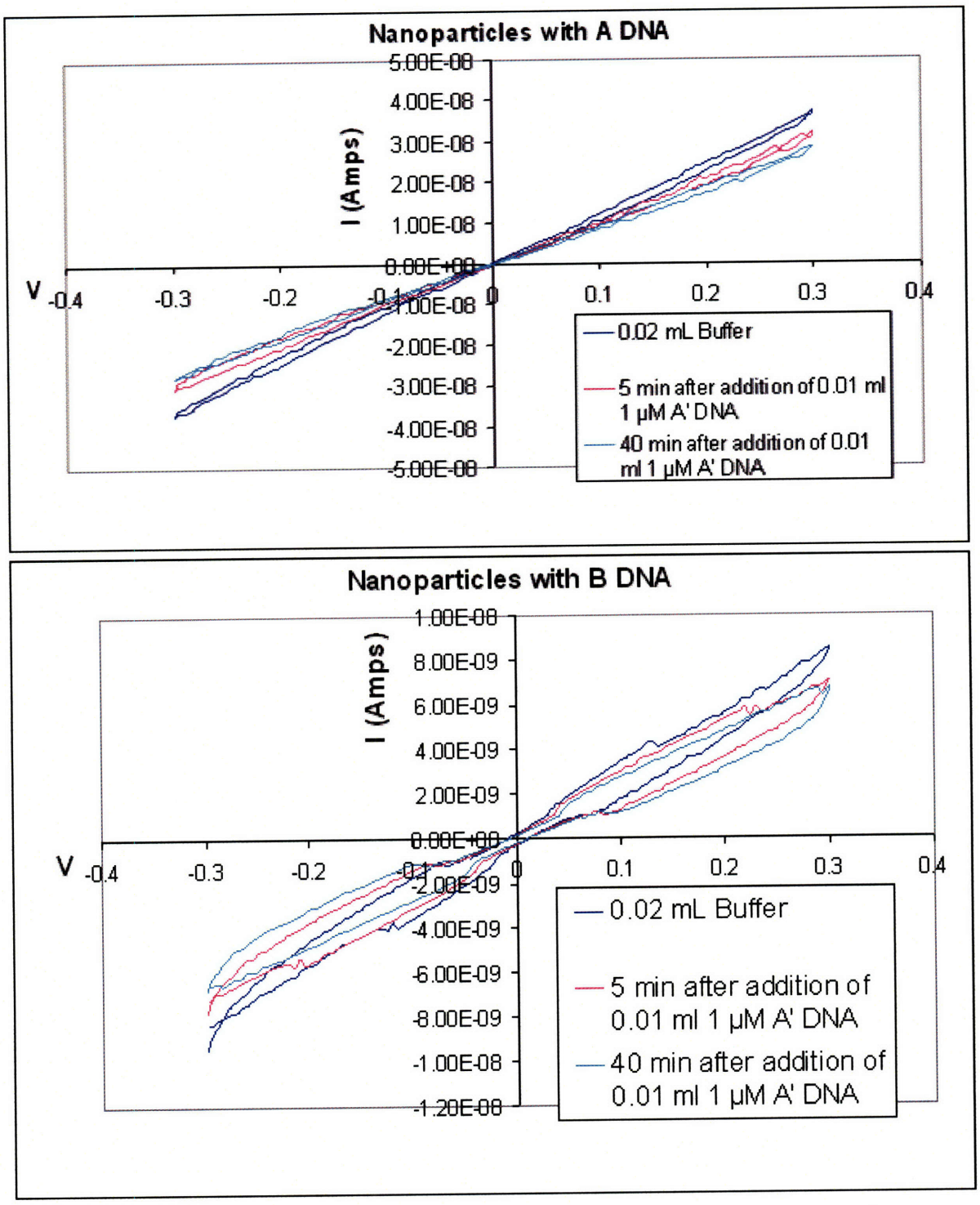

Figure 5.10: Real time measurement of nanoparticle-DNA conjugates before and after the addition of complementary (top) and non-complementary (bottom) DNA.

5.4 Future Work

While these initial efforts at electrical detection of DNA hybridization using nanomanufactured devices have failed, several possible strategies may allow for a sensing device to be achieved.

Using the current gap formation and assembly strategies, more complex electrical measurements may be used for DNA detection. The measurement of capacitance rather than resistance of the particle assembly may be more sensitive to hybridization. The use of AC impedance spectroscopy will allow for changes in phase or device impedance to be measured at AC frequencies which are the most sensitive to these changes. Future experiments may include more sophisticated methods of controlling drop size, electrode-drop contact and drop evaporation rate, allowing for more reproducible electrical measurements.

The ability to further decrease the amount of current that is attributable to ionic conductance through the buffer solution would be valuable to isolate the effects of DNA hybridization on electrical properties of the nanoparticle network. Brousseau utilized the "Bard" method to achieve this goal. In this method the metal electrode is coated with a thin polymer layer. A high electrical field is used to locally melt the polymer, opening a small hole in the insulating layer. Only a very small amount of metal electrode surface area is in contact with the drop, so very little ionic conduction occurs. Using this method on our devices, holes could be opened at the tips of the Au electrodes. DEP of nanoparticles onto these tips would allow for the nanoparticle-DNA conjugate electrical

properties to be measured with very little contribution from the surrounding ionic solution.

The ability to measure the electrical properties of a single particle (rather than an assembly of 20-100 particles) will be the best method to allow for electrical detection of DNA hybridization. If a significantly small particle can be placed across a nanogap, Coulomb charging energies can be measured and used as an indicator of hybridization. The charging energy will be significantly affected by DNA hybridization.

The major obstacle in this work for single particle measurement on a silicon platform is the nanogap size. Gap dimensions of 10-60 nm have been reported and used in this work. Ideally a sub-5 nm gap would be used for the capture of a single 5 nm particle. Efforts to further reduce gap size by better controlling the electromigration/localized melting mechanism (more sophisticated current voltage ramps) will result in smaller, more uniform gaps. Possible refinements to the DEP assembly process to allow for single particle assembly may include the addition of circuit elements (resistors, capacitors) to make the process self-limiting after a single particle assembly. These improvements will allow for the measurement of a single particle-oglionucleotide conjugate and the electrical detection of DNA hybridization.

Appendix A: Other uses of Optical and Electron Beam Lithography

In this appendix, several other projects that I have been involved with using optical and electron beam lithography are described.

A.1 Three Terminal Device Fabrication

A transistor is a three terminal device where the amount of current flowing between two of the terminals can be controlled by changes in the voltage differential between the third and the first terminal; that is the conductance of the circuit between two of the terminals depends on the third terminal. The fabrication of a device with three terminals; a source, drain and gate electrode, is necessary for the construction of a transistor. In order for a nanoparticle to be used as the active element in the transistor, a source-drain gap of approximately the same size as the nanoparticle diameter must be patterned. The gate electrode needs to have a larger gap with respect to the source and drain electrodes, so no current passes between the gate and drain electrodes. The gate electrode must still be close enough to the nanoparticle, however, that it can influence its energy levels. Ideally a 100-500 nm distance is desired.

The fabrication of a two terminal device with a source-drain gap of 20-100 nm was reported in Chapter 2. Here, I report work done on the modification of the fabrication process to produce the desired three-terminal devices by direct patterning with electron beam lithography.

Electron beam lithography was carried out following the steps outlined in section 2.1. Dose matrices with the previously optimized triangular shaped leads along with a new third gate electrode were patterned. Spacing of the third electrode was varied along with the doses of the source, drain and gate electrode. Characterization of gap sizes was performed with SEM imaging

Using electron beam lithography to create 200 nm wires with sub 100 nm gaps requires careful control of the electron beam dose. Dose matrices had been performed to yield two terminal devices with gap sizes from 30 to 100 nm. (section 2.1) The addition of a third gate electrode with a spacing of 300- 500 nm requires consideration of the proximity effect of electrons used to pattern this electrode (electron scattering). After four dose matrices were patterned, optimized doses were found for the source, drain and gate electrode. Patterning the gate electrode with a 865 nm spacing and a dose of 500 $\mu C/cm^2$ result in an average gate spacing of 802 nm (range of 776 – 834 nm). Using the same dose at a patterned spacing of 565 nm results in an average gate spacing of 483 nm (range of 439-513 nm). Source-drain gap sizes on one sample (source-drain patterned at a dose of 500 $\mu C/cm^2$) were found to decrease from 54 nm with no gate to 39.2 nm with a gate spaced 789 nm away (as shown in figure A.1) to 30 nm with a gate spaced 488 nm away.

Wires which overlap at a small junction (desired for devices where the source –drain gap is formed electrically) were optimized at a source drain dose of 500 $\mu C/cm^2$ with a gate electrode

patterned 415 nm away with a 400 $\mu C/cm^2$ dose. This resulted in slightly overlapping wires with a gate electrode ~450 nm away from the overlap.

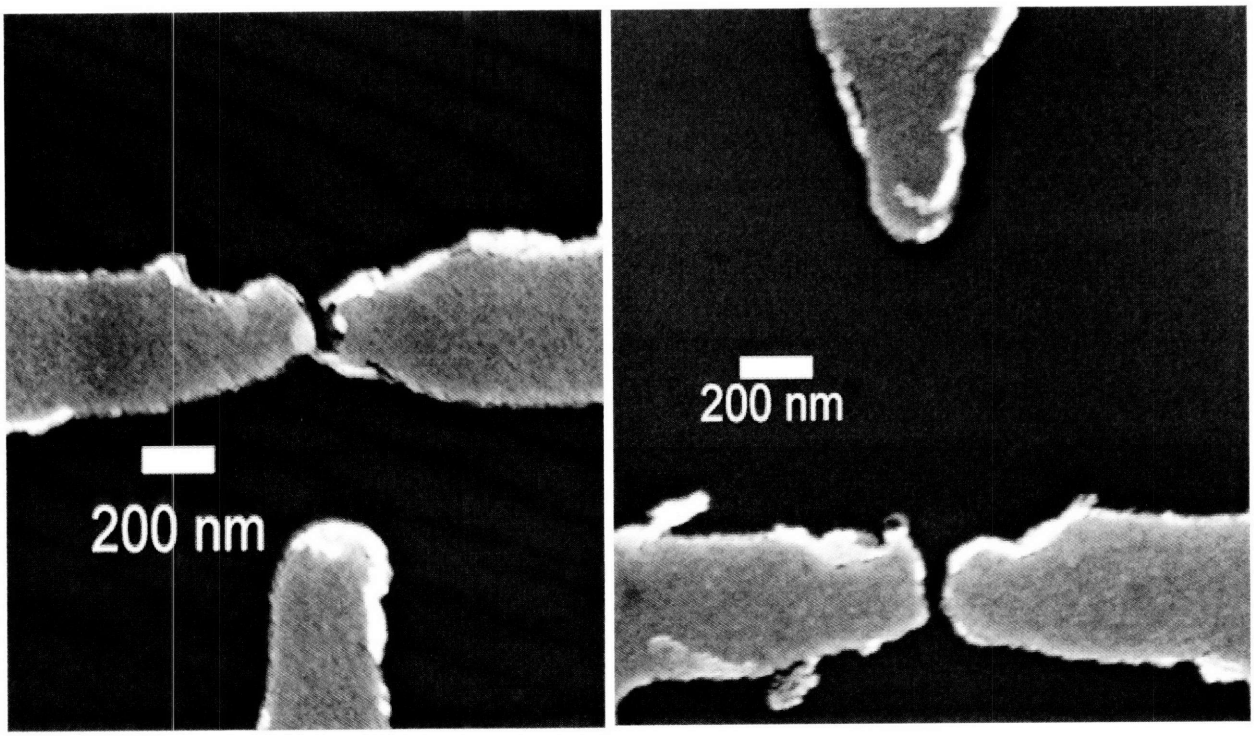

Figure A.1: Three terminal devices patterned with electron beam lithography with a source, drain and gate electrode dose of 500 $\mu C/cm^2$. Increasing the patterned gate electrode spacing from 565 nm (left) to 865 nm drastically increases the actual gate spacing and slightly increases the source-drain spacing.

A.2. Interdigitated electrode for electrical characterization of carbon nano-tubes

Some nano-objects are more difficult to assemble in small gap due to their longer lengths. In order to study the electrical properties of objects such as nanotubes, nanowires and chains of nanoparticles, it is necessary to fabricate interdigitated electrodes which can be patterned over nano-objects randomly dropped on the surface. For this fabrication process, a thicker resist (4% PMMA in anisole) was spun at 3000 RPM to yield a resist with an expected thickness of 215 nm. The thicker resist is acceptable as the feature size of the electrodes are much larger (200-1000 nm) than the dimensions of the wires discussed in chapter 2. Dose matrices were patterned with electron beam lithography to

determine the optimal prepatterned sizes and spaces, and electron beam doses. Table A.1 shows the width of the electrodes and spacing between the interdigitated electrodes (as measured by CMAFM) as a function of prepatterned size and spacing, and electron beam dose. Development, metal evaporation, lift-off and optical lithography of large pads followed a similar procedure to that which was described previously.

Functionalized carbon nanotubes were dropped onto a surface that was then patterned with electron beam lithography. Tapping mode height and phase images (figure A.2) show that carbon nanotubes are trapped underneath the interdigitated electrodes.

Table A.1

Patterned Dimensions(nm) (wire width by gap)	Dose ($\mu C/cm^2$)	Wire actual (nm)	Gap Actual (nm)
500 by 500	324	600	400
	356	625	375
	388	650	350
	421	700	300
	453	700	300
400 by 400	324	450	350
	356	500	300
	388	525	275
	421	575	225
	453	575	225
300 by 300	324	380	220
	356	400	200
	388	400	200
	421	410	190
	453	430	170

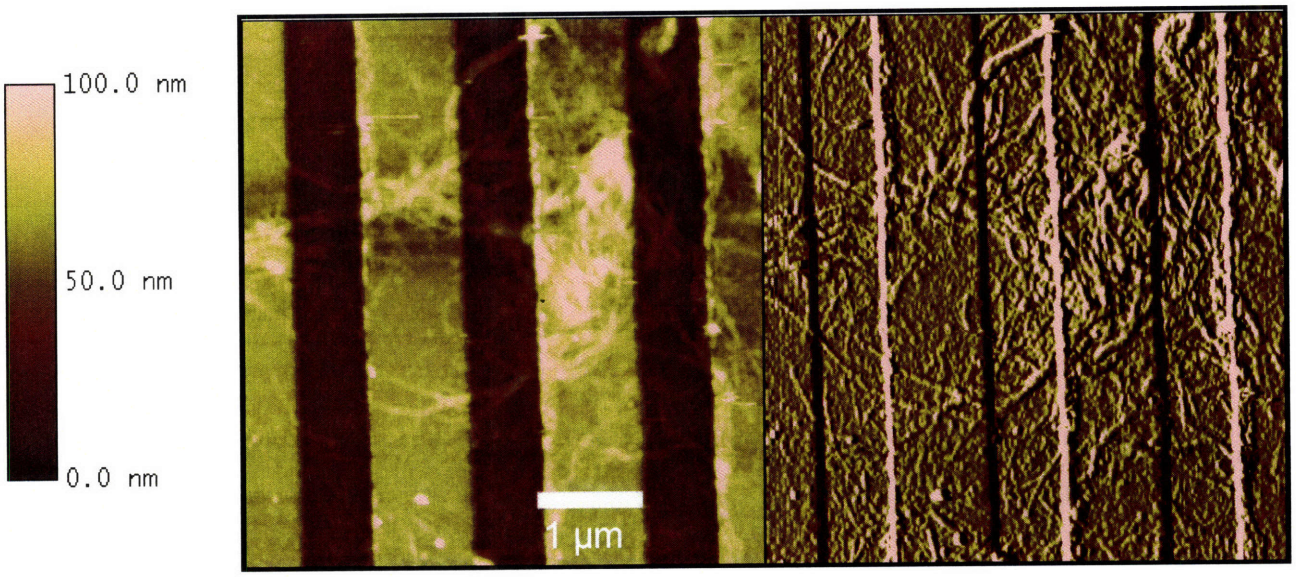

Figure A.2: Tapping mode height and phase images of inter-digitated electrodes patterned over chemically functionalized carbon nanotubes for electrical characterization.

A.3 Master Substrates and molds for Supramolecular Nano Stamping (SuNS)

SuNS is a method developed by Amy Yu and Francesco Stellacci to replicate patterns on the nanoscale using the hybridization properties of DNA.[186-188] A master pattern is required for the stamping technique. In order to fabricate a centimeter-scale master patterns, a mask was made with an array of 10µm by 10 µm square features having a 20µm pitch. I used optical lithography with this mask to create a polymer resist mold on a silicon substrate. This mold was used to generate a PDMS master substrate for SuNS. This PDMS master was used to print on optically transparent substrates.

I used this same mask to pattern an array of gold squares on a silicon substrate. The gold on silicon surface was used to print patterns onto large area PDMS surface which is introduced to the master in liquid form. Fluorescent images of the surface labeled with complementary DNA show the successful pattern transfer (figure A.3).

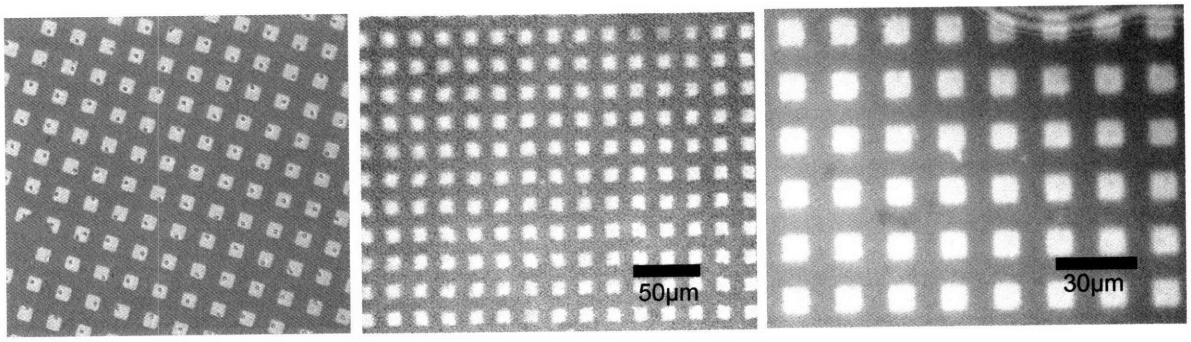

Figure A.3: Fluorescent microscopy images of (left) the master Au on Si substrates and (center, right) stamped PDMS substrate showing successful pattern transfer.

Appendix B: Other uses for Dip Pen Nanolithography

In this appendix, I outline work I have done on other projects using Dip Pen Nanolithography.

B1. DPN patterned gold wires

A unique approach to pattern metallic wires utilizes Dip Pen Nanolithography. DPN is used to pattern octadecanethiol (ODT) on a Au surface. The ODT monolayer serves as a resist when the substrate was immersed in a ferrocyanide etchant. This procedure has been shown to produce gold wires as thin as 50 nm.[158] We used this to method to produce relatively thick gold wires (1 μm) which showed conductivity 33% of bulk gold[159] as described in the section 3.1.

Unfortunately, it has been difficult to create thin wires with good electrical conductivity. Figure B.1 shows a representative gold wire with a 380 nm width and 7 nm height, whose resistivity was found to be $6*10^{-5}$ ohm-m, 3 orders of magnitude worse than that of bulk gold ($2.2*10^{-8}$ ohm-m).[159] This can be attributed to several reasons. The first major problem area deals with intrinsic DPN limitations. The dimensions of features patterned with DPN are a function of the writing speed used to pattern them. At the high writing speeds needed to pattern features with small dimensions, there is insufficient time for good self-assembled monolayer (SAM) formation to occur. An imperfect, less dense monolayer acts as a poor resist allowing for over-etching of the features. As the dimensions of the wires become smaller, small defects in the SAM can lead to discontinuous wires, as shown in figure B.1.

The second major problem area deals with the use of wet etching. Dip Pen Nanolithography can only protect the top of the Au surface with an ODT resist. Once the etching process has begun, the unprotected sides of the wires become exposed to the etchant. (figure B.1) This becomes a bigger problem as the lateral dimensions of the wire get smaller. The use of a polycrystalline gold film on a Si surface is also detrimental to the process, as the etchant molecules preferentially attack the gold grain boundaries, where the SAM has the highest density of defects.

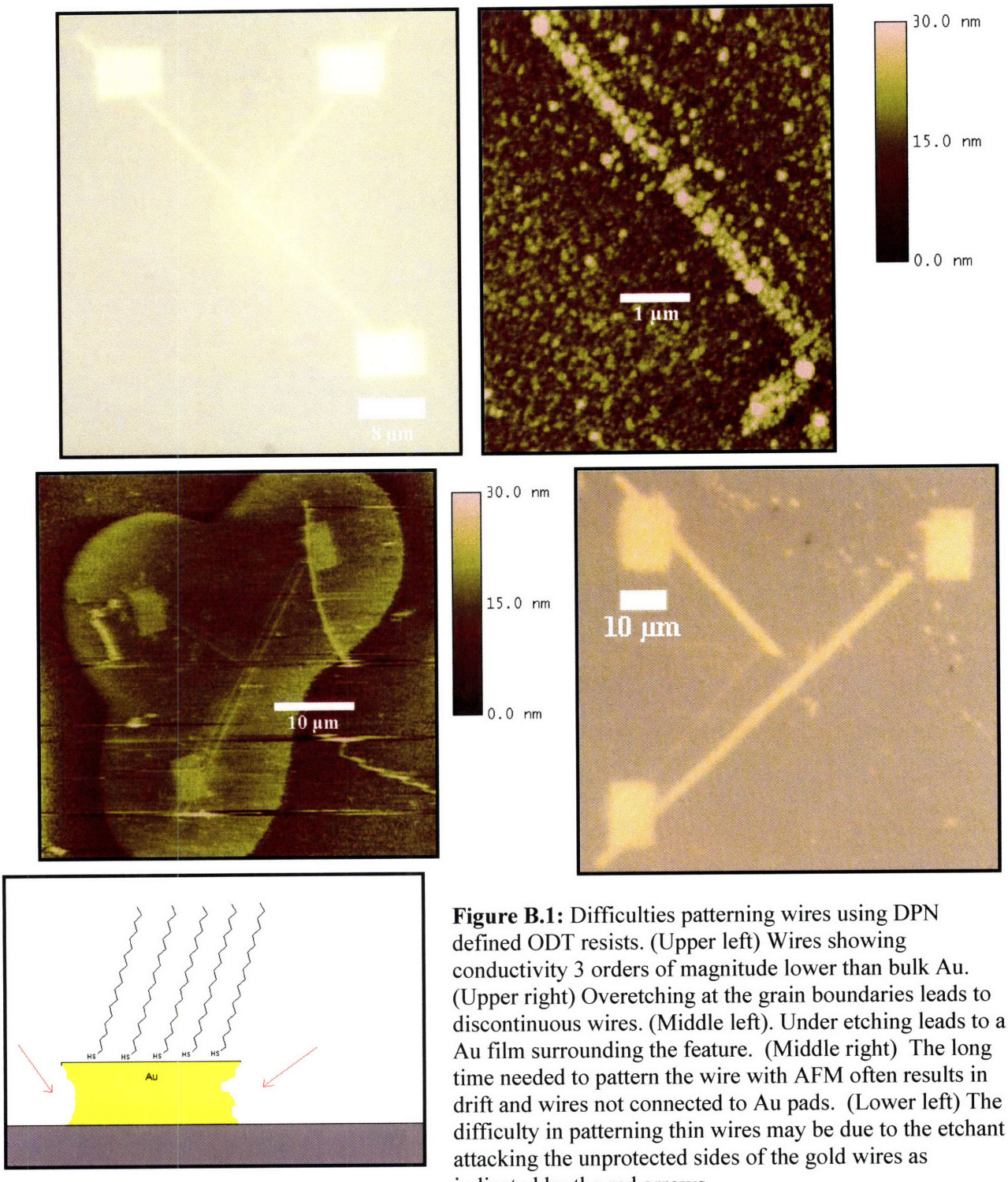

Figure B.1: Difficulties patterning wires using DPN defined ODT resists. (Upper left) Wires showing conductivity 3 orders of magnitude lower than bulk Au. (Upper right) Overetching at the grain boundaries leads to discontinuous wires. (Middle left). Under etching leads to a Au film surrounding the feature. (Middle right) The long time needed to pattern the wire with AFM often results in drift and wires not connected to Au pads. (Lower left) The difficulty in patterning thin wires may be due to the etchant attacking the unprotected sides of the gold wires as indicated by the red arrows.

DPN is a serial process, making this an extremely slow lithography technique. This presents two problems for the patterning of metallic wires and contact pads using DPN

defined resists. First, there is a tendency for some drift in AFM. Over the multiple hours required for patterning this drift may mean that the patterns do not connect properly. The second difficulty is the patterning speed. Patterning large areas with high quality SAMs is an extremely slow process, possibly two slow for even basic research applications. Parallel writing techniques described in section 1.3.1 may make patterning Au features with DPN a more effective technique.

B.2 Soft Lithography Master for SuNS

A gold on mica substrate was patterned with a 40μm by 40μm ODT square with DPN. This substrate was used as a master for SuNS.[186-188] The master was dipped in 4μM primary DNA solution. It was expected that only the gold surface, and not the ODT pattern, would be covered by DNA. After hybridization with complementary DNA modified with thiol functional groups, this pattern was transferred onto a secondary substrate. The printed pattern was immersed in a solution of primary DNA strands labeled with Rhodamin green dye. After cleaning, the secondary substrate was imaged with a fluorescence microscope using a green filter.(figure B.2) In the fluorescence image, the darker box, compared to the brighter background, shows that the printing was successful. This is an example proving SuNS is compatible with soft lithographies.

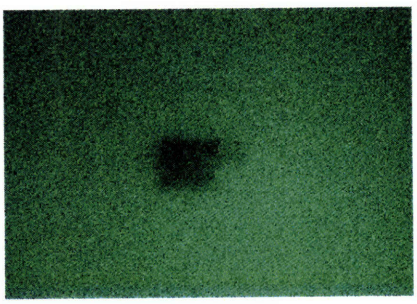

Figure B.2: Fluorescent image of the stamped substrate, showing the pattern transfer of the 40 μm by 40 μm ODT square written on the master substrate with DPN.

B.3 Chemically Directed Assembly

B.3.1 Chemically Directed Assembly of Au Nanorods

The ionic based chemically directed assembly strategy described in section 3.1.2 has been used to direct the assembly of Au nanorods, 10-20 nm in width with aspect ratios of ~2-3. DPN was again used to pattern nanoscale features of MHA on the surface. Cu^{2+} ions were used to create an electrostatic "sandwich" between the surface bound carboxylate and the carboxylate groups on the MUA functionalized nanorods. Due to their slower kinetics of diffusion, long immersion times were needed to assemble the Au nanorods. This caused nanorod aggregation and excess non-specific absorption. To avoid these problems, a slow solvent evaporation method was used (figure B.3), whereby the substrate was suspended vertically in an open vial of the nanorod solution. As the solvent evaporates, gravity helps to prevent non-specific absorption. The nanorods are forced into contact with the MHA-Cu^{2+} patterned features. Using this method, nanorods were successfully assembled on 5 lines of MHA patterned with DPN. Tapping mode AFM phase images allow for the imaging of individual rods. (figure B.3)

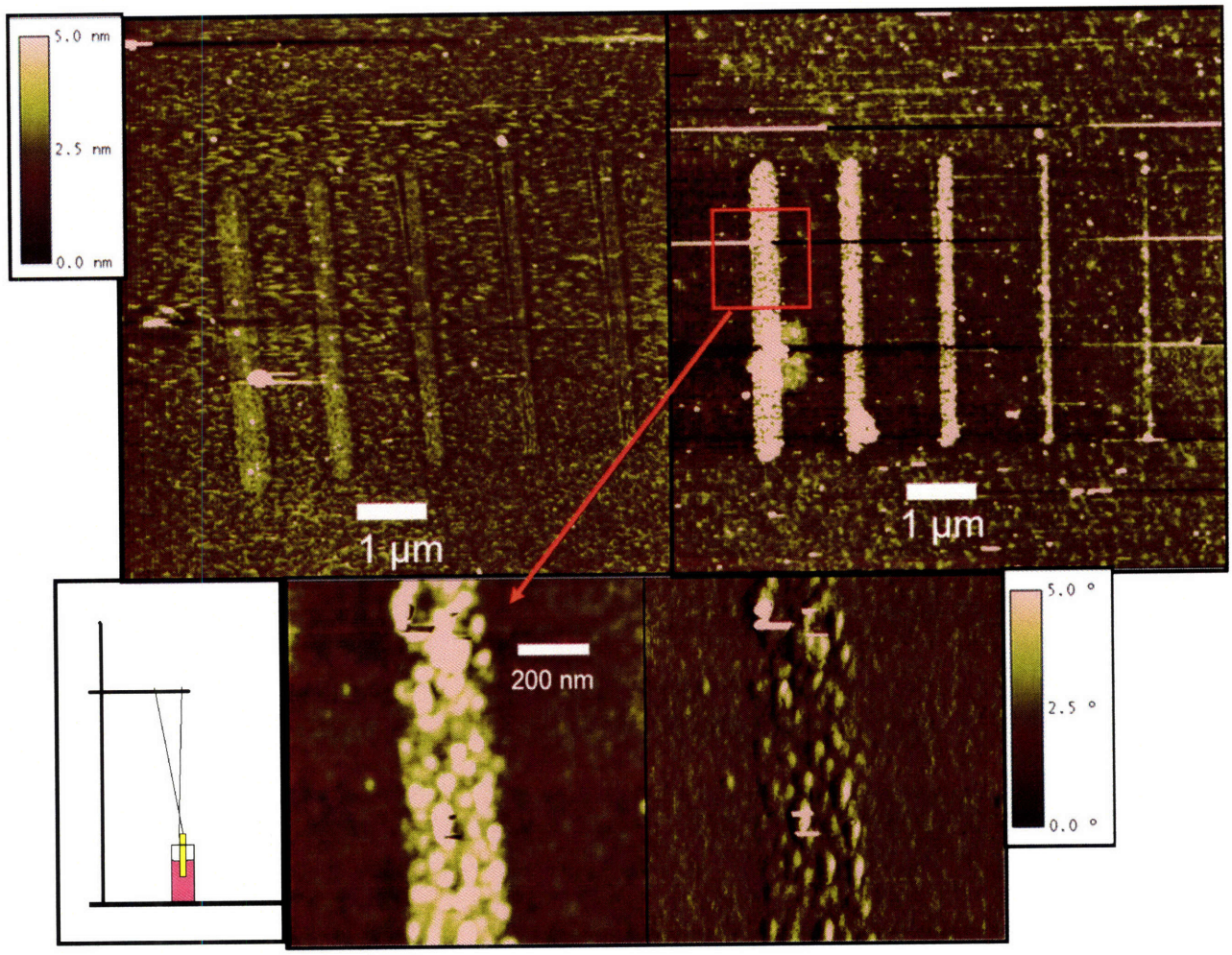

Figure B.3: Contact mode AFM images of MHA features (top left) before and (top right) after Au nanorods assembly using Cu^{2+} ions. (Bottom left) A slow solvent evaporation method is used to assemble the nanorods. Tapping mode (bottom center) height and (bottom right) phase images show individual assembled nanorods.

B.3.2 Chemically Directed Assembly of Viruses

DPN has also been used to pattern features of thiolated streptavidin onto Au surfaces in a collaboration with the Belcher group. Viruses with biotin groups can be assembled onto the patterned features via the streptavidin-biotin bond. Figure B.4 shows LFM images of

patterned thiolated streptavidin and the directed assembly of viruses on the patterned feature.

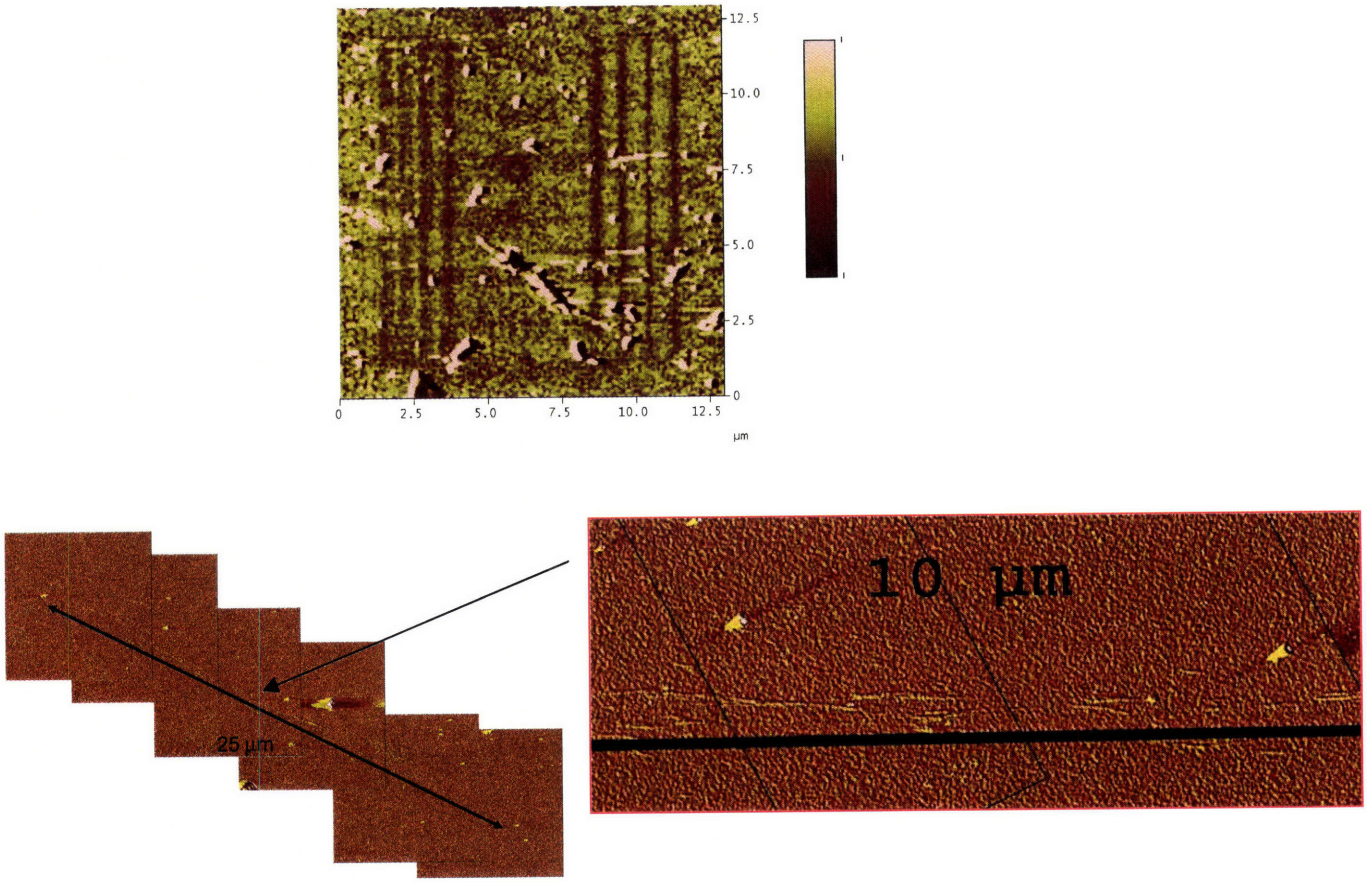

Figure B.4: (top) Frictional force image of lines of thiolated streptavidin patterned with DPN. (bottom) Tapping mode height images of the chemically directed assembly of viruses with biotin groups onto a 25 µm long line of thiolated streptavidin patterned with DPN.

References

[1] D. L. Feldheim, C. D. Keating, *Chemical Society Reviews* 1998, *27*, 1.

[2] M. Brust, M. Walker, D. Bethell, D. J. Schiffrin, R. Whyman, *Journal of the Chemical Society-Chemical Communications* 1994, 801.

[3] G. Frens, *Nature-Physical Science* 1973, *241*, 20.

[4] M. J. Hostetler, S. J. Green, J. J. Stokes, R. W. Murray, *Journal of the American Chemical Society* 1996, *118*, 4212.

[5] M. J. Hostetler, A. C. Templeton, R. W. Murray, *Langmuir* 1999, *15*, 3782.

[6] D. L. Klein, P. L. McEuen, J. E. B. Katari, R. Roth, A. P. Alivisatos, *Applied Physics Letters* 1996, *68*, 2574.

[7] H. Park, A. K. L. Lim, A. P. Alivisatos, J. Park, P. L. McEuen, *Applied Physics Letters* 1999, *75*, 301.

[8] M. F. Lambert, M. F. Goffman, J. P. Bourgoin, P. Hesto, *Nanotechnology* 2003, *14*, 772.

[9] A. Zabet-Khosousi, Y. Suganuma, K. Lopata, P. E. Trudeau, A. A. Dhirani, B. Statt, *Physical Review Letters* 2005, *94*.

[10] L. F. Sun, S. N. Chin, E. Marx, K. S. Curtis, N. C. Greenham, C. J. B. Ford, *Nanotechnology* 2005, *16*, 631.

[11] R. Krahne, T. Dadosh, Y. Gordin, A. Yacoby, H. Shtrikman, D. Mahalu, J. Sperling, I. Bar-Joseph, *Physica E-Low-Dimensional Systems & Nanostructures* 2003, *17*, 498.

[12] S. M. Dirk, S. W. Howell, S. Zmuda, K. Childs, M. Blain, R. J. Simonson, D. R. Wheeler, *Nanotechnology* 2005, *16*, 1983.

[13] M. M. Deshmukh, A. L. Prieto, Q. Gu, H. Park, *Nano Letters* 2003, *3*, 1383.

[14] M. D. Fischbein, M. Drndic, *Applied Physics Letters* 2006, *88*.

[15] S. Ghosh, H. Halimun, A. K. Mahapatro, J. Choi, S. Lodha, D. Janes, *Applied Physics Letters* 2005, *87*.

[16] G. S. McCarty, *Nano Letters* 2004, *4*, 1391.

[17] A. R. Champagne, A. N. Pasupathy, D. C. Ralph, *Nano Letters* 2005, *5*, 305.

[18] M. A. Reed, C. Zhou, C. J. Muller, T. P. Burgin, J. M. Tour, *Science* 1997, *278*, 252.

[19] P. Visconti, A. Della Torre, G. Maruccio, E. D'Amone, A. Bramanti, R. Cingolani, R. Rinaldi, *Nanotechnology* 2004, *15*, 807.

[20] Y. V. Kervennic, D. Vanmaekelbergh, L. P. Kouwenhoven, H. S. J. Van der Zant, *Applied Physics Letters* 2003, *83*, 3782.

[21] M. G. Blamire, *Superconductor Science & Technology* 2006, *19*, S132.

[22] W. Wernsdorfer, D. Mailly, A. Benoit, *Journal of Applied Physics* 2000, *87*, 5094.

[23] P. Steinmann, J. M. R. Weaver, *Applied Physics Letters* 2005, *86*.

[24] M. A. Guillorn, D. W. Carr, R. C. Tiberio, E. Greenbaum, M. L. Simpson, *Journal of Vacuum Science & Technology B* 2000, *18*, 1177.

[25] Y. V. Kervennic, H. S. J. Van der Zant, A. F. Morpurgo, L. Gurevich, L. P. Kouwenhoven, *Applied Physics Letters* 2002, *80*, 321.

[26] P. Visconti, G. Maruccio, E. D'Amone, A. Della Torre, A. Bramanti, R. Cingolani, R. Rinaldi, *Materials Science & Engineering C-Biomimetic and Supramolecular Systems* 2003, *23*, 889.
[27] A. F. Morpurgo, C. M. Marcus, D. B. Robinson, *Applied Physics Letters* 1999, *74*, 2084.
[28] C. Z. Li, H. X. He, N. J. Tao, *Applied Physics Letters* 2000, *77*, 3995.
[29] C. Zhou, C. J. Muller, M. R. Deshpande, J. W. Sleight, M. A. Reed, *Applied Physics Letters* 1995, *67*, 1160.
[30] S. B. Carlsson, T. Junno, L. Montelius, L. Samuelson, *Applied Physics Letters* 1999, *75*, 1461.
[31] Q. T. Do, H. Clemens, A. Lorke, *Proceedings IEEE- Nano 2003* 2003, *2*, 774.
[32] P. Steinmann, J. M. R. Weaver, *Journal of Vacuum Science & Technology B* 2004, *22*, 3178.
[33] E. P. De Poortere, H. L. Stormer, L. M. Huang, S. J. Wind, S. O'Brien, M. Huang, J. Hone, *Applied Physics Letters* 2006, *88*.
[34] J. Choi, K. Lee, D. B. Janes, *Nano Letters* 2004, *4*, 1699.
[35] G. K. Ramachandran, M. D. Edelstein, D. L. Blackburn, J. S. Suehle, E. M. Vogel, C. A. Richter, *Nanotechnology* 2005, *16*, 1294.
[36] A. K. Mahapatro, S. Ghosh, D. B. Janes, *Ieee Transactions on Nanotechnology* 2006, *5*, 232.
[37] G. Esen, M. S. Fuhrer, *Applied Physics Letters* 2005, *87*.
[38] D. R. Strachan, D. E. Smith, D. E. Johnston, T. H. Park, M. J. Therien, D. A. Bonnell, A. T. Johnson, *Applied Physics Letters* 2005, *86*.
[39] M. Austin, S. Y. Chou, *Journal of Vacuum Science & Technology B* 2002, *20*, 665.
[40] A. K. Mahapatro, A. Scott, A. Manning, D. B. Janes, *Applied Physics Letters* 2006, *88*.
[41] A. N. Shipway, E. Katz, I. Willner, *Chemphyschem* 2000, *1*, 18.
[42] R. D. Piner, Z. Jin, X. Feng, S. H. Hong, C. A. Mirkin, *Science* 1999, *283*, 661.
[43] S. H. Hong, J. Zhu, C. A. Mirkin, *Science* 1999, *286*, 523.
[44] S. Rozhok, R. Piner, C. A. Mirkin, *Journal of Physical Chemistry B* 2003, *107*, 751.
[45] J. Y. Jang, S. H. Hong, G. C. Schatz, M. A. Ratner, *Journal of Chemical Physics* 2001, *115*, 2721.
[46] B. L. Weeks, A. Noy, A. E. Miller, J. J. De Yoreo, *Physical Review Letters* 2002, *88*, 255505.
[47] D. S. Ginger, H. Zhang, C. A. Mirkin, *Angewandte Chemie, International Edition* 2004, *43*, 30.
[48] A. Ivanisevic, C. A. Mirkin, *Journal of the American Chemical Society* 2001, *123*, 7887.
[49] H. Jung, R. Kulkarni, C. P. Collier, *Journal of the American Chemical Society* 2003, *125*, 12096.
[50] S. E. Kooi, L. A. Baker, P. E. Sheehan, L. J. Whitman, *Advanced Materials* 2004, *16*, 1013.
[51] B. W. Maynor, Y. Li, J. Liu, *Langmuir* 2001, *17*, 2575.

[52] Y. Li, B. W. Maynor, J. Liu, *Journal of the American Chemical Society* 2001, *123*, 2105.
[53] L. M. Demers, D. S. Ginger, S. J. Park, Z. Li, S. W. Chung, C. A. Mirkin, *Science* 2002, *296*, 1836.
[54] J. H. Lim, C. A. Mirkin, *Advanced Materials* 2002, *14*, 1474.
[55] L. Fu, X. G. Liu, Y. Zhang, V. P. Dravid, C. A. Mirkin, *Nano Letters* 2003, *3*, 757.
[56] R. McKendry, W. T. S. Huck, B. Weeks, M. Fiorini, C. Abell, T. Rayment, *Nano Letters* 2002, *2*, 713.
[57] G. Degenhart, B. Dordi, H. Schonherr, G. J. Vansco, *Langmuir* 2004, *2004*, 6216.
[58] M. Su, V. P. Dravid, *Applied Physics Letters* 2002, *80*, 4434.
[59] P. E. Sheehan, L. J. Whitman, *Physical Review Letters* 2002, *88*, 156104.
[60] K. Salaita, S. W. Lee, X. F. Wang, L. Huang, T. M. Dellinger, C. Liu, C. A. Mirkin, *Small* 2005, *1*, 940.
[61] M. Zhang, D. Bullen, S. W. Chung, S. Hong, K. S. Ryu, Z. F. Fan, C. A. Mirkin, C. Liu, *Nanotechnology* 2002, *13*, 212.
[62] D. Bullen, S. W. Chung, X. F. Wang, J. Zou, C. A. Mirkin, C. Liu, *Applied Physics Letters* 2004, *84*, 789.
[63] P. E. Sheehan, L. J. Whitman, W. P. King, B. A. Nelson, *Applied Physics Letters* 2004, *85*, 1589.
[64] R. G. Chapman, E. Ostuni, L. Yan, G. M. Whitesides, *Langmuir* 2000, *16*, 6927.
[65] J. Hyun, S. J. Ahn, W. K. Lee, A. Chilkoti, S. Zauscher, *Nano Letters* 2002, *2*, 1203.
[66] L. M. Demers, C. A. Mirkin, *Angewandte Chemie-International Edition* 2001, *40*, 3069.
[67] H. H. J. Persson, W. R. Caseri, U. W. Suter, *Langmuir* 2001, *17*, 3643.
[68] H. J. Himmel, K. Weiss, B. Jager, O. Dannenberger, M. Grunze, C. Woll, *Langmuir* 1997, *13*, 4943.
[69] S. T. Liu, R. Maoz, J. Sagiv, *Nano Letters* 2004, *4*, 845.
[70] S. T. Liu, R. Maoz, G. Schmid, J. Sagiv, *Nano Letters* 2002, *2*, 1055.
[71] H. Zhang, K. B. Lee, Z. Li, C. A. Mirkin, *Nanotechnology* 2003, *14*, 1113.
[72] R. C. Major, X. Y. Zhu, *Journal of the American Chemical Society* 2003, *125*, 8454.
[73] F. P. Zamborini, L. E. Smart, M. C. Leopold, R. W. Murray, *Analytica Chimica Acta* 2003, *496*, 3.
[74] H. Zhang, Z. Li, C. A. Mirkin, *Advanced Materials* 2002, *14*, 1472.
[75] Y. N. Xia, G. M. Whitesides, *Angewandte Chemie-International Edition* 1998, *37*, 551.
[76] R. Maoz, E. Frydman, S. R. Cohen, J. Sagiv, *Advanced Materials* 2000, *12*, 424.
[77] L. Yan, X. M. Zhao, G. M. Whitesides, *Journal of the American Chemical Society* 1998, *120*, 6179.
[78] J. Liu, T. Lee, D. B. Janes, B. L. Walsh, M. R. Melloch, J. M. Woodall, R. Reifenberger, R. P. Andres, *Applied Physics Letters* 2000, *77*, 373.

[79] C. H. Lu, F. Wei, N. Z. Wu, L. Huang, X. S. Zhao, X. M. Jiao, C. Q. Luo, W. X. Cao, *Langmuir* 2004, *20*, 974.
[80] B. Kannan, R. P. Kulkarni, A. Majumdar, *Nano Letters* 2004, *4*, 1521.
[81] S. Hoeppener, R. Maoz, S. R. Cohen, L. F. Chi, H. Fuchs, J. Sagiv, *Advanced Materials* 2002, *14*, 1036.
[82] Q. G. Li, J. W. Zheng, Z. F. Liu, *Langmuir* 2003, *19*, 166.
[83] J. W. Zheng, Z. H. Zhu, H. F. Chen, Z. F. Liu, *Langmuir* 2000, *16*, 4409.
[84] L. M. Demers, S. J. Park, T. A. Taton, Z. Li, C. A. Mirkin, *Angewandte Chemie-International Edition* 2001, *40*, 3071.
[85] K. B. Lee, J. H. Lim, C. A. Mirkin, *Journal of the American Chemical Society* 2003, *125*, 5588.
[86] S. W. Chung, D. S. Ginger, M. W. Morales, Z. F. Zhang, V. Chandrasekhar, M. A. Ratner, C. A. Mirkin, *Small* 2005, *1*, 64.
[87] H. A. Pohl, *Dielectrophoresis*, Cambridge University Press, Cambridge, 1978.
[88] P. J. Burke, in *Encyclopedia of Nanoscience and Nanotechnology, Vol. 6* (Ed.: H. S. Nawla), American Scientific Publishers, Stevenson Ranch, CA, 2004, pp. 623.
[89] M. P. Hughes, *Nanotechnology* 2000, *11*, 124.
[90] R. Pethig, *Critical Reviews in Biotechnology* 1996, *16*, 331.
[91] A. Rosenthal, B. M. Taff, J. Voldman, *Lab Chip* 2006, *6*, 508.
[92] A. Rosenthal, J. Voldman, *Biophysical Journal* 2005, *88*, 2193.
[93] B. M. Taff, J. Voldman, *Analytical Chemistry* 2005, *77*, 7976.
[94] G. Fuhr, H. Glasser, T. Muller, T. Schnelle, *Biochimica Et Biophysica Acta-General Subjects* 1994, *1201*, 353.
[95] F. F. Becker, X. B. Wang, Y. Huang, R. Pethig, J. Vykoukal, P. R. C. Gascoyne, *Proceedings of the National Academy of Sciences of the United States of America* 1995, *92*, 860.
[96] L. F. Zheng, J. P. Brody, P. J. Burke, *Biosensors & Bioelectronics* 2004, *20*, 606.
[97] L. F. Zheng, S. D. Li, J. P. Brody, P. J. Burke, *Langmuir* 2004, *20*, 8612.
[98] K. H. Bhatt, O. D. Velev, *Langmuir* 2004, *20*, 467.
[99] K. D. Hermanson, S. O. Lumsdon, J. P. Williams, E. W. Kaler, O. D. Velev, *Science* 2001, *294*, 1082.
[100] S. O. Lumsdon, E. W. Kaler, O. D. Velev, *Langmuir* 2004, *20*, 2108.
[101] A. Bezryadin, C. Dekker, G. Schmid, *Applied Physics Letters* 1997, *71*, 1273.
[102] A. Bezryadin, R. M. Westervelt, M. Tinkham, *Applied Physics Letters* 1999, *74*, 2699.
[103] I. Amlani, A. M. Rawlett, L. A. Nagahara, R. K. Tsui, *Journal of Vacuum Science & Technology B* 2002, *20*, 2802.
[104] I. Amlani, A. M. Rawlett, L. A. Nagahara, R. K. Tsui, *Applied Physics Letters* 2002, *80*, 2761.
[105] A. M. Rawlett, T. J. Hopson, I. Amlani, R. Zhang, J. Tresek, L. A. Nagahara, R. K. Tsui, H. Goronkin, *Nanotechnology* 2003, *14*, 377.
[106] S. I. Khondaker, *Iee Proceedings-Circuits Devices and Systems* 2004, *151*, 457.
[107] S. I. Khondaker, Z. Yao, *Applied Physics Letters* 2002, *81*, 4613.

[108] H. Fudouzi, M. Kobayashi, N. Shinya, *Journal of Nanoparticle Research* 2001, *3*, 193.
[109] S. H. Hong, H. K. Kim, B. C. Kim, Y. S. Choi, J. S. Hwang, D. Ahn, S. K. Kwak, D. J. Ahn, S. W. Hwang, *Journal of the Korean Physical Society* 2004, *45*, S665.
[110] S. O. Lumsdon, D. M. Scott, *Langmuir* 2005, *21*, 4874.
[111] J. Y. Chung, K. H. Lee, J. H. Lee, R. S. Ruoff, *Langmuir* 2004, *20*, 3011.
[112] S. N. Lu, J. Chung, R. S. Ruoff, *Nanotechnology* 2005, *16*, 1765.
[113] H. W. Seo, C. S. Han, D. G. Choi, K. S. Kim, Y. H. Lee, *Microelectronic Engineering* 2005, *81*, 83.
[114] R. Krupke, F. Hennrich, M. M. Kappes, H. V. Lohneysen, *Nano Letters* 2004, *4*, 1395.
[115] Z. B. Zhang, X. J. Liu, E. E. B. Campbell, S. L. Zhang, *Journal of Applied Physics* 2005, *98*.
[116] D. L. Fan, F. Q. Zhu, R. C. Cammarata, C. L. Chien, *Physical Review Letters* 2005, *94*.
[117] D. L. Fan, F. Q. Zhu, R. C. Cammarata, C. L. Chien, *Applied Physics Letters* 2004, *85*, 4175.
[118] J. J. Boote, S. D. Evans, *Nanotechnology* 2005, *16*, 1500.
[119] A. Subramanian, B. Vikramaditya, L. Dong, D. Bell, B. Nelson, in *Robotics Science and Systems I* (Eds.: S. Thrun, G. Sukhatme, S. Schaal, O. Brock), MIT Press, Cambridge, 2005, pp. 327.
[120] D. V. Averin, K. K. Likharev, *Journal of Low Temperature Physics* 1986, *62*, 345.
[121] J. H. Fendler, *Nanoparticles and nanostructured films : preparation, characterization and applications*, Wiley-VCH, Weinheim, 1998.
[122] J. B. Barner, S. T. Ruggiero, *Physical Review Letters* 1987, *59*, 807.
[123] D. L. Feldheim, C. A. Foss, *Metal nanoparticles : synthesis, characterization, and applications*, Marcel Dekker, New York, 2002.
[124] G. L. Timp, *Nanotechnology*, AIP Press, New York, 1999.
[125] H. Grabert, M. H. Devoret, North Atlantic Treaty Organization. Scientific Affairs Division., *Single charge tunneling : Coulomb blockade phenomena in nanostructures*, Plenum Press, New York, 1992.
[126] P. J. Thomas, G. U. Kulkami, C. N. R. Rao, *Chemical Physics Letters* 2000, *321*, 163.
[127] D. L. Feldheim, K. C. Grabar, M. J. Natan, T. E. Mallouk, *Journal of the American Chemical Society* 1996, *118*, 7640.
[128] R. P. Andres, T. Bein, M. Dorogi, S. Feng, J. I. Henderson, C. P. Kubiak, W. Mahoney, R. G. Osifchin, R. Reifenberger, *Science* 1996, *272*, 1323.
[129] N. K. Chaki, T. G. Gopakumar, T. Maddanimath, M. Aslam, K. Vijayamohanan, *Journal of Applied Physics* 2003, *94*, 7379.
[130] C. Thelander, M. H. Magnusson, K. Deppert, L. Samuelson, P. R. Poulsen, J. Nygard, J. Borggreen, *Applied Physics Letters* 2001, *79*, 2106.
[131] E. E. Foos, J. Congdon, A. W. Snow, M. G. Ancona, *Langmuir* 2004, *20*, 10657.

[132] Y. Joseph, I. Besnard, M. Rosenberger, B. Guse, H. G. Nothofer, J. M. Wessels, U. Wild, A. Knop-Gericke, D. S. Su, R. Schlogl, A. Yasuda, T. Vossmeyer, *Journal of Physical Chemistry B* 2003, *107*, 7406.
[133] C. A. Xu, H. van Zalinge, J. L. Pearson, A. Glidle, J. M. Cooper, D. R. S. Cumming, W. Haiss, J. L. Yao, D. J. Schiffrin, M. Proupin-Perez, R. Cosstick, R. J. Nichols, *Nanotechnology* 2006, *17*, 3333.
[134] P. E. Trudeau, A. Escorcia, A. A. Dhirani, *Journal of Chemical Physics* 2003, *119*, 5267.
[135] L. C. Brousseau, Q. Zhao, D. A. Shultz, D. L. Feldheim, *Journal of the American Chemical Society* 1998, *120*, 7645.
[136] C. A. Mirkin, R. L. Letsinger, R. C. Mucic, J. J. Storhoff, *Nature* 1996, *382*, 607.
[137] A. P. Alivisatos, K. P. Johnsson, X. G. Peng, T. E. Wilson, C. J. Loweth, M. P. Bruchez, P. G. Schultz, *Nature* 1996, *382*, 609.
[138] D. Zanchet, C. M. Micheel, W. J. Parak, D. Gerion, S. C. Williams, A. P. Alivisatos, *Journal of Physical Chemistry B* 2002, *106*, 11758.
[139] D. Zanchet, C. M. Micheel, W. J. Parak, D. Gerion, A. P. Alivisatos, *Nano Letters* 2001, *1*, 32.
[140] T. M. Herne, M. J. Tarlov, *Journal of the American Chemical Society* 1997, *119*, 8916.
[141] S. R. N. Pena, S. Raina, G. P. Goodrich, N. V. Fedoroff, C. D. Keating, *Journal of the American Chemical Society* 2002, *124*, 7314.
[142] W. J. Parak, T. Pellegrino, C. M. Micheel, D. Gerion, S. C. Williams, A. P. Alivisatos, *Nano Letters* 2003, *3*, 33.
[143] D. J. Maxwell, J. R. Taylor, S. M. Nie, *Journal of the American Chemical Society* 2002, *124*, 9606.
[144] R. Elghanian, J. J. Storhoff, R. C. Mucic, R. L. Letsinger, C. A. Mirkin, *Science* 1997, *277*, 1078.
[145] S. J. Park, T. A. Taton, C. A. Mirkin, *Science* 2002, *295*, 1503.
[146] T. A. Taton, R. C. Mucic, C. A. Mirkin, R. L. Letsinger, *Journal of the American Chemical Society* 2000, *122*, 6305.
[147] T. A. Taton, C. A. Mirkin, R. L. Letsinger, *Science* 2000, *289*, 1757.
[148] G. P. Lopez, H. A. Biebuyck, G. M. Whitesides, *Langmuir* 1993, *9*, 1513.
[149] R. J. Barsotti, M. S. O'Connell, F. Stellacci, *Langmuir* 2004, *20*, 4795.
[150] C. Bain, E. B. Troughton, Y. T. Tao, J. Evall, G. M. Whitesides, R. G. Nuzzo, *Journal of the American Chemical Society* 1989, *111*, 321.
[151] M. D. Porter, T. B. Bright, D. L. Allara, C. E. Chidsey, *Journal of the American Chemical Society* 1987, *109*, 3559.
[152] A. Ulman, *Chemical Reviews* 1996, *96*, 1533.
[153] G. E. Poirier, E. D. Pylant, *Science* 1996, *272*, 1145.
[154] S. H. Hong, J. Zhu, C. A. Mirkin, *Langmuir* 1999, *15*, 7897.
[155] M. Buck, M. Grunze, F. Eisert, J. Fischer, F. Trager, *Journal of Vacuum Science & Technology a-Vacuum Surfaces and Films* 1992, *10*, 926.
[156] D. S. Karpovich, G. J. Blanchard, *Langmuir* 1994, *10*, 3315.
[157] K. B. Lee, S. J. Park, C. A. Mirkin, J. C. Smith, M. Mrksich, *Science* 2002, *295*, 1702.

[158] H. Zhang, S. W. Chung, C. A. Mirkin, *Nanoletters* 2003, *3*, 43.
[159] *CRC Handbook of Chemistry and Physics*, 2002.
[160] P. M. Mendes, S. Jacke, K. Critchley, J. Plaza, Y. Chen, K. Nikitin, R. E. Palmer, J. A. Preece, S. D. Evans, D. Fitzmaurice, *Langmuir* 2004, *20*, 3766.
[161] F. Shi, Z. Q. Wang, N. Zhao, X. Zhang, *Langmuir* 2005, *21*, 1599.
[162] H. X. He, H. Zhang, Q. G. Li, T. Zhu, S. F. Y. Li, Z. F. Liu, *Langmuir* 2000, *16*, 3846.
[163] S. S. Bae, D. K. Lim, J. I. Park, J. Cheon, I. C. Jeon, S. Kim, *Applied Physics a-Materials Science & Processing* 2005, *80*, 1305.
[164] K. Akamatsu, J. Hasegawa, H. Nawafune, H. Katayama, F. Ozawa, *Journal of Materials Chemistry* 2002, *12*, 2862.
[165] J. Lahiri, L. Isaacs, J. Tien, G. M. Whitesides, *Analytical Chemistry* 1999, *71*, 777.
[166] G. H. Degenhart, B. Dordi, H. Schonherr, G. J. Vancso, *Langmuir* 2004, *20*, 6216.
[167] J. Lahiri, E. Ostuni, G. M. Whitesides, *Langmuir* 1999, *15*, 2055.
[168] R. J. Barsotti, F. Stellacci, *Journal of Materials Chemistry* 2006, *16*, 962.
[169] S. Y. Kang, K. Kim, *Langmuir* 1998, *14*, 226.
[170] K. C. Grabar, P. C. Smith, M. D. Musick, J. A. Davis, D. G. Walter, M. A. Jackson, A. P. Guthrie, M. J. Natan, *Journal of the American Chemical Society* 1996, *118*, 1148.
[171] K. Park, S. R. Simmons, R. M. Albrecht, *Scanning Microscopy* 1987, *1*, 339.
[172] V. Y. Rudyak, S. L. Krasnolutskii, *Technical Physics* 2002, *47*, 807.
[173] S. Cabrini, R. J. Barsotti, A. Carpentiero, L. Businaro, R. P. Zaccaria, F. Stellacci, E. Di Fabrizio, *Journal of Vacuum Science & Technology B* 2005, *23*, 2806.
[174] R. J. Barsotti, M. D. Vahey, R.Wartena, Y. M. Chiang, J. Voldman, F. Stellacci, *Small* 2006 (submitted).
[175] S. H. Brewer, W. R. Glomm, M. C. Johnson, M. K. Knag, S. Franzen, *Langmuir* 2005, *21*, 9303.
[176] Y. H. M. Chan, R. Schweiss, C. Werner, M. Grunze, *Langmuir* 2003, *19*, 7380.
[177] H. C. Li, P. L. De Bruyn, *Surface Science* 1966, *5*, 203.
[178] R. J. Kershner, J. W. Bullard, M. J. Cima, *Journal of Colloid and Interface Science* 2004, *278*, 146.
[179] M. Cardenas, J. Barauskas, K. Schillen, J. L. Brennan, M. Brust, T. Nylander, *Langmuir* 2006, *22*, 3294.
[180] V. Dharuman, I. Grunwald, E. Nebling, J. Albers, L. Blohm, R. Hintsche, *Biosensors & Bioelectronics* 2005, *21*, 645.
[181] K. S. Ma, H. Zhou, J. Zoval, M. Madou, *Sensors and Actuators B-Chemical* 2006, *114*, 58.
[182] C. Tlili, H. Korri-Youssoufi, L. Ponsonnet, C. Martelet, N. J. Jaffrezic-Renault, *Talanta* 2005, *68*, 131.
[183] M. Steichen, C. Buess-Herman, *Electrochemistry Communications* 2005, *7*, 416.

[184] Y. Z. Fu, R. Yuan, L. Xu, Y. Q. Chai, X. Zhong, D. P. Tang, *Biochemical Engineering Journal* 2005, *23*, 37.
[185] L. Brousseau, *Journal of the American Chemical Society* 2006, *128*, 11346.
[186] A. A. Yu, T. Savas, S. Cabrini, E. diFabrizio, H. I. Smith, F. Stellacci, *Journal of the American Chemical Society* 2005, *127*, 16774.
[187] A. A. Yu, T. A. Savas, G. S. Taylor, A. Guiseppe-Elie, H. I. Smith, F. Stellacci, *Nano Letters* 2005, *5*, 1061.
[188] A. A. Yu, F. Stellacci, *Journal of Materials Chemistry* 2006, *16*, 2868.